DOCTORAL SCHOOL

UNIVERSITY OF MILANO-BICOCCA

Department of
PHYSISCS GIUSEPPE OCCHIALINI

Ph.D. in Physics and Astronomy - XXXII Cycle

APPLICATION AND DEVELOPMENT OF SCINTILLATION BASED DETECTORS FOR THE INVESTIGATION OF NEUTRINO PHYSICS IN DOUBLE BETA DECAY EXPERIMENTS

Beretta Mattia
Registration Number 748086

Tutor: Prof. Ezio Previtali

Coordinator: Prof. Marta Calvi

Academic year 2019/2020

Contents

1 Introduction **3**

2 Neutrino Physics and the Double Beta Decay **6**
2.1 A quick summary of the Standard Model . . . 6
2.2 Neutrino Oscillation and their implication . . . 8
2.2.1 Neutrino mass models . . . 10
2.3 The Double Beta Decay . . . 11
2.3.1 Nuclear Matrix Element . . . 14
2.3.2 Two neutrino Double Beta Decay investigation . . . 18

3 Experimental search for $0\nu\beta\beta$ **21**
3.1 Parameter for $0\nu\beta\beta$ search . . . 21
3.1.1 Sources of radioactive and cosmogenic background . . . 23
3.1.2 $2\nu\beta\beta$ background . . . 27
3.2 Experimental strategies . . . 28
3.2.1 Source≠Detector approach . . . 28
3.2.2 Source=Detector approach . . . 29
3.3 Scintillation detectors as possible candidate for next generation $0\nu\beta\beta$ searches . . . 32
3.3.1 The scintillator characteristics . . . 33
3.3.2 Multiple readout detectors . . . 34
3.3.3 Innovative scintillation detectors . . . 34

4 The results of CUPID-0 experiment **36**
4.1 The CUPID-0 detector . . . 36
4.2 Data analysis procedure . . . 39
4.3 Light-Heat decorrelation . . . 43
4.3.1 Single angle minimization . . . 46
4.3.2 Double angle minimization . . . 47
4.3.3 Chosen minimization method and total result . . . 48
4.4 $0\nu\beta\beta$ analysis . . . 49
4.5 Background Model . . . 53
4.5.1 Analysis of experimental spectra . . . 54
4.5.2 Simulation of background contributions . . . 54
4.5.3 Definition of the background model . . . 56
4.5.4 Model fit and result analysis . . . 59
4.6 Search of Lorentz Violation in $2\nu\beta\beta$ . . . 64
4.6.1 Predicted effect of Lorentz Violation in $2\nu\beta\beta$ . . . 65
4.6.2 Experimental test of the effects on $2\nu\beta\beta$ . . . 66
4.6.3 Systematic tests on the fit . . . 68

4.7 Conclusion and outlook 71

5 Development of innovative scintillators **74**
5.1 The FLARES strategy 74
5.1.1 Isotope choice and scintillating crystal properties 75
5.1.2 The SDD detectors 80
5.1.3 Measurement with pixelate SDDs 84
5.1.4 Characterization of large single-anode SDDs 92
5.1.5 Scintillation measurements on large area SDDs 99
5.2 The ESQUIRE project 104
5.3 Summary of the results 114
5.3.1 FLARES 114
5.3.2 ESQUIRE 114

6 Conclusion **116**

Bibliography **118**

List of figures **127**

List of tables **129**

Chapter 1

Introduction

Double beta decay ($\beta\beta$) is a rare spontaneous nuclear transition in which a nucleus (A,Z) decays to a member of the same isobaric multiplet (A,Z+2). This process can happen both with the emission of two electrons and two antineutrinos ($2\nu\beta\beta$) and with the emission of two electrons no neutrinos ($0\nu\beta\beta$). The former process is predicted by the Standard Model of particle physics (SM) and has been observed for a dozen of isotopes, while the latter is still object of research. The detection of $0\nu\beta\beta$ would unambiguously prove the existence of a lepton number violating process. Moreover, its evidence would also state that the neutrinos are Majorana fermions, that they get their mass in a fundamentally different way than the charged leptons. if $0\nu\beta\beta$ occurs, it is extremely rare. The current limits on the half-life are $> 10^{25} - 10^{26}$ years for many isotopes). The next generation of detectors must improve their sensitivity by improving the signal to noise ratio for the detection of $0\nu\beta\beta$. The experimental sensitivity is improved on one side by increasing the number of candidate isotopes under observation, the experimental live time and the detector energy resolution, and on the other by reducing the background in the region of interest (ROI) originating from spurious events. There are both technological and cost issues when trying to increase the isotope mass, while optimizing the background level and the detector energy resolution.
In this landscape, the application of scintillation detectors, containing the $0\nu\beta\beta$ candidate isotope, provides a possible solution towards the next generation of experiments. The use of scintillation detectors provide flexibility in the choice of the candidate isotope and possible mass scalability by reproducing a single performing module. In addition, the time development of scintillation light emission provides an effective tool for the reduction of spurious background. Since α particles and $\beta/\ \gamma$ particles have different scintillation characteristics, α backgrounds can be easily identified and rejected in such detectors. The drawback in the application of detectors based only on the light readout is their not optimal energy resolution. This is a fundamental requirement for a $0\nu\beta\beta$ detector, since it is needed to identify the $0\nu\beta\beta$ signal over the unavoidable background provided by the upper tail of $2\nu\beta\beta$ spectrum. This feature can be addressed in different ways.

In this thesis I present two different approaches for the application of scintillators to the search for $0\nu\beta\beta$. On one side, I show the performances of scintillating cryogenic calorimeters as powerful tools for the investigation of $\beta\beta$. In particular I present the results of CUPID-0, the fist running experiment based on this technique, designed for the investigation of the $\beta\beta$ of ^{82}Se.
CUPID-0 detector combines the high efficiency and energy resolution of bolometric detectors to the background rejection capabilities of scintillators. The detector is made of 26 cylindric ZnSe crystals of different dimensions, each coupled to two high purity germanium bolometers operated as light detectors. An energy deposition in the crystal causes both a temperature increase and a light emission due to the scintillation of ZnSe, measured by the light detectors. The heat signal gives an extremely performing energy resolution to the detector. The analysis of the light signal allows instead to reject efficiently all the α interactions in the crystal, strongly reducing the background

in the ROI. These characteristics allowed to set the best lower limit on the half life of ^{82}Se $0\nu\beta\beta$: $T^{0\nu}_{1/2} > 3.5 \cdot 10^{24}$ yr (90 % credible interval), unambiguously proving the performances of this approach.
My work in this experiment has been mainly devoted to data analysis. In particular, I took part in the definition of the background model of the experiment. Starting from this result, I performed a shape analysis on the $2\nu\beta\beta$ spectrum, putting a limit on the violation of Lorentz symmetry in the neutrino sector. Alongside this main task, I worked on the data monitoring and detector maintenance and on the definition of a method to decorrelate the emitted light from the acquired heat, further increasing the energy resolution.

As a second possible application, I present the research and development of new scintillation detectors, based on the use of high performance solid state detectors to read the light emitted by scintillation crystals containing a $0\nu\beta\beta$ candidate isotope. These scintillators are limited in resolution by the number of collected photons, but are characterized by the possibility to be mass-scaled with relative ease, while keeping a low level of spurious background.
The work I present is divided between two different R&D projects:

- the FLARES (Flexible Light Apparatus for Rare Events Search) project, which proposes the development of a detector based on the use of Silicon Drift Detectors (SDD) to read the light emitted by large scintillation crystals, cooled at 120K.
- the ESQUIRE (Experiment with Scintillating QUantum dots for Ionizing Radiation Events) project, based on the development of a new generation of radiation detectors based on scintillating nanocrystals.

The FLARES approach to the resolution problem is based on the application of Silicon Drift Detectors (SDD) for the readout of scintillation light. These detectors are characterized by high quantum efficiency and low electronic noise, especially when cooled to minimize the contribution of the leakage current. The use of scintillation detectors provide flexibility in the choice of the candidate isotope and easy mass scalability, while the usage of SDDs enhances the attainable energy resolution. Moreover, both scintillation crystals and SDDs can be produced with high purity materials, thus lowering the radioactive contaminations and the experimental background. The chosen scintillating crystal has to contain a suitable $0\nu\beta\beta$ candidate isotope while being a performing scintillator. These constraints lead to the selection of two crystals: $CdWO_4$ and $CaMoO_4$, containing respectively ^{116}Cd and ^{100}Mo as candidate isotopes for $0\nu\beta\beta$. To put the FLARES design to test, I performed different measurements with large area SDDs (3x3cm^2) produced by Fondazione Bruno Kessler (FBK) in the framework of the RedSOX project. I characterized the response of these devices to X-ray excitation and to scintillation light emitted by scintillating crystals, cooling the system at $\sim$120 K. The results showed, as expected, a low level of electronic noise. The attainable energy resolution with scintillators is although limited, and it has been possible to address such limit to a variable efficiency in charge collection across the surface of the SDD. The results of these studies led to the design of new SDDs with improved charge collection efficiency.
On the other hand the goal of the ESQUIRE project is the development of a new family of scintillation detectors based on the application of scintillating nanocrystals. These crystals can be produced containing $0\nu\beta\beta$ candidate isotopes and can be designed to have high light output and low self absorption. In the first R&D phase of the project we selected the first samples containing $CsPbBr_3$ scintillating perovskite nanocrystals mixed with a wavelength shifting dye. After the initial optical characterization, I performed the measurements of this samples coupled to Silicon PhotoMultiplier (SiPM) detectors, to quantify the light emission after the interaction with different sources of ionizing radiation. Only a limit could be set on the light yield value, although we unambiguously proven that, even with the first non-optimized sample, we could detect scintillation light. Thanks to this result, we could highlight the necessary design steps for the production of new, better performing, samples.

In conclusion, my thesis work was devoted to show the potentialities of scintillator application to $0\nu\beta\beta$ searches. With the CUPID-0 detector, based on scintillating calorimeters, I could put a limit to anomalous Lorentz-violating coupling of neutrinos, alongside the full characterization of the measured background. The CUPID-0 success proves that this approach can be applied to new generation experiments, capable of exploring the inverted hierarchy region of neutrino masses. Alongside these analysis result, I performed different technical work for the development of new detector concepts for the search of rare decays. The test of FLARES SDD+Scintillator design proved that this detector concept can be put in operation. The obtained result showed that the path to the improvement of energy resolution passes trough the increase in charge collection efficiency. My work in ESQUIRE project allowed the testing of the first nanocrystal-based scintillator prototype, providing a first step towards the development of a new family of scintillators.

The outline of the present work is as follows: in chapter 2 the characteristics of $0\nu\beta\beta$ will be discussed, alongside the physics needed to motivate the search for this decay. In chapter 3 an overview of the current and next generation experimental techniques for the $0\nu\beta\beta$ investigation will be presented, with particular detail on the scintillation-based detectors. In chapter 4 the physics results of CUPID-0 experiment will be discussed, proving the potentiality of scintillation-based technique. In chapter 5, the development of new scintillation detectors will be presented, with the obtained results and an outline of future possible investigations.

Chapter 2

Neutrino Physics and the Double Beta Decay

In the actual landscape of particle physics great efforts are devoted to the investigation of new phenomena beyond the Standard Model predictions. Among different sectors of the model, the weak interaction has always been an area of major interest. Between the particles involved in such interaction, the neutrino in particular has puzzled the scientists from its theorization up to its current inclusion in the SM. And yet, after years of theoretical predictions and experimental measurements, many aspects of this particle still remain unknown.
Originally theorized as a massless fermion, neutrino is now proven to be a massive particle, since it can oscillate. Such discovery changed neutrino role in our theory, leaving new questions about how its mass is generated. Since no Standard Model mechanism could produce such phenomenology, beyond the Standard Model Physics has been addressed to as the response for such dilemma. Also the nature of this particle has been questioned, because the standard Dirac fermion cannot be used to describe the non-standard neutrino behaviour. The so-called Majorana picture is a more valid candidate for this task, but the consequences of its introduction are particularly significant. A Majorana-type fermion, in fact, is identical to its antiparticle. As a consequence, if the Majorana neutrino is a true fact, then the conservation of the total number of lepton has to be violated. Such behavior has strong consequences for cosmology, since it can be related to the matter/antimatter asymmetry.
The most powerful testing ground for this theory is the neutrinoless double beta decay. This process would only be possible if neutrino are massive Majorana fermions, and its detection would unambiguously state the existence of beyond the Standard Model Physics, characterized by the violation of the lepton number conservation. Being a nuclear process, the neutrinoless double beta decay also involves the description of the nuclear structure, an aspect still lacking a complete and exhaustive explanatory model. These brief forewords show how much unknown phenomena are hidden in a so tiny bit of our reality, demanding a dedicated investigation of its details.

In this chapter the physics of massive neutrinos will be quickly discussed, summarizing its most important characteristics and phenomenologies. The mechanism of neutrinoless double beta decay will be presented, alongside its implication and the issues related to the nuclear physics involved in this process. A final space will be also dedicated to the standard double beta decay, with a discussion on possible new physics investigations allowed by the study of this process.

2.1 A quick summary of the Standard Model

The Standard Model (SM) of particle physics is based on the symmetry group SU(2) x U(1), combining the quantum electrodynamics (U(1) gauge group) with the weak interaction (SU(2) gauge group) [1]. Alongside the interactions, the model includes three fermion families, divided in quarks and leptons. Each family transforms as an SU(2) doublet and is a left-handed field. The

three quark families are:

$$\begin{pmatrix} u_i \\ d_i \end{pmatrix}_{i=1...3} = \left\{ \begin{pmatrix} u \\ d \end{pmatrix}, \begin{pmatrix} c \\ s \end{pmatrix}, \begin{pmatrix} t \\ b \end{pmatrix} \right\} \tag{2.1}$$

constituted by the up (u), down (d), charm (c), strange (s), top (t) and bottom (b) quarks. The three lepton families, instead, are:

$$\begin{pmatrix} \nu_i \\ l_i^- \end{pmatrix}_{i=1...3} = \left\{ \begin{pmatrix} \nu_e \\ e^- \end{pmatrix}, \begin{pmatrix} \nu_\mu \\ \mu^- \end{pmatrix}, \begin{pmatrix} \nu_\tau \\ \tau^- \end{pmatrix} \right\} \tag{2.2}$$

each constituted of a neutrino (ν) and a lepton (l) and characterized by one of three flavours: electronic (e), muonic (μ) or tauonic (τ). For each of these particles the theory also include an anti-particle, with mass identical to the original particle but with opposite charge and chirality[1]. In addition, also right-handed doublet exist, which are not considered by the SU(2) part of the symmetry group. The amount of right-handed component is proportional to the mass of the particle, and affects the probability of interaction for massive particles. The SU(2) x U(1) interactions are mediated by the gauge bosons: the photon (A) for the U(1) group and the $W^\pm$ and Z^0 for the SU(2) group. In addition to these representative of the interaction forces, the model includes also the Higgs Boson (H), responsible for the masses of all the other particles trough the *Higgs mechanism* [1]. For each particle, the mass depends on the coupling with the Higgs field and the higgs vacuum expectation value (v), parameters fixed by measurements. The interaction giving rise to particle mass is a Yukawa coupling with the Higgs field, given by:

$$\mathcal{L}_M \propto \bar{\psi} H \psi \tag{2.3}$$

where H is the scalar Higgs boson and ψ is the considered field. Such coupling connects right-chiral to left-chiral components of the field. Since νs only interact as left-handed particles, their mass in the SM is zero.

The combination of these elements gives the minimal model with predictive power for the phenomenology of elementary particles interactions, and different experimental results proved the effectiveness of such theory [1]. Besides, the basic SM cannot explain many observed features. For example, the strong force, responsible for the bound states of quark inside baryons, is not included in the minimal model. The Quantum Chromodynamics (QCD) theory, which explain these states, has been included in the SM resulting in the more complete SU(3) x SU(2) x U(1) gauge theory.

In addition, the weak sector of SM shows features unexplained by the general theory. Since each family of quark is an SU(2) doublet, the interaction mediated by the electoweak bosons ($W^\pm$ and Z^0) should live in a single family and should conserve the Charge-Parity symmetry (CP). On the contrary, off-family interactions violating CP were observed. The explanation was given with the definition of the Cabibbo-Kobayashi-Maskawa (CKM) matrix [2, 3]. This matrix is the operator linking up-type quarks to down-type quarks, and is the combination of the operators responsible for the mass-to-flavour bases transformation in quark sector. The quark mass eigenstates, in fact, do not coincide with the flavour eigenstates, responsible for the observed interactions. This matrix is a 3x3 complex unitary matrix, fully defined by three angles and one complex phase. The phase is responsible for the CP violation in weak quark decays, since it acts in differentiating the relative probability of a process and its CP transform.

As this discovery shows, weak interaction provides a powerful tool to evaluate the coherency and stability of SM prediction. The small cross section of weak processes, in fact, allows unpredicted features to be detected.

Inside the weak sector, νs are particularly sensitive probes, given the nature of their phenomenology

[1] Anti-particles are noted as particle with a bar sign over the name

2.2 Neutrino Oscillation and their implication

In the SM, νs are neutral massless leptons, interacting only by the means of weak force both in charged current (CC) or neutral current (NC) reactions. Mediated by $W^{\pm}$ or Z^0 bosons respectively. They are characterized by a flavour, based on the nature of the charged lepton with which a ν interacts. Electronic neutrinos (ν_e) are produced with a positron (e^+) or produces an electron (e^-), as well as muonic neutrinos (ν_μ) are related to muons ($\mu^{\pm}$) and tauonic neutrinos (ν_τ) are related to tauons ($\tau^{\pm}$). The different flavour states provide a base to describe νs and, for each flavour l, ν_l (antineutrinos, $\bar{\nu}_l$) interact only as left-handed (right-handed) chiral eigenstates. Since in SM neutrinos are massless particles, their flavour is conserved in each interaction.
In spite of these assumptions, in recent years different experiments detected neutrino oscillations. This phenomenon consist in the transitions in flight between the different flavour neutrinos ν_e, ν_μ and ν_τ, caused by nonzero neutrino masses and neutrino mixing [4, 5, 6, 7]. The different evidences unambiguously prove that lepton flavour is not conserved in neutrino sector. Such feature can be addressed by introducing neutrino flavour mixing in vacuum. The meaning of the mixing is that each left-handed flavoured neutrino ν_l entering in CC or NC reaction is a linear combination of three neutrinos ν_j with $m_j \neq 0$:

$$\nu_l = \sum_{i=1}^{3} V_{l,j}\nu_j \tag{2.4}$$

The matrix V, known as Pontecorvo-Maki-Nakagawa-Sakata (PMNS) matrix, is a 3x3 complex unitary matrix, defined by 3 angles and 1 phase, in complete analogy to the CKM matrix [8, 9]. The PMNS matrix therefore acts as a base transformation between mass base and flavour base. Neutrinos are firstly created as a flavour eigenstate in a weak interaction. They then travel in space as a superimposition of mass eigenstates, each one represented as a plane wave with a velocity given by the E/m ratio. At detection, they interact as a flavour eigenstate built, according to Eq. 2.4, as the combination of the mass eigenstates in the interaction point. Since the sum of the mass component varies with space, as different mass particles have different velocities, the flavour can change with a given probability. Calling θ_{ij} with $i, j = 1 \dots 3$ the mixing angles and δ the CP violating phase, the PMNS matrix has the form

$$V = \begin{bmatrix} c12c13 & s12c13 & s13e^{-i\delta} \\ -s12c23 - c12s23s13e^{-i\delta} & c12c23 - s12s23s13e^{-i\delta} & s23c13 \\ s12s23 - c12c23s13e^{-i\delta} & -c12s23 - s12c23s13e^{-i\delta} & c23c13 \end{bmatrix} \tag{2.5}$$

where $cij = \cos(\theta_{ij})$ and $sij = \sin(\theta_{ij})$.
Thanks to the mixing matrix it is possible to calculate the transition probability from a flavour l to a flavour l', given by [10]:

$$P(\nu_l \to \nu_{l',(L)} = |\left\langle \nu_{l'(L)} \middle| \nu_l(0) \right\rangle|^2 = \delta_{ll'} + \tag{2.6}$$

$$+ P^{1,2}_{l,l'} \sin^2(\psi_{12}) + P^{2,3}_{l,l'} \sin^2(\psi_{23}) + P^{1,3}_{l,l'} \sin^2(\psi_{13}) + \tag{2.7}$$

$$\pm \ 8J \sin(\psi_{12}) \sin(\psi_{23}) \sin(\psi_{13}) \sum_{j=1}^{3} \epsilon_{ll'j} \tag{2.8}$$

where the - sign holds for neutrinos, the + sign for anti-neutrinos, ϵ is the Ricci-Levi-Civita tensor and

$$P^{i,i'}_{l,l'} = -4Re(V_{li}V_{l'i}V^*_{l'i}V^*_{li'}), \quad 8J = \cos(\theta_{13}) \sin(2\theta_{13}) \sin(2\theta_{12}) \sin(2\theta_{23}) \sin(\delta), \quad \psi_{ij} = \frac{\Delta m^2_{ij}}{4} \frac{L}{E} \tag{2.9}$$

$P^{i,i'}_{l,l'}$ is the amplitude of transition probability from flavor l to flavor l', considering the bond between the i-th and i'-th mass eigenstates. Such quantity depends on the mixing angles between the mass eigenstates and on the composition of the two flavored ν in the mass base.

$8J$ is the factor proportional to the magnitude of CP violation in the neutrino sector. This factor depends both on the angles and on the possible values of δ, the Dirac CP violating phase. Current data on θ_{ij} imply $0.026(0.027) \cdot |\sin(\delta)| \lesssim |J| \lesssim 0.035|\sin(\delta)|$ [1] . Based on the current indication that $\delta \sim 3\pi/2$, the CP-violation in the lepton sector is approximately 3 orders of magnitude larger than the same factor for quarks, and its effects in neutrino oscillations would be relatively large.
Lastly, ψ_{ij} is the factor related to the periodicity of neutrino oscillation. Such characteristics is in the L/E variable, and it is ruled by the period $\Delta m^2_{ij} = m^2_i - m^2_j$. Since the periodicity is given by a $\sin^2$ function, the oscillation measurement in vacuum are not sensible to the sign of the mass differences. Different experiment measured the ν oscillations, obtaining values both for the mixing angles and the Δm^2_{ij}. The current phenomenological results identify only two mass splitting [1]:

$$\delta m^2 = \Delta m^2_{12} = 7.37^{+0.59}_{-0.44} \cdot 10^{-5}\text{eV}^2 \tag{2.10}$$

$$\Delta m^2 = \Delta m^2_{31}\ (\Delta m^2_{23}) = 2.56^{+0.13}_{-0.11}\quad (2.54^{+0.12}_{-0.12}) \cdot 10^{-3}\text{eV}^2 \tag{2.11}$$

called respectively solar (δm^2) and atmosferic (Δm^2) oscillation parameters. These names depend on the neutrino source used for the evaluation of such oscillation.
In the case of sun neutrinos, alongside the effects of vacuum oscillation it has to be considered the effect of matter interaction [1, 10, 11]. As νs travel from the sun nucleus towards the earth, in fact, they cross regions of high density, where νs can interact. Among the possible interaction, the $\nu - e$ coherent elastic scattering is the most important channel, and it affects differently ν_e, ν_μ and ν_τ. Such asymmetry leads to a different neutrino refractive index between ν_e and $\nu_{\mu,\tau}$, resulting in a different propagation in matter. Such effect is relevant and allowed to quantify δm^2 both in modulus and in sign, giving the ordering between 2 out of 3 mass eigenstates.
The measurement of oscillation unambiguously prove that νs are massive particles. The values of flavoured νs masses are not known yet, and only the mass differences between the mass eigenstates have been determined. From the data, we know that two mass eigenstates have similar mass, while one is very different. The hierarchy between the two similar masses is known (δm), but not the global ordering of these three values. As a consequence, two scenarios are possible, respectively called normal hierarchy (NH) or inverted hierarchy (IH) (Figure 2.1):

$$\text{NH:}(m_1 < m_2) < m_3 \quad \text{or} \quad \text{IH:}m_3 < (m_1 < m_2) \tag{2.12}$$

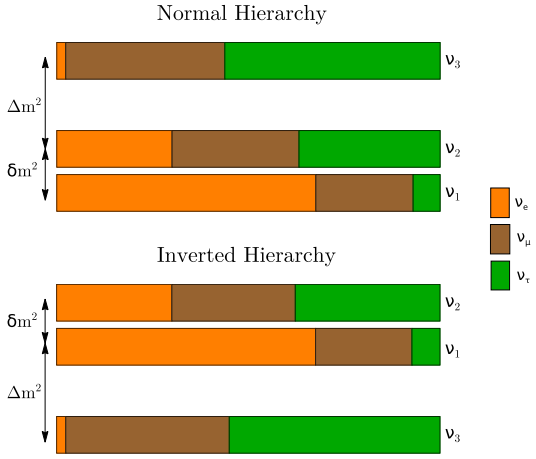

Figure 2.1: Graphic view of the possible mass hierarchies of neutrinos. The view of the probability to find one of the flavour eigenstates if the neutrino is in a certain mass eigenstate is also reported. The CP-violating phase is assumed zero in this plot, taken from [12].

The determination of the hierarchy is a big open question in the field of neutrino physics, with different experiments trying to evaluate this ordering.

Alongside the order evaluation, direct neutrino mass measurement are carried out. These measurements are usually based on the kinematics of charged particles emitted with neutrinos in weak decays. By reconstructing the decay kinematics it is possible to evaluate the mass of flavoured ν, given by a precise combination of the three mass eigenstates (Eq.2.4). The most sensitive neutrino mass measurement to date, involving electron type antineutrinos, is based on fitting the shape of the beta spectrum. In presence of massive neutrinos, in fact, the measured end point of a beta decay is lower than the Q-value of the nuclear transition, because of the mass energy of the emitted neutrino. Still no direct measurement of neutrino mass has been measured, and only limits are currently available. The latest results, summarized in [1], are reported in Table 2.1.

Neutrino	Mass limit	Reaction used
$\overline{\nu}_e$	<1.1 eV (90% C.L.)	^{3}H β^- Decay [13]
ν_e	<225 eV (95% C.L.)	^{136}Ho Decay
ν_μ	<0.19 MeV (90% C.L.)	Combination of Modes
ν_τ	<18.2 MeV (95% C.L.)	Combination of Modes

Table 2.1: Limits on flavoured neutrino masses reported, unless otherwise stated, in [1] (pp. 1006-1007).

2.2.1 Neutrino mass models

The evidence of ν masses forces the definition of SM extensions capable of explaining massive neutrinos. The mass term can be included either in *Dirac* or *Majorana* formalism [12, 10].
The *Dirac* mass term is based on the assumption that neutrino is a massive Dirac fermion, getting its mass from the Higgs mechanism through a Lagrangian term of the form:

$$\mathcal{L}_m^{Dirac} = \lambda_\nu \bar{L} H \nu_R \tag{2.13}$$

where $L = \binom{l}{\nu}_L$ is a left SU(2) doublet, ν_R is a right handed neutrino and λ_ν is the Yukawa coupling of ν to the Higgs field. The predicted neutrino mass would therefor be $m_\nu = \lambda_\nu v$, with v the vacuum expectation value for the Higgs field. The actual limit on neutrino mass eigenvalue $m_\nu \leq 0.1$eV [10] forces the coupling to be $\lambda_\nu \sim 10^{-12}$. This mechanism explains the neutrino oscillation, yet the consistence of this mass term with the other terms of the electroweak lagrangian implies that only the left-handed neutrino (ν_L) or the right-handed antineutrino, ($\overline{\nu}_R$) can interact by means of the electroweak force. As a consequence, ν_R (and $\overline{\nu}_L$) must be included in the model as a *sterile neutrino*, only capable of gravitational interactions, coincident to the *wrong* helicity component of the massive ν. Furthermore the small neutrino mass forces λ_ν to be unresonably small with respect to the one of the other fermions. This inclusion is therefore *unnatural*, since it overloads the model with an additional data driven parameter and since it forces the inclusion of a non interacting particle.
On the other hand, in *Majorana* theory ν is included as a spin 1/2 fermion identical to its own antiparticle. As a consequence, there is no need to theorize the existence of sterile neutrinos and the difference between ν and $\overline{\nu}$ processes is related to the different helicity of the particle. In Majorana framework the mass term origins from a non renormalizable operator of the form [10, 14]:

$$\mathcal{L}_m^{Majo} = \frac{\lambda_\nu}{\Lambda} \overline{L}^C H H^T L \tag{2.14}$$

where L is the Majorana neutrino and Λ is a new energy scale which automatically suppresses the effect of Higgs coupling. This operator naturally violates the lepton number conservation, because it provides a transition from ν to $\overline{\nu}$. The operator of Eq.2.14 can be represented with the Feynman diagram:

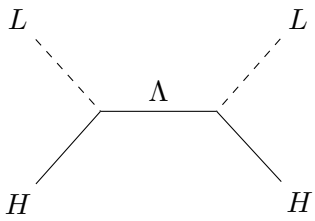

where new particle (or particles) with mass scale Λ is propagated. This new mass scale can be both on the order of current energy frontier searches [15] or extremely higher, depending on the corresponding mass generation model.
The simplest model introducing such mass generation mechanism is the so called *see-saw type I*, introducing as Λ scale particle the right handed Majorana neutrino ν_R^M [16]. In such model, the mass lagrangian gets the matricial form:

$$\mathcal{L}_m = \begin{pmatrix} \overline{\nu}_L & \overline{\nu}_R^M \end{pmatrix} \begin{pmatrix} 0 & m_D \\ m_D & M_N \end{pmatrix} \begin{pmatrix} \nu_L \\ \nu_R^M \end{pmatrix} \tag{2.15}$$

where m_D is a dirac mass due to a Yukawa coupling to the Higgs field, and $M_N \sim \Lambda$ is the mass of the heavy mediator in 2.14. The eigenvalues of such mass matrix are:

$$m_{\nu_R^M} \sim M_N \sim \Lambda \tag{2.16}$$

$$m_{\nu_L} \sim \frac{m_D^2}{M_N} \sim \frac{\lambda_\nu v}{\Lambda} \tag{2.17}$$

resulting in the mass of the standard left neutrino (m_{ν_L}) to be small in force of the size of the mass of the right Majorana neutrino (Λ). This heavy counterpart of the standard neutrino is a sterile particle, with respect to the weak interaction, and only acts in case of lepton violating processes. Its mass has to be of the order of $\Lambda \sim 10^{15}$ GeV to lead coherent SM predictions [10].
Alongside this simple model, more complex mass theory have been developed, with many possible Λs. Keeping fixed the operator of Eq.2.14, the Λ scale can be provided by a complex triplet of spin zero Higgs-like particles (type II see-saw) or by a fermion triplet (type III see-saw) [10]. Other more exotic solutions are also provided, such as radiative models [17] or the introduction of singlet Majorana masses in combination with radiative mechanisms [18].

2.3 The Double Beta Decay

The experimental test of such models has to consider that no effects can be measured from kinematic experiments, since both Dirac and Majorana picture of neutrinos share the kinematic part of the lagrangian. As a consequence, the difference between Dirac and Majorana pictures can only be seen in processes where both ν mass and helicity play a leading role. In addition, the process studied should also have a small probability, in order to be affected by the massive neutrino fenomenology, usually characterized by small cross sections.
One of the most important testing ground for neutrino physics is the *double beta decay* ($\beta\beta$) of even-even nuclei [19]. This process is a rare nuclear transition in which an initial nucleus (A,Z) decays to a member (A,Z+2) of the same isobaric multiplet with the simultaneous emission of two electrons. Such process is strongly disfavoured in odd mass number nucleons, where the minimum energy is reached trough subsequent single β decays. In case of even mass number nuclei, instead, the nuclear pairing force causes nuclei with even numbers of proton and neutrons to be lighter than the odd-odd nucleus that would be their final state in case of single β decay (see Fig 2.2). As a consequence, singe β decay for even-even nuclei is energetically disfavoured, while being allowed for odd-odd nuclei. In order to reach an energy minimum, even-even nuclei can undergo $\beta\beta$ decay, which is possible for these nuclei, although suppressed because it is a second order weak process. In

Table 2.2 are reported the properties of the most commonly investigated $\beta\beta$ candidates, to provide an overview of the characteristics of this decay. The half lives of these decays ($T^{2\nu}_{1/2}$) are always $\geq 10^{19}$y, because this is a second order weak process.

Isotope	$Q_{\beta\beta}$[keV]	Isotopic abundance [%]	$T^{2\nu}_{1/2}$ [10^{19}y]
^{48}Ca	4274	0.2	$4.4^{+0.6}_{-0.5}$
^{76}Ge	2039	7.6	193±9
^{82}Se	2999	8.7	9.2±0.7
^{96}Zr	3348	2.8	2.3±0.2
^{100}Mo	3034	9.6	0.71±0.04
^{116}Cd	2814	7.5	2.85±0.15
^{130}Te	2582	34.2	69±13
^{136}Xe	2458	8.9	220±6
^{150}Nd	3368	5.6	0.82±0.9

Table 2.2: Properties of most commonly investigated $0\nu\beta\beta$ candidates. Data are taken from [20].

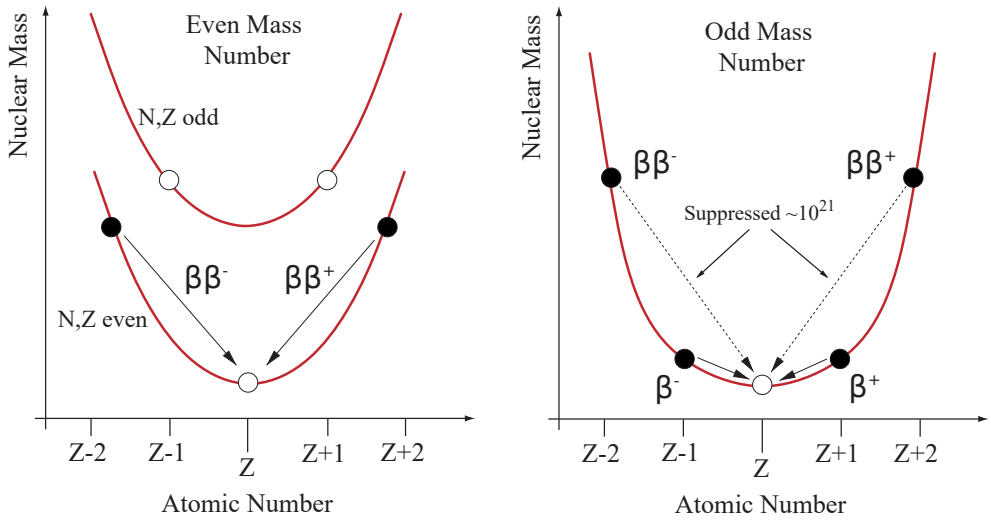

Figure 2.2: Nuclear mass as a function of the atomic number Z in the case of an isobar candidate with A even (left) and B odd (right). In the even A case, so for nuclei with even Z and N, the single β decay is energeticaly forbidden. This happens because the final nucleus for this decay will be odd both in N and Z, bein characterized by higher mass whith respect to the initial nucleus. Therefore even-even nuclei can undergo de-excitation through $\beta\beta$ decay. The figure is taken from [19].

At nuclear level, the double beta decay consists in the conversion of two neutrons into two protons and can occur in the 2ν mode ($2\nu\beta\beta$)

$$ {}^{A}_{Z}X \rightarrow {}^{A}_{Z+2}X + 2e^{-} + 2\overline{\nu}_{eR} \tag{2.18} $$

which obeys lepton number conservation and is predicted by the SM as a second order weak interaction, and 0ν mode ($0\nu\beta\beta$)

$$ {}^{A}_{Z}X \rightarrow {}^{A}_{Z+2}X + 2e^{-} \tag{2.19} $$

which violates the lepton number by two units and can happen only outside the SM.
$0\nu\beta\beta$ is the most interesting of the decay modes because it is the only practical way to determine experimentally the nature of neutrinos. In fact this transition can occur only if neutrinos are Majorana particles, since its mechanism is based on the equivalence of neutrino and antineutrino [21]. In the framework of type I see-saw mass model, $0\nu\beta\beta$ can be derived from $2\nu\beta\beta$ assuming a *Racah sequence* of two single beta decays in which the (anti) neutrino emitted at one vertex

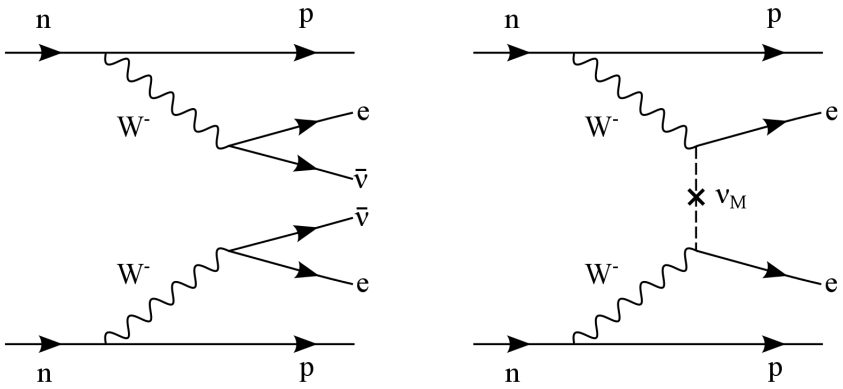

Figure 2.3: Tree level Feynman diagrams for $2\nu\beta\beta$ (left) and $0\nu\beta\beta$ (right). In the $0\nu\beta\beta$ a right Majorana neutrino is emitted at the first vertex and a left Majorana neutrino is absorbed at the second vertex. This sequence is possible only if neutrinos are massive Majorana fermions, because they must have a wrong helicity component in order to be exchanged between the two electroweak vertexes.

is absorbed at the other (see Fig. 2.3). The exchanged neutrino is a light particle, therefore the interaction as a wide range, involving all the nucleus. The exchanged light neutrino has the electron flavour and, according to Eq.2.4, is a combination of three possible mass eigenstates. As a consequence, its mass is an effective combination of the various mass eigenstates m_i, defined as

$$m_{\beta\beta} = |\sum_{i=1}^{3} U_{ei}^2 m_i| \tag{2.20}$$

where U is not the PMNS matrix defined in 2.5, but a combination of this matrix with 2 Majorana phases [1]. These additional parameters come from the fact that, in type I seesaw, 3 heavy right Majorana neutrinos (one for each flavour) must be introduced in the model. Their presence leaves PMNS matrix unaffected, but plays a role whenever the lepton number violating physics enters in the processes, such as in the case of $0\nu\beta\beta$. This effective mass enters in the calculation of the livetime of this decay, given by the formula:

$$[T_{1/2}^{0\nu}]^{-1} = \frac{|\langle m_{\beta\beta}\rangle|^2}{m_e^2} G^{0\nu} |M^{0\nu}|^2 \tag{2.21}$$

where $G^{0\nu}$ is the phase-space integral, $M^{0\nu}$ is the $0\nu\beta\beta$ nuclear matrix element and m_e is the electron mass. As it will be discussed later in this work, the most efficient way to search for the $0\nu\beta\beta$ is to look at the spectrum of the two electrons emitted in the $\beta\beta$ process. The searched signature is a monochromatic peak at the energy of $0\nu\beta\beta$ Q-value ($Q_{\beta\beta}$), superimposed to the tail of the continuous spectrum of the electrons emitted by the $2\nu\beta\beta$ (see Fig. 2.4). The superimposition is natural, since $0\nu\beta\beta$ is a special case of $\beta\beta$ decay, and it forces the study and comprehension of both the decay modes to correctly characterize the problem.
Since all the masses play a role in the determination of $T_{1/2}^{0\nu}$, also the mass hierarchy affects the possible results. As shown in Fig.2.5, in fact, different dependencies are expected for $\langle m_{\beta\beta}\rangle$ in the two different orderings. By convention, $\langle m_{\beta\beta}\rangle$ is reported as a function of the lightest neutrino mass eigenvalue (m_{lightest}) of the chosen hierarchy.
For $m_{\text{lightest}} > 10^{-1}$eV the prediction for HR and IH are degenerate, since the value of the lightest mass is bigger than $\sqrt{\Delta m^2} \sim 5 \cdot 10^{-2}$eV.
As m_{lightest} lowers, the IH predicts $\langle m_{\beta\beta}\rangle$ to become constant. In IH the two eigenvalues separated by δm^2 are the more massive (see Fig.2.1) and are separated by the mass splitting $\sqrt{\Delta m^2}$ from the lowest mass eigenstate. As a consequence, as m_{lightest} decreases, $\langle m_{\beta\beta}\rangle$ stabilizes around $\sqrt{\Delta m^2}$.
In NH picture, instead, the two close states are the low mass ones, therefore their contribution decreases as m_{lightest}. The only remaining mass (m_3) enters $\langle m_{\beta\beta}\rangle$ with a small mixing angle,

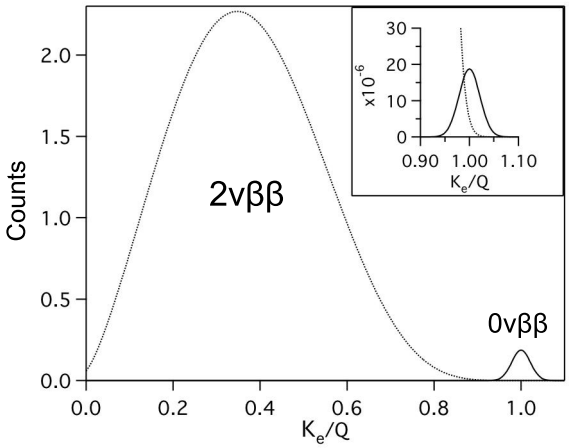

Figure 2.4: Energy spectrum for $\beta\beta$ decay modes. The continuum is related to the $2\nu\beta\beta$, the single peak to the $0\nu\beta\beta$. The representation is not to scale, and is reported for graphical purposes. In the inset, the two signal superimposition in case of finite detector resolution is shown.

therefore the total effective mass can reach extremely low values [22]. The prediction on $\langle m_{\beta\beta} \rangle$ are deeply affected by the uncertainties on the PMNS matrix element, but above all by the uncertainty on the 3 phases (1 for the PMNS, 2 for the Majorana heavy neutrinos) entering in Eq.2.20. The bands in Fig.2.5 take into account these variations.
The previous discussion is valid in case of the type I see-saw mechanism, but the underlying process is defined and consistent in every theory introducing lepton number violation. It has to be noted that depending on the theory, the expression linking $T^{0\nu}_{1/2}$ to the theory parameters is different, leading to different possibility for theoretical predictions. Nevertheless, the key point in $0\nu\beta\beta$ search is that such phenomenon happens in each theory including Majorana neutrinos, regardless of its energy scale. As a consequence, searching for this process allows to prove a generic channel of lepton number violation, without constraints on the energy scale of the new physics involved (Schechter-Valle theorem, [21]).

2.3.1 Nuclear Matrix Element

Alongside the uncertainties of $\langle m_{\beta\beta} \rangle$, the theoretical evaluation of $T^{0\nu}_{1/2}$ is also affected by the calculation of the nuclear matrix element of the double beta decay process, $M^{0\nu}$ (see Eq.2.21). This calculation is carried out with different methods, each of which characterized by different approximation. These methods will be briefly discussed, starting from the information reported in [22].
The solution of a nuclear structure is a many body problem extremely difficult to handle, since it is based on the physics of bounded quarks, for which no analytical complete solution is known. As a consequence, the so called *ab initio* methods to calculate nuclear physics are extremely difficult, and more often approximate methods are used to evaluate the probability of processes involving heavy nuclei.
The first method describing the nuclear structure has been the Shell Model (SHM), describing the nucleus as a potential well for protons and neutrons. These particles occupy different quantized energy levels of this system, divided in shells, and the final occupation level describes the total nucleus properties. A key point of this model is the hypothesis that each closed shell does not take part in nuclear transitions. Only the higher energy states are therefore taken into account in the calculation of nuclear matrices, reducing the degrees of freedom of this problem. The active levels are a combination of ortogonal Slater determinants defining the active state of the nucleus, on which an effective Hamiltonian acts. The shell model is effective for ground state calculations, but cannot handle effectively collective nuclear behaviour, such as rotational levels or vibrational excitation, nor it can fully explain the paring term of nuclear mass formula, particularly effective in the calculation for $0\nu\beta\beta$.
To relax the SHM approximation of closed nuclear core, all the levels have to be considered si-

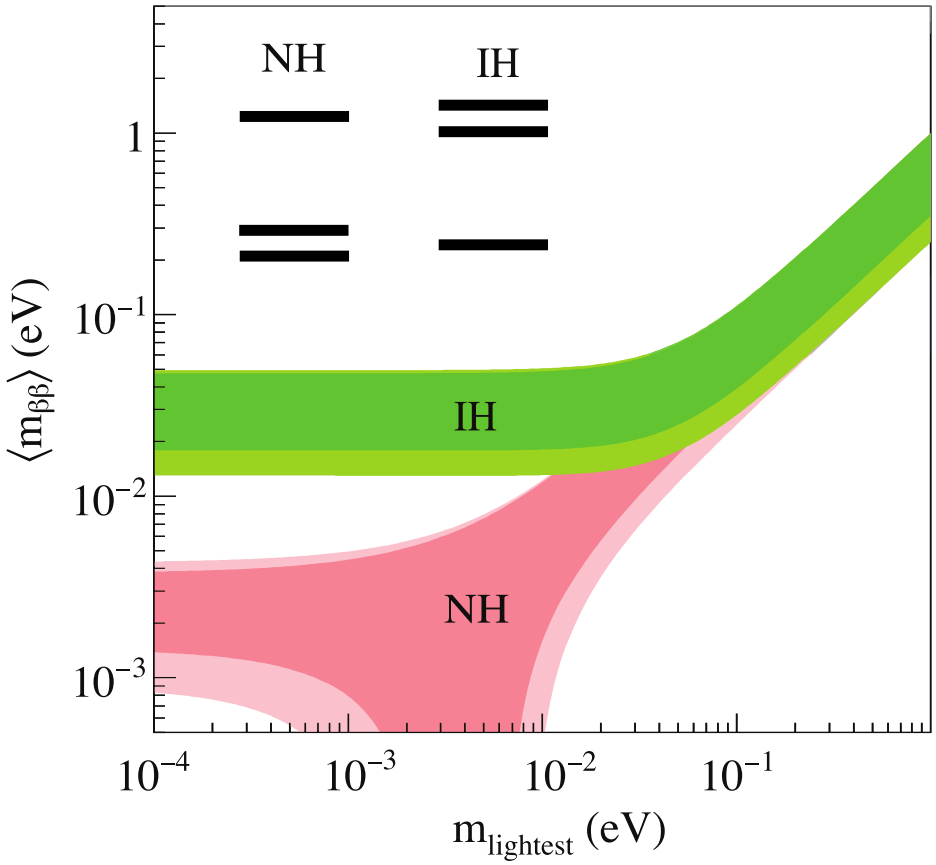

Figure 2.5: Effective Majorana Mass as a function of the lighest neutrino mass, both for normal hierarchy (NR, red) and inverted hierarchy (IH, green) ordering. The width of the bands depends on the uncertainty of the elements of the mixing matrix and of the phases involved in the calculation. The figure is adapted from [22].

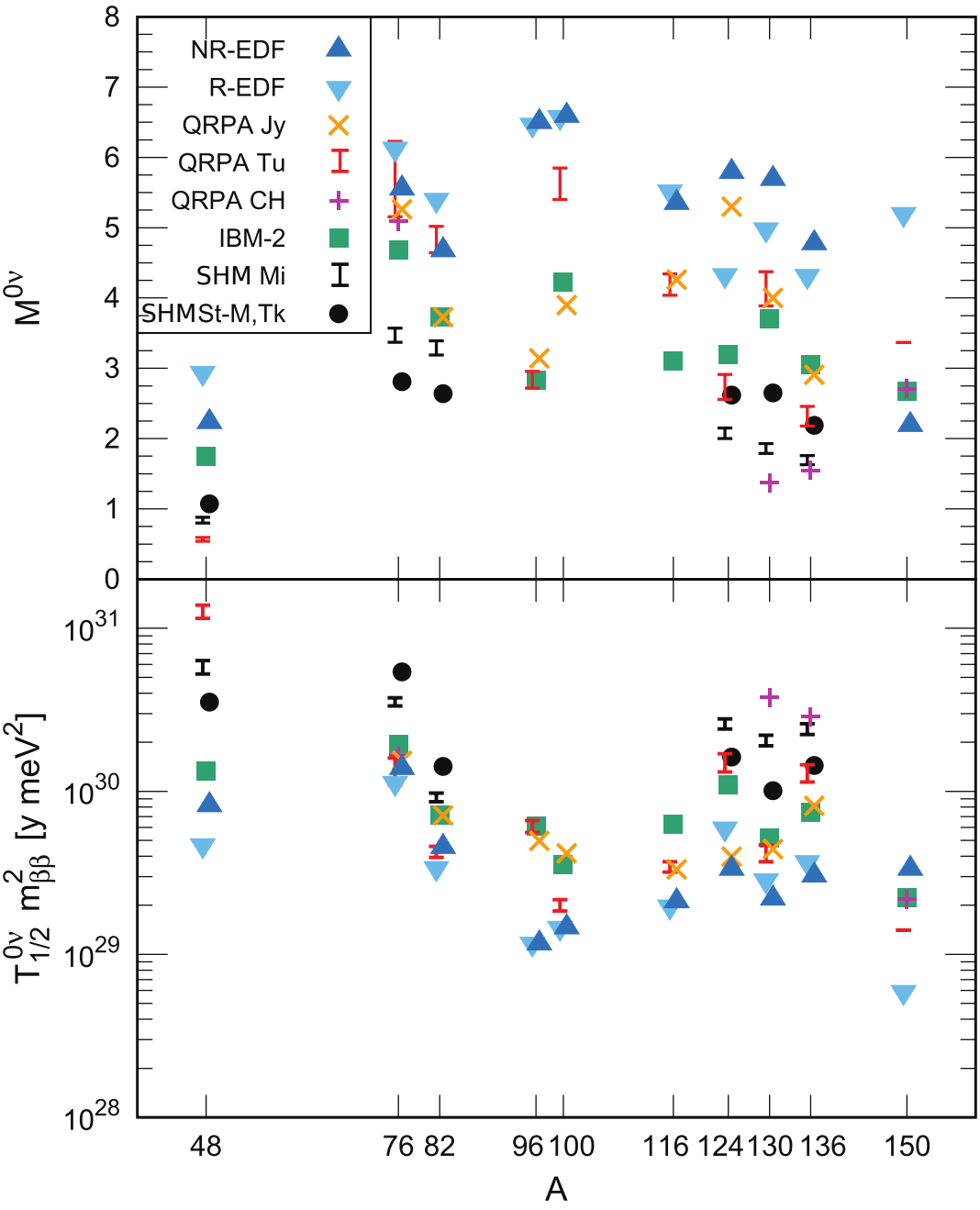

Figure 2.6: Matrix element for different Neutrinoless Double Beta Decay candidates (upper panel) and corresponding $T^{0\nu}_{1/2} \cdot m_{\beta\beta}$ (lower panel). The different methods are: Energy Density Functional Theory (EDF), Quasi-Particle Random Phase approximation (QRPA), Interactive Boson Model (IBM) and Shell Model (SHM). The general assumptions are explained in the text, for the specification refer to [22]. The spreading in values is wide, since different models rely on different approximation with different validity ranges. The figure is taken from [22].

multaneously active. To avoid the explosion of the calculation dimensionality, only the Slater determinant minimizing the Hartree-Fock energy equation is chosen. A sum of direct potential and an exchange potential is used to express the energy to be minimized and, in order to avoid calculation complexity, a random phase is chosen for each state, resulting in the so-called *Random Phase Approximation* (RPA). The obtained state is expressed as a combination of quasi particle creation/destruction operators on a *vacuum* state, obtaining a final method called Quasi-particle RPA (QRPA). This calculation stratagem uses a single Slater determinant defined over all the nucleons, on which an effective potential acts. The relaxation of the closed nucleus approximation allows to take into account some global nuclear rotation and vibration. In addition, the presence of creation-annihilation operators allows the inclusion of the pairing interaction into the model. The strength of such interaction, usually referred to as g_{pp}, is although usually overestimated by this model, forcing a data-driven renormalization of the theory. Unfortunately, this normalization affect heavily the $\beta\beta$ calculations, making extremely difficult to calculate exact uncertainties on the matrix element evaluation.

In trying to incorporate simultaneously the SHM capability to address Fermi surface interaction and the QRPA ability to consider the collective nuclear interactions, the Interactive Boson Model (IBM) has been developed. In IBM, a nucleus is modelized as if composed by bosons, defined as correlated pairs of nucleons. Each boson can have 6 parity states: a single state with zero angular momentum or 5 states with angular momentum 2. The total hamiltonian is written as an ensamble of creation-annihilation operators, thanks to which the different matrix element are calculated. This model is close both to the shell model and to atom-like description of the nucleus, but suffers from the definition of the bosonic states, which are basically abstract degrees of freedom. This inclusion forces this model to be based on data fitting for the tuning of its parameters, although good results could be obtained with particlar modifications [23].

To avoid the definition of a particular state, the Energy-Density Functional theory (EDF) proposes the mean nuclear fields obtained minimizing a custom-defined functional combining energy to a density (number density, spin density, ...). This minimization is constrained to particular values, in order to get physical predictions. After obtaining the minimal functional, its minimization with respect to its arguments allows to get the ground state observables. These values are subsequently fitted to data to tune the parameters of the energy-density functional in order to replicate the measured parameters. This method is therefore a fully effective theory, able to describe some features, but lacking of the direct inclusion of the pairing force, leading to an overestimation of pairing-based matrix element (see Fig.2.6).

Once a method is chosen for the modelization of the nuclear structure, the matrix element for the $\beta\beta$ is calculated splitting the process in a cascade of two β decays. From the initial nucleus ground state ($|I\rangle$) a first matrix elements leads to an energy level of the intermediate nucleus ($|n\rangle$), and a final transition leads to the ground state in the final nucleus ($|F\rangle$). The total transition amplitude has therefore the form

$$M_{\beta\beta} \propto \sum_n \langle F| \hat{O}_{Fn} |n\rangle \langle n| \hat{O}_{nI} |I\rangle \tag{2.22}$$

with the sum in principle running over all the possible states of the intermediate nucleus. The $\hat{O}_{Fn}$ and $\hat{O}_{nI}$ operators depend on the energy levels of the various states and on the decay channel considered. As a consequence, the calculation is different for the 2ν and 0ν modes of the $\beta\beta$ decay. Since considering a sum over all the possible states of a virtual nucleus would make the calculation to diverge, the sum in 2.22 is solved in the so-called *closure approximation*, where only few of the possible $|n\rangle$ states are considered. Since in $0\nu\beta\beta$ the momentum transferred by the light ν is on the order of 100 MeV and the addenda of Eq.2.22 have a factor $\propto \frac{1}{q+E_n-E_I}$, with $E_I \sim$ MeV, the sum can be neglected and substituted with a passage on a single state, with average energy $\overline{E}$. On the contrary, since in $2\nu\beta\beta$ the momentum transfer is limited by the Q value of the nuclear transition ($\sim$MeV), the closure approximation cannot be used there. For this reason, the calculation of $M^{2\nu}_{\beta\beta}$ are more complex, and require a different set of hypotheses [24]. Two models in particular are

used to constraint the calculation of $M^{2\nu}_{\beta\beta}$: the single state dominance (SSD) or the higher state dominance (HSD) [25]. In SSD approximation, only the lowest energy states of the intermediate nucleus is held responsible for the $2\nu\beta\beta$. In particular, the process can be split in two different single β decays: the first connecting the ground state of the initial nucleus with the 1^+ state of the intermediate one and the second one going from this state to the final ground state. Alternatively, the HSD approximation postulates a dominance in the process of the higher energy nuclear states, characterized by the Gamow-Teller resonance. The decision on these models can, in the present framework, be done only with the comparison of prediction to experimental data.
From the comparison of predicted and measured matrix elements, a peculiar feature emerges: the matrix element for β and $2\nu\beta\beta$ are systematically over-estimated. Such overestimation has been addressed to the strength of the Gamow-Teller operator, which is the combination of Pauli Matrices ($\boldsymbol{\sigma}$) and the isospin rising/lowering operator ($\tau^{\pm}$). Their combination $\boldsymbol{\sigma}\tau^{\pm}$ acts on a nuclear state changing a proton into a neutron or vice-versa, and its strength is ruled by the square of the axial coupling constant $g_A = 1.27$ [1]. Since the calculation overestimate the matrix elements, a quenching of the g_A coupling was proposed to fit the prediction to the measurement. As reported in [22], this correction depends on the nuclear mass and is remarkably high: the value of the effective coupling calculated is in fact $g_{A,\text{eff}} \sim 0.7$, corresponding to a $\sim 50\%$ underestimation of the parameter. This feature can be measured only comparing the prediction to an effective measurement. Consequently, it is evaluated with $2\nu\beta\beta$ decay and then transmitted to $0\nu\beta\beta$ calculation. If this correction is the symptom of an effective physical quenching, the predicted intensities for the $0\nu\beta\beta$ suggest that this process would be almost undetectable, since it would be further suppressed. Currently no explanation for this behavior is known, although two motivation are being investigated: the presence of pion-mediated 2 body currents in $2\nu\beta\beta$ not considered in the current calculations, or the effect of higher energy orbitals of the intermediate nucleus, neglected in the various form of the closure approximation [22].
In Fig.2.6 the values of $M^{0\nu}$ calculated in different nuclear models are shown. As previously stated, all models have different imperfections and, as a consequence, the results of these calculation are extremely different. Besides the difference in the mean value, it is important to notice that the reported uncertainties, calculated differently for each method, do not allow a direct comparison of the result. No account is taken for the systematics due to the model choice, nor is it possible in the current state with enough significance. This summary of results reflects the actual status of our knowledge of the nuclear structure: the theoretical model must be adjusted onto experimental data to reproduce them and therefore end up lacking of actual general predictive power for unmeasured processes. Such framework gives an extreme importance to the search of rare nuclear decays, since it is the only possible way to constraint the known nuclear theories.

2.3.2 Two neutrino Double Beta Decay investigation

The detailed study of $2\nu\beta\beta$ is a key issue for $0\nu\beta\beta$ searches. As a matter of fact, each nucleus candidate to the $0\nu\beta\beta$ is also a $2\nu\beta\beta$ decaying isotope. Consequently, each experiment designed to look for $0\nu\beta\beta$ implicitly measures $2\nu\beta\beta$. The latter decay mode is an unavoidable source of background for the search of the former decay. Its presence can although also be used to constraint some aspects of the the nuclear matrix element calculation. As stated in 2.3.1, in fact, the current nuclear models need a direct data comparison to constraint their different parameters. In particular, the comparison is useful to address the observed quenching of different phenomena and to understand the reasons behind this observation. The decay time for $2\nu\beta\beta$ ($T^{2\nu}_{1/2}$) is given by

$$[T^{2\nu}_{1/2}]^{-1} \;=\; g_A^4 G^{2\nu} |M^{2\nu}|^2 \tag{2.23}$$

where $M^{2\nu}$ is the nuclear matrix element and $G^{2\nu}$ is the phase space factor. The strong dependency on g_A gives high sensitivity on this parameter. Being a second order weak decay, $2\nu\beta\beta$ has a long decay time, thus it can be affected by phenomenology beyond the standard model. In particular, the

analysis of the two emitted electrons sum spectrum gives insight on such theories. This spectrum is characterized by the spectral index n, determined by the phase space factor $G^{2\nu} \sim (Q_{\beta\beta} - E_{sum})^n$, where $Q_{\beta\beta}$ is the Q value of the nuclear transition and E_{sum} is the sum of the two emitted electron energies. The SM $2\nu\beta\beta$ has $n = 5$, while new physics model predict different values [26]. For example, the $\beta\beta$ decay can happen with contestual emission of single or multiple Majorons, defined as the supersymmetric partner of massive neutrinos [27]. In the case of a single Majoron emission the possible values for the spectral index are $n = 1, 2, 3$, while in the case of multiple Majoron $n = 3, 7$ [28]. In addition to the emission of exotic particles, also the presence of violation of fundamental

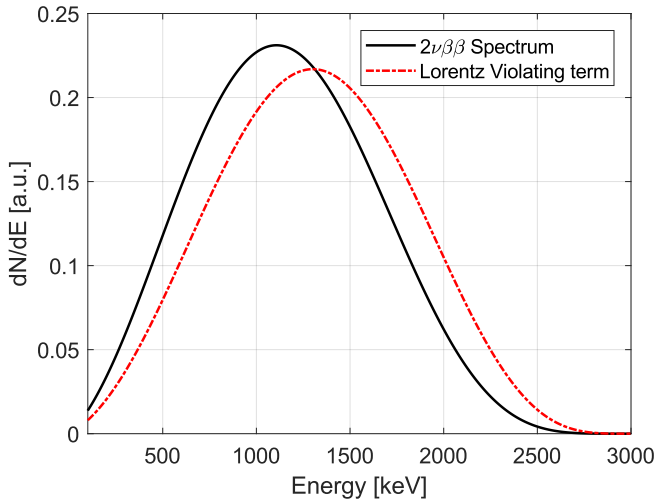

Figure 2.7: Comparison between standard (black) and Lorentz violating (red) $2\nu\beta\beta$ calculated electron spectra for ^{82}Se. The spectra are normalized to the same integral. The region where higher differences appear is above 2 MeV.

symmetries affects the electron sum spectral shape. Different solutions to the definition of a coherent quantum gravitation theory, for example, hypothesize the existence of unconventional physical phenomena at the Planck scale ($\sim 10^{19}$ GeV), violating Lorentz and CPT (Charge-Parity-Time reversal) symmetries [29]. Since this new phenomenology arises at unreachable energies, a direct observation cannot be performed. However, as discussed in [30], the violation of Lorentz invariance or of CPT symmetry may induce observable deviations from Standard Model predictions. Such new Physics can modify the Standard Model (SM) predictions as an effective theory, characterized by Lorentz symmetry violation (LV) [30]. The Standard Model Extension (SME) proposed in [31, 32, 33], includes LV with background fields with non-zero vacuum expectation values, resulting in the sponaneous breaking of space-time symmetry [34]. SM particles interact with these fields with a strength parameterized by SME parameters [35], resulting in LV-induced modifications of SM processes. Neutrinos interact with different operators, and in particular with a renormalizable LV operator, known as the *countershaded operator*, having mass dimension three and thus inducing also CPT violation.
This interaction modifies the quadrimomentum of neutrinos from $q^\alpha = (\omega, \boldsymbol{q})$ to $\tilde{q}^\alpha = (\omega, \boldsymbol{q} + \boldsymbol{a}^{(3)}_{\rm of} - \mathring{a}^{(3)}_{\rm of}\hat{\boldsymbol{q}})$, where $\boldsymbol{a}^{(3)}_{\rm of}$ and $\mathring{a}^{(3)}_{\rm of}$ are the directional and isotropic SME coefficient for the countershaded operator coupling to neutrinos [36]. The former can be studied in experiments directly sensitive to particle directions, while the latter when directions are not taken into account [30]. In $2\nu\beta\beta$ experiments measuring only the energy of the two emitted electrons, only $\mathring{a}^{(3)}_{\rm of}$ remains as possible source for LV. The standard $2\nu\beta\beta$ electrons sum spectrum is modified in shape, with a sizable modification parameterized by $\mathring{a}^{(3)}_{\rm of}$. This effect is characterized by spectral index $n = 4$, modifying the shape of the spectrum. The differential spectrum can be expressed with

$$\begin{aligned}\frac{d\Gamma}{dE} =& C \cdot F(Z, t_1)\sqrt{t_1(t_1+2)}(t_1+1)\cdot \\ & F(Z, E-t_1)\sqrt{E-t_1(E-t_1+2)}(E-t_1+1)\cdot \\ & [(Q-E)^5 + 10 \cdot \mathring{a}_{\text{of}}^{(3)}(Q-E)^4)] \\ =& C \cdot \left(\frac{dI_{2\nu,\text{SM}}^{\text{Theo}}}{dE} + 10 \cdot \mathring{a}_{\text{of}}^{(3)}\frac{dI_{2\nu,\text{LV}}^{\text{Theo}}}{dE}\right)\end{aligned} \tag{2.24}$$

where t_1 is the energy of one of the two emitted electrons, E is the sum of the two emitted electrons kinetic energy, Q is the Q-value of the $2\nu\beta\beta$, C is the factor taking into account the nuclear matrix element and normalization constants [36, 37], F is the Coulomb correction [38] and $\frac{dI_{2\nu,\text{SM}}^{\text{Theo}}}{dE}$ and $\frac{dI_{2\nu,\text{LV}}^{\text{Theo}}}{dE}$ are the SM and LV terms of the decay amplitudes respectively. The LV is represented as an additive term, characterized by a different spectral shape and whose weight is given by $\mathring{a}_{\text{of}}^{(3)}$. The effect due to the LV interaction is represented in Fig.2.7, in the case of ^{82}Se, where a difference in shape is evident over all the spectral distribution. A detailed study of the $2\nu\beta\beta$ spectrum, therefore, has the power to test different physics models, further increasing the importance of direct studies of this decay. I will show the results of this search in chapter 4.

Chapter 3

Experimental search for $0\nu\beta\beta$

The incontrovertible evidence of massive neutrinos has been given by the measurement of their flavour oscillations. These results demonstrate that the electroweak sector of the Standard Model is incomplete and that new Physics is necessary to correctly model the observed phenomena. In particular, the neutrino quantum field structure and its mass mechanism have yet to be explained. In this landscape, a unique role is played by the Neutrinoless Double Beta Decay ($0\nu\beta\beta$). This decay, if detected, would simultaneously prove the Majorana nature of the neutrinos and provide a value to their absolute mass scale.
Such investigation is therefore of capital importance, and different efforts are made to develop detectors capable of increasing our sensitivity for this process. On the basis of known experimental limits and theoretical predictions, $0\nu\beta\beta$ has an half-life greater than $10^{26} - 10^{27}$ y. Such value is equivalent to few event/year per tonne of candidate isotope. Such extreme target demands the development of detectors with mass on the tonne scale and spurious background $\leq$1 counts/ton/year. Current generation experiments are facing the technical and financial challenges related to meet these requests, exploiting different strategies to push the sensitivity as high as possible.
In this chapter different way to search for the $0\nu\beta\beta$ will be investigated. A particular detail on scintillators will also be given, since this detector concept is exploited in next generation $0\nu\beta\beta$ experiments.

3.1 Parameter for $0\nu\beta\beta$ search

The experimental search of $0\nu\beta\beta$ relies on the detection of the two electrons emitted in the process. Since the recoil energy of the nucleus is negligible, the two electrons carry a total kinetic energy equal to the Q-value of the nuclear transition. Counting these events is therefore possible to calculate the decay half-life of the transition, using the equation:

$$T_{1/2}^{0\nu} = \ln 2 \frac{N_{\beta\beta} T_{mis}}{N_{0\nu}} \tag{3.1}$$

where $T_{1/2}^{0\nu}$ is the decay half-life, $N_{\beta\beta}$ is the number of decaying candidates, T_{mis} is the measurement live-time and $N_{0\nu}$ is the number of detected decays. The $0\nu\beta\beta$ decay rate, in case of virtual neutrino exchange, is proportional to the square of the so-called effective Majorana mass ($|\langle m_{\beta\beta}\rangle|$) and is given by

$$[T_{1/2}^{0\nu}]^{-1} = \frac{|\langle m_{\beta\beta}\rangle|^2}{m_e^2} G^{0\nu} |M^{0\nu}|^2 \tag{3.2}$$

where $G^{0\nu}$ is the two-body phase-space integral, $M^{0\nu}$ is the $0\nu\beta\beta$ nuclear matrix element and m_e is the electron mass. Detecting the $0\nu\beta\beta$ is also a powerful tool to set a constraint on the absolute scale of the Majorana mass (see Chapter 2). Generally, the theoretical contribution to the decay

rate is referred to as the *nuclear factor of merit*, given by $F_N^{0\nu} = G^{0\nu}|M^{0\nu}|^2$. This factor is useful when comparing the sensitivity for $|\langle m_{\beta\beta}\rangle|$ achievable with different isotopes, because $F_N^{0\nu}$ contains all the nuclear and kinematics characteristic of the decay.
The performances of a given $0\nu\beta\beta$ detector are given in terms of the *experimental sensitivity*, $F_D^{0\nu}$, defined as the process half-life corresponding to the maximum signal that can be observed at a given statistical confidence level (CL). At 1σ level this is given by:

$$F_D^{0\nu} = T_{1/2}^{back.fluct.} = \ln 2 \; N_{\beta\beta}\epsilon\frac{T_{mis}}{n_{bkg}} \tag{3.3}$$

where ϵ is the two electron detection efficiency and n_{bkg} is the maximum number of counts hidden by a background fluctuation. $F_D^{0\nu}$ can be further specialized expanding its factors in terms of detector design parameters.
The factor $N_{\beta\beta}$ can be written as:

$$N_{\beta\beta} = N_{\beta\beta}^{\text{nuclei}}\eta = \frac{M}{A}N_{\text{Av}}\eta \tag{3.4}$$

where $N_{\beta\beta}^{\text{nuclei}}$ is the total number of candidate nuclei, M is the detector mass, A is the mass number of $\beta\beta$ candidate, N_{Av} is the Avogadro number and η is the isotopic abundance of the $\beta\beta$ candidate. On the other hand, assuming that the background scales with M, the total number of background counts N_{bkg} can be expressed as:

$$N_{bkg} = T_{mis}\;\Delta\;B\;M \tag{3.5}$$

where B is the specific background rate per unit mass, time and energy (usually measured in counts/keV/kg/y) and Δ is the full-width-at-half-maximum (FWHM) energy resolution of the detector. This expression, assuming that N_{bkg} follows a Poisson statistics, allows to calculate n_{bkg} at 68% C.L. as:

$$n_{bkg} = \sqrt{N_{bkg}} = \sqrt{T_{mis}\;\Delta\;B\;M} \tag{3.6}$$

Such approximation holds if N_{bkg} is big enough to ensure that the Poisson distribution is well approximate with a Gaussian, with $\sigma = \sqrt{N_{bkg}}$. Substituting equations (3.6) and (3.4) into equation (3.3), the following expression is obtained for the experimental sensitivity:

$$F_D^{0\nu} = ln2\frac{\eta\epsilon N_{Av}}{A}\sqrt{\frac{T_{mis}M}{B\;\Delta}}\;(68\%\text{ C.L.}) \tag{3.7}$$

showing that the sensitivity, that is to say the highest detectable half-life, is greater when a huge number of candidates can be observed for a long time, with high energy resolution, low background and high efficiency [19]. Usually, this expression is rearranged defining two quantities:

$$\text{Exp} = T_{mis}M \quad \text{and} \quad B_{\text{ROI}} = B\;\Delta \tag{3.8}$$

the Exposure and the Background in the region of interest. Exp is proportional to the total number of observed nuclei, while B_{ROI} represents the expected background below the $0\nu\beta\beta$ peak.
If $\text{Exp}\cdot B_{\text{ROI}}$ product is compatible with zero, the so-called *zero background condition* is met. In this domain the approximation of the Poisson with a Gaussian fails, and n_{bkg} is substituted by a constant term n_L, defined as the maximum number of counts compatible (at a given C.L.) to the observed background. With this substitution, the sensitivity becomes

$$F_D^{0\nu} = ln2\frac{\eta\epsilon N_{Av}}{A}\frac{T_{mis}M}{n_L} = ln2\frac{\eta\epsilon N_{Av}}{A}\frac{\text{Exp}}{n_L}\;(68\%\text{ C.L.}) \tag{3.9}$$

In this condition the sensitivity is directly proportional to exposure. The effects of Exp and B_{ROI} are therefore extremely relevant, since they change dramatically the dependence of sensitivity on the detector parameters [19].
Equations 3.7 and 3.9 summarize efficiently the most important design criteria for $0\nu\beta\beta$ detectors:

- High detector performances in terms of energy resolution and detection efficiency (Δ and ϵ)
- Low levels of background counts, with proper techniques devoted to its reduction (B)
- Stable and easily maintainable technologies, to guarantee long live times (T)
- High detector masses (M), possibly enriched in the isotope under study (η).

In between such criteria, the background reduction plays a leading role. This parameter can be reduced more easily than the other factors in the $\text{Exp} \cdot B_{\text{ROI}}$ product, heavily contributing in reaching the zero background condition, in which the sensitivity scales directly with mass and live time. In the next section an insight to the typical background sources of a $0\nu\beta\beta$ experiment will be given.

3.1.1 Sources of radioactive and cosmogenic background

The most common sources of radioactive background for rare events searches are the nuclear decays, the cosmic muons (μ) and the neutrons (n).

Radioactive decays

The decaying isotopes can be isolated (for example the ^{40}K or the ^{147}Sm) or contained in a decay chain, and they can contaminate both the detector and the laboratory in different ways. Typically the contamination are divided between surface contaminations and bulk contaminations, with respect to the position of the isotope (or chain) [39]. The nuclear decays generate γ, β and α particles, responsible for undesired signals when interacting with the detector. The most important chains of natural decays are the ^{232}Th chain and the ^{238}U chain, represented in figures 3.1 and 3.2.

γ decays Different decays are characterized by γ emissions, but within a specified energy range. The most energetic photons emitted, in fact, are the 2615 keV γ from ^{208}Tl (^{232}Th chain) and the 3269 keV γ from ^{214}Bi (^{238}U chain). Higher γ energies are achievable only when different photons interact simultaneously with the detector. This occurrence is generally rare for uncorrelated decays, but is made more likely when a particular decay sequence generates correlated decays separated by a small time interval. For example, ^{208}Tl undergoes a β^- decay followed by a γ de-excitation, that can happen with the subsequent emission of two photos at 2615 keV and 583 keV. Such emissions are separated by a small time, therefore these events can be detected simultaneously with consistent probability. Such situation is made more likely if the radioactive source is near the detector active volume, therefore a careful control of radioactive contamination can reduce this background contribution. Among different decays, a common signature is the ^{40}K γ-peak, at an energy of 1460 keV.

β decays Another product of the decay chains are the β particles, characterized by a continuous spectrum below the Q-value of the nuclear reaction, referred to as *end-point*. The interaction mechanism of β particles can be both direct, due to electrons scattering against matter, and mediated by the emission of bremmstralhung photons. The β contribution to the background can be reduced both by selecting clear materials for the inner detector parts and by shielding the detector core. However the latter solution causes the bremmstrahlung cross section to grow, therefore increasing the number of background events. As a consequence, the shielding has also to contain layers built with clean materials with lower density then lead, capable of stopping the β particles while keeping low the number of bremmstrahlung photons.

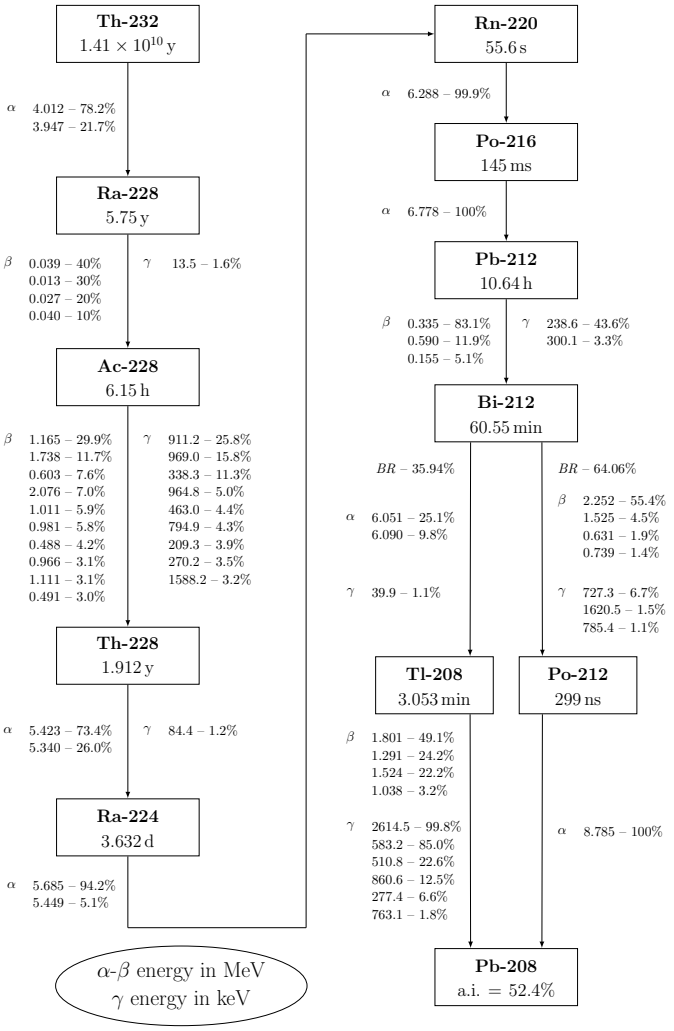

Figure 3.1: Decay chain of ^{232}Th. The γ decays have different energies, but the highest line is the 2614 keV γ from ^{208}Tl. Higher γ energies are achievable only when different photons are detected simultaneously, especially when emitted by correlated subsequent decays. The α decays have energies between 4 MeV and 8 MeV, but surface effects and interaction with dead layers lower their energies. As a consequence, α particles cause an almost flat background in energies lower than 4 MeV. In the lower part of the chain the *Bi-Po sequence* can be seen.

α decays Last but not least, the nuclear decays belonging to the natural chains provide α particles, characterized by monochromatic energies between 4 MeV and 9 MeV. While the α particles coming from bulk contamination release all their energy in the active volume of the detector, the particle coming from surface or external contaminations lose part of their energy interacting with insensitive elements, for example the structure holding the detector. These *degraded α particles* generate a flat background below 9 MeV, unavoidable in experiments sensitive only to the energy deposition. Fortunately the α particles are easily absorbed by materials because of their high stopping power. Therefore the main source of α background is related to the contamination of materials building the active detector itself or the structures directly facing the active region of the detector.

Cosmogenic background

The cosmogenic background is mostly composed by μ, minimum ionizing particles generated at $\sim$15 km from the sea level by the interaction of cosmic rays. The typical value for μ flux at sea level is $\sim$ 0.02 $\mu/cm^2/s$ [40], therefore its contribution cannot be neglected especially for high volume detectors. The contribution to the background of direct μ interactions as well as of the muon generated electromagnetic showers, can be reduced by anti-coincidence cuts between different detectors. On the other hand, γ and n background arising from μ interactions in the setup are very dangerous, and the presence of high density shields makes the situation even worse [41]. As a consequence the flux of μ has to be reduced, in order to ensure the reduction of the corresponding background. This reduction can be obtained placing the detector underground, using facilities

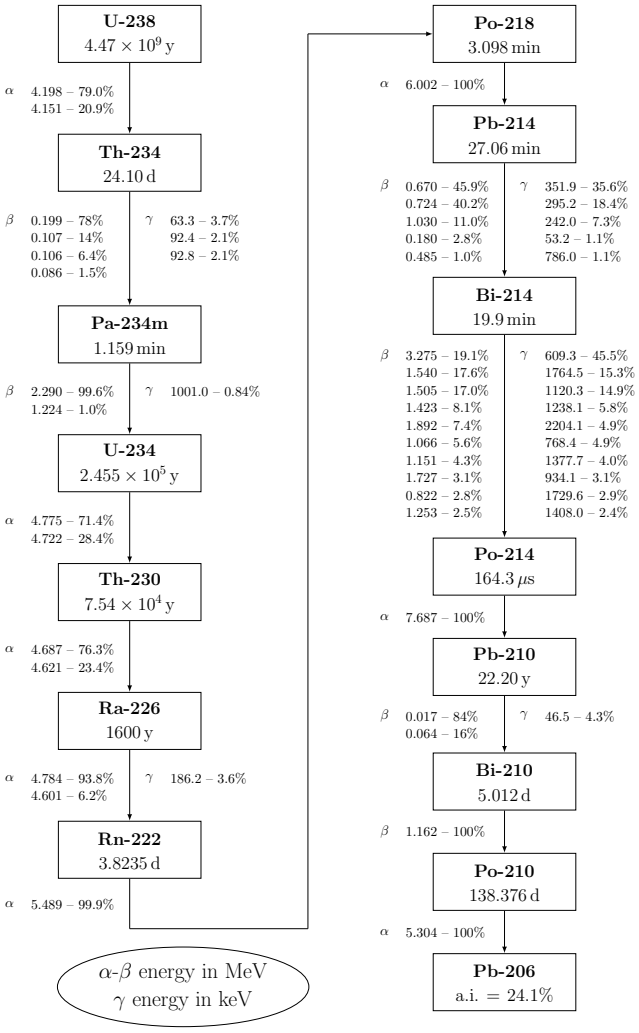

Figure 3.2: Decay chain of ^{238}U. The γ decays have different energies, the highest line is the 3269.7 keV γ from ^{214}Bi. Higher γ energies are achievable only when different photons are detected simultaneously, especially when emitted by correlated subsequent decays. The α decays have energies between 4 MeV and 7 MeV, but surface effects and interaction with dead layers lower their energies. As a consequence, α particles cause an almost flat background in energies lower than 4 MeV.

with an adequate depth (usually expressed in meters water equivalent, m.w.e.). For example, at the Laboratori Nazionali Gran Sasso (LNGS), the flux is reduced by about six orders of magnitude with respect to the outside flux by the 3600 m.w.e. shield, provided by the mountain itself. The average integrated μ flux in the underground site is $\sim 3 \times 10^{-8}$ $\mu/cm^2/s$ [41], therefore ensuring a good reduction of μ induced background. Alongside direct ionization, μ interactions cause the activation of radioactive isotopes in different materials. As a consequence, the storage of materials has to be performed avoiding the direct exposition to cosmic rays, thus reducing the creation of dangerous contaminants. An example is the ^{65}Zn, activated in Zn/based materials, which decays emitting a γ ray of 1116 keV. Such cosmogenic contaminant contributes, as will be reported in chapter 4, to the background af CUPID-0 detector, built with ZnSe crystals.

n background

The n flux is due to different mechanism, which generate particle with a large energy range. Below $\sim$10 MeV the flux is mainly due to spontaneous fission (from ^{238}U) and to (α,n) nuclear reactions due to the interaction of naturally emitted α particles with different materials. Otherwise, n with energy greater than $\sim$10 MeV are produced by nuclear reactions due to cosmic μ interactions. The n induced background is dangerous because it provides both direct interactions, (n,γ) reactions and activation of radioactive isotopes by the means of n based nuclear reactions. As a consequence, the detector has to be shielded from n interactions, using materials capable of moderating and absorbing the incoming n. Many current experiments use B and Li loaded polyethylene shields

[41], capable of combining the two needed features.

Mixed background

When two background events are separated by a time interval shorter than the detector time resolution, the corresponding signal superimpose. Such superimposition, referred to as *pile-up* is a crucial issue to be addressed. The lack of pile-up control and rejection, in fact, causes the surge of new background families. Such effect increases anomalously background sources otherwise controllable. The pile-up can be either homogeneous, when two identical particles superimpose, or heterogeneous, when particles of different kinds add their effects.
Both these two kind of pile-up can happen on a random base, when two totally uncorrelated events happen in the same instant, or when two events are correlated by a particular decay chain. In the former case, the pile-up probability depends on the intensity of the background rate, while in the latter on the positioning of the source with respect to the active region of the detector.

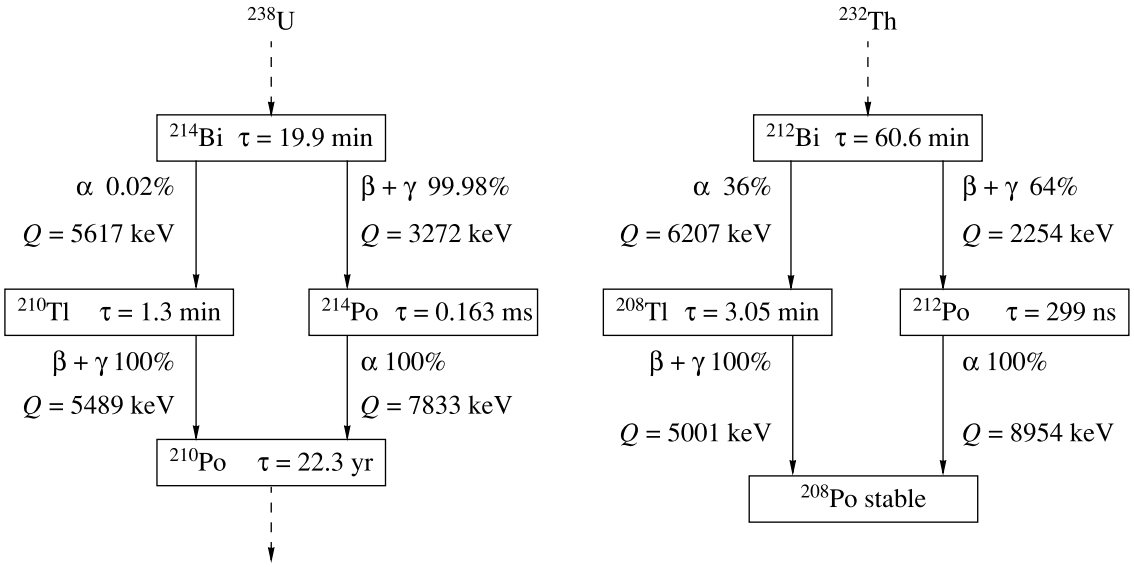

Figure 3.3: Bi-Tl and Bi-Po sequences in ^{238}U and ^{232}Th chains. The pile-up of β from Bi decay and α from Po decay is possible, given the short time of such decay, and may lead to undesired background. On the other branch of the chain, the α - β sequence due to Bi-Tl decay is not likely to give a pile-up event. The time correlation between the two decays can although be used to tag β Tl decays, responsible for background events mimicking the $\beta\beta$ signal up to 5 MeV.

The homogeneous pile-up happens for every species of background, and can be reduced excluding radioactive contamination near the detector active volume. A typical example of this kind of pile-up is ^{208}Tl, which undergoes a β decay followed by two subsequent γ de-excitations, emitting two photons at 583 keV and 2615 keV. Since these two decays happens almost instantaneously, their pile-up is likely, especially if the Tl contamination is close to the detector active volume.
On the other hand, heterogeneous pile-up is characteristic of particular sources, since its probability is high enough only when a physical correlation exist between two events. The main source of heterogeneous superimposition is related to the so called *Bi-Po sequence*, which is a part of the natural radioactive chains (see fig.3.3). This sequence of radioactive decays occurs in the following mode:

$$^{232}\text{Th}) \quad ^{212}\text{Bi} \xrightarrow{61\text{min}} ^{212}\text{Po} + \beta^- \xrightarrow{3\cdot10^{-7}\text{s}} ^{208}\text{Pb} + \beta^- + \alpha \tag{3.10}$$

$$^{238}\text{U}) \quad ^{214}\text{Bi} \xrightarrow{20\text{min}} ^{214}\text{Po} + \beta^- \xrightarrow{0.15\text{s}} ^{208}\text{Pb} + \beta^- + \alpha \tag{3.11}$$

Since the second decay is much quicker than the first one, the two particles are emitted and therefore detected simultaneously. These simultaneous events generate a pile-up signal which has

both β and α characteristics. Since β events have a continuous energy spectrum and α particles are often degraded upon detector interaction, such events acquire a wide range of energies, providing background well outside their characteristic sum energy.
On the other branch of the chain, the α - β sequence due to Bi-Tl decay is not likely to give a pile-up event, since the time characteristics of the decay are long. The time correlation between the two decays can although be used to tag β Tl decays, responsible for background events mimicking the $\beta\beta$ signal up to 5 MeV. The application of α-delayed coincidences can therefore provide effective background reduction strategies, given the possibility to tag the α father decay.

3.1.2 $2\nu\beta\beta$ background

The $2\nu\beta\beta$ is a possible decay channel for all the $0\nu\beta\beta$ candidates. Unfortunately its half-life time is shorter than the one of $0\nu\beta\beta$, causing the signature of this decay to be hidden by the counts of $2\nu\beta\beta$ near to its end point (see Fig. 2.4). This effect can be effectively reduced only enhancing the detector resolution, thus avoiding the broadening of the $2\nu\beta\beta$ spectrum below the $0\nu\beta\beta$ peak. In fact, an approximate expression for the ratio between $0\nu\beta\beta$ signal (S) and $2\nu\beta\beta$ background (B) at the Q value can be written as:

$$\frac{S}{B_{2\nu}} \backsim \frac{T^{2\nu}_{1/2}}{T^{0\nu}_{1/2}} \frac{Q^5_{\beta\beta}}{\Delta^6} \tag{3.12}$$

showing that resolution plays the most important role in reducing this form of background, alongside the choice of high Q-value $0\nu\beta\beta$ decaying isotopes. In Fig.3.4, $\frac{S}{B_{2\nu}}$ for ^{82}Se and ^{130}Te is reported as a function of Δ. At equal resolution, ^{130}Te has the higher signal-to-noise ratio, since it has a longer $T^{2\nu}_{1/2}$ (See Table 2.2 at page 12). It is worth noticing also that, for $\Delta \leq 80$ keV (corresponding to a relative energy resolution of 2.6% for ^{82}Se and 3% for ^{130}Te) the ratio is greater than 10. Therefore increasing the resolution is really helpful, and a good goal to guarantee a negligible $2\nu\beta\beta$ contribution to background is $\Delta \leq 0.02 \cdot Q_{\beta\beta}$. In addition, fast $2\nu\beta\beta$ decays can increase the chance of pile-up between two events, especially if the detector is enriched in the candidate isotope ot it is characterized by slow response times [20]. This is the case of ^{100}Mo, characterized by $T^{2\nu}_{1/2} \sim 7 \cdot 10^{18}$ y.

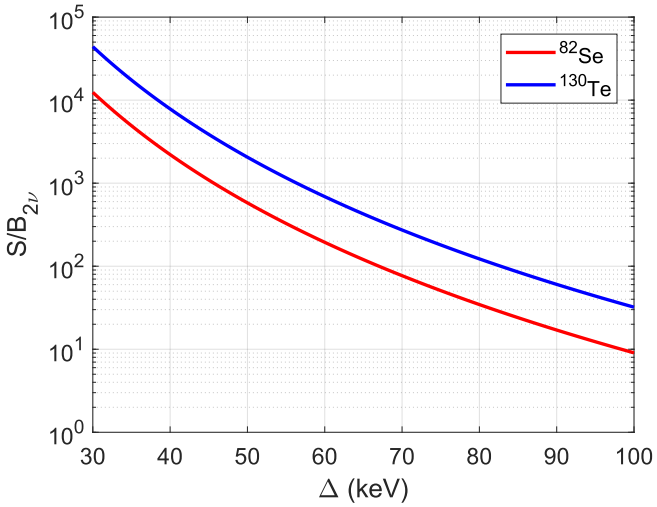

Figure 3.4: Ratio between 0ν signal and 2ν background for ^{82}Se (red line) and ^{130}Te (blue line) as a function of the resolution (Δ). As predicted by Eq.(3.12), at equal Δ ^{130}Te has the higher signal-to-noise ratio, since it has a longer $T^{2\nu}_{1/2}$ (See Table 2.2 at page 12). It is worth noticing also that, for $\Delta \leq 80$ keV (corresponding to a relative energy resolution of 2.6% for ^{82}Se and 3% for ^{130}Te) the ratio is greater than 10.

3.2 Experimental strategies

To address the request for high sensitivity, different possible approaches can be pursued. These strategies can be divided in two main groups:

Source=Detector: where the detector contains the candidate $0\nu\beta\beta$ isotope in its active part (calorimetric approach);

Source≠Detector: where the candidate $0\nu\beta\beta$ isotope is external to the detector.

The experiments belonging to both groups are characterized by their experimental sensitivity. On one side, the choice of the $0\nu\beta\beta$ candidate isotopes poses some limitation. On the other, the detector has to be developed to enhance the sensitivity. According to Eq.(3.7) and (3.12), the design goals are:

- *Performing resolution* Δ. The capability to distinguish between two energies has to be the highest possible, to ensure the reduction of $2\nu\beta\beta$ induced background. In addition, a good resolving detectors also increases the sensitivity over a spurious background.
- *Low spurious background index* B. Reaching as close as possible to the zero background condition (Eq.(3.9)) demands careful selection of materials, underground facilities and the possibility to implement active strategies for background reduction.
- *High detector masses* M. Looking to the highest possible number of candidate nuclei is mandatory, and demands the development of mass-scalable technologies. In addition, the possibility to use enriched materials as to be taken under consideration.
- *Long and stable operation* T *and* ϵ. Long observational times are inalienable. As a consequence, stable detectors has to be designed, with high efficiency and low dead times.

These features are difficult to be met simultaneously in a single detector. Consequently, each experimental approach has its weaknesses to be dealt with. A careful design demands to push as much as possible the most better properties of a detector, keeping the highest possible sensitivity.

3.2.1 Source≠Detector approach

In between the two approaches mentioned earlier, Source≠Detector approach is the one with lowest background and strong exposure limitations. In this practical implementation, $\beta\beta$ candidate isotopes are collected in sources put between active detector layers. Different techniques are explored (scintillators, solid state detectors, gas chambers), and the main advantage of this design is the possibility to reconstruct the event topology. Such identification capabilites allow to reach low background conditions, since $\beta\beta$ events are selected with high precision. This characteristic gives those detectors the possibility to easily perform analysis on $2\nu\beta\beta$ spectral shape, that can be reconstructed in a wide energy range. The poor energy resolution ($\sim$10%) is however a strong limitation due to the unavoidable $2\nu\beta\beta$ background. This characteristic is strictly correlated to the self-absorption of the electrons inside the source, forcing the sources to be made as thin as possible to prevent this feature. Such constraint makes difficult to gather high masses of isotopes, thus limiting the sensitivity in this implementation. In addition, the external sources result in low detection efficiency ($\sim$30%), further disfavouring their application [19].

NEMO-3

The state of the art for this category of detectors is represented by the Neutrino Ettore Majorana Observatory (NEMO-3) detector. This experiment was built with the goal of measuring the two electrons emitted by a $\beta\beta$ decay, to maximize the purity of the selected events. Its design [42]

is based on the repetition of circle sectors where a source foil, containing the decay candidate, is placed between scintillation detectors in a magnetic field, acting as trackers for the two electrons. NEMO-3 is built to investigate simultaneously different isotopes, thus proving the flexibility in terms of isotopes of this experimental strategy. In this detector type, a candidate event would look like the one reported in Fig.3.5. The full topology reconstruction, actuated with the simultaneous tracking and energy measurement, allows the full identification of particle events. The background reduction capabilities originating from the combination of these informations, allowed to put limits on different $0\nu\beta\beta$ [43], and allowed the full characterization of $2\nu\beta\beta$ spectral shape [44].

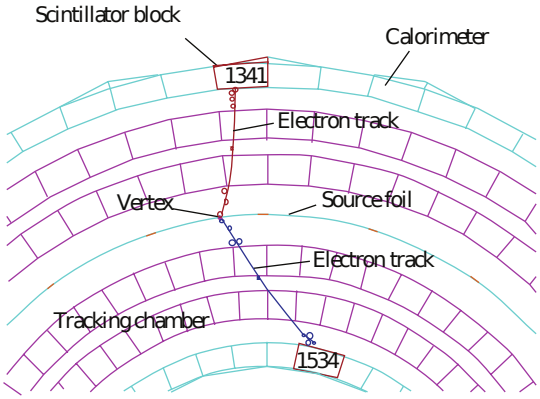

Figure 3.5: Candidate $\beta\beta$ event in NEMO-3 detector. The two electrons emitted in the source foil are tracked and detected, with full reconstruction of the event topology. The picture is taken from [19].

The main limitation of this technique are both the low source mass and poor energy resolution, that limit the possible increase in sensitivity. As a consequence, a further development including >100 kg of isotopes is extremely difficult (if not impossible) for this detector technique. An upgrade of the NEMO detector has been proposed as the Super-NEMO project [45]. This detector is fully commissioned, and plans in reaching the 100 kg of isotope under study, to perform the study of eventual left-right asymmetries in the $\beta\beta$ decay.

3.2.2 Source=Detector approach

So far [12], the most stringent bounds to the half-life of $2\nu\beta\beta$ have been achieved exploiting the Source=Detector approach. In these detectors, the $\beta\beta$ candidate is contained in the active volume, remaining sensitive to the total energy of the emitted electrons. This strategy is characterized by high electron detection efficiency, because the source is a part of the detector, and allows the observation of large masses of candidate isotope. In addition, very high resolution is achievable with the proper type of detector ($\sim$0.1% FWHM with germanium diodes and bolometers). In spite of this advantage, the event topology reconstruction is usually difficult, with the exception of liquid or gaseous Xenon time proportional chambers (TPC), which have however lower energy resolutions. As a consequence, many solid calorimetric experiments exploit hybrid technologies with a double readout (i.e. ionization and scintillation or phonons and scintillation), allowing to reduce the background via particle identification techniques, while maintaining their high resolution feature.
The ultimate goal of these detectors is the exploration of the inverted hierarchy region of the neutrino masses [20]. In this region, the effective Majorana mass has the lower limit $|\langle m_{\beta\beta}\rangle| \gtrsim 10$ meV, corresponding to $T^{0\nu}_{1/2} \gtrsim 10^{27}$ y. Such sensitivity can be obtained only with masses of the order of 1 ton and background $<10^{-3}$ counts/keV/kg/y. Current and next generation experiments are therefore directed toward the lowering of the background and the increase of isotope mass, exploiting enrichment procedure to gather as much candidate nuclei as possible. In the next section a brief discussion of the main technologies implemented for this search is presented, to give an overview of the possible solutions.

Tracking Time Proportional Chambers

As discussed in Sec.3.2.1, tracking the particles is an excellent tool for background reduction, since $0\nu\beta\beta$ has a well defined topology. Such potentiality is generally unavailable in the Source=Detector approach, but can be usefully exploited in the study of $0\nu\beta\beta$ for the ^{136}Xe, that can be easily included in Time Proportional Chambers (TPC). Liquid Xe, in fact, produces both scintillation light and ionization signal when hit by impinging radiation. By detecting the scintillation light, the energy of the radiation (signal amplitude) and its interaction time (arrival of light signal) are measured. On the other hand, the charge signal gives the localization of the interaction in the plane, alongside its tracking in time. Such combination is powerful, since it has the efficiency and mass scalability of Source=Detector approach, while maintaining tracking capabilities. Unfortunately, since this technology relies on light signals to perform energy measurement, it is affected by poor resolution. Such feature makes it difficult to disentangle the $0\nu\beta\beta$ peak from the $2\nu\beta\beta$ tail, therefore compromising the attainable limit. This drawback is although limited by the fact that the $2\nu\beta\beta$ mode for ^{136}Xe is amongst the lowest ever measured, assuring a limited ingerence of this unavoidable background. EXO-200 [46] has been a running experiment based on this technology, that demonstrated the high performance of this technique. It could put a limit both on the $T^{0\nu}_{1/2}$ of ^{136}Xe [47] and on exotic processes, by the study of $2\nu\beta\beta$ electron spectrum [37]. Current R&D work is devoted to the development of the next generation version of EXO-200 concept: nEXO (next-generation Enriched Xenon Observatory) [48]. The design of this next-generation experiment is based on EXO-200, increasing the dimension and reducing the detector components.

Germanium Detectors

The application of high purity germanium detectors (HPGe) to the search of $0\nu\beta\beta$ of ^{76}Ge has a long story [49], and it is well motivated by the excellent performances of HPGe detectors as gamma spectrometers in the MeV range. Currently, the major experiments exploiting this technique are MAJORANA [50] and GERDA [51] (GERmanium Detector Array), that are tacking data and cooperating to built a next generation, tonne-scale, HPGe based detector: LEGEND (Large Enriched Germanium Experiment for Neutrinoless Double beta decay) [52]. The typical energy resolution is $\sim 0.2\%$ around 2 MeV, thus making negligible the background due to $2\nu\beta\beta$. The high purity attainable for the materials in this detectors allows to control background levels, further lowered by the means of pulse shape analysis (PSA) techniques for the rejection of multi-site events, incompatible with the $\beta\beta$ expected signature. Such feature is necessary, given the fact that ^{76}Ge $Q_{\beta\beta}$ is 2039 keV, in a region where the radioactive background due to γ interaction is high (see Sec.3.1.1 at page 23). A consistent fraction of the background in the ROI is therefore due to multiple Compton events due to higher energy γ rays. This is the dominant contribution due to sources far from the detectors, while close contamination also contributes with β and α events. In the case of γ or $\beta + \gamma$ interactions, the topology is characterized by multi-site events (MSE). On the opposite, single-site events (SSE) extend over small volumes and are related to single Compton scattering, photoelectric effect or very close multiple energy depositions. The latter category includes electron induced interactions and double escape events. Double beta events are therefore SSE. MSE and SSE are characterized by different pulse shapes, due to the lack of uniformity of the field inside the HPGe diode. Indeed, MSE spread charge over regions with a non-negligible potential gradient, resulting in slower pulses with respect to SSE [51]. Such discrimination has to be optimized depending on the design of the used detector, but unambiguously permits a strong reduction of background. Furthermore, the HPGe detectors can be built with germanium enriched in ^{76}Ge, making the mass increase more effective. This point is crucial for such detectors, since the mass increase is limited in this technology, and can only be accessed by repeating relatively small performing modules. In addition, the limit on the application of this technique is that only ^{76}Ge can be investigated, thus making such frontier detector unable to investigate different candidate isotopes.

Liquid Scintillators

Liquid scintillators experiments had an enormous success in the study of neutrino oscillation, given their extreme masses and low level of background. Such features makes them favorable candidates for $0\nu\beta\beta$ searches, to which they can be adapted with limited work. The main experiments following this route are KamLAND-Zen [53] and SNO+ [54], all designed as neutrino detectors and now ongoing technical work to be dedicated to $0\nu\beta\beta$ searches. These detectors are based on the measurement of optical photons emitted by an organic liquid scintillator (LS), usually a benzene-based compound, loaded with $0\nu\beta\beta$ candidate isotopes. The emitted photons are proportional to the energy deposited in the scintillators and, by looking at the photon emission with different ligh-sensitive detectors, the topology and position of the event can be reconstructed. The latter feature is possible given the fast ($\sim$ns) scintillation time of the used compounds, allowing such devices to be position-sensitive. Such feature allows to select events happening only in the volume containing the $0\nu\beta\beta$ source, and thus limiting the possible background. In addition, such fiducial volume is filled with high purity LS and usually surrounded by a water-based Cherenkov detector, acting as an active veto against radiation coming from the outside of the detector core. Extremely low background levels can be obtained with this techniques, although extremely high masses ($\sim$10 ton) are employed in such detectors. In the application to $0\nu\beta\beta$, the main limit of these detectors is the poor energy resolution This issue is connected to the mechanism used to measure the energy. The resolution in scintillation detectors, in fact, is limited by the statistical fluctuation on the number of collected photons. Therefore the relative resolution worsen, if the absolute number of collected photons decreases. Typical values of $\Delta \sim 0.06 \cdot Q_{\beta\beta} \sim 200$ keV have been measured [19], therefore making the ingerence of $2\nu\beta\beta$ non negligible. Such low resolution forces also the development of comprehensive background model, to allow the identification of the different spectral contributions. In addition, the fact that in some of these detectors is necessary to add the $0\nu\beta\beta$ candidate to the detector core demands high radiopurity, since the addition of contaminants in the fiducial volume is not excluded. This class of detectors has the highest expectation in terms of isotope mass and, if the radiopurity can be maintained, also in terms of background. The possibility to switch between different $0\nu\beta\beta$ candidates also guarantees flexibility in the application, making these detectors capable of pushing the current sensitivity for different isotopes.

Bolometers

A bolometer is a thermal detector constituted by a particle absorber, usually a diamagnetic crystal, kept at temperature $\sim$ 10 mK by means of a thermal machine, usually a diluition refrigerator.
The extreme temperatures are needed to minimize the heat capacitance of crystals, C_{H}. In these conditions, in fact, $C_{\mathrm{H}} \propto (T/T_{\mathrm{D}})^3$, where T_{D} is the Debye temperature of the material. Each energy deposit in the crystal (E_{Dep}) induces a temperature increase (ΔT), given by:

$$\Delta T = \frac{E_{\mathrm{Dep}}}{C_{\mathrm{H}}} \tag{3.13}$$

which is inversely proportional to the third power of the temperature. This increase generates phonons in the crystal, characterized by an energy of few μeV[1]. Phonons propagate trough the lattice and are recorded by a dedicated sensor thermally connected to the absorber. A bolometer, therefore, acts as a calorimeter, only sensitive to energy deposition. Building bolometers containing $0\nu\beta\beta$ allows their application to its search, with the possibility to select different materials and, therefore, different candidate isotopes. The major running experiment exploiting this technique is CUORE (Cryogenic Undergorund Observatory for Rare Events), built with TeO_2 crystals to search for the $0\nu\beta\beta$ of ^{130}Te [55]. The energy resolution of such detectors is their main characteristics, and it is only limited by the thermal noise and by eventual imperfection of thermalizations. Since the average energy of a phonon is $\sim$ μeV, the average number of phonons created by a $\sim$MeV

[1] $E = k_b T = 8.16 \cdot 10^{-5}\mathrm{eVK}^{-1} \cdot 10$ mK $\sim \mu$eV

interaction is extremely large, allowing only small thermal fluctuation. Resolution of few keV at the MeV energy range are obtained, therefore the $2\nu\beta\beta$ has a negligible contribution to the background. This feature puts no limit on the $2\nu\beta\beta$ decay time of the chosen isotope, since its ingerence is always limited by the resolution. However, the response time of such detectors is extremely slow ($\sim$ 100 ms), thus making the pile-up extremely likely (see Sec.3.1.1) both in case of spurious background and fast $2\nu\beta\beta$ decays [20]. The limits to the application of such detectors to the search for $0\nu\beta\beta$ are the mass scalability, arising from the need of complex thermal machines to keep the extremely low temperatures needed for their operation, and the impossibility to tag background events. Regarding the former problem, the experience of CUORE recently showed that these detectors can be built with masses on the tonne scale, paving the way to the development of next generation calorimetric detectors [56]. For the latter, instead, on one side enormous efforts have been made to use clean materials, but still the limiting factor are the degraded α particles, which can be reduced but not completely eliminated [19]. Thus arises the need to develop new technologies to overcome such limitation. In particular, hybrid thermal-scintillation detectors are foreseen as the most suitable candidate to address such goal [20]. The main reason is that α and β particles present different scintillation signals, therefore allowing an efficient background tagging. Different projects are currently running and are foreseen, and will be discussed with more detail in the next sections and chapters.

3.3 Scintillation detectors as possible candidate for next generation $0\nu\beta\beta$ searches

In the current framework of $0\nu\beta\beta$ searches, the next generation experiments are directed towards the investigation of the inverted hierarchy of neutrino masses [20]. A sensitivity $> 10^{27}$ years is needed for such goal and the important characteristics for a candidate detector are (see Eq.(3.7)):

- minimization of the continuous background (i.e. lowering B factor), achievable by :
  - placing experiment underground, in order to reduce the cosmic ray contribution to experimental background;
  - building the detector with radiopure materials, in order to minimize the γ and β contribution to background
  - cleaning the surface of materials from radioactive contaminations, in order to reduce the degraded α particle contribution to background;
  - shielding of the detector active volume with lead and copper layers, in order to reduce the external and setup radioactivity;
  - developing particle identification techniques, in order to discriminate degraded α particle from electrons signals;
  - choosing a $0\nu\beta\beta$ candidate isotope with high $Q_{\beta\beta}$, in order to reduce β and γ events from the ROI and enhance the $0\nu\beta\beta/2\nu\beta\beta$ ratio;
- observation of large isotope mass (i.e. increasing M factor), achievable by:
  - choosing a $0\nu\beta\beta$ candidate isotope with high natural isotopic abundance (high η);
  - choosing a detector technology that allows easy mass scalability, that is to say possibility to have high masses without huge technological issues;
- achieve good energy resolution (i.e. decreasing Δ factor), to reduce the $2\nu\beta\beta$ background in the ROI (see Eq.(3.12));
- long time of observation (i.e. increasing T_{mis} factor) achievable by choosing stable detectors with low maintenance issues.

The Source=Detector experiment have proven successfully in trying to address some of these issues, but no technology exist able to simultaneously guarantee the fulfilling of all requirements.
In the search for performing approaches, the scintillation-based devices have proven to be effective in addressing some of these issues.

3.3.1 The scintillator characteristics

Scintillation detectors are composed by two main elements: the particle absorber, which is also a light emitter, and the photon detector. The basic working principle of these instruments is the existence of radiative de-excitation channels for electrons. Such feature allows the electrons brought by ionizing radiation to higher energy states to release the excess energy with the emission of optical photons [57]. The number of emitted photons (N_{Ph}) is directly proportional to the deposited energy (E_{Dep}), by the means of the *Light Yield* (LY) of the materials, defined as the average number of photons emitted by a certain energy deposition:

$$N_{\mathrm{Ph}} = \mathrm{LY} \cdot E_{\mathrm{Dep}} \tag{3.14}$$

The photon emission is not istantaneous, and it is ruled by at least one de-excitation time, characteristic of the chosen material. Such emission time has a strong dependency on the ionization which produces the light emission, in particular by discriminating short-range ionization by long-range ionization. Such difference allows to distinguish between α particles, characterized by short-range heavy ionization, and electrons, characterized by wider ionization volumes. As a matter of fact, the time analysis of scintillation signals can provide efficient particle identification techniques. This characteristics makes these detectors suitable for low background searches [58].
In addition, it is possible to produce large arrays of identically-performing scintillation detectors, thus making it possible to build large detector masses with modular approach [58]. This stratagem, exploited by different detectors such as HPGe-based observatories or bolometric experiments, has already been demonstrated as a feasible pathway towards tonne-scale detectors, further favoring this kind of detectors.
The LY is a peculiar characteristic of the given scintillator, and is affected by the different properties of the chosen material. Since the photon emission is a constant average process, it is ruled by Poisson statistics. As a consequence, N_{Ph} fluctuates around its mean value, with a variance identical to it. If $N_{\mathrm{Ph}} \gtrsim 10$, a reasonable approximation for E_{Dep} ~MeV, the distribution tends to a gaussian, with standard deviation $\sigma_{\mathrm{Ph}} = \sqrt{N_{\mathrm{Ph}}}$. The relative uncertainty on N_{Ph} is therefore given by $R = 1/\sqrt{N_{\mathrm{Ph}}}$. Such relation is valid at the photons generation, and is worsened by the global photon detection efficiency α_{Ph}, defined as the probability with which an emitted photon is collected by the sensor. As a consequence, on average, only $N_{\mathrm{Ph}}^{\mathrm{Meas}}$ photons are detected:

$$N_{\mathrm{Ph}}^{\mathrm{Meas}} = \mathrm{LY} \cdot E_{\mathrm{Dep}} \cdot \alpha_{\mathrm{Ph}} \tag{3.15}$$

resulting in the fact that the final FWHM resolution will be at least equal to

$$R_{\mathrm{Ph}}^{\mathrm{Meas}} = \frac{2.355}{\sqrt{\mathrm{LY} \cdot E_{\mathrm{Dep}} \cdot \alpha_{\mathrm{Ph}}}} \tag{3.16}$$

The factor α_{Ph} is therefore a crucial quantity to be taken into account, since it gives an ultimate limit to the attainable detector resolution. Such factor can be expressed as the product of the probability that a photons actually reaches the sensor and the sensor detection efficiency. This value vary from detectors to detectors, but usually their product is around 30%-50%. As a consequence, the actual attainable energy resolution is usually not as performing as the LY would allow to predict. Such resolution is furthermore worsened by the noise introduced in the readout of the signal and by eventual non-idealities in photon production or by self-absorption of scintillation photons by the material. Such limit has strong implication for the application of scintillators to $0\nu\beta\beta$ searches, demanding a strategy to be addressed efficiently.
Two approaches will be analyzed in the next sections: the hybridization of such detectors and the improvement of standard scintillators.

3.3.2 Multiple readout detectors

The choice of a an experimental technique based on a single information carrier is always limited by its unfavorable characteristics. Simultaneous combination of multiple carrier readout has been shown as an effective way to overcome some limitations, for example in TPCs [46]. Such multi-messenger approach can be the key to define a new detection strategy for $0\nu\beta\beta$ searches, capable of addressing different important features. Among the techniques described previously, the bolometric detectors have been shown as the most versatile in terms of possible isotopes investigation at $\sim$ ton scale masses. Moreover, the performing energy resolution makes negligible the $2\nu\beta\beta$ contribution to background, almost for all the investigable isotopes. Unfortunately, only the energy is detected, therefore no background identification can be performed, intrinsically limiting the sensitivity. On the other hand, scintillation-based detectors shown impressive background identification capabilities, since different particles have different scintillation mechanisms, but the statistical fluctuation of collected photons although limits their achievable energy resolution.
The combination of these two techniques, resulting in scintillating bolometric detectors, was proposed in 1989 for solar neutrino experiments [59]. The first application $0\nu\beta\beta$ searches with α background suppression were performed with crystal facing standard light detectors, such as photodiodes [60], and where limited by the technical difficulties in using standard LDs at non-standard cryogenic temperatures. The tables turned with the proposal of using bolometers as custom low-temperature photon detectors [61], leading to new possibilities [62]. The main advantages of using bolometric LDs is that they are sensitive to a wide band of photon wavelenght, compared to standard detectors, and are characterized by an high quantum efficiency. On the other hand, they cannot be applied in single photon counting and are characterized by slower response time with respect to standard photodetectors (ms versus ns or even less). Different studies have been performed exploring the possibilities of this technique [63, 64, 65], proving the background rejection capabilities and the possibility to investigate different isotopes. Such success paved the way for the construction and running of pilot experiments based in this technique, capable of putting limits on the half-life of different $0\nu\beta\beta$ isotopes [66, 67].
Alongside the demonstration that such technique has the needed performances, the astonishing technical results obtained by CUORE showed that it is possible to run a tonne scale bolometric experiment, overcoming the mass-scalability limitation related to the use of a diluition refrigerator. Such results paved the way to the definition of next generation projects based on this technique, such as CUPID (Cuore Upgrade with Particle Identification) [68, 69]. The main goal of this project is the design and operation of a tonne-scale detector dedicated to the investigation of the IH region of neutrino masses [20]. Current R&D projects are foreseen for the development of this idea [70], based on the excellent results provided by the CUPID-0 demonstrator [66]. A more detailed insight on this technique, with the obtained physics results, will be given in chapter 4.

3.3.3 Innovative scintillation detectors

As mentioned above, the scintillation-based detectors are suitable candidates for the search of $0\nu\beta\beta$, but are limited by the achievable energy resolution. Such limit arise from the low light detection efficiency, giving a dominant statistical contribution to the energy resolution. Such limit can be overcome defining new design for performing scintillation detectors.
Such development is centered on the improvement in resolution, and has the target of FWHM $\leq 0.02 \cdot Q_{\beta\beta}$, to ensure at least a limited effect ($\leq$10%) of $2\nu\beta\beta$ on the background. The chosen design is the Source=Detector, therefore suitable scintillators containing $0\nu\beta\beta$ isotopes have to be chosen for this application. In such context, suitable stands for highest possible LY and fast scintillation time. With such characteristics, the detector would not be limited by the crystal properties, allowing major improvements based on readout system upgrades.
Such improvements will be related to the increase in LY, optimization of photon extraction and optimization of readout chain.

For the increase in LY the operation at cryogenic temperatures is helpful. When the vibrational modes of a scintillating material are deactivated, in fact, the vibrational non-radiative de-excitation is damped. As a consequence, the LY increases [71]. On photon extraction, different wrapping strategies can be implemented, surrounding the crystal with materials capable of re-direct the outgoing scintillation photons toward the photodetector. Lastly, the choice of an efficient photon detector is the most important aspect to be considered, since at this first measurement stage the actual level of the collection efficiency is determined. As a consequence detectors with high quantum efficiency have to be preferred, in order to obtain better performances [58]. Also consideration of gain fluctuations, non uniform efficiency and readout noise have to be considered, since all these aspects take part in spoiling the resolution. The FLARES (Flexible Light Apparatus for Rare Events Search) project, tried to follow this concept. It proposed the development of a detector based on the use of Silicon Drift Detectors (SDD) to read the light emitted by large scintillation crystals, cooled at 120K. SDDs are characterized by low noise and high quantum efficiency, while the scintillators containing $0\nu\beta\beta$ candidates can be enhanced in their performances by the low temperatures.
Considering a completely different approach, the resolution problem can be addressed by selecting more performing scintillating materials. In this framework, the scintillating nanocrystals play an important role. These new generation of compounds, in fact, is characterized by extremely high light emission, and they can be designed to work at a certain wavelength, thus making the optimization of their readout chain easier. In addition, they are characterized by extremely fast scintillation times, given their simple band structure. Such features provide the perfect scintillator, but have to be carefully exploited to produced a scintillator for ionizing radiation detectors. The accumulation of great masses of nanocrystals is, in fact, problematic, since the self-absorption limits the light output. In addition, such compounds are produced as powders, needing a matrix to be arranged in more useful structures. Such difficulties prevented their application to the scintillation-based detection of radiation. In this framework, the ESQUIRE (Experiment with Scintillating QUantum dots for Ionizing Radiation Events) project proposes a possible pathway to the development of new scintillation detectors, aimed to a final application to the search of $0\nu\beta\beta$. Such final goal is feasible since many scintillating nanocrystals can be built with candidate isotopes to the $0\nu\beta\beta$, such as Cd, Se or Te. As a consequence, once optimized as standard scintillators, they can be easily used in such searches.
These strategies, quickly outlined here, will be discussed with more detail in Chapter 5, with an outline of the obtained results and future perspective.

Chapter 4

The results of CUPID-0 experiment

CUPID-0 is an experiment based on the technique of scintillating bolometers, running to put a new limit on the $0\nu\beta\beta$ half-life of ^{82}Se. This experiment is running 26 ZnSe crystals, simultaneously operated as bolometers and scintillators, interleaved with Ge bolometric light detector.
The combination of heat and light readout allows to distinguish α interactions from β/γ ones, eliminating an important contribution to the background in the search for $0\nu\beta\beta$ decay. In addition, the possibility to exploit two different information increases the detector capabilities, especially in the comprehension of background sources. CUPID-0 is therefore candidate to explore not only the $0\nu\beta\beta$, but also the $2\nu\beta\beta$ and its possible deformation due to Physics beyond the Standard Model. In spite the fact that CUPID-0 is a small detector, designed to be an R&D toward next generation experiments, its performances allowed different physics investigation. This small prototype hence showed that, with the correct technique, also small exposure can provide interesting results.
In this chapter, the structure of CUPID-0 will be presented (section 4.1), and the analysis methods used to extract physics information will be discussed (section 4.2 and 4.3). The results obtained in the search for $0\nu\beta\beta$ will then be described (section 4.4), as well as the reconstruction of the measured background spectrum (section 4.5). The obtained background model will then be used to put a limit on the Lorentz symmetry violation in neutrino sector (section 4.6), proving the extended capabilities of CUPID-0 design. Lastly, an overview of the obtained results and a brief overview of their significance for future experiments will be given (section 4.7).

4.1 The CUPID-0 detector

CUPID-0 detector is the first array of enriched scintillating bolometers for the investigation of $\beta\beta$ decay in ^{82}Se [72]. It is composed of 26 scintillating bolometers of ZnSe, 24 enriched at 95% in ^{82}Se and 2 naturals (i.a.(^{82}Se) = 8.82%). These crystals act as absorbers and are kept at $\sim$ 10 mK with an Oxford 1000 ^{3}He/^{4}He dilution refrigerator, installed in the hall A of Gran Sasso National Laboratory (Italy). The detector is built repeating single modules, composed by a ZnSe crystal and a high purity Germanium wafers, operated as bolometric light detector (LD). These modules are arranged in 5 columns, as shown in Fig.4.1, thermalized through a mechanical copper structure and PTFE supports. The sequence of modules result in each ZnSe to be surrounded by two LDs: one above (Top) and one below (Bottom). In between the colums, four contain 5 modules and one 6. This division has been performed to have same weight ($\sim$2 kg) and height ($\sim$30 cm) in the different columns. The total detector is referred to as a single tower, composed by the different columns. The total number of ^{82}Se nuclei under observation is $4.1 \cdot 10^{25}$, comprehending both natural and enriched crystals. The temperature signals in both the ZnSe and the LDs are collected with a Ge Neutron Transmutation Doped (NTD) thermistor [73], directly glued to the detector. On both ZnSe and LD a Si Joule heater is glued, to allow the injection of a known temperature increase, useful to monitor and correct the detector thermal response over time.

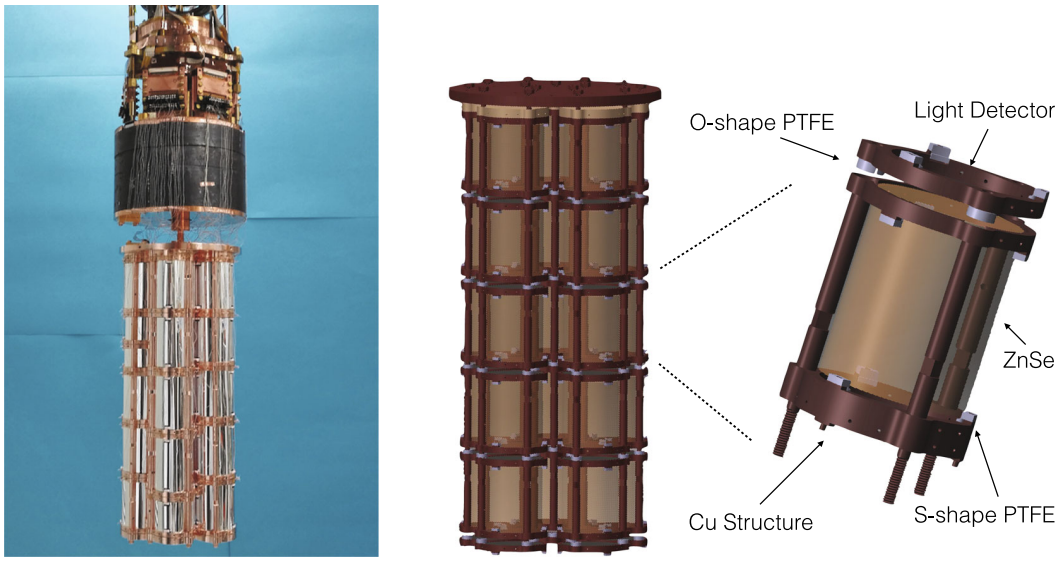

Figure 4.1: Picure (left) and rendering (right) of CUPID-0 detector, with a detail on the single module. The pictures are taken from [72].

ZnSe crystals were grown from selected Se powders, characterized with dedicated measurements [74]. The crystal growth process, described in [75], was followed by a cleaning an lapping procedure carried out in the Darkside clean room at the Gran Sasso National Laboratory. This facility has an efficient Radon-abatment system, ensuring ^{222}Rn concentration $\leq$ 20 mBq/m^3 [76]. The contamination of crystals where therefore limited, especially in their superficial (and most dangerous) component.
The LDs where built from 170 μm thick high purity germanium wafers, with focus on two characteristics: the noise level and signal amplitude. Such features have capital importance in ensuring efficient particle discrimination. The former is enhanced trough optimization of the detector operation parameters [77]. The latter, instead, is enhanced by collecting more photons. On one side it was enhanced wrapping each ZnSe crystal with a Vikuity^{TM} reflective foil and, on the other, by the application of an anti-reflective SiO_2 coating (ARC) on the LD. Such layer performs a refractive index matching between vacuum ($n = 1$) and Germanium ($n \sim 2.4$), and is optimized in thickness to match the maximum in ZnSe emission spectrum, $\lambda \sim 645$ nm. The ARC effect is a 35% increase in light collection, contributing to the increase of the measured light amplitude [72]. Only one LD side has the ARC, therefore only the Top LD for each ZnSe has the increased light collection efficiency.
The NTD sensors have been produced irradiating germanium wafers with neutrons, using a nuclear reactor [72]. The target doping level is $\sim 10^{16}$atoms/cm^3, at which the resistence of the sensor (R^{NTD}) at cryogenic temperatures is given by

$$R^{\mathrm{NTD}} = R_0^{\mathrm{NTD}} e^{\sqrt{(T_0/T)}} \tag{4.1}$$

where T_0 depends on the NTD doping level and R_0^{NTD} on the doping level and on the sensor geometry. These sensors increase their resistivity as the temperature lowers. Such correspondence is exploited to correct the fluctuation of the thermal capacitance, acting as a gain, due to changes in temperature (see Sec.3.2.2).
To build the tower holder ultra-pure NOSV copper was used, to limit the radioactive contaminations close to the detector core. In addition, a detailed cleaning procedure was performed to remove the superficial layer, thus reducing dangerous surface contaminations.
The whole tower is hosted in the same cryogenic infrastructure of Cuoricino [78] and CUORE-0 [79]. The device is an Oxford TL1000 dilution refrigerator with a copper He dewar. The ^{3}He/^{4}He dilution unit has a cooling power at 100 mK of about 1 mW, ensuring the possibility to install in the

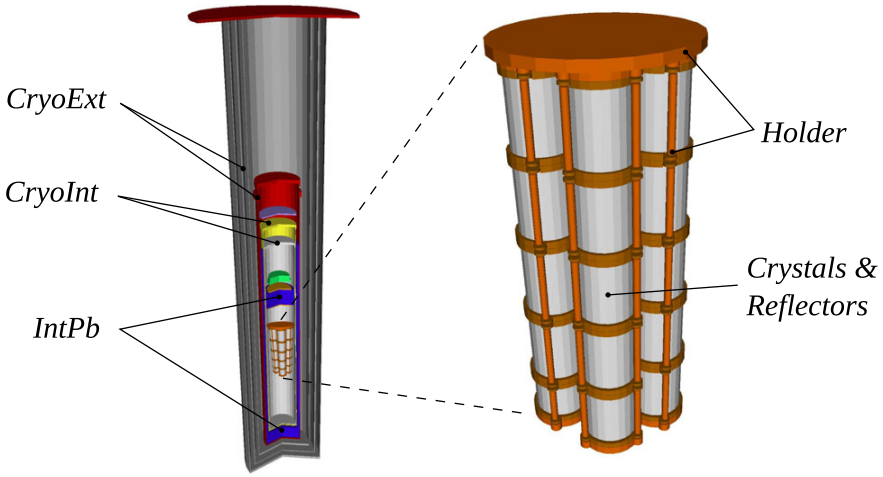

Figure 4.2: Schematical representation of CUPID-0 cryostat, used in the GEANT-4 based simulations of the detector. This drawing does not include the external lead and neutron shields. The figure is taken from [39].

system a large number of read-out channels. The installation of the LDs required an improvement of the anti-vibrational damping system [80], because these detectors are more sensitive than standard crystals and therefore more vulnerable to vibrations. The structure of the cryostat can be briefly summarized with a radial division in concentric sections. In the outer layer, the system has borated poliethylene neutron shield and a modern lead shield, to stop radiation coming from the outside. Inside this first section, the external cryostat parts (CryoExt) are found: the main bath, the outer vacuum chamber (OVC), the super-insulation and the inner vacuum chamber (IVC). This section is separated from the detector core by a layer of roman lead shield (IntPb), characterized by low content in ^{210}Pb. This material is chosen to limit the bremmstralhung emission from β rays, characteristics of standard lead shieldings [81]. Inside IntPb, the remaining shield of the cryostat (CryoInt) are located: the 600 mK stage and the 50 mK stage, built with ultra-pure copper. At the center of this shield succession, the CUPID-0 tower is hang to the diluition unit with a cold finger. The schematic representation of these section is reported in figure 4.2. Such division will be used from now on to identify the section of the cryostat, especially when specifying the location of the background sources of the experiment (see Sec.4.5).
The readout of the sensor is performed similarly to CUORE [82]. The voltage at the extremes of each NTD is read with a JFET-based low-noise preamplifier and passes trough a programmable Bessel filter, wich removes the high-frequency components noise components and acts as an anti-aliasing filter. The resulting voltage signals, labelled with a channel number unique to each detector, are digitized by a commercial 18-bit resolution analog to digital converter (ADC) with programmable sampling frequency up to 500 kSamples/s. The whole acquisition system is programmable, and is managed with a dedicated software, called APOLLO, described in detail in [83]. This system is designed to acquire continuously the different detector voltages, applying a derivative trigger to mark the position of a candidate particle signal. The software is designed to allow the selection of each channel acquisition parameters. ZnSe and LD differ in the sampling frequency used, that is 1 kHz and 2 kHz respectively. Such difference is due to the different speed of the two detectors, ruled by their thermal capacitance. The ZnSe signal are characterized by a rise-time[1] of 10 ms and a decay-time[2] of 40 ms. On the other hand, LD signals are faster because of their smaller dimensions and have a rise-time of a few ms and decay-time of about 8 ms. The usual trigger rates are $\sim$2 mHz for background measurements (i.e. withouth external sources) and few Hz during calibrations.
The performances of the detectors are benchmarked with a dedicated calibration, performed with

[1]Time in which the pulse grows from 10% to 90% of its maximum.
[2]Time in which the pulse falls from 90% to 30% of its maximum.

a ^{232}Th source. The results show an average FWHM energy resolution of ∼20 keV for the ZnSe detectors, and a global signal-to-noise ratio of ∼ 140 for the LDs. Given the LD low mass, it is impossible to perform a direct calibration of these detectors, therefore no direct measurement of their energy resolution is available. The obtained performances are good, and in the next section will be further discussed in terms of the attainable physics performances.
The data acquisition is divided in DataSets (DS), composed by different runs and usually spanning a period of one-two months. Each run lasts approximately two days, being stopped each time the cryostat needs liquid He refill. Each DS begins end ends with a dedicated ^{232}Th calibration, used to monitor the detector performances and to calibrate the detector response. The runs where no source is present inside the crystal are referred to as physics runs, and are the time periods used for the investigation of $0\nu\beta\beta$ and other rare events.

4.2 Data analysis procedure

The data analysis procedure is focused on extracting the needed physics information from the acquired pulses. The pulse amplitude of heat signals has to be evaluated efficiently, to exploit the high energy resolution of the detector. The shape of light signal, moreover, has to be evaluated to guarantee the needed particle discrimination capabilities [84]. The analysis is carried out within a custom framework, called DIANA, originally developed for CUORE and transferred, with needed modifications, to CUPID-0. The main issue to be addressed is how to handle the scintillation signals, whose trigger needs to be synchronized to the heat signal one. The synchronization is managed trough an off-line trigger, forcing the identification of a LD pulse after each triggered ZnSe pulse. Since only ∼1% of the energy deposited in ZnSe undergoes radiative de-excitation, in fact, the standard derivative trigger would miss all the small (or noisy) LD signals.
Each detected trigger identifies a time window where the signal is located. For ZnSe pulses, the window is 5 s long: 1 s before the trigger and 4 s after. Since the LD have much smaller response time with respect to the ZnSe, the window is 1 s: 0.2 s before the trigger and 0.8 s after. The pre-trigger samples are used to calculate the baseline value, proportional to temperature. An example of CUPID-0 pulses is shown in Fig.4.3, where the difference between Top and Bottom light amplitude, due to the Top-only ARC, can be appreciated.

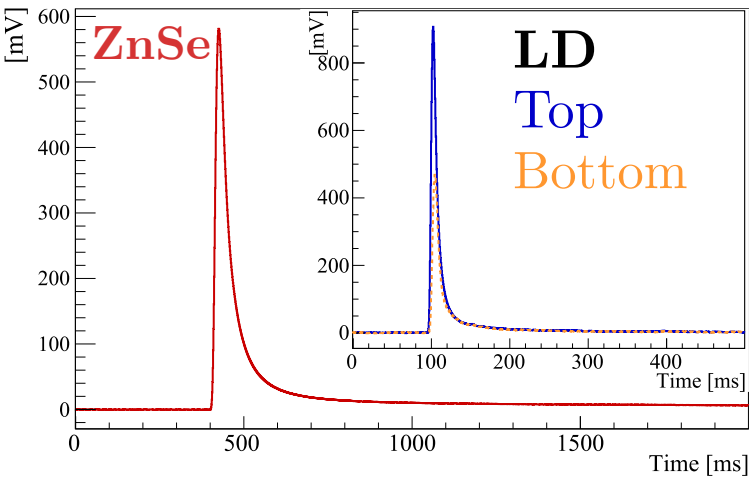

Figure 4.3: Example of ZnSe and LD pulses from CUPID-0. The difference in amplitude between Top and Bottom LD, due to the anti-reflective coating of Top LD, is evident.

The analysis steps immediately following the trigger are equal for ZnSe and LD, and are designed to extract the needed information from the pulses.
The first step is the evaluation of basic pulse parameters, such as the baseline average value and the baseline standard deviation (BLRMS). The baseline average is proportional to the temperature.

As a consequence, it can be used to correct thermal fluctuations, resulting in thermal capacitance variation and therefore gain fluctuations (see Sec.3.2.2). For this purpose the Si joule heater signal (Pulser) is used as a reference, enabling the derivation and subsequent correction of each detector gain fluctuation.
Following the stabilization, the matched filter algorithm is used to extract the amplitude while reducing the noise [85, 86]. This digital filtering technique requires two ingredients for each channel: the template of the response to a particle-like event (S) and the average noise power spectrum (N), evaluated without the inclusion of signal components. With these ingredients the transfer function of the filter H is defined, in Laplace space, as:

$$H(\omega) = \frac{S(\omega)}{N(\omega)} e^{i\omega t} \tag{4.2}$$

The application of this filter allows the rejection of noise-dominated frequencies and the contextual emphasis on signal-dominated ones. Such procedure is usually referred to as *optimum filtering* (OF), since it can be demonstrated to be the filter with maximal signal-to-noise ratio (SNR). Since the noise is deconvolved from the filtered pulse, major information about the signal shape are accessed. As a consequence a more sensitive characterization of pulse shape can be obtained. To exploit such feature, the Test Value Left (TVL) and Test Value Right (TVR) are calculated. These variables correspond to the χ^2 between the generic filtered pulse and the template, both before and after the pulse maximum. They are evaluated with:

$$\mathrm{TVL} = \frac{1}{\delta_{\mathrm{L}}} \sqrt{\sum_{i=i_M-\delta \mathrm{L}}^{i_M} (y_i - A s_i)^2} \tag{4.3}$$

$$\mathrm{TVL} = \frac{1}{\delta_{\mathrm{R}}} \sqrt{\sum_{i=i_M}^{i_M+\delta \mathrm{R}} (y_i - A s_i)^2} \tag{4.4}$$

where y_i is the filtered pulse, A and i_M are its maximum amplitude and position, s_i is the template pulse scaled to unitary amplitude and aligned to y_i and δ_L (δ_R) is the left (right) width at half maximum of s_i.
The OF is based on the assumptions that S and N are the true signal and noise templates, and maximizes the SNR ratio with respect to them. As a consequence, particular care has to be taken in S and N definition, to ensure a complete signal identification. For both ZnSe and LDs, N is constructed by averaging the power spectra of different ($\sim$100) acquisition window marked with a random trigger and selected to discard windows with signal-like features. S, instead, is calculated differently for ZnSe and LD. First, S is calculated for ZnSe, averaging $\sim$100 high amplitude events collected during calibration. After this first processing, the ZnSe are calibrated with the γ lines produced by ^{232}Th: 511 keV (pair production), 583 keV (^{208}Tl), 911 keV (^{228}Ac), 968 keV (^{228}Ac) and 2615 keV (^{208}Tl). After this first calibration, another S is evaluated, using the events with energy$\geq$ 1800 keV. With this new selection a more specific ensemble of events is used, improving the knowledge level on the template pulse of ZnSe. In figure 4.4 an example of ZnSe templates for pulse and noise are reported. It is important to notice, in the signal template, the fact that the baseline is not recovered after the pulse decay time. This is due to the fact that ZnSe is a peculiar crystal, characterized by anomalously long de-excitation times due to trap-like behaviour in the lattice. Such feature is small in amplitude, but as a non negligible area. This miss-integration causes loss of information, resulting in non ideal behavior of CUPID-0 detector.
For LDs, instead, the selection has to be performed with higher accuracy, because the scintillation signal from different particles has different time evolution. The selection of an almost pure β template is therefore necessary to ensure the possibility to distinguish this class from α-induced events. This selection is performed after the energy calibration of ZnSe crystals. It comprehends LD pulses corresponding to ZnSe events with 1800 keV<Energy<2645 keV. Moreover, the emitted light

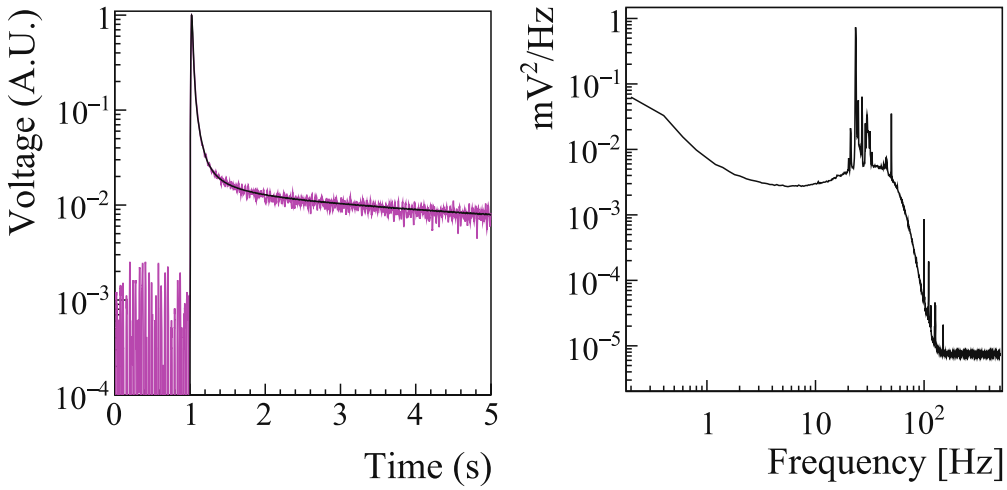

Figure 4.4: In the left panel are reported a typical template of a ZnSe response (black line) overlapped to a single pulse acquired by the same detector (magenta line). The lack of baseline restoration can be clearly seen. In the right panel the typical average noise power spectrum of a ZnSe detector is reported. The microphonic noise peaks and the roll-off due to the anti-aliasing active Bessel filter are clearly visible. The picture is taken from [84].

is requested compatible with the one produced by scintillation of electrons, thus discarding events produced by scintillation of α particles, or events with no associated light emission (electronics noise, interactions in the NTD Ge sensor). Finally, spurious events are rejected, such as pile-ups or those in which a second pulse was detected in the same acquisition window. Such selection ensures good statistic, while keeping only β-induced signals. In figure 4.5 an example of LD templates for pulse and noise are reported.

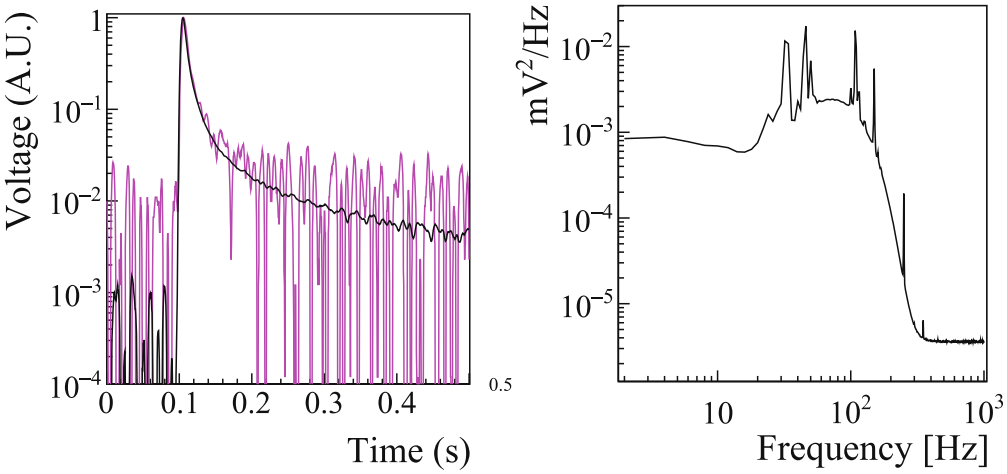

Figure 4.5: In the left panel are reported a typical template of a LD response (black line) overlapped to a single pulse acquired by the same detector (magenta line). The lack of baseline restoration can be clearly seen. In the right panel the typical average noise power spectrum of a LD is reported. The microphonic noise peaks and the roll-off due to the anti-aliasing active Bessel filter are clearly visible. The picture is taken from [84].

After the average definition, OF is applied to the LD, and the signal amplitude and shape parameters are calculated. Among the possible shape parameters, the one providing best particle identification is the TVR, SP from now on [84]. In figure 4.6 the α/β distinction in CUPID-0 is shown. The boundary is chosen to select the alpha distribution up to 3σ. Such selection is possible only above 2 MeV, because for lower energies the noise meddling in the LDs prevent an effective discrimination. Such threshold is not a problem for $0\nu\beta\beta$, having a $Q_{\beta\beta} = 2997.9 \pm 0.3$ keV [87].

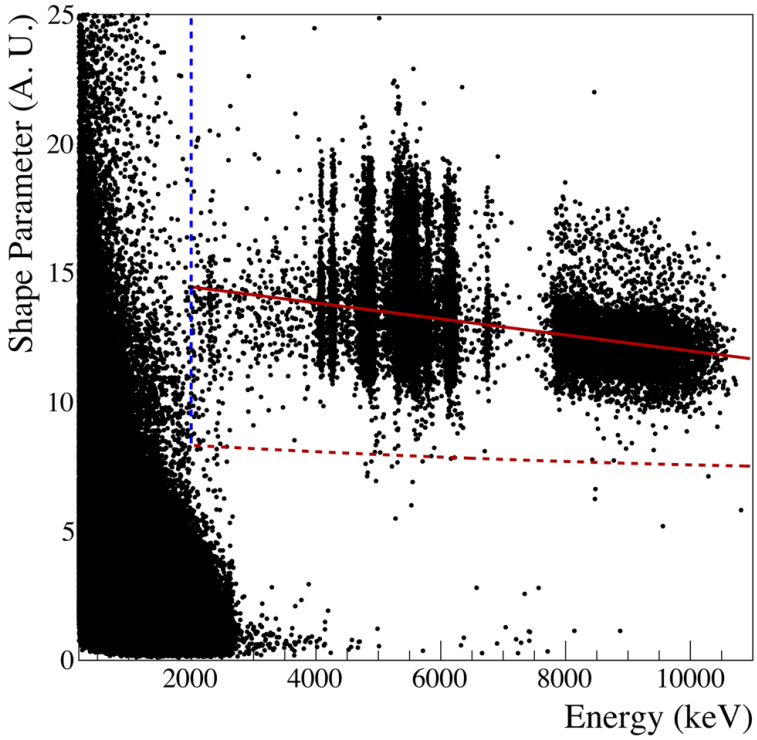

Figure 4.6: Shape parameter (SP) of light pulses as a function of particle energy. The red solid line is the mean value of α particles SP ($\mu_\alpha(E)$), while the red dashed line is $\mu_\alpha(E) - 3\sigma_\alpha(E)$. This is the chosen boundary to separate the two classes. The blue dashed line at 2 MeV shows the energy below which the particle identification is not applied. The picture is taken from [39].

Having defined the templates, ^{232}Th calibration is used to evaluate the ZnSe performances in terms of energy resolution. In figure 4.7 the calibration spectrum is shown, with the full calibration statistics collected. From the observation of the line shape in the calibration spectrum, a function modelling the response of the detector to monocromatic energy depositions is deduced. To take into account the peak asymmetry, a sum of two Gaussians is used. Deviation from single Gaussian response function have already been reported in other bolometric experiments [88], and are usually addressed to lattice imperfections or thermal coupling defects. In figure 4.7, the fit of the 2615 keV line with the response function is reported. From this function, the resolution is evaluated as the FWHM of the peak. The FWHM as a function of the energy for the ^{232}Th main γ lines is modelled with a first order polynomial, and the expected resolution at the $Q_{\beta\beta}$ of ^{82}Se is extracted: FWHM=(23.0 ± 0.6) keV. Since this value is necessary to control the sensitivity of the experiment, a second calibration has been performed to cross-validate the results. A ^{56}Co source has been chosen, emitting γ at consistent branching ratio up to ~3500 keV. In figure 4.8 the measured ^{56}Co spectrum is reported. With this additional measurement, the updated prediction for resolution at $Q_{\beta\beta}$ is FWHM=(23.5 ± 1.2) keV, fully consistent with the previous value. The FWHM as a function of the energy is reported in figure 4.8. The ^{56}Co calibration allows to extract the detector parameters both below and above the $Q_{\beta\beta}$, increasing the precision of extrapolated values. The time needed to collect sufficient peaks near $Q_{\beta\beta}$ is of the order of three weeks, compared to the 1 week necessary for ^{232}Th calibration. As a consequence, this source cannot be used for the routine calibration, since it would spoil the live-time of our detector.
The obtained value for FWHM is enough to ensure a rejection of $2\nu\beta\beta$ background of more than $1/10^4$ (see Fig.3.4 on page 27), making this contribution negligible. If compared to the resolution of other bolometric experiments, although, it appears poor. For example, CUORE has FWHM=(7.7 ± 0.5) keV at 2582 keV [55]. As a matter of fact, ZnSe are difficult to grow and CUPID-0 crystals demanded the development of a new dedicated procedure [75]. The obtained

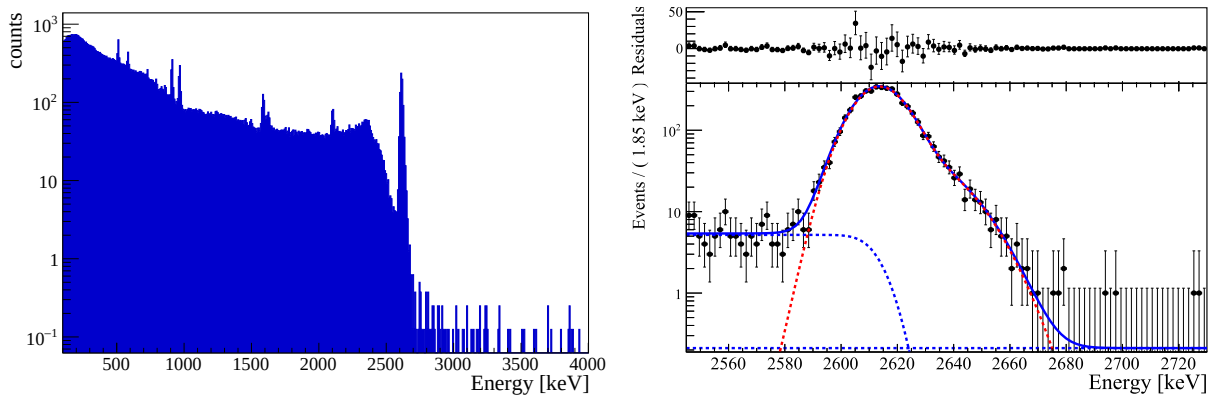

Figure 4.7: Left: ^{232}Th calibration spectrum. The main peaks are: 511 keV (pair production), 583 keV (^{208}Tl), 911 keV (^{228}Ac), 968 keV (^{228}Ac) and 2615 keV (^{208}Tl). Right: response function of CUPID-0 (blue continuous line), evaluated on the 2615 keV peak of ^{232}Th calibration. The double Gaussian (red continuous line) is used to address the bump on the right side of the peak. Two shapes where used to address the background in the fit procedure (blue dashed line): a error function to model the multi-Compton events and a constant function to model the remaining background events.

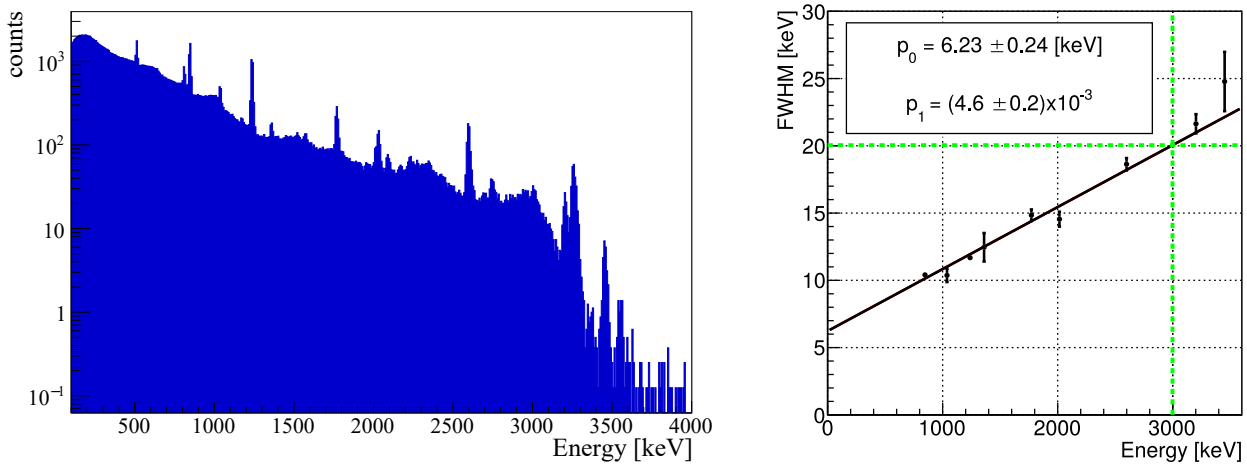

Figure 4.8: Left: ^{56}Co calibration spectrum. Right: FWHM resolution as a function of the energy. Data are fitted with a linear function FWHM = $p_0 + p_1 E$. The prediction for resolution at $Q_{\beta\beta}$ is FWHM=(20.05 ± 0.34) keV, marked from the green dashed lines.

crystals showed different imperfections and a general lack of homogeneity, which spoil the attainable energy resolution.
Alongside the imperfection of crystals, the presence of scintillation emission also takes part in the resolution worsening. The total energy deposited in ZnSe, in fact, is split into light emission and heat increase, with different ratio in each energy deposition. As a matter of fact, the average energy available to create phonons changes on an event-base and consequently the resolution is worsened. In the next section, a method to decorrelate the two emission is presented, showing the attainable energy resolution gain.

4.3 Light-Heat decorrelation

In figure 4.9, the light/heat scatter plot for a ZnSe and its corresponding Top LD is reported. The events belonging to the 2615 keV γ line show the correlation between the two variables. This correlation is expected in standard scintillating crystals, due to the conservation of the energy [89]. The energy emitted as heat and as light, in fact, should always add up to the total energy deposited in the crystal. As a consequence, the more light is emitted, the less phonons are created,

resulting in an anti-correlation. The correction of this feature basically leads to the definition of a corrected amplitude, simultaneously considering both light and heat emission, and therefore reducing the attainable resolution. ZnSe crystals are characterized by a correlation between light and heat, although characterized by opposite behaviour with respect to standard scintillators. For β/γ depositions in ZnSe, in fact, a positive correlation is observed: more measured light corresponds to more measured heat. This feature currently has no exhaustive explanation, but it may be addressed to the non-ideal characteristics of ZnSe crystals. As shown in figure 4.4, the measured heat signals are characterized by a long tail, corresponding to a considerable miss-integrated signal. As a direct consequence, the amplitude calculated with OF does not take into account all the heat generated in the crystal, probably resulting in the non-ideal positive light/heat correlation. In spite the lack of a complete explanation, this correlation can still be exploited to enhance the attainable energy resolution of the detector.

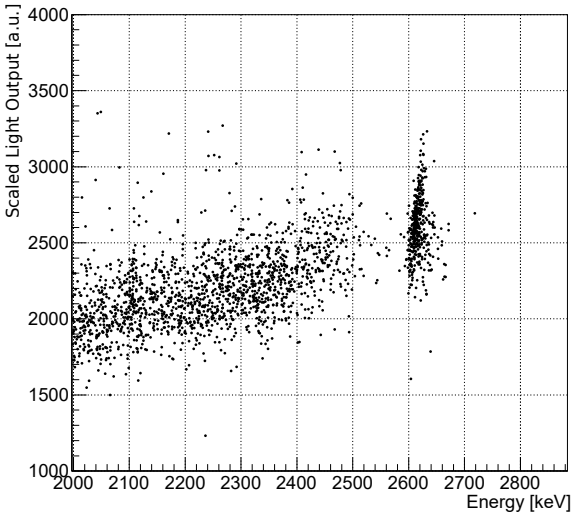

Figure 4.9: Light/Heat scatter plot. The 2615 keV line clearly shows the correlation between the two variables. The resolution difference between heat and light channel can be appreciated. The heat axis was calibrated using the most prominent gamma peaks of a ^{232}Th source (including the 2615 keV line shown in the plot). The light axis was re-scaled by assigning the nominal energy of the 2615 keV line to the corresponding scintillation peak.

The correlation between two variables can be corrected both by calculating a new variable combining light and heat information [90] or by finding a geometrical transformation minimizing the resolution. Given the geometrical aspect of the correlation, the optimal transformation to be applied is a counterclockwise rotation of the light/heat scatter plot. In the former method the corrected variable is calculated using standard deviation and correlation of the light/heat distribution, evaluated analytically [91]. In the latter method the optimal rotation angle is chosen trying different possible values with an iterative algorithm.
The two methods are mathematically equivalent. With the proper transformations, in fact, a rotation in the light/heat plane can be expressed as a weighted sum of heat and light variables. As a consequence, the minimization can be performed choosing the optimal weight analytically or the optimal angle numerically. Nevertheless, the practical application of these two strategies has different constraints, due to their different hypothesis. The analytical method is less computationally expensive than the second one, since it finds a complete expression for the weighting factor minimizing the resolution. This expression, reported in [91], depends on the standard deviations of heat and light distribution, as well as on the correlation factor between these two variables. It has to be pointed out that this derivation minimizes the *variance*. This quantity is proportional to the FWHM resolution when the involved variables have a Gaussian distribution. When this assumption is violated, the analytical evaluation of the best weight is not guaranteed to minimize the FWHM. This is our case, since the heat variable is not distributed as a Gaussian. In addition, all the parameters of the optimal weight have to be calculated numerically from the heat/light distributions, like the one in figure 4.9. Such evaluations are spoiled by the presence of non-flat background, which cannot be completely excluded in a simple way. Moreover, the quantities to be

decorrelated, heat and light, are characterized by the presence of uncorrelated noise due to various sources (electronics, thermal noise, ...). The evaluation of variance and covariance of the two variables cannot distinguish between signal-related spreading and noise-related spreading. Therefore, the variance calculated numerically includes also the latter contribution, totally uncorrelated to the signal behavior. When the noise-related variance is smaller than the signal-related one, it does not affect the variance calculation. On the contrary, the presence of a dominant noise component leads to an uncorrected evaluation of the variance. Our light signal belongs to the latter case (see Fig.4.5), therefore the effect of the signal-related variance is hidden by the instrumental noise, negatively affecting the analytical decorrelation.
On the other hand, finding the optimal rotation which minimizes the heat resolution is based on the observation of changes in the heat channel FWHM resolution only. As a consequence, the poor signal-to-noise ratio (SNR) of the light channel does not affect heavily its performances. Moreover, the evaluation of the FWHM can be performed taking into account the background with a properly defined fit procedure. This characteristic avoid the bias due to the inclusion of unmodelled structures. In addition, no assumption is made on the shape of the distributions used in this transformation, except for the existence of a correlation. The numerical method is also flexible, since different algorithms for angle selection can be tested, choosing the one with the best performances. Given these a priori information, the numerical method has been chosen with respect to the analytical one to perform the decorrelation.
To find the rotation angle minimizing the resolution (θ_{MIN}), different angles (θ) are varied following an adequate minimization algorithm. For each θ, the variable to be optimized is the FWHM evaluated at the 2615 keV peak with an unbinned maximum likelyhood fit, as shown in figure 4.10.

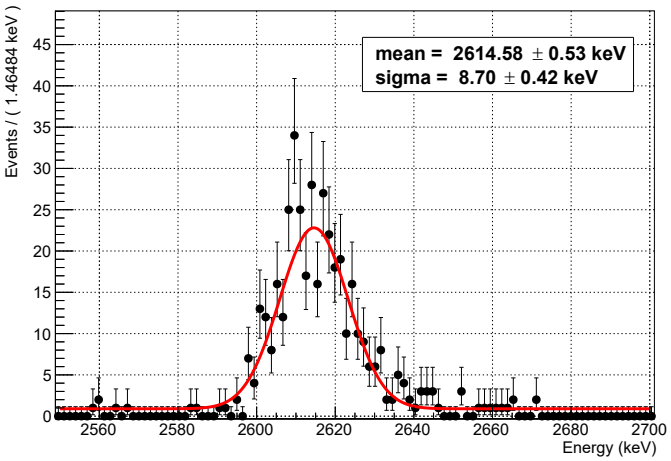

Figure 4.10: Unbinned maximum likelihood fit of the 2615 keV line, modelled with a single Gaussian with a constant background.

The resolution enhancement will be then evaluated with the Resolution Gain (RG), defined by:

$$\mathrm{RG} = \frac{\mathrm{FWHM}(\theta_{\mathrm{MIN}})}{\mathrm{FWHM}(\theta = 0)} \cdot 100. \tag{4.5}$$

By construction, RG is expected ≤ 100 when the resolution is enhanced (FWHM is smaller), and $\sim$100 when no effects are produced by the minimization routine chosen. The value of the RG parameter is calculated for each ZnSe after the search for θ_{MIN}, in order to check the goodness of the minimization procedure. In addition, the gain value is evaluated for different energy peaks, with the ^{56}Co calibration, assessing both the energy stability of this minimization method and the evaluation of the minimization effect both above and below $\mathrm{Q}_{\beta\beta}$.

4.3.1 Single angle minimization

To find θ_{MIN} for Top and Bottom LDs two separate one-dimension minimizations are performed. The chosen algorithm is the Golden-Section search [92], which successively narrows the range of values where the minimum is known to exist. This algorithm is efficient and guarantees a correct termination in ∼20 iterations. The results obtained performing independently the Top and Bottom best rotations for each channel are shown in figure 4.11.

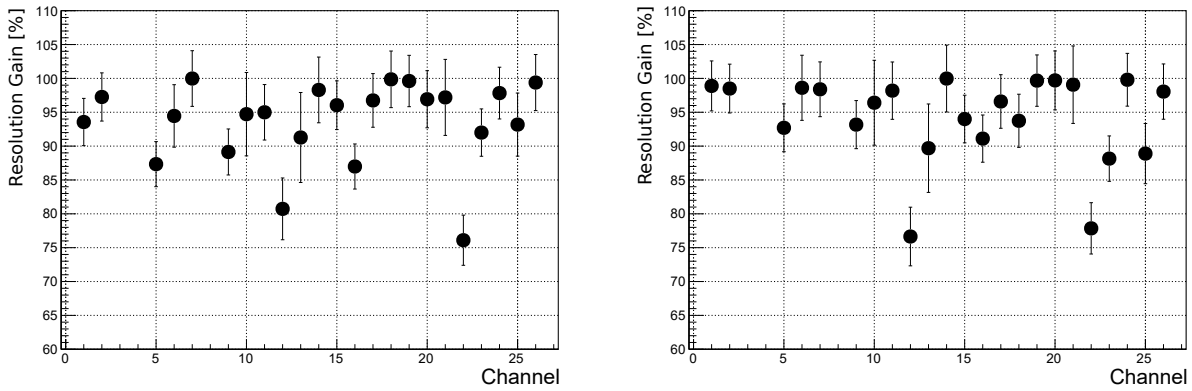

Figure 4.11: Results for one-dimensional minimization for all the heat channels in a single DS after Bottom (left) and Top (right) optimized rotations. The RG varies between channels with an average of ∼90 %, depending on the strength of the correlation in each detector. The best results are obtained for channel 12 and channel 22.

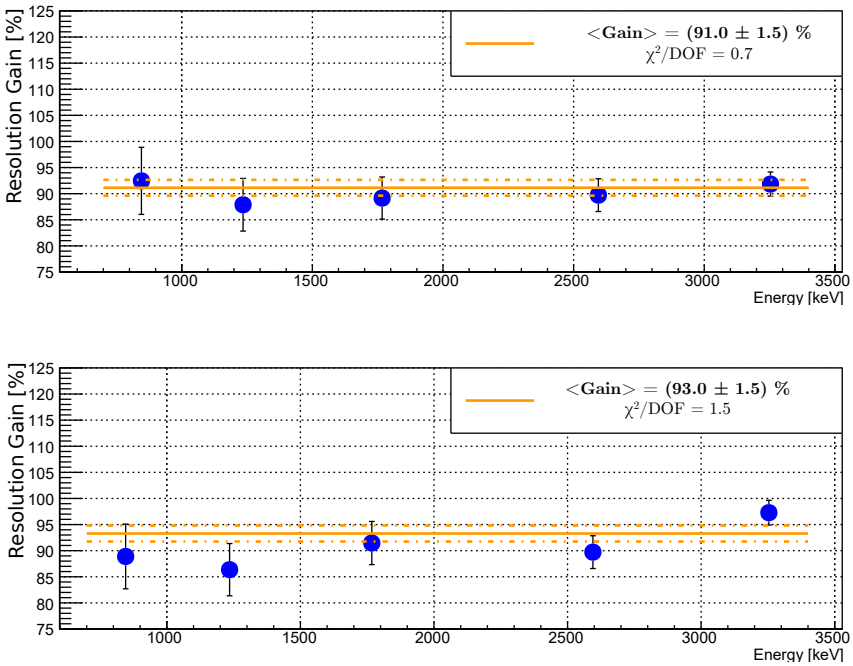

Figure 4.12: $\overline{\text{RG}}$ evaluation for Bottom (up) and Top (low) decorrelations on ^{56}Co calibration. In both cases the RG is constant with energy, proving the effectiveness of this technique both below and above ^{82}Se $Q_{\beta\beta}$. The solid line represents the $\overline{\text{RG}}$ value, while the dashed lines delimit its 68 % confidence interval.

The obtained RG varies between channels depending on how much the correlation between light and heat amplitudes is evident in each detector. The best results are obtained for channel 12 and channel 22. In particular channel 22 is the detector getting the higher benefit from this procedure,

reaching RG = (76 ± 6) %. Both channel 12 and channel 22 are characterized by lower noise level with respect to the other channels. Such feature makes the correlation more evident, thus increasing the attainable gain with the proposed correction.
To investigate a possible dependency of RG on the energy, $\overline{\text{RG}}$ has been evaluated with the ^{56}Co calibration over the (800-3000) keV energy range. As shown in figure 4.12, the resolution enhancement affects all the energies, with the average values of $\overline{\text{RG}}_{\text{Top}}$ = (93.0 ± 1.5) % and $\overline{\text{RG}}_{\text{Bottom}}$ = (91.0 ± 1.5) %. In both cases no energy dependence exists, proving that all possible β/γ signals share the same correlation.

4.3.2 Double angle minimization

Since the Top and Bottom light amplitudes are related to the same heat signal, a combined decorrelation has been performed, taking into account these two information. This strategy helps in dealing with channels characterized by different Top and Bottom correlations. For these detectors, both the Top and Bottom rotations have to be performed to minimize the FWHM, whose minimum cannot be reached exploiting only one light/heat correlation. In figure 4.13 the mapping of the effect of double rotation is reported for channel 18, characterized by this anomalous behavior.

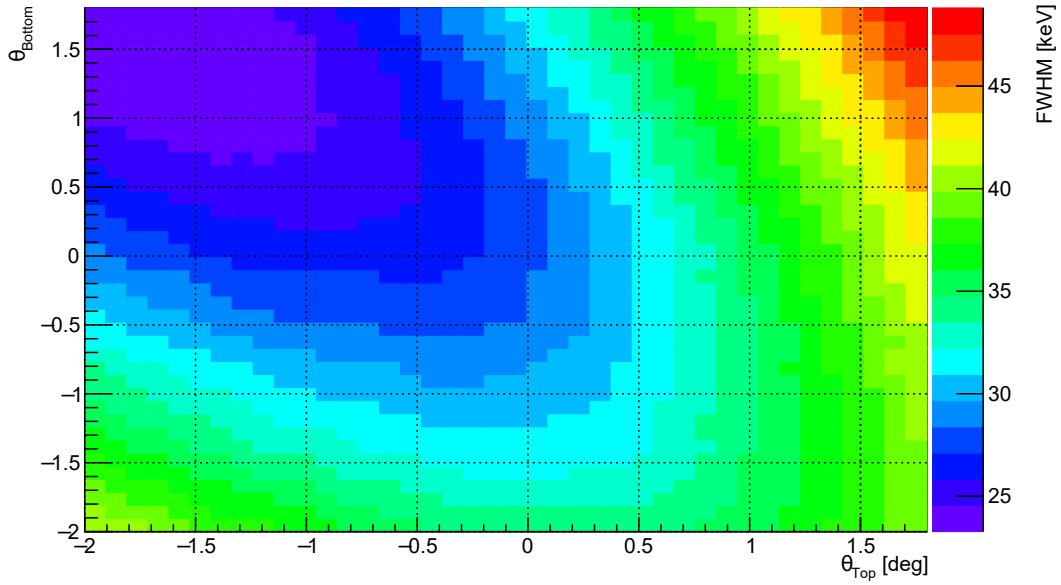

Figure 4.13: Mapping of the effect of double rotation for channel 18. The region for minimum resolution (purple) is characterized by positive θ_{Bottom} and negative θ_{Top}, meaning rotation in different directions for the two light/heat scatterplots. Such feature means that the light-heat correlation in some ZnSe is different when the LD changes. A mismatch between some crystal emission spectrum and ARC acceptance may result in this different behaviur.

A possible explanation resides in small differences in the emission spectrum of the various ZnSe crystals of the CUPID-0 detector. Such differences may cause a mismatch between crystal emission and ARC acceptance, resulting in a difference between measured Top and Bottom light amplitudes. The loss of light causes a different shape of the light/heat scatter plot for the two detectors, raising the need to perform different rotations for the two detectors. To exploit both these features, a combined decorrelation has been performed by means of two subsequent one-dimensional rotations. Firstly θ_{Bottom} is found as described in the previous section, then the Bottom rotation is fixed and a new rotation angle minimizing the resolution is found in the Top light/Bottom corrected heat plane. This order has been chosen since the Bottom light/heat plane gives slightly better results on the average of all the channels, if compared to the Top light/heat plane. However, since the

rotation angles are small, the two rotations almost commute making this order almost arbitrary. The results, reported in figure 4.14, show for the anomalously correlated channels (such as channel 18) the expected reduction and a $\overline{\text{RG}}$ value for the ^{56}Co calibration compatible with the one obtained for the single Bottom minimization (see figure 4.12). The obtained result is aligned with the assumptions made for the definition of this analysis procedure, proving the consistency of the obtained results.

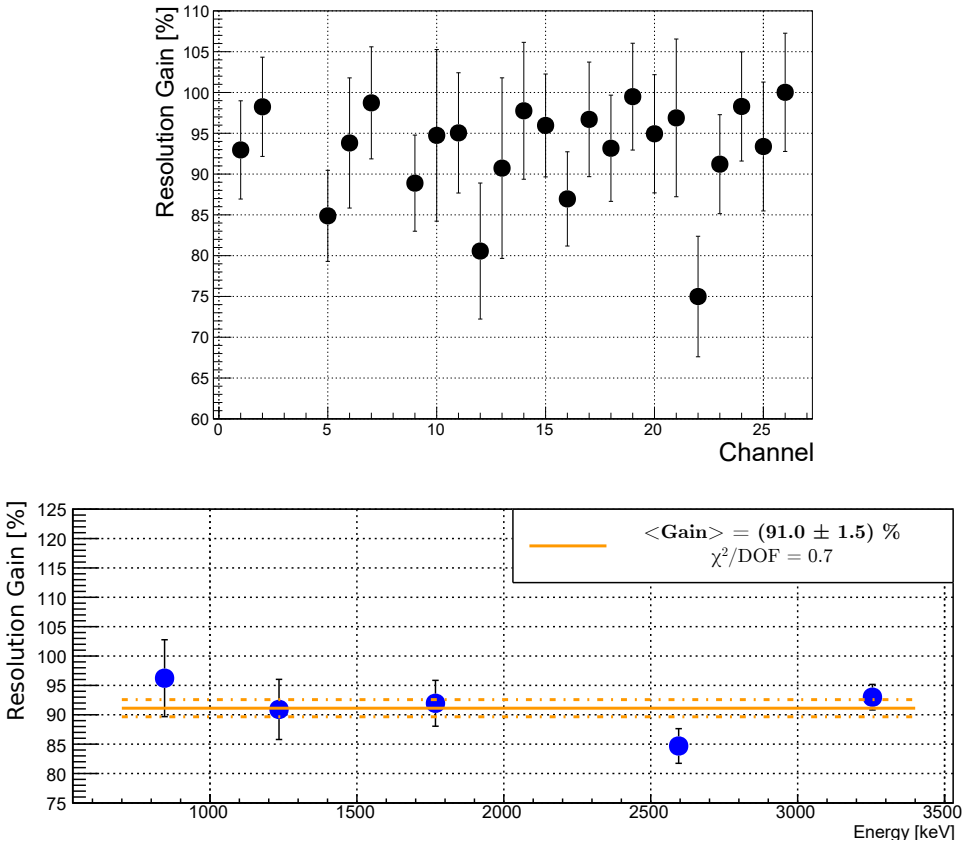

Figure 4.14: $\overline{\text{RG}}$ evaluation with two subsequent rotations, the first in the Bottom light/heat plane and the second in the Top light/Bottom corrected heat plane. The angle used are obtained with two distinct one-dimensional minimization. In the upper panel the RG for each channel is shown. Comparing with figure 4.11, an improvement for channel 18 can be appreciated, as a consequence of the combined minimization. In the lower panel the $\overline{\text{RG}}$ evaluation on ^{56}Co calibration is shown. A comparison with figure 4.12 shows the compatibility between this method and the single angle rotation. The solid line represents the $\overline{\text{RG}}$ value, while the dashed lines delimit its 68% confidence interval.

4.3.3 Chosen minimization method and total result

Comparing all obtained results, the best method to select the optimal rotation angle is to apply two subsequent one-dimensional rotations. This procedure allows to preserve the enhancement obtained with the single rotation, while exploiting the particular features of some channels. In figure 4.15 the effect of the combined rotation is shown on the whole ^{232}Th calibration statistics acquired by CUPID-0. An average $\overline{\text{RG}} = (90.5 \pm 0.6)\%$ is obtained over all the energies, corresponding to a change from $\overline{\text{FWHM}} = (20.7 \pm 0.5)$ keV to $\overline{\text{FWHM}} = (18.7 \pm 0.5)$ keV at the 2615 keV peak.

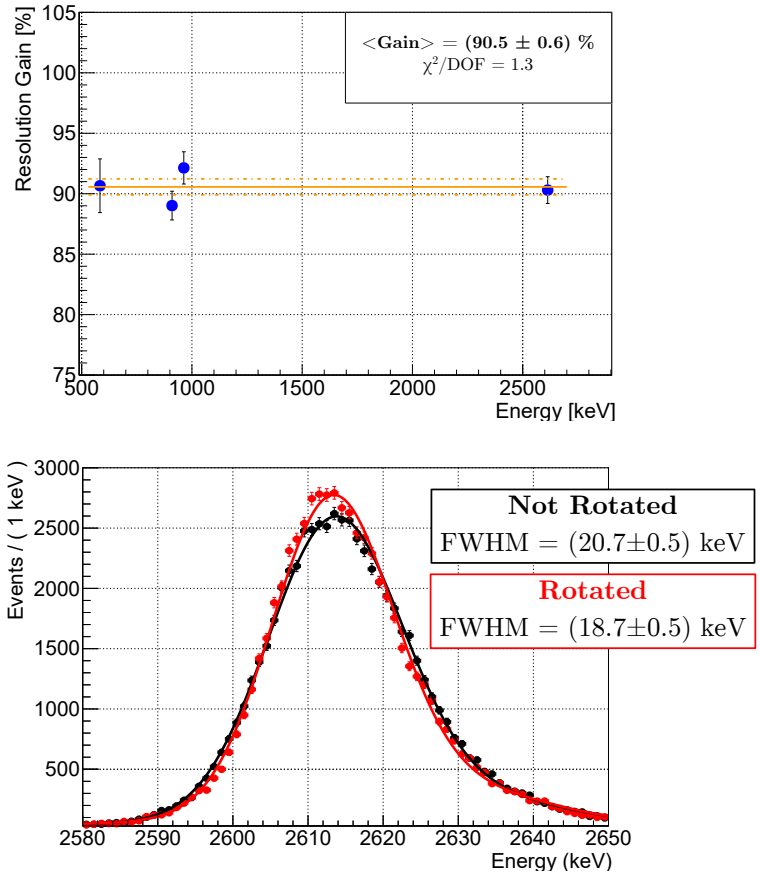

Figure 4.15: Application of the best rotation method to the full calibration statistic of the CUPID-0 experiment. In the upper panel the Resolution Gain over the energy is shown. The obtained gain is $\overline{\text{RG}}$ = (90.5±0.6) %, corresponding to a change from FWHM = (20.7±0.5) keV to FWHM = (18.7±0.5) keV. The solid line represents the $\overline{\text{RG}}$ value, while the dashed lines delimit its 68 % confidence interval. In the bottom panel the shape of the 2615 keV peak is shown before and after the rotation. The main effect of the rotation is the narrowing of the peak, while the line shape is unaffected.

4.4 $0\nu\beta\beta$ analysis

CUPID-0 continuously took data from June 2017 to December 2018, with a total live-time for physics measurement of 74%. The residual 26% has been used for calibration and detector maintenance. The total ZnSe exposure is 9.95 kg × yr, corresponding to a ^{82}Se-only exposure of 5.29 kg × yr (3.88×10^{25} ^{82}Se nuclei×yr). In between the acquired data, the events of interest for the $0\nu\beta\beta$ search have to be selected. Different selection cuts have been applied to select two electrons signal, each one characterized by a certain efficiency.
First, the non-particle-like events have been excluded. These events, such as electronic noise burst or thermal effects, are excluded with basic cuts based on the shape parameters of the heat signals. In particular, 6 parameters proven to be more effective for this evaluation: decay-time, rise-time, baseline slope, delay and TVL. To uniform the selection on these parameters, their energy dependence has to be removed, both in average and resolution (Fig.4.16, left panel). Since standard calibrations produces β-like signals only below 3 MeV, a calibration with an Am:Be external neutron source has been performed. The neutron irradiation produces γ rays up to few MeV, allowing a complete scan of the energy dependence of the shape parameters. Once performed the Am:Be measurement, the energy spectrum is divided in adjacent slices and for each of them the median and the MAD (median average deviation) are calculated for the different shape parameters. Subsequently a polynomial function is fit to the median and MAD points, obtaining the shape parameter

trend for all energies, included $Q_{\beta\beta}$. The functions obtained with the fit are used to correct the shape parameters in the physics run. The correction is made subtracting the median value and dividing for the MAD one, thus obtaining a distribution centered around zero with a width expressed as MAD multiples (see Fig.4.16, right panel).

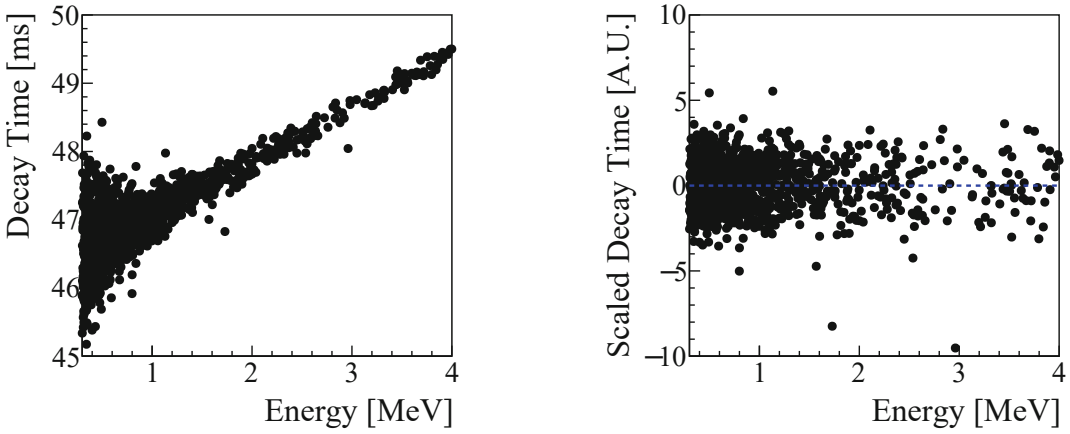

Figure 4.16: Renormalization of shape parameters, in the case of decay time. Left panel: parameter before renormalization, evaluated on AmBe source calibration. Right panel: parameter after renormalization.

To choose the cut value, expressed in MAD units, an efficiency study has been performed, exploiting ^{65}Zn, produced by the cosmogenic activation of the Zn contained in the crystals. This unstable isotope undergoes electron-capture decay with $T_{1/2}$=224 days and a Q_{value} of 1351.9 keV, followed by the emission of a γ ray with energy of 1116 keV. The events under this peak are used as a signal sample, while its side-bands are treated as background. As shown in figure 4.17, the efficiency is calculated by fitting the ^{65}Zn+background spectrum with a Gaussian subtending an exponential background and by dividing the respective area before and after the application of the cut. The choice of this isotope is particular to CUPID-0, given the natural presence of an high amount of Zn in the chosen crystals. In figure 4.18, the efficiency value for signal and background as a function of the MAD multiple at which the cut is performed is reported as an example, alongside the signal/background ratio. The plot shows that efficiency on signal is bigger than on background, although not dramatically. This comes from the fact that in the sidebands of ^{65}Zn peak many $2\nu\beta\beta$ events fall, correctly unaffected from the signal cuts. To select the best cut value to keep the highest efficiency on signal while suppressing the spurious events, the signal/background ratio is calculated. The chosen cut is the value at which this value reaches a stable plateau.

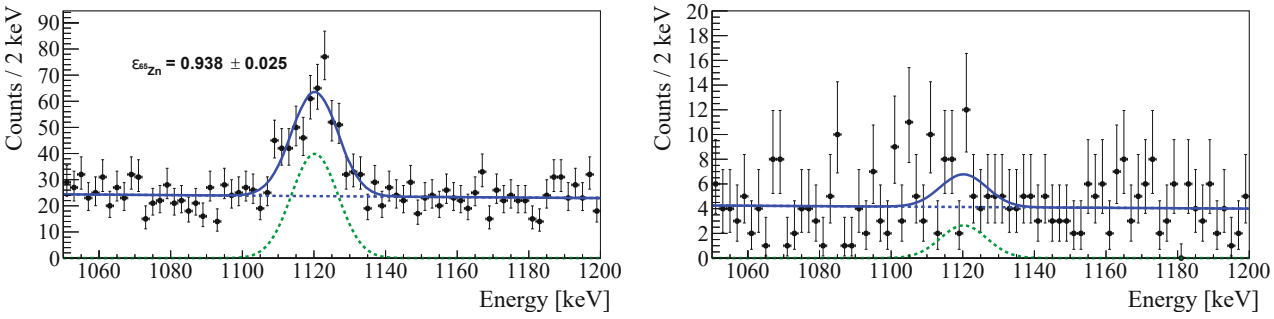

Figure 4.17: Efficiency evaluation on ^{65}Zn peak. Left panel: events passing the selection cuts. Right panel: events removed by the selection cuts. Both fits are modelled with a Gaussian subtending an exponential background. The efficiency is calculated both on signal and background.

The efficiency is calculated for each dataset and subsequently averaged, deriving a selection efficiency of (93±2)% [93]. To cross validate the ^{65}Zn peak method, the selection efficiency is evaluated on the events simultaneously triggering different crystal. In CUPID-0, the coincidence window is

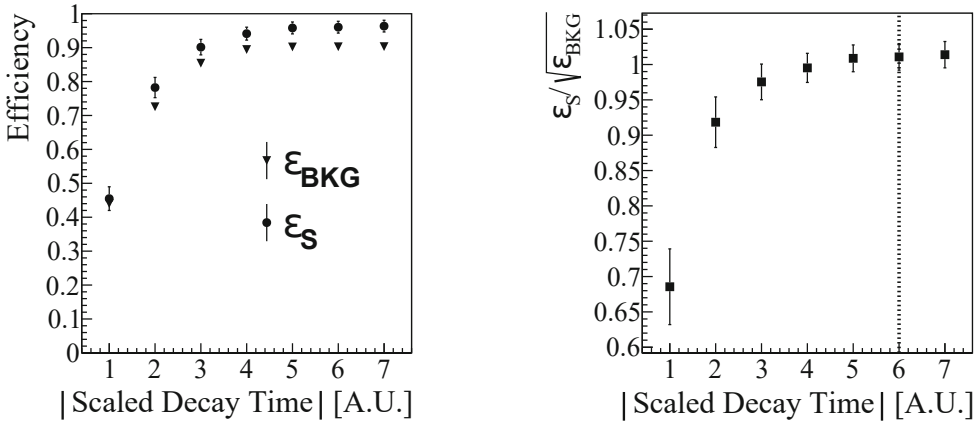

Figure 4.18: Efficiency and Signal/Background ratio for Decay time cuts. The vertical dotted line represents the chosen cut value. These plots refer to the scaled decay-time, the other parameters show the same behavior.

a symmetric 20 ms window centered around the trigger position of a pulse. The number of simultaneously triggered crystals in such window is called multiplicity. Multiplicity 2 events are an almost pure sample of particle-like events, since spurious coincidence, proportional to the trigger rate squared, are negligible. The ratio of events before and after applying the selection criteria is compatible with the efficiency at the ^{65}Zn for energies up to 2.6 MeV. As a consequence the method chosen to evaluate the signal efficiency is correct.
The events used for the $0\nu\beta\beta$ analysis are the one in which only a crystal is triggered, therefore the ones with Multiplicity 1. With such choice, the containment efficiency for $0\nu\beta\beta$ signal is $(81.0 \pm 0.2)\%$. This value is calculated with a dedicated Monte Carlo simulation of the whole detector. More detail on the characteristics of these simulations will be given in section 4.5.
To evaluate the trigger efficiency, which is prior to the analysis, the Si joule heater on each crystal are used. Thanks to the programmable front end, a train of heater pulses are sent in each detector, which is acquired with the usual DAQ chain. The trigger efficiency is calculated as the ratio of triggered to sent heater pulses. With this measurement, also the energy reconstruction efficiency can be calculated, as the probability of the monoenergetic heater pulse to be reconstructed within 3 Gaussian standard deviations of its expected value. The combined trigger+reconstruction efficiency is $(99.44 \pm 0.01)\%$.
These first selection steps reduce the total acquired background to the particle-produced one, characterized by a single-crystal topology. After this basic selection, possible in CUPID-0 as well as in any other bolometric detector, the scintillation based α tagging follows. As shown in Fig.4.6, the TVR on the Top LD allows a clear selection of the alpha pulses above 2 MeV. To further enhance the selection capability, TVR for Top and Bottom LD are averaged. The efficiency on β/γ signal selection is calculated on the pulses due to muon-induced electromagnetic showers. These events simultaneously involve multiple detectors, therefore can be selected requesting Multiplicity>4. The cut on the combined shape parameter has been set to keep a 98% efficiency on muon-induced events. Such selection causes a rate of α mis-identification lower than 10^{-7}. Such discrimination power proves the effective light-based selection capability of scintillating bolometers [93].
As an ulterior advantage due to the α tagging, the background can be further reduced with the identification of $\alpha-\beta$ events in the ^{212}Bi-^{208}Tl cascade (see Fig. 3.3 on page 26). The ^{212}Bi α decays (branching ratio of $\sim$25%) are tagged requesting an alpha event with 2 MeV<energy<6.5 MeV. The lower limit is given by the selection α boundary, while the upper from the Q_{value} of ^{212}Bi decay. After each one of these events, a 7 ^{208}Tl half life window is opened ($7 \cdot 3.03$ min = 21.21 min). The β/γ events falling into this time veto are discarded from the analysis. Such selection introduces a 6% dead time, that has to be taken into account in the efficiency computation.
The different performed selections are characterized by different efficiencies, and are evaluated on

the basis of the residual background in the region of interest (ROI) for the $0\nu\beta\beta$. The ROI is a 400 keV energy window symmetric around $Q_{\beta\beta}$, therefore ranging from 2.8 MeV to 3.2 MeV. In this region, the background is evaluated with an unbinned extendend maximum likelyhood (UEML) fit. The ROI background for each selection cut is reported in detail in table 4.1. The total cut efficiency is $(86 \pm 1)\%$. Combined with the simulated containment efficiency of $0\nu\beta\beta$ events in a single crystal $(81.0 \pm 0.2)\%$, a total $0\nu\beta\beta$ efficiency of $(70 \pm 1)\%$ is obtained. The final background in the ROI is $(3.5^{+1.0}_{-0.9}) \times 10^{-3}$ counts/(keV kg yr). This background index is the lowest ever measured with a bolometric detector, and is indeed an extremely important achievement for the CUPID-0 experiment. The not-optimal energy resolution of the detector although poses a limit to the achievable sensitivity (see eq. (3.7)). Nonetheless, the capability of getting rid off the degraded α background is a major turning point for the bolometric detectors. In figure 4.19 the effect of the different selection cuts are reported, showing the final ROI background [93].

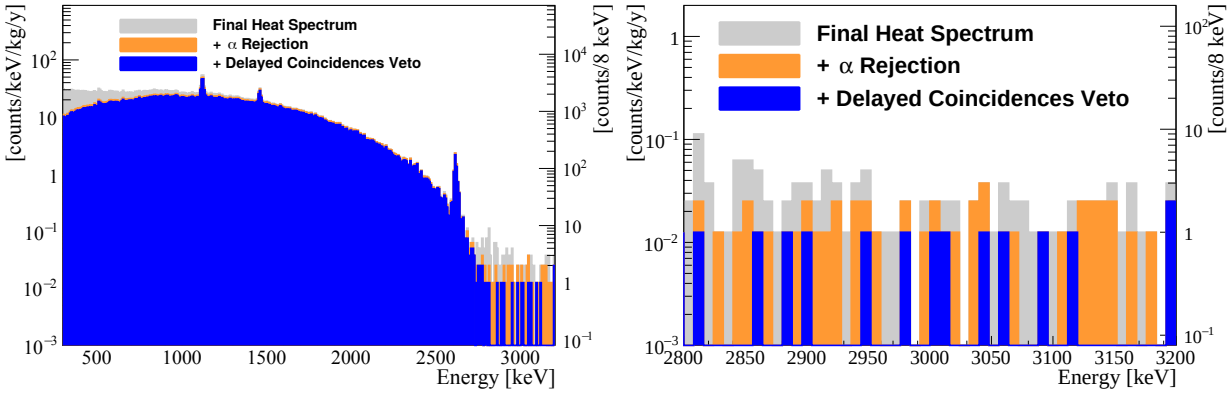

Figure 4.19: CUPID-0 background spectrum with different background selection cuts: heat shape (grey), α rejection (orange) and $\alpha - \beta$ delayed coincidences (blue). The visible peaks are: 1116 keV (^{65}Zn), 1460 keV (^{40}K), 2615 keV (^{208}Tl). The left panel shows the full spectrum, while the right panel reports the region of interest for the $0\nu\beta\beta$.

Cut	Background $[10^{-3}$counts/(keV kg yr)]
Heat shape	(32 ± 4)
α Rejection	(13 ± 2)
Delayed Coincidence	$(3.5^{1.0}_{-0.9})$

Table 4.1: Effect of different selection cuts. The values are stacked, therefore the last includes the previous.

After the final UEML evaluation of the background, the same fit is performed adding the response expected for a $0\nu\beta\beta$ signal: a double gaussian centered at $Q_{\beta\beta}$ with resolution predicted with the ^{56}Co calibration. The different Dataset are fit independently, keeping the background index and the decay rate for $0\nu\beta\beta$ ($\Gamma^{0\nu}$=$1/T^{0\nu}_{1/2}$) as common free parameters. The systematics uncertainty considered in the fit are:

- the uncertainty on the energy scale, affecting the position of the expected $0\nu\beta\beta$ signal (common to all dataset);
- the uncertainty on the energy resolution, affecting the shape of $0\nu\beta\beta$ signal (dataset dependent);
- the efficiency and its uncertainty, reducing the measurable $\Gamma^{0\nu}$ (dataset dependent);
- the exposure and its uncertainty, needed to convert counts/keV to counts/(keV kg yr).

Each of these effects is included as a Gaussian weight in the likelihood. No evidence of $0\nu\beta\beta$ is detected by the fit, therefore only a limit can be placed on $\Gamma^{0\nu}$. The posterior probability density

function (pdf) for $\Gamma^{0\nu}$ is obtained with Bayes theorem by multiplying the likelihood for a flat prior ($0\ y^{-1}<\Gamma^{0\nu}<0.5\times10^{-24}\ y^{-1}$) and marginalizing over the background index nuisance parameter. With the posterior pdf it is possible to define the 90% credible interval limit $\Gamma^{0\nu}<0.2\times10^{-24}\ y^{-1}$, corresponding to a lower limit on $0\nu\beta\beta$ half-life for ^{82}Se:

$$T^{0\nu}_{1/2} > 3.5 \times 10^{24} \text{y} \tag{4.6}$$

The posterior is reported in figure 4.20. This is the best limit ever obtained on ^{82}Se $T^{0\nu}_{1/2}$, and has been made possible by the excellent background rejection capabilities of CUPID-0 [93]. The median sensitivity of the experiment has been calculated with 1000 toy Monte Carlo, generating different CUPID-0-like experiments, obtaining $T^{0\nu}_{1/2}>5.0\times10^{24}$ y. The probability to obtain a better limit with respect to the measured one is 80%. This sensitivity is the final result of CUPID-0 phase one [93], and marks an improvement with respect to the previously published median sensitivity: $T^{0\nu}_{1/2}>2.3\times10^{24}$ y [66]. This ∼220% improvement comes both from the exposure increase (from 1.83 kg × yr to 5.29 kg × yr) and from the resolution increase due to light-heat decorrelation ((9.5 ± 0.6)% reduction). Further increase in exposure, with contextual decrease of background, is foreseen for the phase-II of CUPID-0, based on the results of the background model of the experiment.

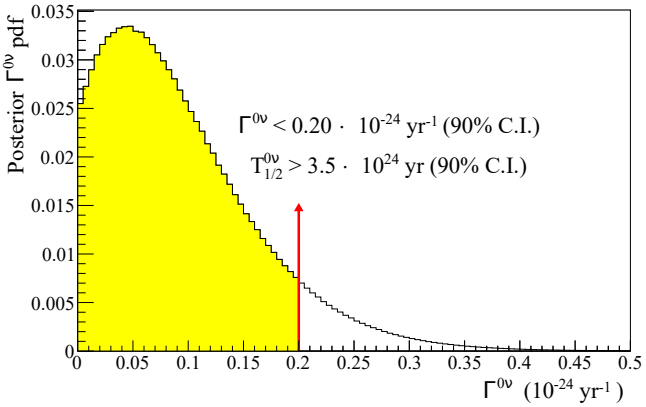

Figure 4.20: $\Gamma^{0\nu}$ posterior distribution. The yellow histogram marks the 90% area of the Credible Interval Bayesian limit. The posterior is calculated by the integration of a likelihood and is weighted to take into account the systematic uncertainties of energy scale, resolution, efficiency and exposure.

4.5 Background Model

The definition of a model for the background of CUPID-0 is a crucial step for this experiment. The comprehension of the background affecting the $0\nu\beta\beta$ source is, in fact, necessary to understand, and possibly overcome, the limits of CUPID-0 background reduction techniques. The background model is also the only way to evaluate the low level of radioactive contamination of the materials building the detector. Consequently, it is a fundamental element to be considered in the design of next-generation experiments.
This analysis start from the experimental data, to deduce the contamination of the detector. The modellization of the identified contributions with Monte Carlo simulations follows, together with the definition of a comprehensive model. This model is then fit to data in order to reconstruct the measured spectrum. From the analysis of the reconstruction conclusions are then drawn, identifying the most important sources of the measured background.

4.5.1 Analysis of experimental spectra

The different possible background sources are deduced by the observation of the experimental spectrum, as well as from previous measurements performed on the detector materials. In particular, the background model of CUORE-0 is used as a guideline, since it was performed in the same cryostat [94]. The identified sources are:

- the $2\nu\beta\beta$ decay of ^{82}Se contained in the crystals;
- the natural radioactive contaminants in the detector, the cryostat and in different shieldings. In particular, the natural chains of ^{232}Th, ^{235}U and ^{238}U, ^{40}K and ^{147}Sm;
- cosmogenically activated isotopes, such as ^{60}Co and ^{54}Mn in copper and ^{65}Zn in ZnSe;
- cosmic μ, environmental γ and neutrons.

These contributors to background have been identified in the experimental data. To allow the disentaglement of the different signatures, the α identification and the event multiplicity were used to construct four spectra, simultaneously used in the analysis: single hit spectra of α and β/γ particles ($\mathcal{M}_{1\alpha}$ and $\mathcal{M}_{1\beta/\gamma}$), double hit spectrum ($\mathcal{M}_2$) and the double hit spectrum where the energy is the sum of the two hit energy (Σ_2). The α identification, as shown in figure 4.6, could only be exploited above 2 MeV, where the measurement of the different light output allowed to distinguish α from β/γ particles [84, 39]. Below 2 MeV, the low signal-to-noise ratio of the light detectors prevented such discrimination, because the light signal cannot be properly distinguished by the noise. The residual α particles that could not be identified below 2 MeV were added to the β/γ spectrum, thus keeping this information [39]. The spectra are reported in figure 4.21 and 4.22, with the different signature highlighted. In $\mathcal{M}_{1\beta/\gamma}$, the main signature is the $2\nu\beta\beta$ spectrum, giving the dominant continuum between 1.5 MeV and 2.5 MeV. The dominance of this decay makes it difficult to disentangle other signatures, that have to be reconstructed with the other spectra. In $\mathcal{M}_{1\alpha}$, the main peaks (except the 5.3 MeV line of ^{210}Po) are centered at the Q-value of the α decays. This means that the corresponding radioisotopes are located in the bulk or near the surface of ZnSe crystals, because the energy of both α and nuclear recoil is detected. The bumps above 7.5 MeV are due to the cascade Bi-Po decays (see Fig.3.3 on page 26), producing a β/α pile-up. Such events are difficult to reconstruct, since the ionization mechanisms of these mixed pile-up signal is different from the standard β-like event. As a consequence, the amplitude obtained with optimum filtering may be affected by a slight miss-calibration. As expected, in Σ_2 the main γ peaks are clearly visible, because the chance of having a single γ interacting in multiple crystal with different Compton interactions is high (see figure 4.22). The combination of the four spectra, therefore, is necessary to correctly constrain the different radioactive contributions, characterized by different topologies and interaction possibilities.

4.5.2 Simulation of background contributions

With the identification of the possible sources, a list of contribution can be made, giving to each source a position in the detector setup. As reported in figure 4.2, the whole CUPID-0 setup can be divided in Crystals, Holder, Reflective foil, CryoInt (inner cryostat shields), ExtPb (Roman lead shield), CryoExt (external cryosat shield), external lead and polyethylene shield. For the parts closer to the detector core (Crystal, Holder and Reflective Foil), the contamination is also divided between bulk and surface of the materials. Such distinction is necessary since a bulk α contamination provides different signatures than a surface one. Consequently, the two level of contamination have to be disentangled.
To perform the actual reconstruction, the theoretical response of the detector to the identified contaminants has to be known. To access this information, dedicated Monte Carlo have been run with the full detector geometry implemented. The simulation where performed thanks to

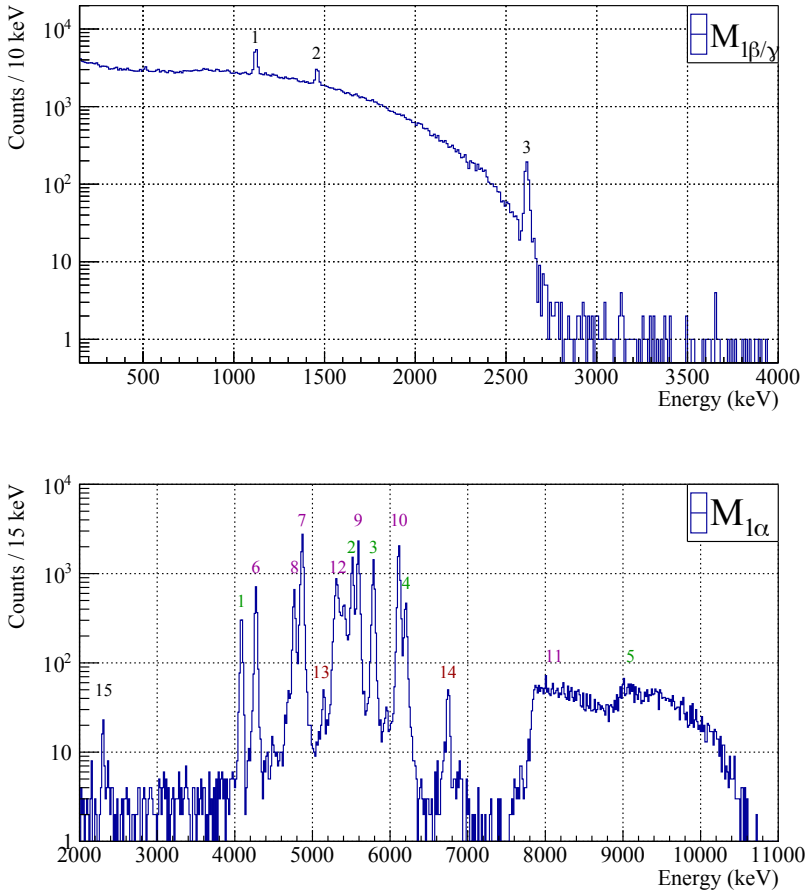

Figure 4.21: CUPID-0 multiplicity one spectra, divided between *beta*/γ events (top, $\mathcal{M}_{1\beta/\gamma}$) and α events (bottom, $\mathcal{M}_{1\alpha}$). In $\mathcal{M}_{1\beta/\gamma}$ the labels stand for: (1) ^{65}Zn, (2) ^{40}K, (3) ^{208}Tl. In $\mathcal{M}_{1\alpha}$ the labels stand for: (1) ^{232}Th, (2) ^{228}Th, (3) ^{224}Ra, (4) ^{212}Bi,(5) ^{212}Bi + ^{212}Po, (6) ^{238}U, (7) ^{234}U + ^{226}Ra, (8) ^{230}Th, (9) ^{222}Rn, (10) ^{218}Po, (11) ^{214}Bi + ^{214}Po, (12) ^{210}Po, (13) ^{231}Pa, (14) ^{211}Bi, (15) ^{147}Sm.

the *Arby* toolkit, developed by the Milano - Bicocca group. *Arby* is a GEANT-4 [95] interface, helping in the definition of the detector geometry and in the management of the decay chains. In particular, the simulation were run with GEANT-4 version 10.02, the particles propagated with the Livermore physics list and the radioactive decays implemented with G4RadioactiveDecay database. In particular, the $2\nu\beta\beta$ simulation was generated under the single-state dominance hypothesis (SSD) in the framework of the Interacting Boson Model (IBM) [96] (see section 2.3.1 on page 14). For each source a position in the geometry is defined, as well as a depth of contamination. Each contribution can be *bulk*, if homogeneously spread in a material, or *surface*, if present only in the first layers. To take into account the diffusion of contaminants and the roughness of surfaces, to each surface contamination an exponential diffusion profile is assigned, characterized by a characteristic length (λ). In particular, two values have been used:

- $\lambda = 0.1$ μm, for *very shallow* contaminations producing sharp peaks at α energy or nuclear recoil energy;
- $\lambda = 10$ μm, for *deep surface* contaminations producing a continuum due to degraded αs.

The difference between bulk and surface contamination is shown in figure 4.23. The bulk contamination in crystals provide the peaks, while the superficial contamination in both crystals and reflectors provide the degraded α continuum.

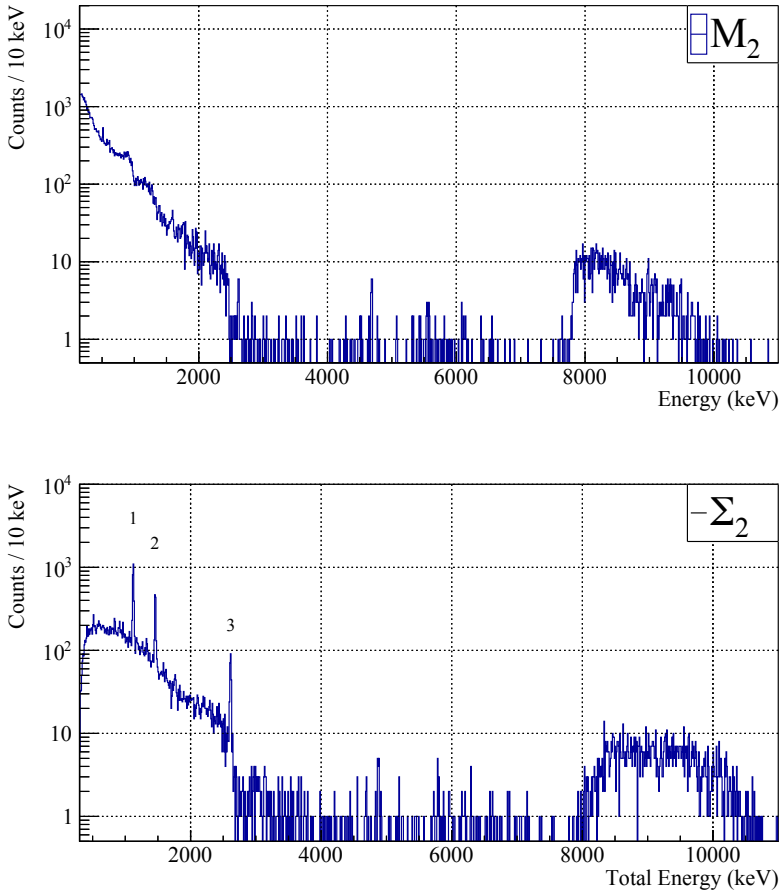

Figure 4.22: CUPID-0 multiplicity two spectra, divided between simple double hit events (top, $\mathcal{M}_2$) and double hit spectrum where the energy is the sum of the two hit energy (bottom Σ_2). In $\mathcal{M}_2$ the labels stand for: (1) ^{65}Zn, (2) ^{40}K, (3) ^{208}Tl.

From the simulation, the energy deposited in the ZnSe crystals, the arrival time of such energy and the particle type were recorded. A second tool was used to implement the detector response, adding the energy and time resolution of the detector, to reconstruct the measured features such as the peak broadening and the pile-up of subsequent events. The particle identification has also been performed, to obtain a complete simulation of the experimental data. These simulated data have been organized as the experimental ones in the four spectra: $\mathcal{M}_{1\beta/\gamma}$, $\mathcal{M}_{1\alpha}$, $\mathcal{M}_2$, Σ_2. For each simulation, all four spectra have been constructed. Since the response function of the detector is non-trivial (see figure 4.7), the four spectra have been created with a variable binning characterized by resolution-wide bins around the peak position. As a consequence, the peak events are all collected in a single histogram entry, allowing an easier data-Monte Carlo comparison. Also the miss-identification of the α below 2 MeV has been kept in the Monte Carlo spectra, thus effectively keeping all the possible information.

4.5.3 Definition of the background model

The background model is composed as a linear combination of the simulated entries in each bin. The coefficients of this linear combination are common to all bins and are the activities of each source. This model is then fit to the data on a bin-by-bin basis, to reconstruct the activities of each source. Such method exploits the bins where both Monte Carlo and data spectra are similarly high to constrain the normalization. As a matter of fact, the main spectral features, such as the peaks, anchor the normalization of the components, while the region where no signatures are present are

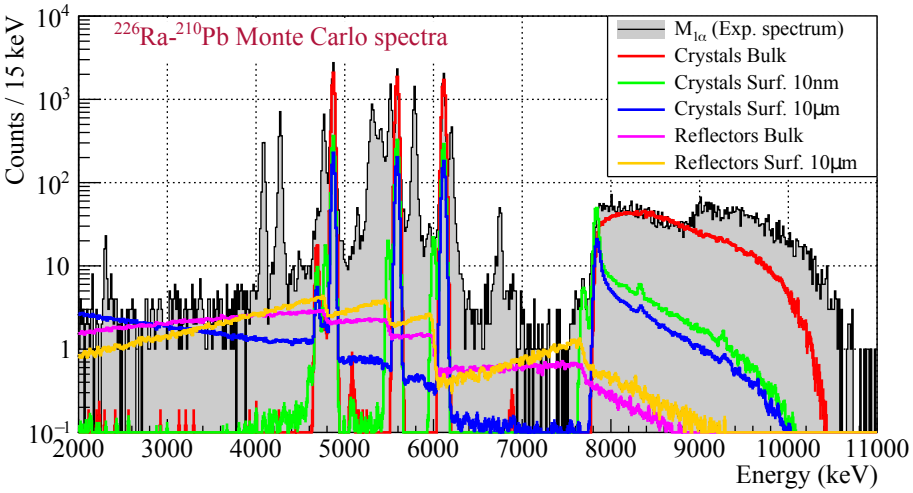

Figure 4.23: Effect of surface and bulk *alpha* contamination, simulated for a ^{226}Rn source in both ZnSe (red, green and blue spectra) and reflective foil (orange and purple spectra), superimposed to the data (grey histogram). The Q-value peaks are evident in the crystal spectra, with also the smaller α energy peaks and the continuum in the surface simulations. Contaminants uniformly distributed in the 70 μm thickness of Reflectors (purple), or simulated with $\lambda = 10$ μm, produce similar step-like spectra, dominated by degraded αs. A custom normalization of MC spectra is chosen to allow easy comparison with the experimental data.

adapted in consequence. To perform the fit, a fully Bayesian approach is chosen. Hence a data-model likelihood is defined and multiplied to a prior distribution for each normalization parameter, to obtain the analytical expression of the joint posterior distribution of all the normalizations.
The definition of the prior distribution for the parameters has a key importance, since the final joint posterior depends on these information. For the majority of the sources, uniform priors have been defined, where possible centered around known values. This is the case of the ^{232}Th contamination of the reflective foil, measured in detail with a Bi-Po detector. These measurements allowed to exclude the upper part of ^{238}U decay chain (whose contribution is negligible), and to set a prior on ^{232}Th chain using the the upper limit on ^{228}Ra contamination. The only unconstrained deep surface contamination of Reflectors is therefore the lower part of ^{238}U chain. Given the thickness (70 μm) and density (0.6 g/cm^3) of the foil, the bulk and surface contaminations give similar signatures. As a consequence, only 10 μm surface contamination were included.
It is worth to spend a few words on the definition of the surface vs bulk prior for the crystal contamination. The disentanglement of these background sources is not easy in CUPID-0, since the presence of the reflective foil around the ZnSe crystals prevent the possibility to have $\mathcal{M}_2$ events characterized by the α particle in one crystal and the nuclear recoil in another. To overcome such limitation, an innovative method has been implemented, exploiting *alpha-alpha* consecutive decays. The ratio between the number of parent decays and the number time-related daughter decays depends, in fact, on the source location. Looking at totally contained events under the Q_{value} peak, in fact, if the contamination is a bulk one, for almost all the father decays a daughter decay is measured. On the other hand, for surface contamination some daughter events are missed, depending on the contamination depth. The possible decay sequences to be used in this case are:

$$^{222}\mathrm{Rn} \xrightarrow[T_{1/2}=3.82\mathrm{d}]{\mathrm{Q}=5.59\mathrm{MeV}} {}^{218}\mathrm{Po} \xrightarrow[T_{1/2}=3.11\mathrm{min}]{\mathrm{Q}=6.12\mathrm{MeV}} {}^{214}\mathrm{Pb} \quad \text{for } {}^{238}\mathrm{U} \tag{4.7}$$

$$^{224}\mathrm{Ra} \xrightarrow[T_{1/2}=3.66\mathrm{d}]{\mathrm{Q}=5.79\mathrm{MeV}} {}^{220}\mathrm{Rn} \xrightarrow[T_{1/2}=55.6\mathrm{s}]{\mathrm{Q}=6.4\mathrm{MeV}} {}^{216}\mathrm{Po} \xrightarrow[T_{1/2}=0.145\mathrm{s}]{\mathrm{Q}=6.9\mathrm{MeV}} {}^{212}\mathrm{Pb} \quad \text{for } {}^{232}\mathrm{Th} \tag{4.8}$$

In the case of ^{238}U the analysis is simple: the number of parent events are evaluated at the 5.59 MeV peak of ^{222}Rn, followed by 6.12 MeV ^{218}Po decay in the same crystal within 3 $T_{1/2}$ time window

($3 \cdot 3.11$ min ~ 10 min). For ^{232}Th, instead, the short $T_{1/2}$ of ^{216}Po decay causes pile-up with the ^{220}Rn daughter decay. To recover and count the target events, a dedicated software tool has been developed. Firstly, the events at the 5.79 MeV peak of ^{224}Rn are selected as father events, and the candidate daughters are tagged in a 3 $T_{1/2}$ time window. The tagged events are processed to identify the two (or more) superimposed pulses with the `TSPectrum` class, belonging to the ROOT package. As shown in figure 4.24, the method identify the position of the two maxima. With this information, it is possible to extract the time difference between the two piled-up pulses. A time difference distribution is built for the two pileup pulses, excluding single pulses and triple (or more) pile-up events falling in the time window. The single events are:

- events where only ^{220}Rn or ^{216}Po events are detected by the same crystal;
- pile-up events with time difference shorter than the detector time resolution, therefore identical to a single pulse with amplitude equal to the sum of the two amplitudes.

In figure 4.25 the spectrum of these events is shown, with the tree signatures highlighted. The triple pile-up events are instead due to spurious coincidences between a ^{220}Rn-^{216}Po pileup and another event. Both the single and triple events have not been considered while building the time distribution of pileup.

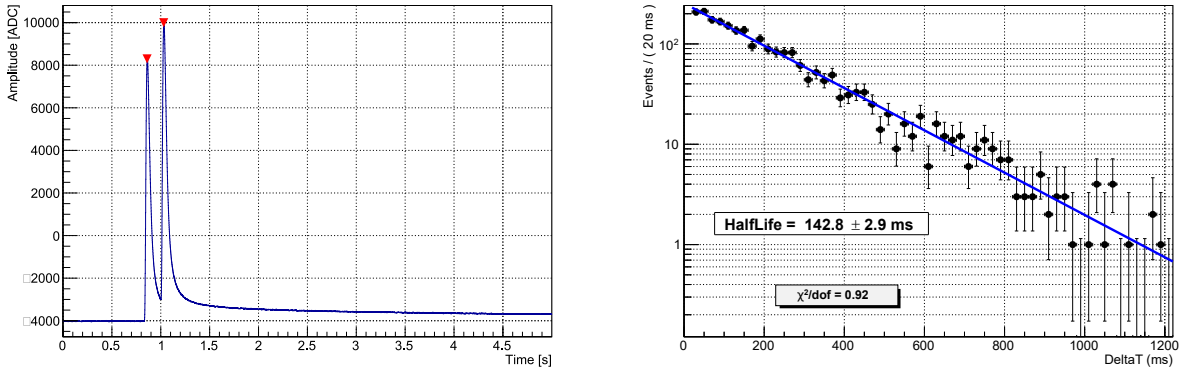

Figure 4.24: Result of *alpha-alpha* delayed coincidences. The left panel presents an example of ^{220}Rn-^{216}Po pile-up signal. The red triangles mark the pulses identified by the algorithm. In the right panel the fit of the total time distribution is shown, with the reconstructed half-life.

From a fit of the time differences distribution with an exponential, the total integral is calculated, obtaining the number of daughter decays fully contained in the same crystal. Also the half-life of the decay is measured, obtaining $T_{1/2} = (142.8 \pm 2.9)$ ms, compatible to the nuclear data table value. Such procedure is an actual zero-background analysis, since the signature of the process is extremely clear. In figure 4.24 a pile-up pulse is reported, alongside the total fitted time distribution. The absence of a significant constant distribution of random coincidences further proves the absence of background processes, that could spoil the obtained result.
Combining this result with Monte Carlo simulations, the ratio of surface versus bulk contaminations of the middle (^{226}Ra - ^{210}Pb) and lower (^{228}Ra - ^{208}Pb) parts of ^{238}U and ^{232}Th decay chains respectively are constrained by a data-driven prior. The results of this analysis prove that bulk contaminations have higher activity than surface ones. In particular, only $\sim$15% ($\sim$5%) of the parent events at the Q-value of ^{222}Rn (^{224}Ra) are produced by surface contaminations. This information sets a precise prior to the ratio between surface and bulk contamination of crystals. For other contaminations this method could not be applied, therefore it has been chosen to leave all those contamination as pure bulk, in order to reduce the ingredients of the model, avoiding the inclusion of too many degenerate simulation spectra.
A particular procedure is also used for the definition of the prior of the μ flux. Since μ interacting in the detector components can produce electromagnetic showers simultaneously triggering different

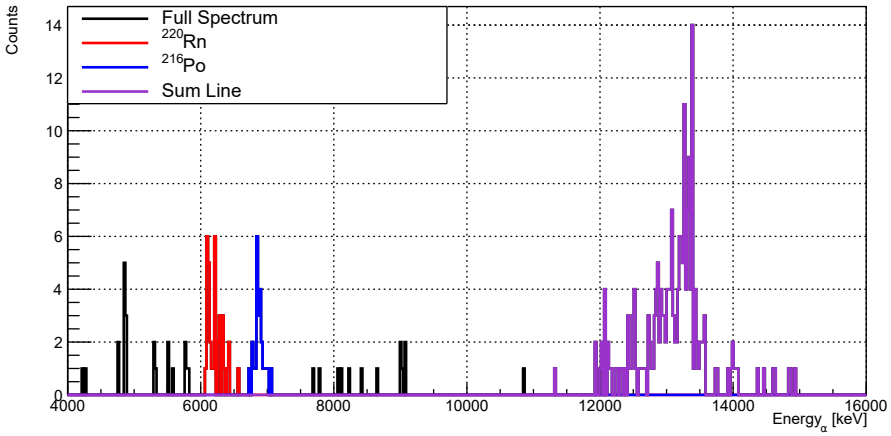

Figure 4.25: Spectrum of single pulses α-α delayed coincidences. The ^{220}Rn (6.4 MeV, red histogram), ^{216}Po (6.9 MeV, blue histogram) and their sum line (∼13 MeV, purple histogram) are visible.

crystals, high multiplicity spectrum is used to constraint such component. With this method μ-induced contribution is determined within a ±15% systematic uncertainty, depending on the selection of experimental high multiplicity events used to calculate the normalization factor. This result is used to set a prior for muons in the background model.

4.5.4 Model fit and result analysis

After likelihood and priors definition, the joint posterior distribution for the activities is sampled with JAGS (Just Another Gibbs Sampler) [97], a software based on a Markov Chain Monte Carlo algorithm. The sampled posterior is subsequently marginalized to obtain the pdf for each normalization parameter. The fit range extends from 300 keV to 5 MeV, and from 2 to 11 MeV for $\mathcal{M}_{1\beta/\gamma}$ and $\mathcal{M}_{1\alpha}$ spectrum, respectively. The multiplicity 2 events used to fill $\mathcal{M}_2$ and Σ_2 spectra are selected requiring both events above 150 keV. The exclusion of low energy events prevent the inclusion of electronic pulses, difficult to disentangle from low energy physics events because of the noise meddling. After the sampling of the joint posterior and the various marginalization, the posterior for each source activity is analyzed. Most of these distribution have a Gaussian shape, hence the activity and its uncertainty are calculated as mean value and standard deviation with a fit. When an activity is compatible with zero, the 90% upper limit is calculated by numerical integration of the posterior distribution. The total ingredients of the model are 33, listed in table 4.2, with the corresponding obtained activities or 90% C.I. limits [39].
The reconstruction of the spectral shape has been efficiently performed in all the considered spectra. As reported in figure 4.26, in fact, the pull distribution considering all the spectra has $\mu = 0.00 \pm 0.07$ and $\sigma = 1.11 \pm 0.06$, meaning a satisfactory agreement. The reconstruction obtained is shown in figures 4.27 for the Multiplicity one and in figure 4.28 for the Multiplicity two spectra respectively. The region below 6 MeV is correctly reconstructed in all the spectra, proving the effectiveness of the chosen model. In particular, $\mathcal{M}_{1\alpha}$ is correctly reconstructed, thanks to the prior used for surface vs bulk α contaminations. It is worth noticing that the α-β/γ discrimination allowed the full identification and reconstruction of the 2.31 MeV ^{147}Sm alpha peak, that otherwise would be hidden below the $2\nu\beta\beta$ events. The only sizable miss-reconstruction emerges around the Bi-Po bumps (β/γ events with Energy>6 MeV), due to the error induced in the energy evaluation by the β/α pile-up.
Since the global reconstruction is successful, the model can be used in the identification of all the contributors to the background in the ROI for $0\nu\beta\beta$ (2.8 MeV-3.2 MeV). This model is the only possible way to perform such analysis, since such prediction has to be made for background on the

Component	Source	Index	Activity (Bq/kg)
Crystals (10.5 kg)	$2\nu\beta\beta$	1	$(9.96 \pm 0.03) \times 10^{-4}$
	^{65}Zn	2	$(3.52 \pm 0.06) \times 10^{-4}$
	^{40}K	3	$(8.5 \pm 0.4) \times 10^{-5}$
	^{60}Co	4	$(1.4 \pm 0.3) \times 10^{-5}$
	^{147}Sm	5	$(1.6 \pm 0.3) \times 10^{-7}$
	^{238}U-^{226}Ra	6	$(5.51 \pm 0.10) \times 10^{-6}$
	^{226}Ra-^{210}Pb	7	$(1.54 \pm 0.02) \times 10^{-5}$
	^{210}Pb-^{206}Pb	8	$(7.05 \pm 0.16) \times 10^{-6}$
	^{232}Th-^{228}Ra	9	$(2.74 \pm 0.10) \times 10^{-6}$
	^{228}Ra-^{208}Pb	10	$(1.20 \pm 0.03) \times 10^{-5}$
	^{235}U-^{231}Pa	11	$(5.3 \pm 0.7) \times 10^{-7}$
	^{231}Pa-^{207}Pb	12	$(7.8 \pm 0.4) \times 10^{-7}$
Holder (3.10 kg)	^{54}Mn	13	$(2.2 \pm 0.3) \times 10^{-4}$
CryoInt (36.9 kg)	^{232}Th	14	$< 4.5 \times 10^{-5}$
	^{238}U	15	$(7 \pm 3) \times 10^{-5}$
	^{40}K	16	$(3.0 \pm 0.6) \times 10^{-3}$
	^{60}Co	17	$(6.8 \pm 1.3) \times 10^{-5}$
IntPb (202 kg)	^{232}Th	18	$< 6.3 \times 10^{-5}$
	^{238}U	19	$< 7.3 \times 10^{-5}$
CryoExt (832 kg)	^{60}Co	20	$(2.6 \pm 0.9) \times 10^{-4}$
ExtPb (36.9 kg)	^{232}Th	21	$(4.3 \pm 0.6) \times 10^{-4}$
	^{238}U	22	$(2.5 \pm 1.2) \times 10^{-4}$
	^{40}K	23	$(2.8 \pm 0.8) \times 10^{-3}$
	^{210}Pb	24	$(7.8 \pm 0.3) \times 10^{-5}$
Surface Component	**Source**	**Index**	**Activity (Bq/m^2)**
Crystals (2574 m^2)	^{226}Ra-^{210}Pb - 0.01 μm	25	$(2.63 \pm 0.15) \times 10^{-8}$
	^{228}Ra-^{208}Pb - 0.01 μm	26	$(6.5 \pm 1.1) \times 10^{-9}$
	^{226}Ra-^{210}Pb - 10 μm	27	$< 2.3 \times 10^{-9}$
	^{228}Ra-^{208}Pb - 10 μm	28	$(4.2 \pm 1.6) \times 10^{-9}$
Reflectors (2100 m^2)	^{232}Th - 10 μm	29	$< 7.3 \times 10^{-10}$
	^{226}Ra-^{210}Pb - 10 μm	30	$(8.7 \pm 1.3) \times 10^{-9}$
	^{210}Pb-^{206}Pb - 10 μm	31	$(1.0 \pm 0.5) \times 10^{-8}$
	^{210}Pb-^{206}Pb - 0.01 μm	32	$(1.43 \pm 0.02) \times 10^{-7}$
Muon Flux μ/(cm^{2}s)		33	$(3.7 \pm 0.2) \times 10^{-8}$

Table 4.2: Results of CUPID-0 backgorund model.The columns contain (1) the name of the component where the source is located with their corresponding mass (or surface), (2) the contaminant, (4) the source index, and (5) the evaluated activity with the statistical uncertainty (limits are at 90% CI).

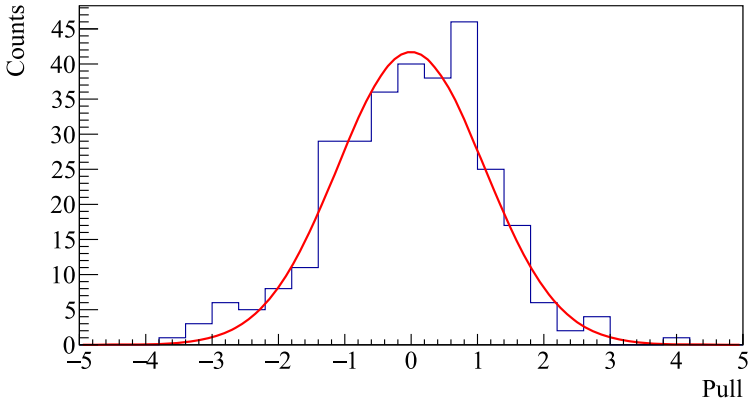

Figure 4.26: Pull distribution of the background model fit, including all the bins. The gaussian fit gives $\mu = 0.00 \pm 0.07$ and $\sigma = 1.11 \pm 0.06$, with $\chi^2/\text{dof} = 18.4/15$. The data-model agreement is therefore good.

order of 10^{-3}counts/(keV kg yr) (see table 4.1). The counts predicted by the model in the ROI are 50.5 ± 1.3, fully compatible with the 52 counts experimentally observed. This evaluations are performed without the delayed coincidence cut, therefore the dominant contribution is due to ^{208}Tl β decays. The reconstruction is shown in figure 4.29. It is worth noticing that the main component below 2.6 MeV is the $2\nu\beta\beta$ decay of ^{82}Se.
Applying the delayed cut both to data and model, 34 ± 1 counts are removed from the model. In the experimental data the rejection of 38 events is observed. The discrepancy can be addressed to the presence of spurious coincidences in the experimental data. After this selection, 16.5 ± 0.8 counts are predicted in ROI by the model, with a precision determined by the high statistics of Monte Carlo simulation used in the reconstruction. This value is in full compatibility range with the 14 measured counts. The predicted background index is $(41 \pm 2) \times 10^{-4}$counts/(keV kg yr), while the measured one is $(35^{+10}_{-9} \times 10^{-4}$counts/(keV kg yr). The main components responsible for this residual background are Th and U chains in Crystals, cryostat reflectors and holders (in order of importance), the tail of $2\nu\beta\beta$ and the μ induced events. The weight of these components is reported in table 4.3. The μ weight for $\sim$40% in the total remaining background, being as a matter of fact the main residual contribution. The background from $2\nu\beta\beta$ appears also as a dominant contribution, but it decreases quickly, becoming $< 3 \times 10^{-6}$ counts/(keV kg yr) if considered in a FWHM window at the $Q_{\beta\beta}$.

Component	Background [10^{-4}counts/(keV kg yr)]
Th/U	$19.8 \pm 1.4^{+6.6}_{-2.7}$
Muons	$15.3 \pm 1.3 \pm 2.5$
$2\nu\beta\beta$	6.0 ± 0.3
Total	$41 \pm 2^{+9}_{-4}$
Experimental	35^{+10}_{-9}

Table 4.3: Background contributors in the ROI, defined in the 2.8 MeV-3.2 MeV energy range. Th/U summarized surface and bulk contaminatin in Crystals, Cryostat, Reflector and Holder. The $2\nu\beta\beta$ value appears dominant, but in [2.95-3.05] MeV range (one FWHM around $Q_{\beta\beta}$), it becomes $< 3\times10^{-6}$ counts/(keV kg yr). The second uncertainty is due to the systematic tests. The values are after the delayed coincidences cut.

The reported reconstruction is based on the assumptions made in the definition of the model. In particular, the source list, their location, the depth of contamination and their priors can affect the values obtained for the activities. Moreover, the choice made on the binning procedure can affect our results, since the bins are the basic ingredients of our model. To check the effect of these choices, different fit are performed varying one (or more) of these constraints. The difference obtained on the reconstructed activities are accounted as systematic uncertainty of the model. In

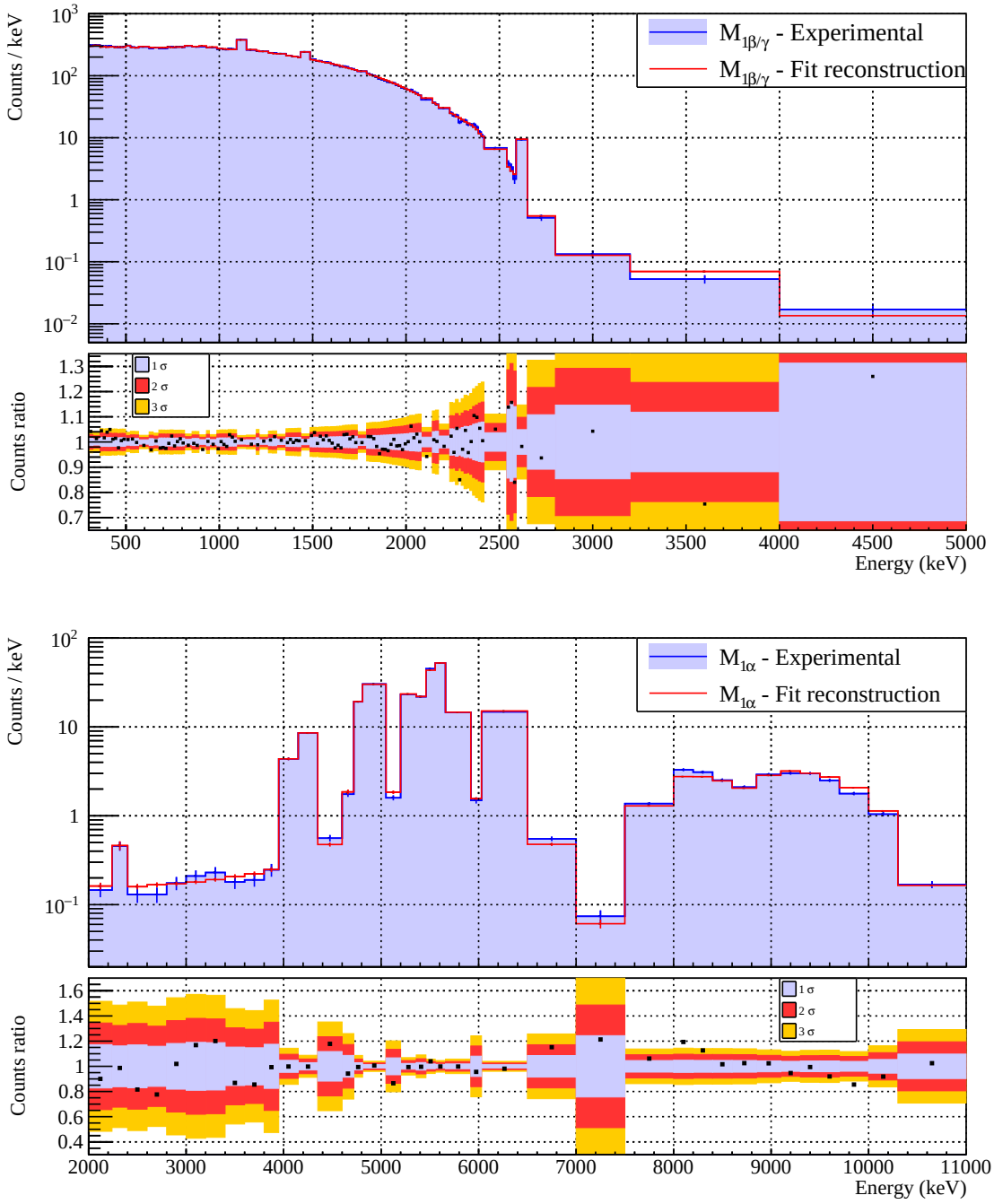

Figure 4.27: $\mathcal{M}_{1\beta/\gamma}$ (top) and $\mathcal{M}_{1\alpha}$ (bottom) reconstruction, compared with the experimental spectrum. In each graph, the bottom panel show the Data/MC ratio as a function of the energy. The corresponding 1,2,3 σ bands are shown with different colored bands. In $\mathcal{M}_{1\beta/\gamma}$ the reconstruction is extremely satisfactory, especially in the 1-5 MeV-2.5 MeV range, dominated by $2\nu\beta\beta$. In $\mathcal{M}_{1\alpha}$ the reconstruction is also good, with sizable deviation only around the Bi-Po bumps (Energy>8 MeV), due to the error induced in the energy evaluation by the β/α pile-up. It is worth noticing that the $\alpha/\beta/\gamma$ discrimination allowed the full identification and reconstruction of the 2.31 MeV ^{147}Sm alpha peak, that otherwise would be hidden below the $2\nu\beta\beta$ events.

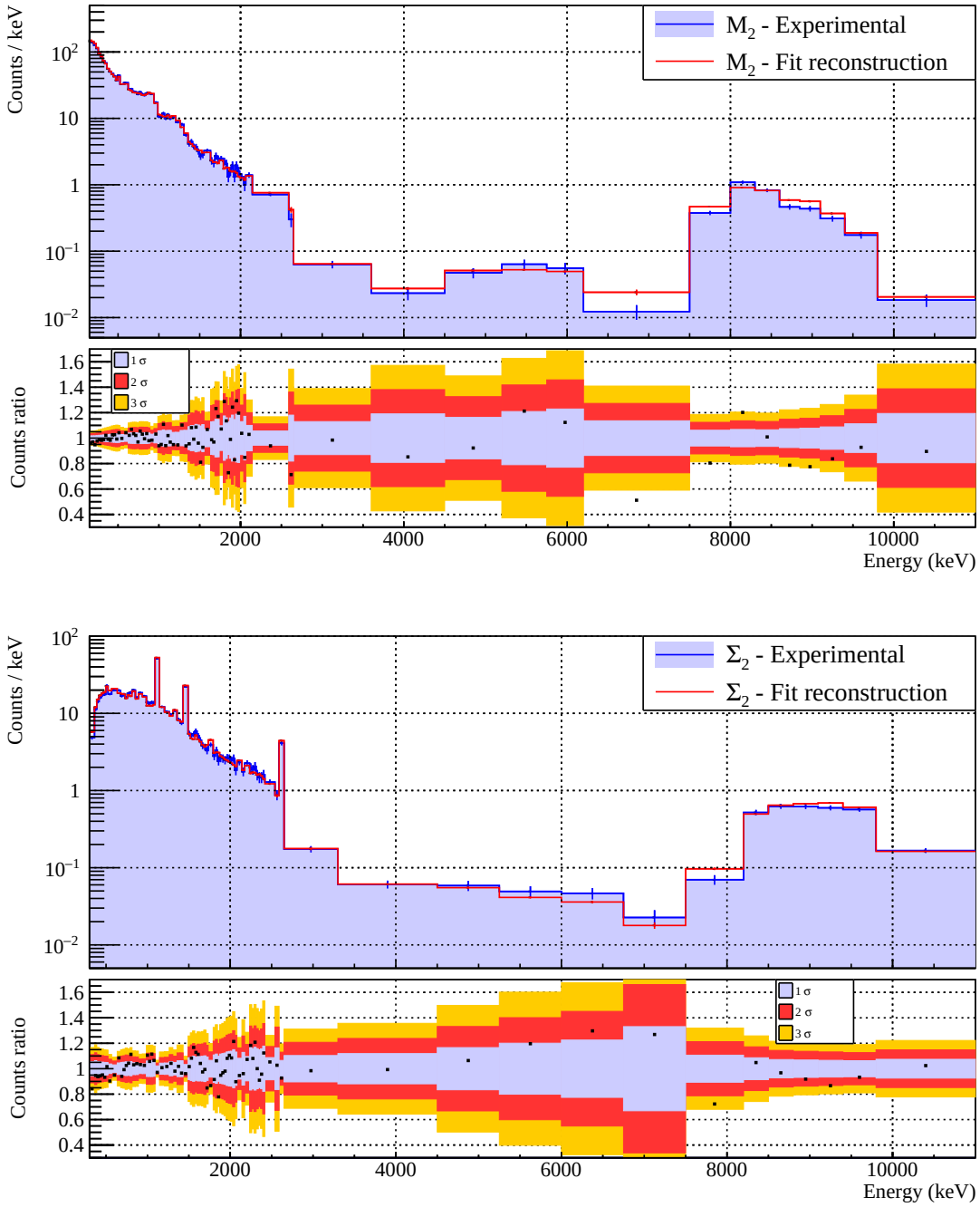

Figure 4.28: $\mathcal{M}_2$ and Σ_2 reconstruction, compared with the experimental spectrum. In each graph, the bottom panel show the Data/MC ratio as a function of the energy. The corresponding 1,2,3 σ bands are shown with different colored bands. The region below 6 MeV is correctly reconstructed in both the spectra, proving the effectiveness of the chosen model. The only sizable deviations emerge around the Bi-Po bumps (Energy>6 MeV), due to the error induced in the energy evaluation by the β/α pile-up.

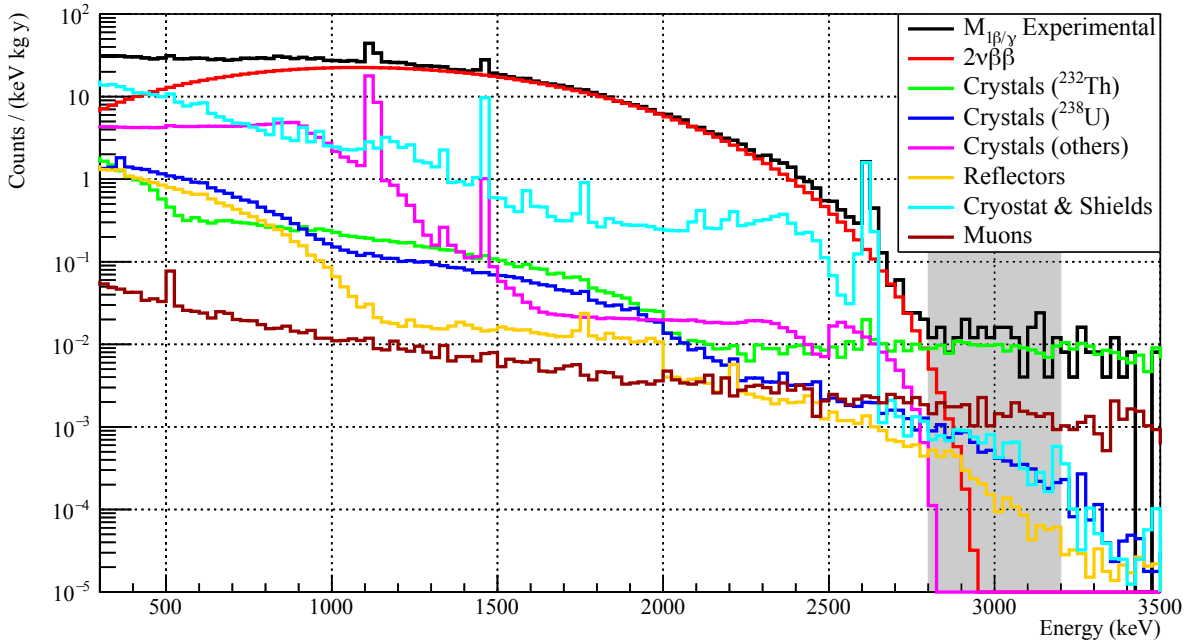

Figure 4.29: Background components in $\mathcal{M}_{1\beta/\gamma}$, with focus on the ROI for $0\nu\beta\beta$ (grey band). The reconstruction and data are reported without the delayed coincidence cut, therefore the dominant contribution is due to ^{208}Tl β decays from the crystal bulk and surface (green histogram). The second major contribution is given by the muons (brown histogram), contributing to ∼40% of the counts after the delayed cut. It is worth noticing that the main component below 2.6 MeV is the $2\nu\beta\beta$ decay of ^{82}Se (red histogram).

[39] a detailed discussion is made on the performed tests. The systematic uncertainty are the major source of error in this model, as reported in table 4.3, since the statistical fluctuation are made negligible by the binning choice and by using high statistic Monte Carlo simulations. It is important to specify that, in all the different test performed, the model never failed to describe our data, and other test have not been reported since the model would be too heavily in tension with the measured spectra. Such feature is a further proof of the stability of the chosen method.
Summarizing, the $2\nu\beta\beta$ contribution to ROI background is negligible at $Q_{\beta\beta}$. The main residual contribution is due to μ-induced electromagnetic showers, producing ∼44% of the observed background. The remaining counts are due to radioactive decays in Crystals (∼33%), in Cryostat and Shields (∼17%), and in Reflectors and Holder (∼6%). On the basis of this analysis, an upgrade for CUPID-0 detector has been performed, directed to background reduction. In the so-called CUPID-0 Phase-II, a muon veto has been installed with plastic scintillators, to tag and exclude at least a portion of the main background source. In addition, the reflective foil have been removed, to test their effect on light collection efficiency and to allow the detection of α events in $\mathcal{M}_2$ and Σ_2. To replace the thermal shielding of the reflective foil, an ultra-pure copper vessel was added around the detector. Such improvement is expected to further reduce the counting rate due to contaminations of cryostat and shields.
The modification have been performed, and the phase II is taking data smoothly since june 2019.

4.6 Search of Lorentz Violation in $2\nu\beta\beta$

The full reconstruction of the background shape achieved in the definition of the background model gives access to the full shape of $2\nu\beta\beta$ spectrum, with which different new physics study can be performed (see section 2.3.2 on page 18). In this particulat analysis, the Lorentz symmetry violation (LV) induced by quantum gravity theories will be tested. The predicted effect of LV on $2\nu\beta\beta$ will be compared to sizable spectral features with a dedicated background model, to constrain the intensity

of LV phenomenology. The hypotheses of the model will be then tested, to take into account the systematic uncertainties. A final limit for the LV in neutrino sector will be given and compared to the current values for this parameter.

4.6.1 Predicted effect of Lorentz Violation in $2\nu\beta\beta$

The LV can be produced at the achievable energy scale by an effective interaction between Standard Model particles and Quantum Gravity operators. The Standard Model Extension (SME) [31, 32, 33] is the framework where the quantum field operators responsible for these interactions are described. LV is included in SME with background fields characterized by non-zero vacuum expectation values, resulting in the spontaneous breaking of space-time symmetry [34]. In between all the possible operators, the countershaded operator is the one responsible for the $2\nu\beta\beta$ spectral distortion [36, 30].
The interaction of neutrinos with this operator changes their quadrimomentum from $q^\alpha = (\omega, \boldsymbol{q})$ to $\tilde{q}^\alpha = (\omega, \boldsymbol{q} + \boldsymbol{a}^{(3)}_{\text{of}} - \mathring{a}^{(3)}_{\text{of}}\hat{\boldsymbol{q}})$, where $\boldsymbol{a}^{(3)}_{\text{of}}$ and $\mathring{a}^{(3)}_{\text{of}}$ are the directional and isotropic coupling coefficient. This momentum modification affects the energy subdivision in $2\nu\beta\beta$ decay between electron and neutrinos. Consequently, it affects the two emitted electron spectrum. In particular, this modification acts as an additive term with spectral index 4, whose matrix element is identical to the SM $2\nu\beta\beta$ except for being multiplied by $\mathring{a}^{(3)}_{\text{of}}$.
The differential decay amplitude therefore acquires the form:

$$\begin{aligned}\frac{d\Gamma}{dE} =& C \cdot F(Z,t_1)\sqrt{t_1(t_1+2)}(t_1+1) \cdot F(Z,E-t_1)\sqrt{E-t_1(E-t_1+2)}(E-t_1+1)\cdot \\ & [(Q-E)^5 + 10\cdot \mathring{a}^{(3)}_{\text{of}}(Q-E)^4)] \\ =& C \cdot \left(\frac{dI^{\text{Theo}}_{2\nu,\text{SM}}}{dE} + 10\cdot \mathring{a}^{(3)}_{\text{of}}\frac{dI^{\text{Theo}}_{2\nu,\text{LV}}}{dE}\right)\end{aligned} \tag{4.9}$$

where t_1 is the energy of one of the two emitted electrons, E is the sum of the two emitted electrons kinetic energy, Q is the Q-value of the $2\nu\beta\beta$, C is the factor taking into account the nuclear matrix element and normalization constants [36, 37], F is the Coulomb correction [38] and $\frac{dI^{\text{Theo}}_{2\nu,\text{SM}}}{dE}$ and $\frac{dI^{\text{Theo}}_{2\nu,\text{LV}}}{dE}$ are the SM and LV terms of the decay amplitudes respectively.
The F function comes from the solution of the Dirac equation for an electron travelling in an extended nuclear charge, given by equation:

$$F(Z,t) = 2(1+\gamma)(2pR_0)^{2(\gamma-1)}e^{\pi\eta}\left|\frac{\Gamma(\gamma+i\eta)}{\Gamma(2\gamma+1)}\right| \tag{4.10}$$

where R_0 is the nuclear radius, $p = \sqrt{t^2 - m_e^2}$ is the electron momentum; $\gamma = \sqrt{1-(\alpha Z)^2}$, $\eta = \alpha Z/\beta$ and Γ is the Gamma function defined on the complex plane.
The integration of the two addends in equation 4.9 gives the prediction of the respective weight of the two decay modes in terms of $\mathring{a}^{(3)}_{\text{of}}$:

$$C \cdot \int_0^Q dE \int_0^E dt_1 \frac{dI^{\text{Theo}}_{2\nu,\text{SM}}}{dE} = C \cdot I^{\text{Theo}}_{2\nu,\text{SM}} \tag{4.11}$$

$$C \cdot 10 \cdot \mathring{a}^{(3)}_{\text{of}} \cdot \int_0^Q dE \int_0^E dt_1 \frac{dI^{\text{Theo}}_{2\nu,\text{LV}}}{dE} = C \cdot 10 \cdot \mathring{a}^{(3)}_{\text{of}} I^{\text{Theo}}_{2\nu,\text{LV}} \tag{4.12}$$

where $I^{\text{Theo}}_{2\nu,\text{SM}}$ and $I^{\text{Theo}}_{2\nu,\text{LV}}$ are the prediction for the standard and Lorentz violating $2\nu\beta\beta$ modes respectively. The left sides of eq.s 4.11,4.12 can be measured experimentally, evaluating the total decay amplitudes for the two $2\nu\beta\beta$ modes. To evaluate $\mathring{a}^{(3)}_{\text{of}}$, and therefore access the level of LV, it is necessary to compare the theoretical prediction for the decay amplitude to the measured ones. In particular, the ratio between 4.12 and 4.11 provides a viable pathway for the evaluation of this

coupling parameter. Defining $\Gamma^{\mathrm{Exp}}_{2\nu,\mathrm{SM}}$ and $\Gamma^{\mathrm{Exp}}_{2\nu,\mathrm{LV}}$ respectively as the standard and Lorentz violating $2\nu\beta\beta$ measured decay rates, $\mathring{a}^{(3)}_{\mathrm{of}}$ can be calculated from:

$$\mathring{a}^{(3)}_{\mathrm{of}} = \frac{1}{10}\frac{I^{\mathrm{Theo}}_{2\nu,\mathrm{SM}}}{I^{\mathrm{Theo}}_{2\nu,\mathrm{LV}}} \cdot \frac{\Gamma^{\mathrm{Exp}}_{2\nu,\mathrm{LV}}}{\Gamma^{\mathrm{Exp}}_{2\nu,\mathrm{SM}}} \tag{4.13}$$

where Γ^{Exp} can be measured from the experimental data and I^{Theo} have to be calculated from eq.4.9.
I calculated the integrals for SM and LV $2\nu\beta\beta$ with the numerical routine of MATLAB$^{\mathrm{TM}}$, implementing the Γ funtion with the Lanczos approximation at the eight order. The ratio of the two integral, needed in 4.13, has the value:

$$\frac{I^{\mathrm{Theo}}_{2\nu,\mathrm{SM}}}{10 \cdot I^{\mathrm{Theo}}_{2\nu,\mathrm{LV}}} = (213.3 \pm 0.7) \cdot 10^{-6}\ \mathrm{GeV} \tag{4.14}$$

where the error is due to the uncertainty on the Q-value of ^{82}Se $2\nu\beta\beta$. The uncertainty on the numerical integration have been evaluated performing the 2-dimensional integration both simultaneously and as a sequence of two one dimensional integration, the first in the t_1 axis and the second in the E one. The results are identical, therefore no systematic uncertainty on the calculation method has been included.

4.6.2 Experimental test of the effects on $2\nu\beta\beta$

The ratio $\Gamma^{\mathrm{Exp}}_{2\nu,\mathrm{LV}}/\Gamma^{\mathrm{Exp}}_{2\nu,\mathrm{SM}}$ can only be measured if the spectral shape of LV $2\nu\beta\beta$ can be distinguished by the one of the SM process. Since the background model reconstruction uses the spectral features to weight the different components of the model, it is the correct tool to perform this study. By adding the LV $2\nu\beta\beta$ spectrum to the total model it is possible to evaluate the probability of its integral, given the total shape of the spectrum. By comparing this value with the one from the SM $2\nu\beta\beta$, $\mathring{a}^{(3)}_{\mathrm{of}}$ can be accessed trough equation (4.13).
To include LV $2\nu\beta\beta$ its simulation has been performed, starting from equations (4.9) and (4.10). These simulations have been validated with a comparison to up to date calculation of $2\nu\beta\beta$ phase space factors [98], allowing their applicability to this analysis. In figure 4.30, the simulations of the two $2\nu\beta\beta$ modes of ^{82}Se are reported. These simulations take into account all the inefficiencies in the two electron collection, such as the detector geometry and the bremmstralhung emission. As shown by the LV/SM ratio, major differences are expected above 2 MeV. As shown in figure 4.29, in the 1.5-2.8 MeV energy range $2\nu\beta\beta$ dominates the background induced by β/γ interactions collected in a single crystal. The search for LV $2\nu\beta\beta$ is therefore expected to reach higher sensitivities in this energy range of the $\mathcal{M}_{1\beta/\gamma}$ spectrum.
The LV spectrum is included in the background model as an additional contribution, resulting in a model composed by 33+1 sources. Since both $2\nu\beta\beta$ modes produce most events in the $\mathcal{M}_{1\beta/\gamma}$, the background sources which are constrained by other spectra, or whose normalization is anchored to a peak in the experimental spectrum, are not affected by the introduction of Lorentz violating $2\nu\beta\beta$ in the model. As a direct consequence, the model has only a limited number of degrees of freedom to accomodate LV $2\nu\beta\beta$. In particular, the unaffected sources are:

- both bulk and surface α sources localized in the ZnSe crystals and in the reflective foil, since their normalization is constrained by the $\mathcal{M}_{1\beta/\gamma}$ spectrum;
- γ sources whose normalization is determined by the intensity of the experimental peaks;
- muons, since they are normalized on the higher multiplicity spectra.

The affected components are 10 components of the model producing a continuum in the 1500-2000 keV energy range:

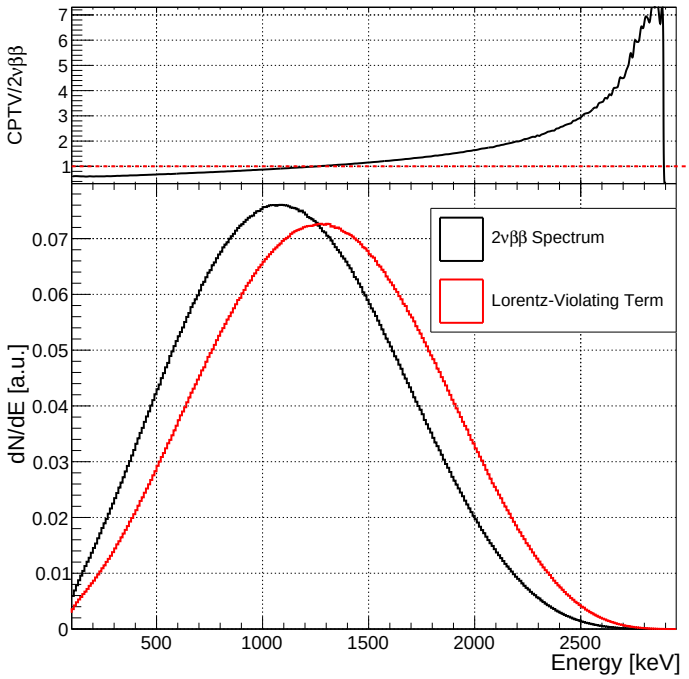

Figure 4.30: Simulation of standard (black) and Lorentz-Violating $2\nu\beta\beta$ (red) spectra for ^{82}Se, performed in the geometry of CUPID-0. The simulation is based on equation espressing the $2\nu\beta\beta$ space phase in function of the spectral index [98]. The emitted electrons are propagated in the detector geometry and the bremsstrahlung emission is also implemented. The spectra are normalized to the same integral. In the upper panel the ratio of the two spectra is reported as a function of the energy.

- ^{40}K in CryoInt and ExtPb;
- ^{60}Co in CryoInt and CryoExt;
- ^{232}Th and ^{238}U in CryoInt, CryoExt and IntPb.

^{232}Th and ^{238}U will be always treated together, since their spectra are quite similar in the region of interest for the LV search.
The LV $2\nu\beta\beta$ is inserted in the model with a non-negative uniform prior. The process is therefore considered as an alternative decay mode for the $2\nu\beta\beta$. As a consequence, $\mathring{a}_{\rm of}^{(3)}$ can be considered as a measurement of the branching ratio of this peculiar mode.
The fit is performed starting with the same assumptions of the background model analysis. The result obtained with these condition will be referred to as *reference fit*. After the sampling of the 33+1 parameters joint posterior pdf, the individual posteriors are obtained with marginalization. In figure 4.31 the marginal posterior for standard and LV $2\nu\beta\beta$ are reported, alongside the correlation between the two normalization parameters. The two contribution are anticorrelated, as expected given the similarity of their shape: the more is SM $2\nu\beta\beta$ likely, the less is LV $2\nu\beta\beta$ and vice-versa. Such anticorrelation results in the deformation of the standard $2\nu\beta\beta$ posterior, due to the limit imposed by the prior to the fluctuation of the LV $2\nu\beta\beta$. Even with such deformation, the reconstructed value of the SM $2\nu\beta\beta$ rate is $(9.8\pm0.1)\cdot10^{-4}$ Bq/kg, while in the background model is $(9.96\pm0.03)\cdot10^{-4}$ Bq/kg (see table 4.2). The stability of SM $2\nu\beta\beta$ rate reconstruction proves the stability of the model, and as a matter of fact excludes the measurement of LV $2\nu\beta\beta$.
As it appears from the posterior shape, the fit cannot give a significant value to the integral of LV $2\nu\beta\beta$, therefore only a limit can be extracted. To extract a limit on $\mathring{a}_{\rm of}^{(3)}$, the $\Gamma^{\rm Exp}_{2\nu,{\rm LV}}/\Gamma^{\rm Exp}_{2\nu,{\rm SM}}$ ratio (see Eq.s 4.11,4.12,4.13) is computed for each sampling of the joint posterior pdf, obtaining its corresponding posterior probability density function, $\mathcal{R}$. The distribution for $\mathring{a}_{\rm of}^{(3)}$ is then calculated

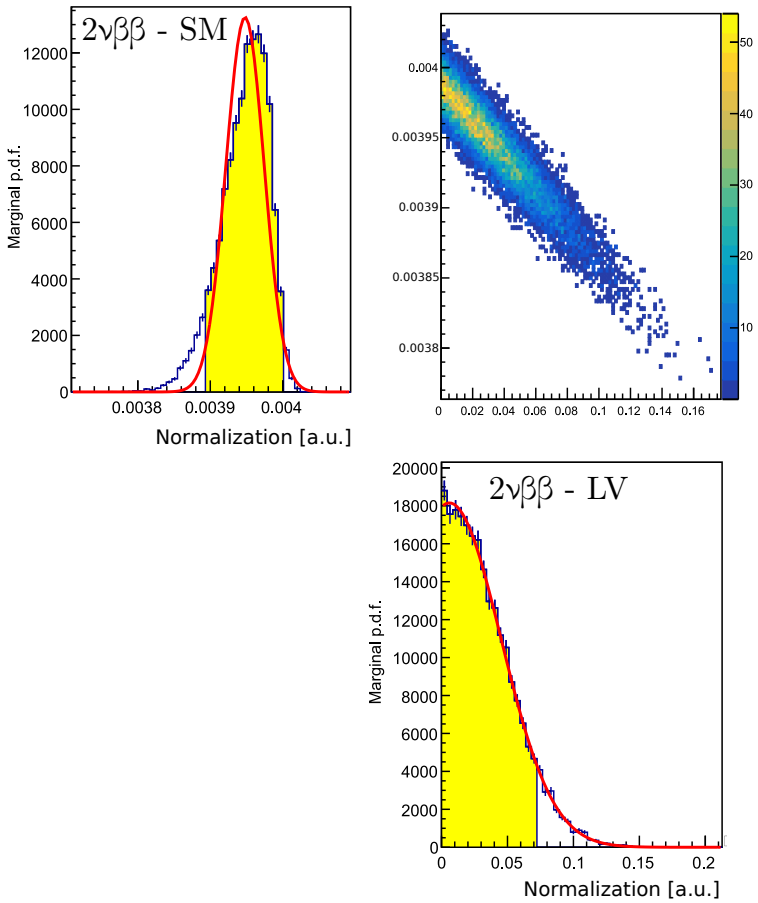

Figure 4.31: Marginal posteriors for standard and Lorentz-Violating $2\nu\beta\beta$ normalization parameters. On the upper right corner, the corresponding correlation is reported. The two contribution are totally anticorrelated, as expected given the similarity of their shape. Such anticorrelation results in the deformation of the standard $2\nu\beta\beta$ posterior, due to the limit imposed by the prior to the fluctuation of the LV $2\nu\beta\beta$.

combining $\mathcal{R}$ with the theoretical value for the reciprocal weight of the two decay modes reported in equation (4.14). A Gaussian distribution for $I^{\text{Theo}}_{2\nu,\text{SM}}/(10 \cdot I^{\text{Theo}}_{2\nu,\text{LV}})$ is built, to fold the uncertainty on this ration into $\mathcal{R}$. The obtained distribution is the posterior pdf for $\mathring{a}^{(3)}_{\text{of}}$, from which a 90% Credible Interval (C.I.) limit can be obtained.

4.6.3 Systematic tests on the fit

This posterior pdf is affected by the correlation with the nuisance parameters of this analysis, i.e. the other normalization coefficients and the influence variables.
The correlation with other model parameters is taken into account during the marginalization of the joint posterior distribution. As a consequence, the extracted limit takes into account all the possible shape similarities and the statistical fluctuations, both in data and in Monte Carlo.
The influence variables instead are arbitrary parameters used in the fit and have to be changed to determine their effect on the analysis result. The bin width used to build the spectra and the lower threshold applied to the data have been considered as influence variables. The following tests have been performed:

- **Bin:** bin values of 30 keV and 50 keV have been used to perform the fit;
- **Threshold:** thresholds of 200 keV, 300 keV and 500 keV have been used in different fits.

Alongside the influence variables, the hypothesis on the source location in the background model constitutes another possible origin for systematic uncertainties. In particular, the positioning of the most correlated source has to be analyzed. While ^{82}Se can only be in crystals, ^{40}K, ^{60}Co and ^{232}Th/^{238}U are more or less ubiquitously spread in the cryostat, therefore a study regarding their positioning has to be performed. In particular, these sources can be present both inside and outside the Roman lead shield, and ^{232}Th/^{238}U can also be localized in the Roman lead shield, providing further variability. During the performed tests, each source has been removed from one of the possible locations, resulting in two tests (internal or external) for ^{40}K and ^{60}Co and three tests for ^{232}Th/^{238}U (no internal, no external, no Roman lead).
An additional influence on the limit also comes from the presence of an unidentified contamination of pure β-emitters. In particular, from the β-decaying isotopes with negligible γ emission, long half life (>100 d) and high Q_{value}. An isotope with this characteristic gives a long lasting contamination to the detector, given the high half life, and provides signals in the energy region of interest for the search of LV $2\nu\beta\beta$. The shape of β spectra, in additions, mimics the shape of $2\nu\beta\beta$ efficiently, and the absence of γ signal makes it impossible for the data to constraint their contamination. Fortunately, the only isotope simultaneously meeting these requirements is the ^{90}Sr, a fission product originating the β decay sequence $^{90}\text{Sr} \rightarrow {}^{90}\text{Y} \rightarrow {}^{90}\text{Zr}$, with Q_{value} of 546 keV and 2281 keV respectively. The first decay has an half-life of 28.79 y, providing long lasting contamination, while the second, characterized by an half-life of 64 h, reaches secular equilibrium with its progenitor and provides events with energy up to 2.2 MeV. To evaluate the effects of this possible contamination, a test has been performed including a ^{90}Sr contamination in the list of sources.
As reported in [93], the energy calibration is affected by bias evaluated over all the interest energies thanks to the ^{56}Co calibration. To control the effects of this bias on the current analysis, an evaluation of the obtained limit is performed using the corrected energy scale.
For each test the $\mathring{a}^{(3)}_{\text{of}}$ posterior is obtained, containing all the effects on the parameters of interest. To combine the different test, a Bayesian approach has been chosen. Considering an ensemble $\{B_i : i = 1, \ldots, N\}$ of disjoint events (B_i) whose union is the total sample space, for any event A in the same space:

$$P(A|I) = \sum_{i=1}^{N} P(A \cap B_i|I) = \sum_{i=1}^{N} P(A|B_i, I)P(B_i|I) \tag{4.15}$$

where $P(A|I)$ is the probability of event A to happen, given a certain set of hypotheses I on which the sample space is defined. Equation (4.15) represents the total probability of an event given the possible configurations of the sample space, defined by a set of given information. In our case the event A is the $\mathring{a}^{(3)}_{\text{of}}$ parameter, and the sample space is composed of all the possible fit with different hypotheses: the thresholds, the binnings, the source location and so on. Each B_i is therefore a result of the fit, characterized by a given prior probability $(P(B_i|I))$ and resulting in a particular posterior distribution for $\mathring{a}^{(3)}_{\text{of}}$ $(P(A|B_i, I))$. The final results on $\mathring{a}^{(3)}_{\text{of}}$ has therefore to be extracted from the total posterior, $P(A|I)$, obtained by summing the different posterior distributions, multiplied by a given prior. To ease the application, it is useful to rewrite equation (4.15) as:

$$P(\mathring{a}^{(3)}_{\text{of}}|I) = \sum_{i=1}^{N_{test}} P(\mathring{a}^{(3)}_{\text{of}}|\text{Test}_i, I)P(\text{Test}_i|I) \tag{4.16}$$

where I represents all the information to the model that are not modified by the tests, such as the data and the total list of sources.
The sum in 4.16 is theoretically normalized by the assumption that the B_i/Test_i are disjoint events representing the total sample space, which needs to be finite or, at least, countable infinite. In this practical case the space is assumed finite, because otherwise a total coverage would be impossible. Unfortunately, in each test family, especially the binning and the threshold, the different test are strictly correlated one another. As a consequence, considering all the different results inside a single test family as equivalent independent results produces a bias to the systematic evaluation.

For example, repeating tests with a great number of different thresholds similar one another does not add information to the total probability, but makes negligible the contribution coming from other test families where the same number of test cannot be performed, such as the different source location. To avoid this outcome, the sum is firstly performed grouping the results obtained by a single test family, using these family results as addends in equation 4.16. Since no prior argument exist to favor a test condition among the others, an identical prior for each test is chosen. Firstly, the fit result of different tests in each family are added, dividing for the number of performed tests. Then the total probability for $\mathring{a}_{\mathrm{of}}^{(3)}$ is obtained summing the posteriors obtained in each family, dividing for the number of families, thus maintaining the normalization. In figures 4.33,4.34,4.35 the posterior distribution for each systematic test family is reported. The most important differences from the reference fit, performed with the same assumptions of the reference background model, arise when changing the location of ^{232}Th/^{238}U and when introducing the ^{90}Sr in the model. Increasing the threshold, on the other hand, produces a narrowing of the posterior, because it excludes the regions where the $2\nu\beta\beta$ becomes compatible with the other backgrounds. It has to be highlighted that the comparison wit the reference fit is only performed for graphical purpose. As previously stated, there is no privileged model, and the final consideration have to be made only on the total posterior probability distribution. In Tab. 4.4, the 90% CI limits on $\mathring{a}_{\mathrm{of}}^{(3)}$ obtained with each test family and the total result are reported.

Variable	Result [10^{-6} GeV]
Influence variables	
binning	<3.7
threshold	<3.5
Different Models	
^{40}K	<4.0
^{60}Co	<3.6
^{232}Th and ^{238}U	<4.2
^{90}Sr	<5.8
Energy scale uncertainty	<4.1
Total	<4.1

Table 4.4: Results of different tests performed to evaluate the systematics effects on the $\mathring{a}_{\mathrm{of}}^{(3)}$ limit. For each row, different values have been tested and combined adding the relative posterior distribution. The total result is obtained as a limit on the sum of all the family posteriors with equal weight.

In the left panel of figure 4.32, the total posterior of $\mathring{a}_{\mathrm{of}}^{(3)}$ is reported. The final limit has the value of $\mathring{a}_{\mathrm{of}}^{(3)} < 4.1 \cdot 10^{-6}$ GeV [99]. This value takes into account the statistical uncertainties, the correlation between different model parameters and the systematics effect due to the arbitrary choices made in the definition of the background model. The reconstruction of the experimental spectrum obtained with the model including LV $2\nu\beta\beta$ is shown in right panel of figure 4.32. The agreement is good over all energies, expecially around the peaks, where the model exploits the relevant spectral features to fix its reconstruction. The distribution of residuals has average compatible with zero, and σ compatible with one, further proving the goodness of this reconstruction.
This result establishes a new bound for $\mathring{a}_{\mathrm{of}}^{(3)}$, obtained for the first time with the shape analysis of the $2\nu\beta\beta$ spectrum measured with a scintillating bolometer. The obtained value is competitive with the results reported in literature from EXO-200 collaboration ($\mathring{a}_{\mathrm{of}}^{(3)} < 7.6 \cdot 10^{-6}$ GeV) [37] and NEMO-3 collaboration ($\mathring{a}_{\mathrm{of}}^{(3)} < 3.5 \cdot 10^{-7}$ GeV) [44], proving the excellent performances of scintillating bolometers.

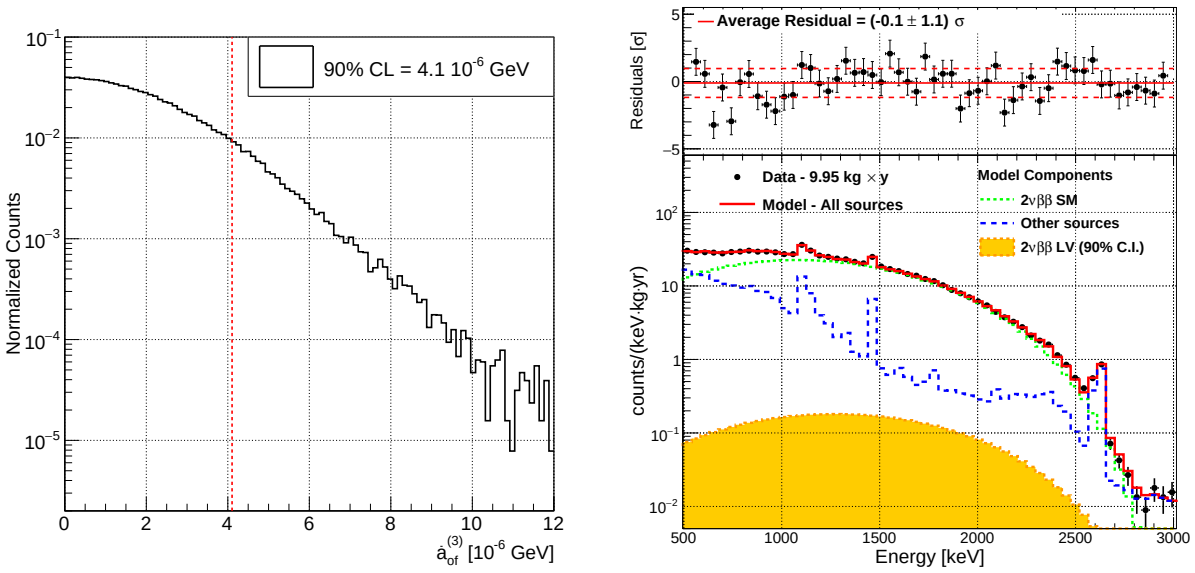

Figure 4.32: Left panel: total posterior distribution for $\mathring{a}^{(3)}_{\rm of}$. The dashed line represents the 90% credible interval, corresponding to $\mathring{a}^{(3)}_{\rm of} < 4.1 \cdot 10^{-6}$ GeV. Right panel: CUPID-0 $\mathcal{M}_{1\beta/\gamma}$ (9.95 kg × yr of ZnSe exposure) (black dots). The red line shows the reconstruction performed with the fit including the LV $2\nu\beta\beta$. The green dashed line is the reconstruction of the standard $2\nu\beta\beta$, while the orange spectrum is the 90% CI limit for the Lorentz violating component. The blue dashed line is the sum of all the other 32 background contributions. In the upper panel, the residuals are reported as a function of the energy. The agreement is good over all energies, expecially around the peaks, where the model exploits the relevant spectral features to fix its reconstruction.

4.7 Conclusion and outlook

CUPID-0 phase I took data from June 2017 to December 2018, collecting an exposure of 9.95 kg × yr of ZnSe. The analysis of these data proved that the technique of scintillating bolometers is a viable pathway for the investigation of rare events.

The possibility to identify α interactions and to tag delayed α/β decays [84] allowed to obtain the lowest background ever measured in a bolometric experiment searching for $0\nu\beta\beta$: $(3.5^{1.0}_{-0.9} \times 10^{-3}$counts/(keV kg yr)[93]. This unprecedented result allowed to put the best known limit to the half life of $0\nu\beta\beta$ for ^{82}Se: $T^{0nu}_{1/2} > 3.5 \times 10^{24}$y. The final median sensitivity associated to this experiment is $T^{0\nu}_{1/2}$>5.0×10^{24} y [93].

The low background measured has then been attributed to different sources with a detailed background model [39]. This analysis allowed the full reconstruction of the measured spectrum and has been made possible thanks to the aforementioned background identification capabilities. The identification of the main background sources driven the design of a second data-taking phase, characterized by the implementation of techniques directed towards the reduction of background. In particular, the installation of a new clean shield close to the detector and the installation of a muon veto are foreseen to accomplish this goal.

The full comprehension of the measured data paved the way to the detailed study of the $2\nu\beta\beta$, since the total spectral shape can be deconvoluted from the other background components. This result allowed to put a limit of the Lorentz symmetry violation in neutrino sector. The anisotropic coupling to the LV countershaded operator [36] has been constrained to $\mathring{a}^{(3)}_{\rm of} < 4.1 \cdot 10^{-6}$ GeV. This result establishes a bound for $\mathring{a}^{(3)}_{\rm of}$, obtained for the first time with the shape analysis of the $2\nu\beta\beta$ spectrum measured with a scintillating bolometer. Even with its limited exposure, CUPID-0 scintillating bolometers allowed to reach a limit competitive with previously published ones by EXO-200 collaboration ($\mathring{a}^{(3)}_{\rm of} < 7.6 \cdot 10^{-6}$ GeV, with an exposure of 100 kg·yr) [37] and NEMO-3

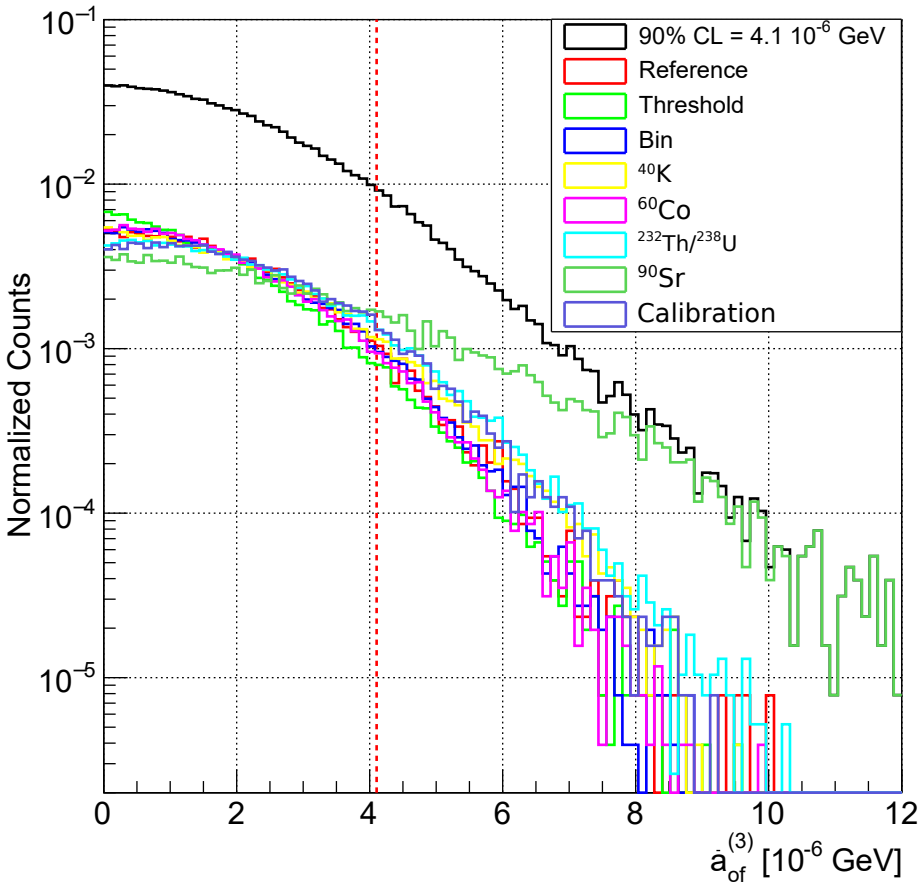

Figure 4.33: Posterior distribution for each systematic test family. The total posterior (black) is shown with the posterior of each family reported as addends (cfr equation (4.16)). The *Reference* word indicate the fit performed with the same assumptions as the background model.

collaboration ($\mathring{a}^{(3)}_{\rm of} < 3.5 \cdot 10^{-7}$ GeV, with 34.4 kg·yr) [44]. This result proves that scintillating bolometers can perform spectral shape studies with high sensitivity, even when using a limited statistics.

In addition, other analysis are foreseen with the same methodology (detailed $2\nu\beta\beta$ half life and matrix element evaluation, $2\nu\beta\beta$ with Majoron emission), for which major improvement with respect to current results are expected.

The outstanding results obtained with CUPID-0 are a viable proof of the potentiality of scintillating bolometers applied to the search of $0\nu\beta\beta$. The actual major limit to greater improvements for this technique are the radiopurity and quality of crystals and the limited exposure attainable. As a consequence, the development of high exposure detectors based on this technique can provide tools to overcome current detectability limits [20]. In addition, this approach can be used to study the $0\nu\beta\beta$ and $2\nu\beta\beta$ for different decaying isotopes. Changing the studied crystals, in fact, allows to perform the same analysis on different isotopes, with comparable sensitivities.

The design of CUPID [70] is aimed to scale-up the scintillating bolometer technique to the tonne scale, by running ~1000 Li_2MoO_4 crystals in a CUORE-like setup built according to the CUPID-0 design. This detector is the main candidate to the investigation of the inverted hierarchy region, and is now ongoing a tough R&D phase. The results of CUPID-0 have undoubtedly paved the way to this development, showing that this technique can, if properly exploited, provide excellent results.

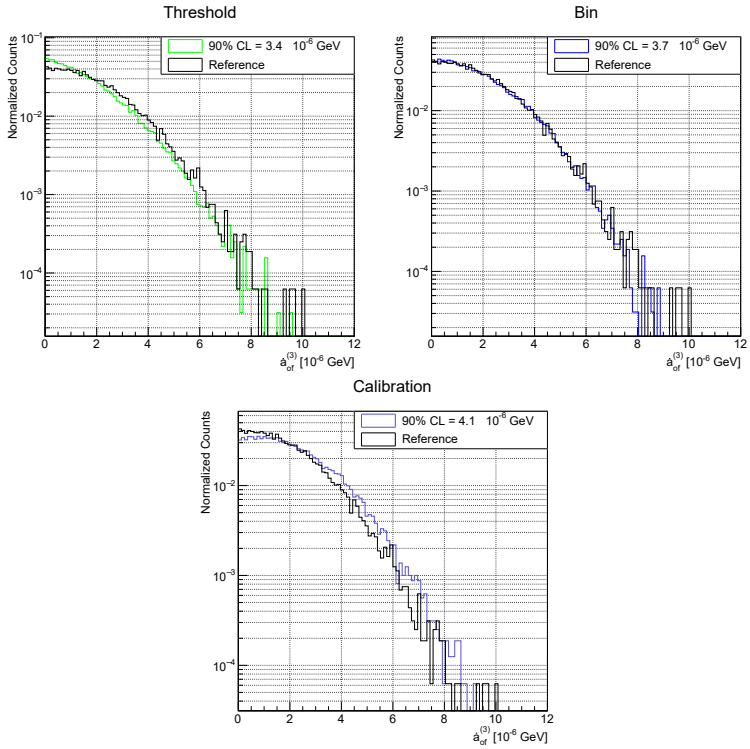

Figure 4.34: Posterior distribution for Bin, Threshold and Calibration systematics. Each posterior is shown superimposed to the *Reference* model (black), indicating the fit performed with the same assumptions as the background model.

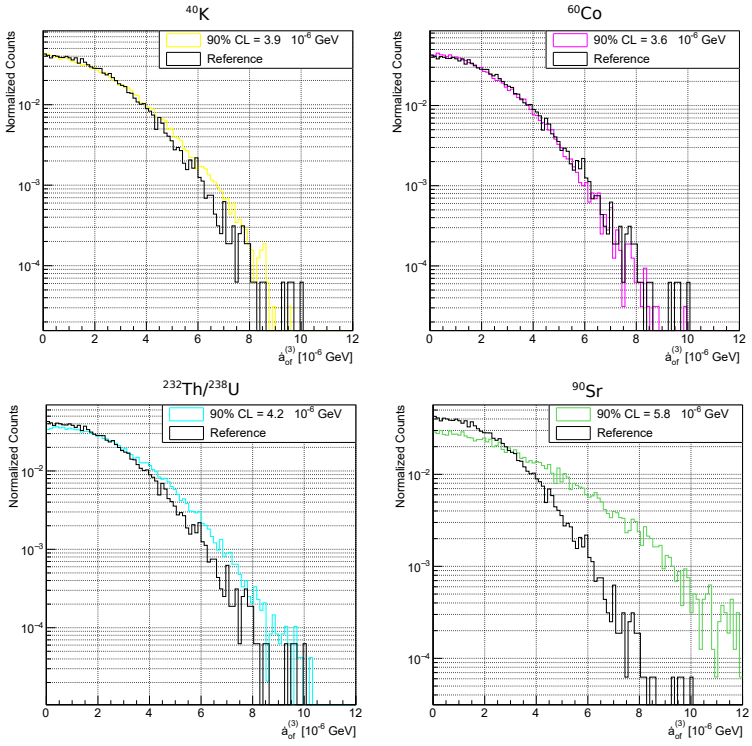

Figure 4.35: Posterior distribution for ^{40}K, ^{60}Co, ^{232}Th,^{238}U, ^{90}Sr systematics. Each posterior is shown superimposed to the *Reference* model (black), indicating the fit performed with the same assumptions as the background model.

Chapter 5

Development of innovative scintillators

The search for $0\nu\beta\beta$ demands detector with high performances in terms of background rejection and energy resolution. The scintillation detectors are viable instruments to deal with both these aspects, although optimization is needed to increase their energy resolution.
This parameter is limited by the statistical fluctuation of detected photons and by the electronic noise introduced by the readout chain. In addition, the non-ideal behavior of parts of the readout chain, from the crystal to the readout electronics, can spoil the performances of the whole detector, needing an accurate investigation. To design a $0\nu\beta\beta$ search grade scintillator, therefore, both a performing light detector and an efficient scintillators are needed. A careful optimization of the total system is then necessary, to harmonize the features of the different components. Two approaches have been investigated in my work, focused on two different key aspects.
The FLARES project (Flexible scintillation Light Apparatus for Rare Events Searches) proposed the definition of a scintillation detector coupling standard scintillating crystals with innovative light detectors, characterized by low electronic noise and high quantum efficiency. On the other hand, the ESQUIRE project (Experiment with Scintillating QUantum dots for Ionizing Radiation Events) proposes the development of nanocrystal based scintillators, characterized by high light emissions in fast times.
In the following sections, the R&D program of the two project will be presented and discussed, showing the work performed in the optimization and first testing of the two detector concepts. The limitations of current designs will also be described and possible solutions for next developments will be presented.

5.1 The FLARES strategy

The FLARES project proposes a new approach to build $0\nu\beta\beta$ detectors, based on the use of inorganic scintillators ([58]).
This choice provides interesting advantages for $0\nu\beta\beta$ search:

- flexibility in the choice of $0\nu\beta\beta$ decaying isotope (different candidates can be grown as inorganic scintillation crystals);
- easy mass scalability (huge array of scintillators are easy to build and maintain);
- different tools for background reduction (pulse shape discrimination, α particle quenching factor ~ 0.2 and high radiopurity of crystals).

Unfortunately, scintillation detectors suffer from poor energy resolution; as a consequence their application in the field of $0\nu\beta\beta$ research is strongly limited (see chapter 3).
This lack of performance is due to the low efficiency of light collection and detection, mostly due to the usage of photomultiplier tubes (PMTs) to read the scintillation light. PMTs convert

scintillation photons into electrons using an alkaline photocatode, characterized by the quantum efficiency (ϵ_Q), defined as the percentage of incident photons converted into electrons. Usually the quantum efficiency of PMTs varies between 20% and 40%, causing the performance of the scintillator to fall sharply. This happens because the relative full width at half maximum energy resolution (FWHM%) scales as

$$\text{FWHM\%} = \sqrt{\frac{1}{N_{ph}\epsilon_Q\alpha_{ph}} + \frac{ENC_e^2}{(N_{ph}\epsilon_Q\alpha_{ph})^2} + R_{\text{Int}}^2} \tag{5.1}$$

where $N_{ph}\epsilon_Q\alpha_{ph}$ is the number of scintillation photons collected by the photodetector (α_{ph} is the collection efficiency), ENC_e is the RMS electronic noise converted into electrons and R_{Int} is the contribution of non-ideal behavior to the resolution.
The goal of FLARES is to demonstrate that it is possible to achieve a FWHM energy resolution of $\sim 1\% - 2\%$ at the 2615 keV line with a scintillation detector. If this condition is met, the background due to $2\nu\beta\beta$ events superimposed to $0\nu\beta\beta$ ones is negligible (see figure 3.4 at page 27). To reach this result, FLARES proposes the usage of silicon drift detectors (SDDs) to read the scintillation light emitted by large inorganic crystals.
The high quantum efficiency in a large bandwith and the low electronic noise of the SDDs make them extremely performing detectors for X-ray and scintillation spectroscopy [100]. In addition, the anode capacitance does not depend on the area of the device, thus allowing the dimensional scaling of the single SDD cell [101].
So far, different tests have already been performed with different crystals, such as CsI(Tl) [102] and LaBr3 [103], obtaining good results in terms of energy resolution. Moreover, it has been shown that an SDDs matrix, built by small SDD detectors operated simultaneously, can handle efficiently the readout of large scintillating crystals [104]. Therefore, the application of SDDs seems the proper way to get the scintillators performant enough for $0\nu\beta\beta$ search.
In addition, the FLARES strategy proposes to operate the whole detector at 120 K. As shown in the next sections, in fact, at this temperature both the crystals and the SDD increase their performances.
In the following sections the different features of the FLARES strategy will be presented, outlying the research and development work necessary to demonstrate the feasibility of the proposed technique.

5.1.1 Isotope choice and scintillating crystal properties

The choice of the $0\nu\beta\beta$ candidate for FLARES has to be focused on the elements that can be included in scintillation crystals. Moreover, these crystals should have suitable scintillation characteristics, such as a high light yield. This constraints lead to the selection of 3 candidates: ^{48}Ca, ^{100}Mo and ^{116}Cd. These isotopes can be grown in different crystals suitable for a scintillator, as reported in table 5.1. Between these possible candidates, ^{48}Ca is the less appealing, since it has lower isotopic abundance compared to the other isotopes.

Isotope	$T_{1/2}^{0\nu}$ (10meV) $[10^{27}y]$	$Q_{\beta\beta}[keV]$	Isotopic abundance [%]	Available scintillators
^{48}Ca	7-100	4274	0.2	CaF_2, $CaWO_4$, $CaMoO_4$
^{100}Mo	1-9	3034	9.6	$CaMoO_4$, $ZnMoO_4$
^{116}Cd	3-10	2814	7.5	$CdWO_4$, $CdMoO_4$

Table 5.1: Selection of the most suitable $0\nu\beta\beta$ candidates contained in available scintillation crystals([58]).

For these reasons, ^{100}Mo or ^{116}Cd have been selected as the best choices for FLARES experiments. Two different crystals containing these isotopes have been selected: $CaMoO_4$ and $CdWO_4$, whose known properties are listed in table 5.2. Both $CaMoO_4$ and $CdWO_4$ show a light yield increase

when operated at temperatures of about 120 K. From equation (5.1) follows that cooling the crystals improves the energy resolution thus enhancing their performances. The FLARES detector will therefore be operated around 120 K, to enhance the attainable performances. Such temperatures are easy to obtain on large masses of detectors, even with standard technical solution. Consequently, this constraint does not limit the mass scalability of this detector design.

Property	$CaMoO_4$		$CdWO_4$	
	300K	120K	300K	120K
Atomic mass [g/mol]	200		360	
Density [g/cm^3]	∼4.3		7.9	
Emission Maximum λ_{max}[nm]	520	∼530	480	480
Light yield [ph/MeV]	∼8900	∼25000	∼18500	∼33500
Scintillation Decay Time [μs]	∼18	∼190	∼13	∼22
Refractive Index	1.98		2.2-2.3	
Absorption Lenght [cm]	∼60		∼60	

Table 5.2: Properties of $CaMoO_4$ and $CdWO_4$ scintillation crystals. The values come from [58].

The data in table 5.2 show that $CdWO_4$ is the most performing scintillator, since it has higher light yield, higher atomic mass and faster scintillation decay time[1]. On the other hand, $CaMoO_4$ contains ^{100}Mo, which is the most interesting $0\nu\beta\beta$ candidate with higher Q-value, shorter $T^{0\nu}_{1/2}$ and higher isotopic abundance (see table 5.1). Since $CdWO_4$ is the most performing scintillator, it has been chosen as the subject for the optimization of the setup and the study of the first detector prototype.
The crystal has to be optimized in order to minimize the attainable energy resolution. Two main aspects have been investigated: the increase in photon collection efficiency and the intrinsic resolution of crystals.

Crystal wrapping to increase photon collection

The number of photons collected by the photodetector is reduced by the photon losses at the surfaces of the crystal. A scintillation photon produced inside the crystal undergoes rifraction once arrived to the surface. It can than be totally reflected back, if the incident angle is below the critical angle, or transmitted outside. The incident angle depends on the interaction position of the scintillation photon on the surface, since the crystal surfaces always presents a texture. Such characteristics is usually referred to as *roughness* of the surface, bigger when the surface is more irregular. If the roughness of the crystal is small, its surfaces has mirror-like appearance and are referred to as optical or smooth surfaces. On the other hand, if the roughness is high, the crystal surfaces tend to diffuse the light instead of reflecting it, thus being referred to as rough surfaces.
Different roughness on different faces cause the number of extracted photons to vary, therefore different value have to be tested to determine the surface texture giving the best resolution. In addition, a reflective material can be put around the crystal faces not directly coupled to the photon detector. This material, referred to as *wrapping*, is used to reflect back inside the crystal the outgoing photons. Different materials have different effects, and the best solution for a given crystal has to be searched with dedicated measurement. Different materials, in fact, have a wavelength-dependent reflectivity, meaning that the wrapping has to be tuned for each crystal emission.
To choose the best surface texture and the best wrapping, several measurements have been performed, coupling different $CdWO_4$ crystals, with different wrappings, to a PMT. The target variable is the FWHM energy resolution at the 511 keV line, measured from the emission of a ^{22}Na source placed nearby the crystal. The crystal is coupled to the PMT by the means of an optical grease,

[1] As a consequence, in literature can be found articles related to the application of $CdWO_4$ for scintillation detectors [105], while there is no known application of $CaMoO_4$ crystals in this field.

the BC-630, produced by Saint Gobain. This material has a refractive index of ∼1.5 at different wavelengths, providing a good match between the ∼2.5 refractive index of $CdWO_4$ and the air. The effect of this grease is to reduce the difference in refractive index, and thus reducing the probability of total reflection of photons inside the crystal. The critical angle, in fact, changes from ∼23° in case of $CdWO_4$-air surface to ∼36° in case of $CdWO_4$-grease surface, meaning a substantial reduction of total reflection. Alongside the refractive index matching, the grease act as a glue, ensuring a full adhesion of the crystal to the PMT entrance window.
The different measurements have been performed with 3x3x3 cm^3 crystals with the following surface textures:

- all 6 faces equally rough;
- all the 6 faces equally optical;
- 4 faces rough and 2 faces optical, coupled by to the PMT by the means of an optical face.

For each of them the following wrappings have been used:

- aluminum foil;
- white teflon tape;
- VM2000 reflective foil by 3M.

The results of the different measurements are reported in figure 5.1.
In between the different textures, the 4 rough + 2 smooth surface one is the best, even without wrapping. This happens because the smooth face coupled to the PMT ensures good coupling and the other smooth face, opposite to the PMT, act as mirrors reflecting the backward directed photons towards the PMT. The side rough faces, instead, diffuse the outgoing light, increasing the probability to redirect photons to the PMT. On the other hand, the full-smooth and full-rough crystals share only one side of these benefits, resulting on average worse in terms of resolution.
With respect to the wrappings, the VM2000 presents mechanical problems when used to cover the faces of the used cubic crystals. Being a rigid sheet, in fact, VM2000 is difficult to be shaped to be fully adherent to the crystal faces. As a consequence, the wrapping quality depends on the manuality of the operator and is non-replicable. In addition, the VM2000 act as a perfect reflector, meaning that it does not randomize the reflected photon direction. As a consequence, not all its possible test have been performed, and the VM2000 has not been chosen as the definitive wrapping.
The alluminum foil proved to be an effective wrapping material, although not the best over all and still affected by an imperfect adherence to the faces of the crystal.
The best material tested is the white teflon tape. The use of multiple layers ensures a good reflectivity, and the softness of this material ensures easiness of application on all the possible geometries. Teflon tape, in addition, diffuse light, randomizing the path of photons after each reflection. Such step effectively increases the probability of redirecting a side-escaping photon towards the photodetector, thus ensuring an actual increase in the number of collected photons.
Given the presented results, the 4 rough+2 smooth crystal with 5 layers of teflon wrapping is the best configuration to increase the resolution. In the following tests, where not differently specified, the crystal used will follow this rule.

Control of the light emission non proportionality

A remarkable aspect outlined by different studies [106] is that the light yield of a crystal calculated with β/γ energy depositions is not constant as the deposited energy increases. This characteristic, referred to as *non-proportionality*, prevents the correct reconstruction of the absorbed energy, affecting the energy calibration. In addition, the light yield dependency on energy increases the so-called intrinsic contribution to the FWHM energy resolution. A single ionizing particle, in fact, usually

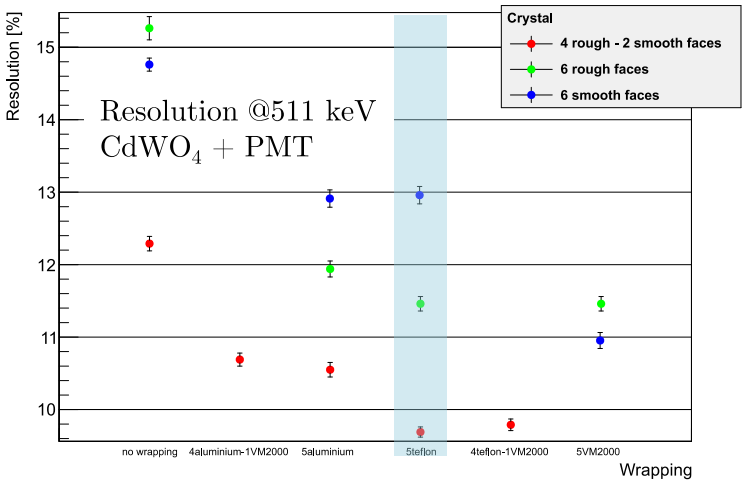

Figure 5.1: Effect on different wrapping and surface texture on scintillator resolution. The different surface textures (different colours) are used with the different wrappings to find the combination giving the best resolution. The only type of reflector not used on all the possible crystals is the VM2000 foil. Being difficult to correctly fit onto crystals, its configuration cannot be reproduced and therefore it has been discarded as a possible wrapping material. In addition, its fully reflective behavior tends to worsen than increase the attainable energy resolution, depending on the considered texture. The material over all giving best reproducibility and resolution is the teflon tape, in particular if applied to the 4 rough + 2 smooth crystal.

produces many energy depositions, each of which differently affected by the *non-proportionality*. The final effect of this feature is therefore that particle with the same energy produce scintillation events with different average number of photons, resulting in scintillation spectra with anomalously broad peaks. Since it appears as a limiting factor in the resolution on many scintillation-based detectors [106, 107, 108], a detailed study is demanded to quantify its effect on the crystal chosen for the FLARES project.

In order to characterize the crystal independently from the detector, the light yield *non-proportionality* has been measured as a relative variation with respect to the light yield at the 662 keV γ line of ^{137}Cs, referred to as *relative light yield* (R_{LY}). As the excitation energy lowers, the R_{LY} increases for iodine crystals (NaI and CsI for example) and lowers for oxide crystals (LSO and BGO for example) [57]. Moreover the R_{LY} is bigger in crystals characterized by worst energy resolution [106]: as a consequence, the *non-proportionality* appears to be the fundamental limit to the attainable scintillators energy resolution.

The R_{LY} can be quantified measuring both the energy deposited inside the crystal and the corresponding light output. This can be accomplished using a method called *Compton Coincidence Technique* (CCT), proposed by [109], which exploits the Compton effect to create a monochromatic electron source inside the crystal bulk. This coincidence technique is implemented recording the events in the scintillator only when a Compton scattered photon is simultaneously detected by a second detector located at a fixed angle θ off from the axis formed by the gamma-ray source and the scintillation detector (see figure 5.2).

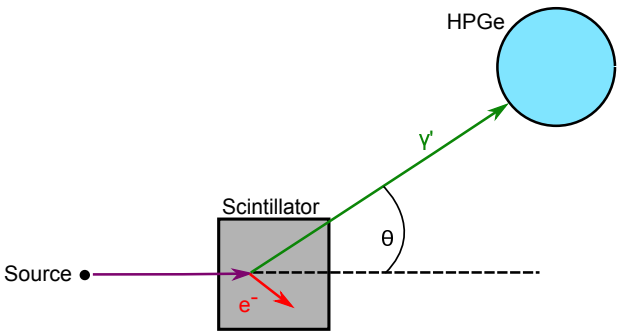

Figure 5.2: Scheme of the CCT experimental setup. Events in scintillator are recorded only when a Compton scattered photon (γ') is simultaneously detected by HPGe, located at a fixed angle θ off of the axis formed by the γ source and the scintillator (dashed line).

Controlling both θ and the source energy E_γ it is possible to fix the energy of the scattered γ ray E'_γ and the Compton electron energy E_{el}, as stated by the Compton equation:

$$E_{el} = E_\gamma - E'_\gamma = E_\gamma - \frac{E_\gamma}{1 + \frac{E_\gamma}{m_e c^2}(1 - cos\theta)} \tag{5.2}$$

An additional advantage of this technique is that E_{el} can be easily changed by varying θ and E_γ. In order to measure precisely E_{el}, E'_γ has to be known with high precision, therefore a high purity germanium detector (HPGe) was used for this purpose.
The scintillating crystal under study, a cubic $CdWO_4$ (3x3x3 cm^3), was coupled to a PMT and faced to a ^{22}Na radioactive source, emitting γs at 511 keV and 1274 keV. The HPGe signal is sent to an amplifier and timing single channel analyser (AMP-TISCA), providing a digital pulse when the maximum amplitude of the amplified signal falls in a window selected with the module controls. The digital signal is used as a trigger for the acquisition of both HPGe and PMT signals, therefore the signals are acquired when the selected energy is detected by the HPGe detector.
The original design of CCT [109, 110] comprehends the use of collimators between the crystal and the HPGe detector in order to precisely select the scattering angle of photons. During these measurements, the physical collimators have been replaced by a software tool, designed to select precise energy windows in the HPGe among those signals found in coincidence with the scintillator. Multiple measurements were then extracted from a single acquisition, optimizing the angular selection and fully exploiting the HPGe resolution. A collimator was instead used between the radioactive source and the crystal, to reduce the number of detected scintillation events.
Once selected the scintillator pulses in coincidence with the correct HPGe signals, the light yield can be calculated with the following equation:

$$LY(E_{el}) = \frac{k \cdot V_{scint}}{E_\gamma - E'_\gamma} = \frac{k \cdot V_{scint}}{E_{el}} \tag{5.3}$$

where V_{scint} is the mean value of the scintillation signal amplitude coincident with the HPGe signal at E'_γ energy and k is the calibration factor from Volts to photons. E'_γ has been evaluated as the weighted mean of the amplitude of the events in the selected energy window in the HPGe spectrum, while V_{scint} as been estimated with an unbinned likelihood fit of the peak in the coincident amplitude spectrum acquired by the scintillator, modelled with a Gaussian subtending a linear background.
This method allowed the measurement of E_{el} in the 15-700 keV range. Below 15 keV the electronic noise of the scintillator avoids the measurement, while above 700 keV the HPGe background covers the few Compton scattered photons at high angles.
The R_{LY} is then quantified with the following expression:

$$R_{LY} = \frac{LY(E_{el})}{LY(662\ \text{keV})} = \frac{k \cdot V_{scint}(E_{el})}{k \cdot V_{scint}(662\ \text{keV})} \frac{662\ keV}{E_{el}} \tag{5.4}$$

As reported in [106], the shaping time (ST) used to process the light signals can affect the slope of the R_{LY} curve. A digital pulse processing algorithm (DPP) has then been applied to the acquired preamplified scintillator pulses to evaluate this effect. The DPP allows to apply different shaping times to the same measurement, without the need of multiple measurements for every configuration. The used algorithm is a trapezoidal filter, whose implementation is described in [111]. Alongside to the DPP technique, the digitalized preamplified pulses were also integrated numerically, estimating the amplitude of the light pulse without selecting a defined bandwidth. This processing steps includes the majority of the scintillation components, being limited by the full chain bandwidth.
The R_{LY} with different STs for $CdWO_4$ is reported in figure 5.3. The obtained result shows that the ST used changes the R_{LY}, and therefore the *non-proportionality* of the scintillating crystals. In particular, longer shaping time correspond to negative non-proportionality values, while shorter shaping time to positively ones. The transition between negative and positive deviation is related

to the scintillation light emission time of the considered scintillator. For the $CdWO_4$, characterized by a scintillation time of $\sim$ 14 μs at room temperature, negative *non-proportionality* appears for ST>10 μs. Fully integrating the scintillation pulses, in particular, gives an overall reduction of the *non-proportionality*, also if applied to other scintillating crystals [112].
The observed correlation between *non-proportionality* and ST can be explained by a dependence with energy of the scintillation component: faster scintillation emission are predominant at lower energies, while higher energy events are characterized by longer scintillation times. The activation probability of scintillation centers should then vary with energy. On one hand, the deposition of small energies activates few sites characterized by a short decay time. On the other hand, an event with higher energy causes multiple activation, involving both short- and long-lived scintillation sites.
Summarizing, the *non-proportionality* in light yield of scintillating crystals depends on the integrated scintillation time components. As a direct consequence, the *non-proportionality* can be reduced by preserving all the frequency components of the scintillation signal. Integrating the whole scintillation signals therefore reduces this effect, since also the longest scintillation components are considered [112].

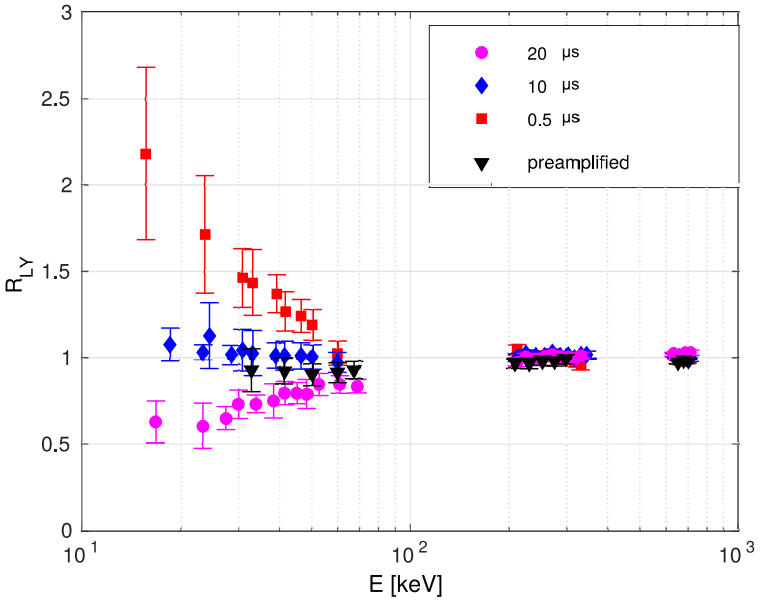

Figure 5.3: Measured non-proportionality behavior for a $CdWO_4$ crystal. The effect of the ST is evident, since it causes the non-proportionality to vary in a range between 0.5 and 2.5. As expected, integrating the preamplifier signal (Preamplified graph, black triangles) causes the crystal to loose its non-proportionality.

Given this result, in all FLARES tests the scintillation pulses detected will be processed with the integration of the whole waveform, to ensure a reduction of this contribution to the attainable energy resolution.

5.1.2 The SDD detectors

The SDD are solid state detectors with low anode capacitance ($\sim$fF). As a consequence, this detector is characterized by low electronic noise and is perfect to achieve high energy resolutions [100]. The SDD functioning is based on a decreasing field directing the electrons toward the collection anode. The typical structure of this detector is reported in figure 5.4. The drift field is created by the means of subsequent p+ electrodes implanted on one side of a n-type silicon wafer. The electrodes surround the anode, creating a concentric structure. Each electrode is biased with a decreasing high voltage, starting from a maximum value farther from the anode. The decrease is ruled by a voltage divider, built with resistances directly lithographed on the device. On the opposite side of the n-type wafer, an homogeneous p+ deposition is applied, used as ground reference electrode. To guarantee

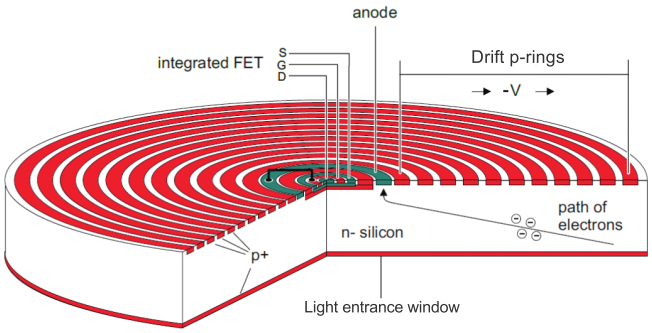

Figure 5.4: Schematical draw of SDD detector. An integrated voltage divider connects each drift ring with its neighbors and defines a linear voltage drop from the anode to the external drift ring. This SDD models present the integrated FET connected to the anode.

this reference, a wire needs to be bonded to the p+ homogeneous window, by fact preventing the possibility to couple this device to a scintillation crystal to detect the emitted photons. To avoid this limitation, a single-side polarization method for these devices has been developed, called *punch-trough polarization* [113]. This method is based on the reach-through effect, occurring when the voltage difference across two p-type electrodes, separated by a depleted n-type bulk, is high enough to create a large hole current between the two aforementioned electrodes. This mechanic is completely analogous to the polarization mechanism of pnp bipolar transistors, and provides a reliable strategy to polarize the SDDs. In this biasing scheme, the p+ window is left floating and voltage on the p+ ring is used to control the detector polarization.
In figure 5.5 a schematics of the process is reported. As the negative voltage on the outer p+ ring increases, the n bulk gets more depleted. The depletion region is deeper below the point with lower voltage and increases up to the natural depletion surrounding the p window. The bulk gets fully depleted when the negative voltage reaches the double depletion voltage of the p-n junction. In these conditions, the most negative p+ ring and the p window are facing a fully depleted region, where a hole current can flow. This current allows the collection of the holes created in the n bulk and favours the full bulk depletion below each p+ ring. The voltage of the p window is controlled by the negative voltage applied to the rings and thus the device is successfully polarized, assuring the drift field for the collection of electrons. The only drawback of this polarization mechanics is the generation of an hole current in the bulk, resulting in a small increase of electronic noise. Such increase is although small, therefore no major effects on noise are expected as a consequence of this operation scheme.

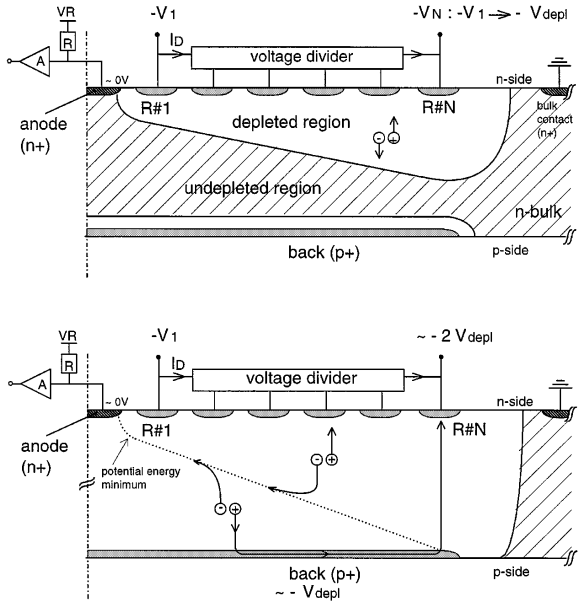

Figure 5.5: Scheme of the Punch-trough polarization mechanism. The drawings show a cross section (not to scale) of a cylindrical SDD with a homogeneous light-entrance window (single back electrode), from the anode (left) to the outer voltage ring (right). The upper panel represents the situation when the detector bulk starts to be depleted given the voltage decrease on the outer tension ring (R#N). In the lower panel the final working condition is reported, when the p window is connected to the voltage rings by the means of the reach-through hole current. The bulk is fully depleted, and the electron drift towards the anode can take place.

With the punch-trough mechanism, the SDDs can be polarized without the need for wires on the p window, that can be used as light entrance window. To obtain the net increase in photon collection, this window can be treated with anti-reflective coating, to maximize the photon collection efficiency. The anode signal from the SDD has to be collected by proper readout electronics, typically a charge sensitive preamplifier, in order to be recorded and analyzed. The front end electronics must be designed to maintain and enhance the qualities of the SDD, therefore it should be characterized by adequate bandwidth and low noise level. In particular the target variable to be minimized is the equivalent noise charge of the system, defined as the input charge signal equivalent to the measured noise. Given a system composed of a detector with a given capacitance C_d and a charge sensitive preamplifier with input capacitance of C_i and input series noise ($\langle e_w^2 \rangle$), followed by a shaping stage with time constant τ, the equivalent noise charge (ENC_e) is given by [114]:

$$ENC_e = (k_1 \frac{\langle e_w^2 \rangle}{\tau} + k_3 A_{1/f})(C_d + C_i + C_p)^2 + 2k_2 q I_l \tau \tag{5.5}$$

where C_p is the parasitic capacitance between the detector and the amplifying circuit, I_l is the leakage current both at the input of the gate of the FET preamplifier and of the solid state detector, q is the electron charge (1.6×10^{-19} C), and τ is the shaping time of the acquired signal. k_1, k_2 and k_3 are parameters dependent on the shaping used to filter the signal (Gaussian, triangular, trapezoidal, etc.). In first approximation they can be considered equal, to evaluate the dependence of the first readout stage.

Since ENC_e scales with the input capacitance of the preamplifier C_i, this element should be designed to be as small as possible, not to spoil the advantage given by the low anode capacitance of the SDD. Moreover, the link between the anode and the preamplifier must not introduce parasite capacitance in the system C_p, because this element would increase the noise level[2]. In addition, by operating the SDD at temperatures of about 120K both the series noise and the leakage current will be strongly reduced, thus reducing the total ENC_e. In particular, the leakage current should decrease exponentially, while the series noise of the preamplifier follows $\langle e_w^2 \rangle = 2k_B T\alpha/g_m$, where k_B is the Boltzmann constant, T is the operating temperature, g_m is the transconductance of the input JFET, and $\alpha = 0.7$ for an ideal JFET. As a consequence, I_l decreases faster than $\langle e_w^2 \rangle$. An optimal configuration therefore corresponds to low temperature operations ($\leq -40°$) to reduce I_l, and a long τ to suppress the effect of $\langle e_w^2 \rangle$.

To accomplish the low noise requests, the anode signal of FLARES SDDs is amplified by a C-MOS CUBE preamplifier [115]. The CUBE preamplifier acts as a pure integrator, therefore its output consists of step-like signals superimposed to a voltage ramp, with slope proportional to the leakage current of the detector. When the amplitude of the ramp saturates the available dynamic range, a reset is given to the system, discharging the feedback capacitor of the preamplifier (see fig. 5.6). The absence of a feedback resistor allows to avoid his leakage current noise, further reducing its effect on the equivalent noise charge. The step-like characteristics of signals allows to use long processing times, reducing the high frequency series noise of the system with a dedicated processing algorithm.

The outlined properties favors the SDD as candidate photodetector for the FLARES detector [58]. Other solid state photodetectors are characterized by similar properties, but present different limitation to the attainable performances. In particular, the SDDs have been preferred with respect to Silicon photomultiplier (SiPM) because they do not suffer from the same limits on the attainable energy resolution. The SiPM, causing an electron multiplication, are characterized by gain fluctuation and linearity issues, spoiling the attainable energy resolution. In addition, two or more photons hitting the same SiPM pixel are accounted as a single photon, causing the loss of detected photons and spoiling the attainable energy resolution.

[2] A possible solution to this problem is the integration of a FET at the anode collection. The technology needed to implement this solution spoils at unacceptable level the production yield of SDDs. Therefore this strategy cannot be currently implemented inside the FLARES project

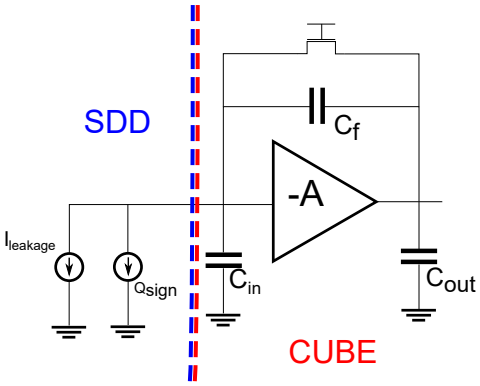

Figure 5.6: Simplified schematic of the CUBE preamplifier. The SDD provides leakage current and signal charge, integrated on the feedback capacitor C_f. The reset mechanism discharges the capacitor once the range is saturated.

The choice of SDDs as candidates for high resolution scintillator spectroscopy is therefore strongly motivated a priori. Such claim has been put to test with different measurements to characterize a posteriori the effective properties of these detectors.

X-ray measurement and their importance

To characterize the SDD-only performances, soft X-ray measurement are usually performed. Two objectives are pursued with these investigations:

1. The calibration of the device in terms of produced electrons;
2. The evaluation of ENC_e at different energies.

After an interaction with an X-ray of given energy (E_X), the number of produced electrons in silicon is given by

$$N_e = \frac{E_X}{\omega_{Si}} \tag{5.6}$$

where ω_{Si} is the average energy for the production of an electron-hole couple in Silicon. For ~ 300 K, $\omega_{Si} = 3.6$ eV/pair, while for lower temperatures this value increases up to 3.8 eV/pair [57]. Since this is a constant average process, N_e follows a Poisson statistics. However, since the production of multiple electrons is not independent, the standard deviation of produced charge carriers is reduced by the phenomenological *Fano factor* (F), according to:

$$\sigma_{N_e} = \sqrt{F \cdot \frac{E_X}{\omega_{Si}}} \tag{5.7}$$

The typical value for this factor in Silicon is $F = 0.115$ [57], resulting in a strong reduction of statistical fluctuation of charge carriers. This fluctuation is not the only source of uncertainty in the measurement of the actual number of produced charge carriers. The stochastic electronic noise, in fact, is considered fully independent by the production of charge carriers and adds an ulterior fluctuation equal to ENC_e. This effect results in a total fluctuation of

$$\sigma_{Tot} = \sqrt{F \cdot N_e + ENC_e^2} = \sqrt{F \cdot \frac{E_X}{\omega_{Si}} + ENC_e^2} \tag{5.8}$$

Which corresponds to a relative resolution, R_{Tot}, of

$$R_{Tot} = \frac{\sigma_{Tot}}{E_X} = \sqrt{F \cdot \frac{1}{E_X \omega_{Si}} + \frac{ENC_e^2}{E_X}} \tag{5.9}$$

This value is expressed in electrons. To obtain the corresponding energy value, R_{Tot} has to be multiplied to ω_{Si}.

These whole discussion is made a priori with respect to the gain induced by the readout and processing chain. To correct with respect to this factor, the first step in a X-ray measurement analysis is an energy calibration of the SDD.
When multiple energy X-ray are measured with a SDD device, the corresponding voltage amplitude and resolution can be calculated for each line. The average amplitudes are used to build the voltage-energy couples, to which a calibration law $E_X^{\text{reco}} = f(V, \theta)$ can be fitted to obtain the θ parameters. With the calibration, the predicted statistical fluctuations can be obtained at each energy with equation (5.7), substituting E_X with E_X^{reco}. Thanks to this information, equation (5.8) can be solved for ENC_e^2 to obtain the electronic component of the resolution as a difference, thus separating the different components of the resolution.
It has to be highlighted that this method incorporates in the electronic noise all the non-idealities of signal treatment. It has to be referred to in a more correct form as the *non-statistical* component of the resolution. In particular, this components also takes into account eventual non-efficiencies in charge collection on the SDD surface and volume, that are extremely difficult to both detect and disentangle from other observable features. While talking about X-ray measurements, this evaluation gives the unavoidable limit of the resolution, characteristics of a particular SDD acquired with a well determined readout chain. Extrapolation from this value to other measurements or to different configurations has to be made carefully, since the modification of parts of the processing chain or of the whole setup can deeply modify the non-statistical component of the resolution. As a consequence, each SDD system has to be characterized in detail once assembled in the final configuration to obtain a realistic evaluation of its real performances.

SDDs used in the FLARES project

The readout of large scintillators ($\mathcal{O}(\text{cm}^3)$) demands the use of wide SDD, in order to fully cover up at least one face of the considered crystals. In particular, the $CdWO_4$ crystals used for FLARES are cubes with 3 cm sides, demanding SDDs of the same size. Two detector geometries have been used in the tests performed in the R&D phases of the project:

- 3x3 matrix of 8x8 mm^2 SDDs;
- 3x3 cm^2 SDDs with single collection anode.

The first device was tested in collaboration with the Politecnico di Milano[3], and has been used to test the effect of pixelized readout on the achievable performances of the scintillators. In fact, a pixelate design (although with extremely wide pitch) can be applied to discriminate the topology of some events, thus providing more particle tagging properties.
The second device, instead, has been specifically designed and produced by Fondazione Bruno Kessler (FBK) for the readout of large scintillation crystals. It is the biggest single anode SDD ever built and, during our tests, has been characterized to determine its actual performances in terms of X-ray and scintillation response.

5.1.3 Measurement with pixelate SDDs

As a first test of the FLARES approach, a SDD matrix of 2.4×1.6 cm^2 total active area, made of 6 SDDs with 8×8 mm^2 area each, is coupled to a 2.3×1.5×2.3 cm^3 $CdWO_4$ scintillation crystal [116].
Both X- and γ-ray measurements have been performed to quantify the performances of this scintillation detector in terms of achievable energy resolution, testing the attainable performences of this detector.
The detector is composed by the photodetector, the scintillator and the signal pre-amplifiers. The photodetector is a monolithic array of nine individual SDD units, arranged in a 3×3 format, each

[3]Department of electronics, information and bioengeneering

with an active area of 8×8 mm^2, as depicted in figure 5.7(a). The contact region between different units is covered by the drift field, ensuring that the whole internal surface of the device is active. The only dead area of the detector is therefore a ∼1 mm thick frame running along the border of the matrix. The SDD array is mounted on an Alumina ceramic carrier with a thermally conductive bi-adhesive layer, to ensure a correct cooling of the whole device. The ceramic carrier hosts CMOS CUBE charge sensing amplifiers [115], filtering capacitors and contains all the important biasing, reset and detector readout interconnections to the detector back. The design of this particular SDD array has been optimized for γ-ray spectroscopy applications, as described in [104]. In particular, a thin light entrance window has been designed and an Anti-Reflective Coating (ARC) has been deposited on to enhance scintillator light collection. All the SDD units are biased using punch-through mechanism [113], thus allowing the coupling to scintillating crystals.
Six adjacent units of the SDD matrix, marked from 1 to 6 in Fig. 5.7(a), are covered by a 2.3×1.5×2.3 cm^3 $CdWO_4$ crystal. This geometry has been chosen to limit the crystal surface coupled to the dead region of the matrix and has been obtained cutting a 3×3×3 cm^3 crystal. The final dimension have been chosen to perform the cutting procedure with best efficiency and quality. All sides of the crystal excluding the optical window are covered with ten layers of PTFE reflector wrapping for a total thickness of ∼0.5 mm to enhance the light collection and the spectroscopic performance of the detection system. However, underneath these PTFE wrappings, the crystal has smooth surface textures. From the results shown in figure 5.1, this configuration does not ensure the best collection efficiency, but it still allows a viable test of the global detector behavior.

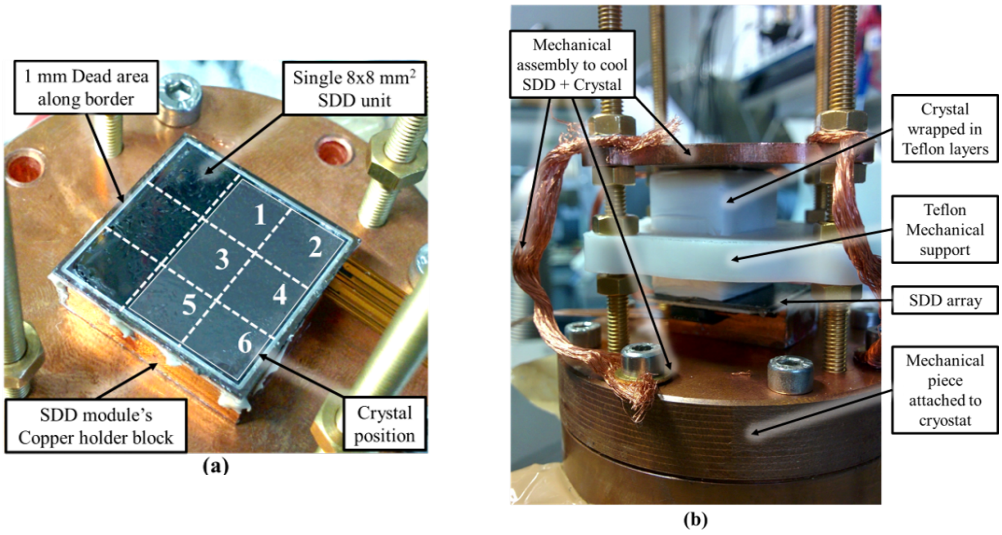

Figure 5.7: (a) Monolithic SDD array with nine individual SDD units can be seen mounted on ceramic carrier and Copper holder block in the experimental setup. Channels selected for scintillator readout have been marked. (b) The 2.3×1.5×2.3 cm^3 $CdWO_4$ crystal wrapped in Teflon layers coupled to six channels of the SDD array can be seen fixed to a cryostat with copper mechanical pieces.

The complete structure with $CdWO_4$ scintillator assembled on top of the SDD array is shown in figure 5.7(b). The crystal and the SDD array are anchored by means of copper and PTFE support to a Ricor K535 cryostat and placed inside a custom designed vacuum chamber to reach temperatures as low as 125 K at detector level. At this temperature, the light yield of the $CdWO_4$ crystal increases (see Table. 5.2) and the leakage current of the SDD reduces, improving the global detector performances.
The acquisition chain for the SDD signal is composed of a buffer board, a digital oscilloscope and other electronics responsible for generating acquisition control signals. The six CUBE preamplifier outputs, corresponding to the six channels facing the scintillator, are connected to a buffer board using a flexible PCB board. This Buffer board acts as line driver to allow connection of the buffered CUBE outputs to National Instruments PXI 5105 board using coaxial cables as depicted in figure

5.8. The PXI 5105 is a 60 MHz, 8-Channel and 12-Bit PXI oscilloscope programmed with a custom LabView^{TM} software to digitize and acquire the buffered CUBE output waveforms once an external trigger is received.

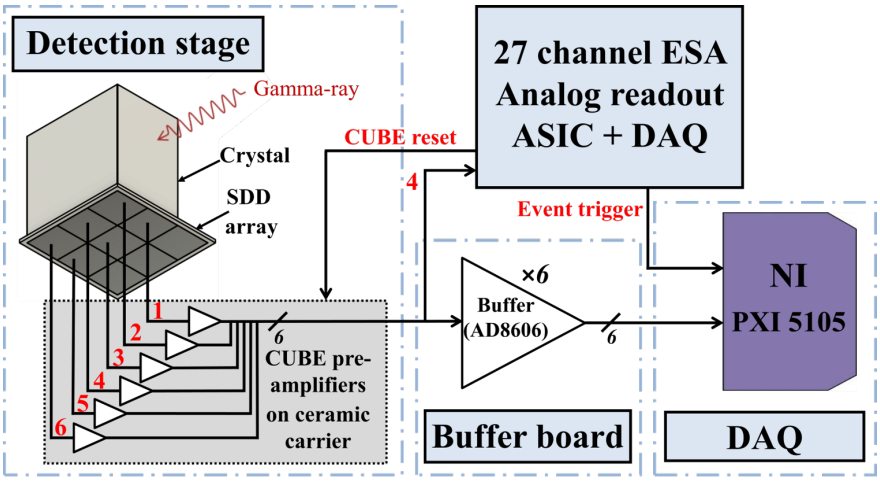

Figure 5.8: Block diagram of the experimental setup demonstrating interconnections of the detection system, buffer board, Data Acquisition system and the Trigger/reset generation block for γ-ray measurements.

The CUBE outputs are all acquired simultaneously by the PXI board at a sampling rate of 20 MHz with a total of 3000 samples per channel for every event trigger. This corresponds to an acquisition window size of 150 μs of CUBE waveform per channel, more than five times the 22 μs scintillation decay time of the $CdWO_4$ crystal (see table 5.2). At this temperature the SDD's charge collection time is of the order of a few 100 ns and therefore the crystal's scintillation decay time is the only parameter to be considered for the choice of acquisition window size. An example of the CUBE outputs sampled during the $CdWO_4$ crystal exposure to a ^{228}Th γ-ray source can be seen in figure 5.9.

As shown in Fig. 5.8, there is an additional block in the experimental setup which is responsible for the generation of CUBE reset and the event trigger. This block consists of a dedicated ASIC capable of reading up to 27 CUBE pre-amplifiers at a time. This chip was developed originally for ESA γ-ray astronomy application [117], and is used in this measurement to generate a trigger signal for the acquisition. Such signal is generated thanks to the Gaussian shaper included on the the ASIC, on which a edge trigger can be performed. In particular, the trigger is generated looking at channel 4. As the scintillation light is simultaneously received by all six SDD channels covered by the crystal, the use of a low enough threshold on a single SDD channel's shaper output ensures that all useful events are acquired. The integrated shaper inside the ESA chip has a maximum programmable peaking time of 6 μs, sufficient to act as a fast shaper for triggering but too fast to process the scintillation light pulse, characterized by a 22 μs decay constant. Thereby the NI PXI board is utilized for signal acquisition and processing.

Once the signal are acquired, an off-line analysis is performed to extract the needed information from the SDD output. As depicted in figure 5.9, the acquisition window saves more than 40 μs of CUBE output waveform prior to the event trigger. This allows us to have an estimation of the baseline of the individual pulses by performing a linear fit of 30 μs of pretrigger waveform. For each waveform the fitted line, extrapolated to the entire window, is subtracted from the original pulse to correct both baseline slope and offset. Later, the amplitude of the digitized pulse is calculated as a numerical integration of the resulting waveform. This technique has been applied to filter out the high frequency noise and has been shown to reduce the non-proportionalities of the $CdWO_4$ scintillator [112]. In addition to the amplitude estimation, different shape parameters of the waveform have been calculated, thus enabling us to exclude any spurious pulses in the following analysis stage.

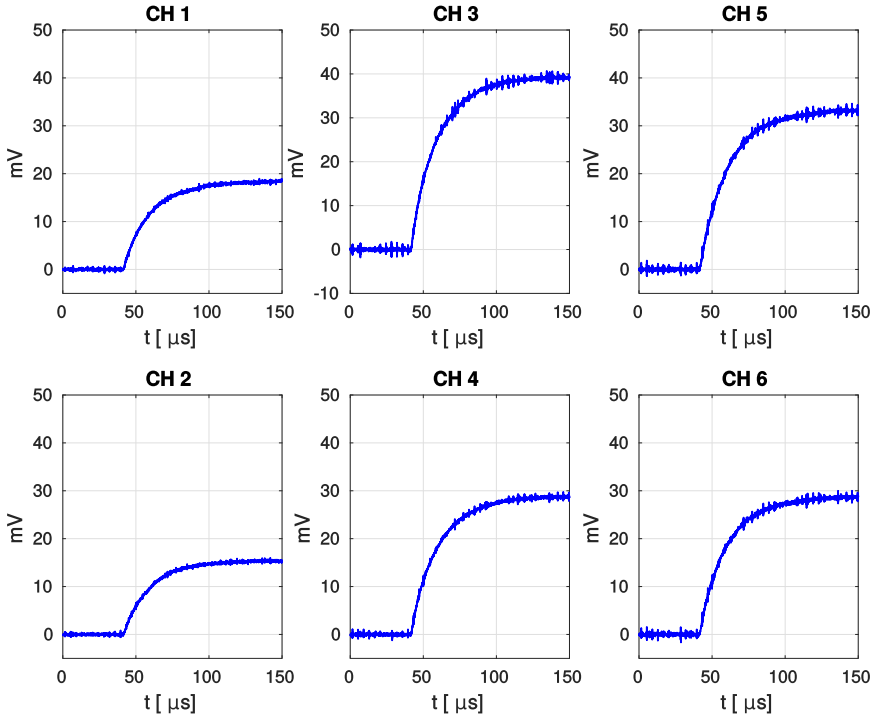

Figure 5.9: Waveforms of CUBE output signals acquired by the NI PXI-5105 with the SDD array coupled to $CdWO_4$ crystal. All waveforms correspond to a single γ-ray event and have been acquired simultaneously with an acquisition window size of 150 μs at a sampling rate of 20 MHz. The difference in the signal amplitude can be ascribed to the dependence of light propagation on the interaction position of the γ-ray.

For the γ-ray pulses, instead, a more detailed processing is performed, based on the pulse fit with the function:

$$I(t) \;=\; A_{Fit}\theta(t-t_0)(A_1(1-e^{\frac{t-t_0}{\tau_1}})+(1-A_1)(1-e^{\frac{t-t_0}{\tau_2}})) \tag{5.10}$$

Here θ is the step function, taking into account the CUBE integration time, while the two exponential terms, dependent on the time constants τ_1 and τ_2, are needed to take into account the two major scintillation time components of the $CdWO_4$ scintillator [118]. The function shape is deduced by considering the integration of the exponential scintillation decays. With this procedure the starting point of the pulse (t_0) can be estimated, thus allowing to control the position of the pulse in the fixed acquisition window. Since the trigger position varies with the amplitude of the triggered pulse (*Amplitude walk* effect [57]), the pulse area is calculated in different intervals for different events. Hence the precise determination of t_0 allows to correct for this variation, assuring that the area of all the pulses is calculated in the same time interval. In addition, the χ^2 test on this fit has been used to distinguish between signal and spurious events, such as reset, pileups or particularly noisy events.
The fit procedure consists of two steps: initially, the six pulses related to a single trigger (see Fig. 5.9) are added sinchronously sample by sample and the resulting sum is fitted with the function (5.10) (Fig. 5.10). Later, individual pulses of all channels are also separately fitted with (5.10), using the results of the previous step to initialize the new fit procedure. Using the sum of all six pulses, it is possible to constraint precisely all pulse parameters, especially the starting points, which are difficult to be determined for smaller signals. After the fit procedure, the amplitude of each acquired signal is evaluated as the numeric integral of the fit function in a fixed range after the starting point t_0, thus obtaining an estimator not dependent on the trigger position. Energy of the incident γ-ray photon can now be evaluated by summing these integrated pulse amplitudes, after performing the SDD calibration with an X-ray measurement.

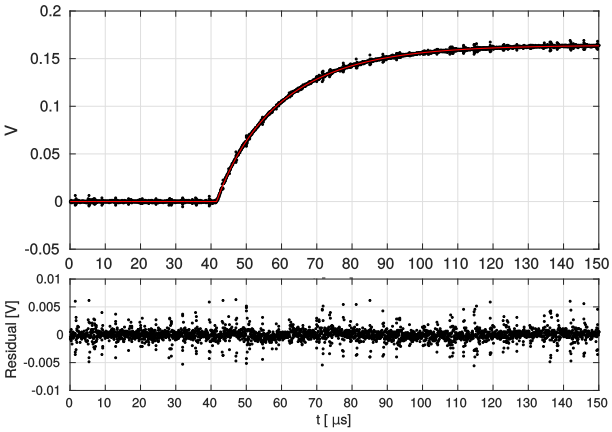

Figure 5.10: Sum of the individual waveforms acquired for a single γ-ray event alongside its fit using (5.10). In the upper panel the fit function is superimposed on the waveform. In the lower panel the residual plot is shown. The presence of low frequency noise can be appreciated in the residual plot.

X-ray calibration

Prior to γ-ray measurements, the six SDD channels and the corresponding readout electronics are characterized by means of X-ray measurements with an uncollimated ^{55}Fe radiation source. In particular, the X-ray spectra are used to perform photo-electron calibration of SDD channels and to align the different pixel gain.
In these measurement, all SDD channels are considered when generating the X-ray event trigger, to characterize in detail each channel. The voltage pulse on CUBE output corresponding to an X-ray event has a rise time much faster than the scintillation measurement, as it is limited only by the diffusion enlargement of the charge cloud during its drift towards the SDD anode.
The histogram of the pulse amplitude acquired for each channel with an acquisition window size of 150 μs is shown in figure 5.11. The peaks centered at zero for a given cell correspond to baseline measurements when no X-ray photon was detected by the cell. In these cases, the X-ray event trigger was provided by another cell with valid X-ray event. The two peaks at higher amplitudes correspond to the 5.89 keV and 6.49 keV lines emitted by the ^{55}Fe source. In the bottom panel of figure 5.11, the same spectra are shown after gain calibration has been performed by linearly transforming the X-axis from Area to Energy in electron-Volts. Since the peak energies in eV are proportional to the number of corresponding photo-electrons through the silicon conversion factor of 3.62 eV/photo-electron, a photoelectron calibration is extracted from this measurement for each channel. This information is used in the following γ-ray measurements to evaluate the total number of photo-electrons corresponding to a specific γ-ray peak.
Gaussian fits of the two peaks are then performed to evaluate the energy resolution and thus the electronic noise contribution of individual SDD channels. Figure 5.12 shows the measured Equivalent Noise Charge (ENC) values for all SDD cells having an average of $\sim$19 rms electrons at 125 K.

γ ray measurements

For the γ ray measurements, the SDD matrix has been coupled to the $CdWO_4$ crystal with a thin layer of BC-630 optical grease, to perform refractive index matching. The detector has been irradiated with a ^{228}Th source with $\sim$ 20 kBq activity, thus performing a γ-ray measurements to evaluate the detector performances in a quite extended energy range. This source is characterized by different γ rays, produced by the various radioactive isotopes of ^{228}Th chain. The most intense direct emissions are the 583 keV, 727 keV, 860 keV and 2615 keV lines.
In order to compensate for possible variation of the SDD cells gain with respect to the ones evaluated with the X-ray calibration, in particular due to optical coupling of SDD array with the scintillator, an iterative gain compensation algorithm is implemented. This algorithm is applied to all the collected data during the off-line analysis and modifies the calibration factors of the different SDD cells. In particular, a variable correction factor is applied to the gain of the different cells, providing

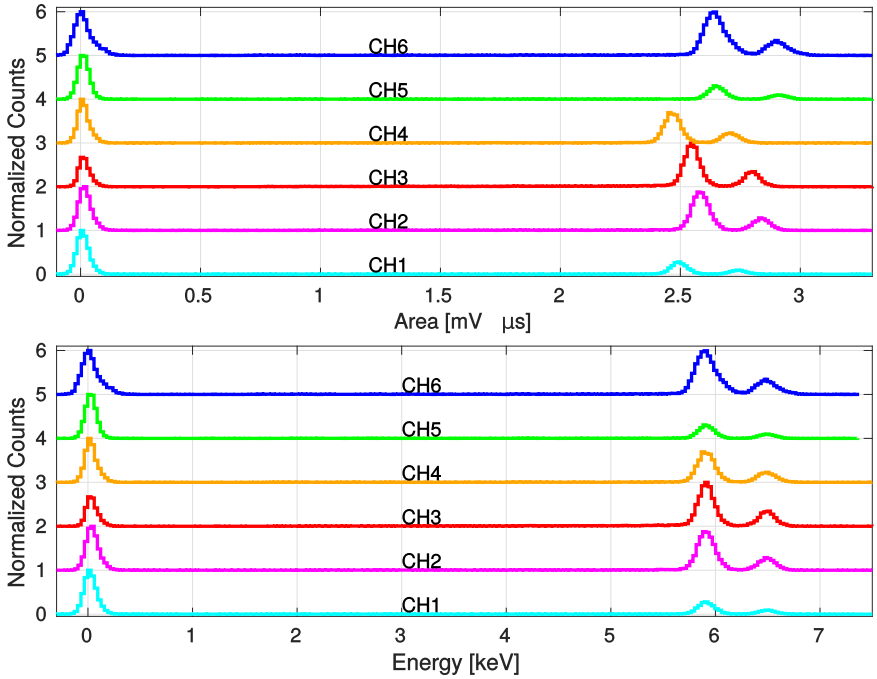

Figure 5.11: ^{55}Fe X-ray spectra acquired with the SDD array cooled down to 125 K before (Top) and after (Bottom) X-ray calibration. The spectra of different channel are spaced on the y-axis to enhance the figure readability.

a modified calibration. With this new calibration, the amplitude of the γ-ray events have been summed and analyzed, extracting the energy resolution of the peaks. The correction factors have been varied independently for each cell, selecting the value giving the best energy resolution at the 2615 keV γ line. In figure 5.13 the results of this algorithm are shown.
With this procedure a new optimized calibration is obtained, with a total 12% change with respect to the X-ray one. Since this may induce a bias on the absolute photoelectron number determination, a 12% systematic uncertainty is considered affecting this value.
Only the pulses characterized by $0.8 < \chi^2/\text{dof} < 1.4$, according to the pulse fit, have been considered during the next steps. This selection preserves 85% of the counts under the peaks, removing all the pulses characterized by anomalous shapes, such as resets, pileups and noisier pulses. The spectrum obtained summing up the amplitudes of all the channels after the performed selection is shown in figure 5.14. This is the result of 1 hour measurement with 50 Hz trigger rate. This spectrum was energy calibrated by means of a linear function evaluated using the channel-energy (Ch,E)

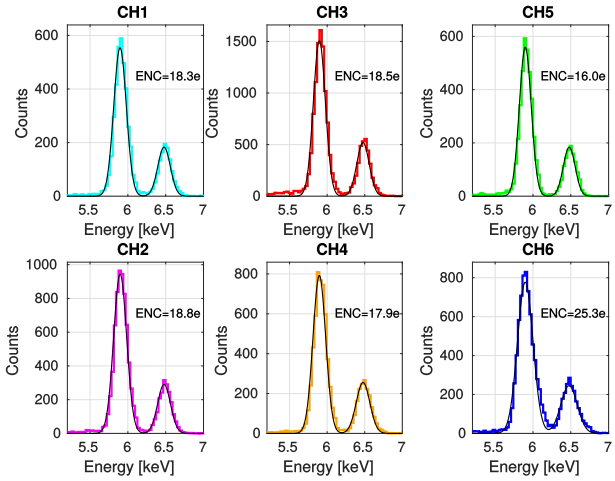

Figure 5.12: Gaussian fit of the calibrated ^{55}Fe Mn-Kα and Kβ peaks demonstrates that the detection system is characterized by an average ENC of 19.1 rms electrons at 125 K.

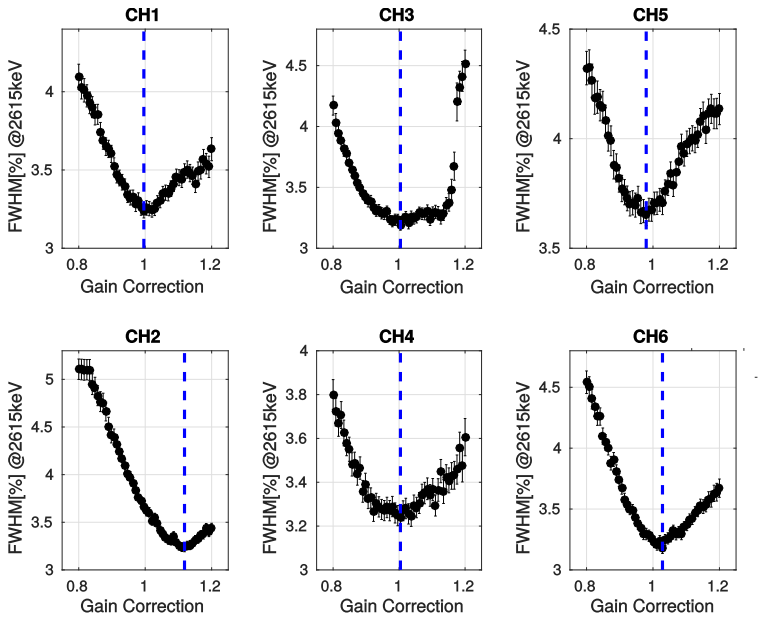

Figure 5.13: Iterative gain correction on the different channels of the matrix. The value on the x-axis is a correction factor applied to the gain obtained with the X-ray calibration. The dashed line marks the chosen gain correction factor.

couples for the 511 keV, 583 keV, 860 keV and 2615 keV peaks. The energy obtained with this procedure has been subsequently used to evaluate the measured light yield, obtained by the means of a linear fit of the photoelectron number - energy couples. This curve is shown in figure 5.15 and is characterized by a maximum deviation of 1.6% from the linearity. From this calibration, a measured light yield of 11.7±0.6 ph/keV can be extracted.

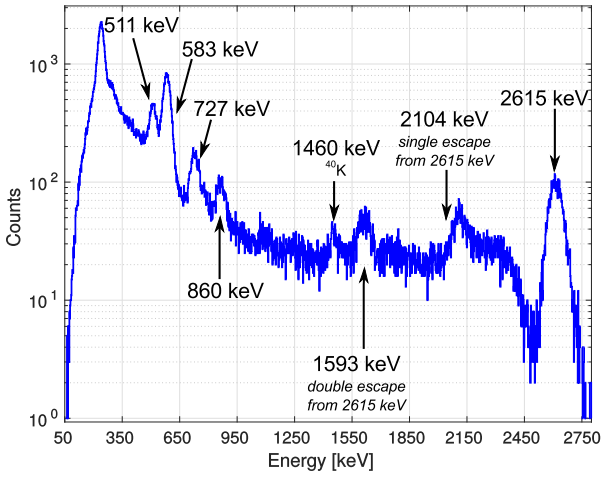

Figure 5.14: Calibrated ^{228}Th spectrum. The main source peaks have been identified thanks to the energy calibration. The single and double escape peaks related to the 2615 keV γ-ray and the ^{40}K background peak are also visible.

The obtained energy resolution (R) for different peaks, defined as $R = 100 \cdot \mathrm{FWHM/E}$, is presented as a function of the energy in figure 5.16. The R values have been obtained fitting the peaks in the γ-ray spectrum with a Gaussian subtending an exponential background. The statistic (R_{stat}) and electronics (R_{ENC}) contributions to the resolution have been evaluated with the following

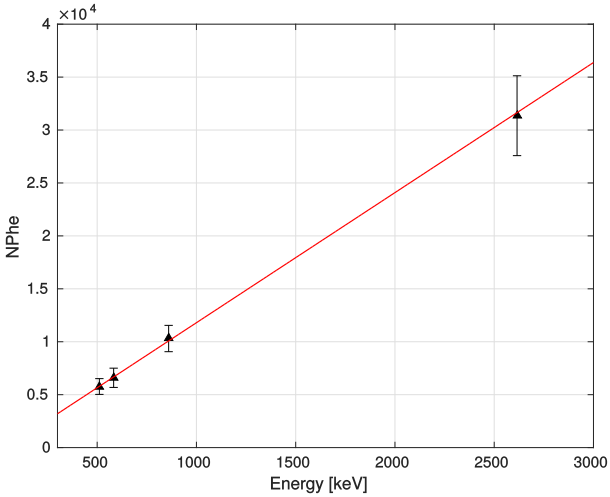

Figure 5.15: Photoelectron calibration of the measured spectrum. A conversion factor of 11.7±0.6 ph/keV can be extracted from the fit.

equations:

$$R_{stat} = 2.355\sqrt{\frac{1}{N_{phe}}} \cdot 100 \tag{5.11}$$

$$R_{ENC} = 2.355\sqrt{\frac{\sum_{i=1}^{N_{SDD}} ENC_i^2}{N_{phe}^2}} \cdot 100 \tag{5.12}$$

where 2.355 is the conversion factor from standard deviation to FWHM, N_{phe} is the number of photoelectrons detected at the examined peak and ENC_i is the equivalent noise charge of the i_{th} SDD of the matrix. The values of R and its components are listed in table 5.3.

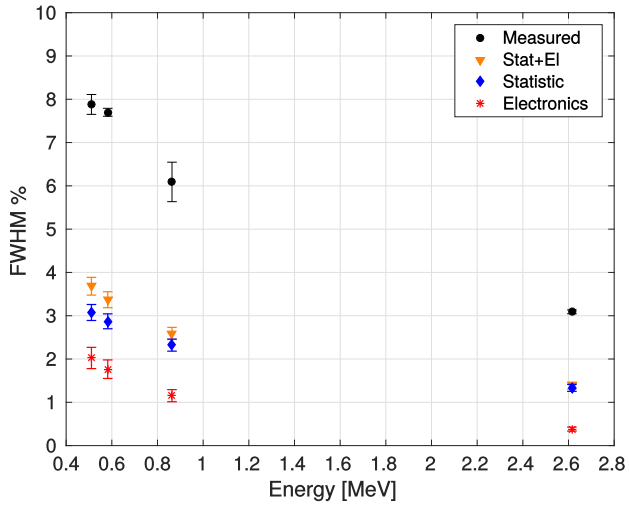

Figure 5.16: Measured FWHM resolution and its components as a function of the γ-ray energy. The orange points correspond to the squared sum of R_{stat} and R_{ENC}.

As it can be seen in figure 5.16, the measured resolutions are bigger than the quadratic sum of R_{stat} and R_{ENC} components. This difference can be partially traced back to crystal inhomogeneities, causing self-absorption of scintillation photons. Moreover, the crystal coupling to the photodetector may have damaged the thin SDD light entrance window, creating dead spots on the surface of the detector. Another possible cause of this worsening may be the position-dependent variations of the sum of the SDDs signals, associated to their different gains. Since the nature of this missing part of the resolution cannot be unambiguously determined, it is not possible to model its evolution with

Peak energy [keV]	R [%]	R_{stat} [%]	R_{ENC} [%]
511	7.8±0.2	3.1±0.2	2.1±0.2
583	7.7±0.1	2.9±0.2	1.7±0.2
860	6.1±0.4	2.32±0.14	1.1±0.14
2615	3.09±0.05	1.33±0.08	0.38±0.05

Table 5.3: Measured resolution and its components for different γ-ray peaks.

energy. As a consequence, it is impossible to define a function to fit the plot in figure 5.16 and correctly interpret its results.
A measured FWHM energy resolution of 3.09±0.05% has been obtained at 2615 keV. Even if this value is larger than the target one for FLARES design ($\lesssim 2\,\%$ at 3 MeV), it clearly indicates that the conceived device is promising. The statistical and noise contributions to the energy resolution are similar to the expected ones [119], while the excess component could be ascribed to photoelectron losses when the photon interaction happens far from the SDD center [120]. As a consequence, the readout of large scintillation crystals with pixelate SDDs is a viable pathway to obtain performing detectors.
On the other hand, the use of multiple channels for a single detector poses a limit to the maximum number of crystals, forcing the development of complex multiplexing systems to reduce the number of cables needed to transmit the signal to the acquisition stage. Moreover, the differences in gain between single cells demand a correction routine, which can be a weak link the whole high-performance readout chain.

5.1.4 Characterization of large single-anode SDDs

Figure 5.17: Picture of large area SDD mounted on the holder. The pcb board hosts the wiring for the detector and preamplifier polarization and readout. The Teflon U-shaped holder is used to block the crystal coupled to the SDD, allowing a free side for the crystal removal.

To perform the readout of large scintillation crystal with minimum number of channels and minimal gain corrections, the use of single anode SDD is necessary. To address this need, large area devices have been developed for the FLARES project, in collaboration with FBK in the framework of the ReDSoX (Research Drift for Soft X-ray). In figure 5.17 a picture of the detector on its holder is shown. The active area of the detector is 3x3 cm^2, with a single collection anode in the center of this area. The detector is designed to be polarized with a punch-trough mechanism, activated with a 180 V negative voltage difference between the internal and the outer rings. The device is covered with a NO_2 anti-reflective coating, to increase the light collection efficiency. Being the first prototype developed with this technology, these detectors present a great fragility on the light entrance window, reflecting into a low durability of the single device upon multiple couplings with scintillation crystal. In addition, the large area of the device causes the leakage current to grow, forcing the operation at low temperatures to thermally limit this phenomenon. The setup has

therefore been positioned in a custom vacuum chamber equipped with a liquid nitrogen cooling circuit, in order to lower the detector temperatures. Since this device was not optimized for cooling application, the lowest achievable temperature is ∼140 K, and the absence of slow control systems made it impossible to carry on measurements longer than a few hours. Even with this infrastructural limitation, the produced device could be characterized both with X- and γ-ray measurement in a wide range of temperatures.
The SDD, equipped with a CUBE ramp preamplifier directly bonded to the anode, is connected with a cable to a control board, managing the correct biasing of the detector and the extraction of CUBE signal mediated with buffers. The whole setup is placed in the LN cryostat and fixed to a copper plate connected to the LN circulation serpentine. To perform the acquisition, a dedicated LabView^{TM} software was developed, to exploit all the characteristics of NI-PXI 5105 digitizer. The designed system is based on a producer-consumer architecture. The producer loop handles the acquisition of up to 8 analog-to-digital channels and feeds the consumer loop with the acquired waveforms, that are saved on binary files. The system constantly digitizes the analog inputs and acquires a fixed window on each channel when a trigger condition is met. The trigger can be sent externally as a digital TTL signal or a leading edge trigger can be performed on one of the digitized channels. Since the ramp on CUBE output prevents the use of a fixed threshold triggering, the preamplifier output is split between the digitizer and a derivative filter, which removes the ramp baseline. The schematic view of the system is depicted in figure 5.18.

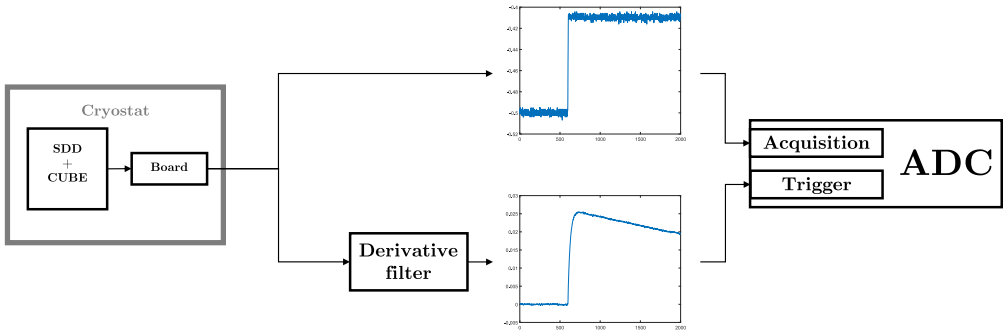

Figure 5.18: Schematic view of the large area SDD acquisition system. The CUBE output, buffered on the control board, is split between the digitizer and a derivative filter, which removes the ramp baseline, allowing a fixed threshold triggering.

After the acquisition, the waveform are analyzed off-line to extract the pulse parameters used to evaluate the pulse amplitude and rise-time. The analysis is built around the fit of the acquired SDD pulse, trough which the baseline is removed, the high frequency noise components are reduced and the amplitude can be evaluated.
The setup is the same for X- and γ-ray measurement, with the difference that the X-ray are directly measured by the SDD, while the γ-ray are absorbed by a $CdWO_4$ scintillating crystal, coupled to the SDD with BC-630 optical grease. Since the time evolution of the two signals (direct ionization and scintillation light) are different, two fit functions are needed to analyze the different measurements. The fit function used for X- and γ-ray pulses are, respectively:

$$A^{\mathrm{X}}(t) = A_{Fit} \int_0^t e^{(\frac{x-t_0}{\sigma})^2} dx + mt + q \tag{5.13}$$

$$A^{\gamma}(t) = A_{Fit}\theta(t-t_0)\left(1 - e^{\frac{t-t_0}{\tau}}\right) + mt + q \tag{5.14}$$

where θ is the step function, A_{Fit} is the amplitude of the CUBE pulse, t_0 is the starting point of the pulse, σ is the width of the rising edge of the X-ray pulse, τ is the scintillation time constant, m is the slope of the CUBE ramp and q is the ramp value at the beginning of the window. In figure 5.19 an example of an X-ray (left) and a γ-ray (right) pulse are reported, with the fit function

superimposed. The form of (5.13) comes from the assumption that the cloud of collected electrons has a Gaussian width. The integration of these electrons, therefore, has a shape well described by an error function. The typical σ values are around 0.5 μs. The typical τ of $CdWO_4$ instead is $\sim$15-20 μs, depending on the temperature. Given the great difference of these two time scales, in (5.14) the error function term, taking into account the Gaussian diffusion of electrons, has been approximated with a step function. This approximation does not affect the correct description of the time evolution of the signal, but significantly lowers the free parameters of the model, allowing a more stable fitting procedure.

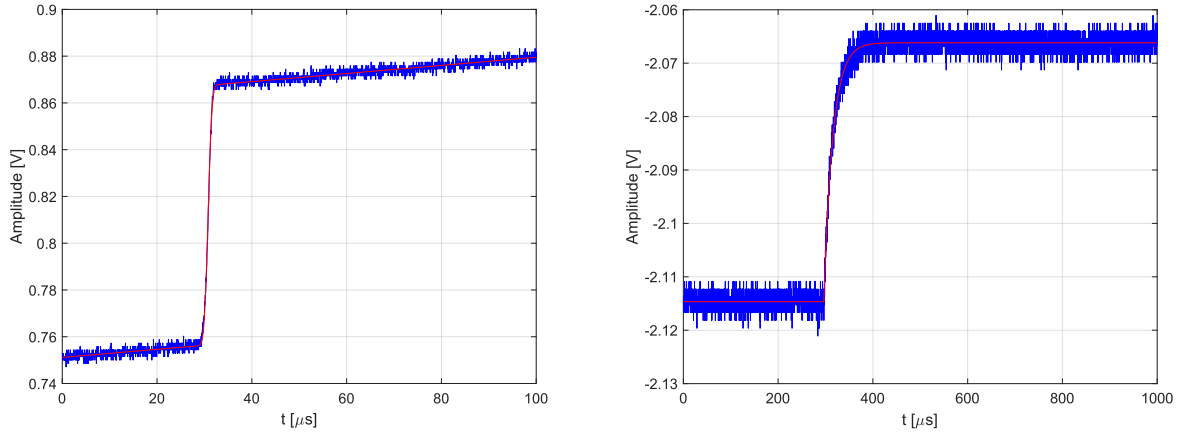

Figure 5.19: CUBE pulses for X-ray (left) and γ-ray (right) measurements. The red line is the fit performed using equations (5.13) and (5.14). The X-ray pulse is much quicker than the γ-ray one, since the γ radiation is measured trough the scintillation of $CdWO_4$ crystal.

The variable used to evaluate the amplitude of the acquired pulse is A_{Fit}. It is the actual amplitude of the digitized step, proportional to the charge integrated by the CUBE feedback capacitance. Its value therefore represents the total amount of collected electrons, and is affected by lower statistical fluctuations. The absence of a particular shaping, moreover, prevents effects such as the ballistic deficit, resulting in a more complete transmission of information. The use of a full pulse fit, moreover, allows to take care of the shape information, useful to perform pulse selection, avoiding the consideration of miss-triggered pulses or pile-up events.

X-ray measurements

The focus of X-ray measurements is to characterize the noise level and response time of the SDDs. The large area of the detector has an impact on the field gradient, therefore on the size of the electron cloud drifting towards the collection anode. As the dimension of the could increases, the time needed to collect all the electron grows, thus affecting the rise-time of the device. In the case of a square SDD with side long L, the drift time from the side to the center can be approximated as [100]:

$$T_{\text{drift}} = \frac{L/2}{v_e} = \frac{L/2}{\mu_e V/(L/2)} \sim \frac{L^2}{\mu_e V} \tag{5.15}$$

where μ_e is the electron mobility and V is the anode-outer ring voltage difference (assumed with constant gradient). This roughly approximate estimate shows that the increase follows the square of the dimension, therefore the large area of the used devices is expected to significantly affect the risetime. This effect is partially balanced by μ_e, which increases as the temperature lowers, given the reduction of phonon-mediated scattering. On the other hand, the drift field is not uniform over the SDD area, leading to a different drift field depending on the electron generation position. As shown by different simulations [100], in region distant from the drift path and the anode the field weakens, thus resulting both in a slower T_{drift} and in a lower charge collection efficiency.

Source	Energy [keV]	Intensity [%]
^{55}Fe	5.89 (K_α)	16.9
	6.49 + 6.53 (K_β)	2.1
^{241}Am	11.9	0.7
	13.7 + 13.9	9.67
	16.8 + 17.06	4
	17.5 + 17.7 + 17.9	7.7
	20.7	1.39
	21.1 + 21.3 + 21.5	1.4
	26.3 (γ)	2.4
	59.54 (γ)	35.9

Table 5.4: Major emission from ^{55}Fe and ^{241}Am. The summed lines cannot be distinguished in the total spectrum, due to the finite detector resolution. Except for ^{55}Fe K_β, the summed lines will not be used in the analysis.

To test these effect on the 3x3 cm^2 SDDs, different measurement have been performed varying the temperature of the device with two different ionizing radiation sources: ^{55}Fe and ^{241}Am. The main emissions of these sources are listed in table 5.4, alongside their relative intensities. The closer lines cannot be distinguished in the spectrum, due to the finite detector resolution. A complex fit procedure would be necessary to disentangle these peculiar structures, since their peak shape would be affected by different non idealities. As a consequence, to limit the analysis complexity (and avoid the ingerence of systematic uncertainties) these energies will not be considered in the analysis, except for ^{55}Fe K_β. After this selection, 5 peaks are considered: 5.89 keV, 6.49 + 6.53 keV, 11.9 keV, 20.7 keV, 26.3 keV and 59.54 keV. An energy scan from 5 to 60 keV is therefore possible, providing a powerful tool to investigate the properties of the detector, such as its linearity and its resolution. Higher energies would even more interesting, but the small thickness of the SDD ($\mathcal{O}(600\mu m)$) causes the efficiency to fall rapidly with the energy, preventing the use of higher energies. The sources have been positioned above the active area of the detector, to maximize the geometrical detection efficiency. In particular ^{55}Fe was collimated over the anode, while ^{241}Am was left uncollimated over a corner of the detector. Such configuration allows to test both the average noise resolution of the system and the difference in response between central and outer regions of the detector. The use of two different sources allows to perform this test in a single measurement, diminishing the number of cooling cycles needed. Temperatures as low as 149 K have been reached, with a first measurement at 243 K, the first temperature at which the large SDDs can be operated. At higher temperatures, in fact, the leakage current is too high and the reset of the CUBE preamplifier happens too often, reducing the time for spectroscopy measurements. On the other hand, 149 K is the lowest temperature achievable with our setup.
In figure 5.20a the joint ^{55}Fe and ^{241}Am energy calibrated spectrum at 149 K is shown. This is the setting with the lowest noise, representing the best operational configuration of our setup. The single energy peaks have been analyzed with a Gaussian fit subtending a constant background, to extract the mean values and the resolution. The detector shows good performances in the whole energy range: the main peaks are well distinguishable, and the resolution are good over all energies, as shown in figure 5.20b. In particular, the resolution at the two ^{55}Fe lines are 170 ± 9 eV and 180 ± 19 eV respectively. The average equivalent noise charge of the system is evaluated averaging the values obtained for the electronic noise component at each peak, resulting in 15.5 ± 1.2 RMS electrons, as shown in figure 5.20c (see equations (5.7), (5.9), (5.8)). Assuming standard values for the energy needed to produce an electron-hole couple, this noise level corresponds to a lower threshold of $\sim$ 12 eV, assuming a 3 RMS detectability level. The possibility to achieve such low treshold on a device that does not multiply electrons is a proof of its performances. The ENC value is mainly constrained by the values obtained on the ^{55}Fe lines, because at these energies the

statistical contribution is lower than the electronic one, allowing a precise determination of the electronic noise of the system. It is worth noticing that the ^{55}Fe K$_\beta$ line (6.5 keV) presents a wider uncertainty on the resolution with respect to the K$_\alpha$ line. This is expected because the K$_\beta$ line is the sum of multiple emission with different energies, spaced enough to change the line shape of the peak (see table 5.4). The single Gaussian fit therefore converges on values characterized by wider uncertainties.

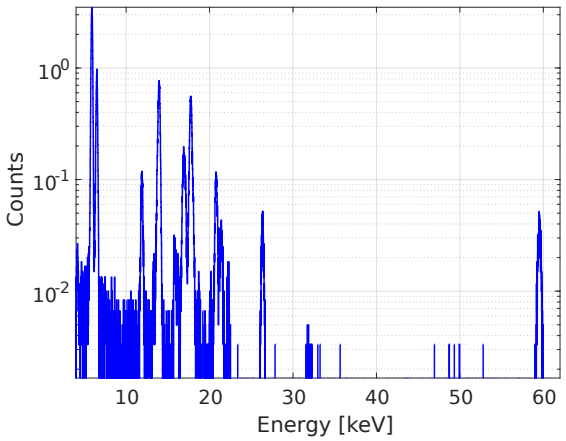

(a)

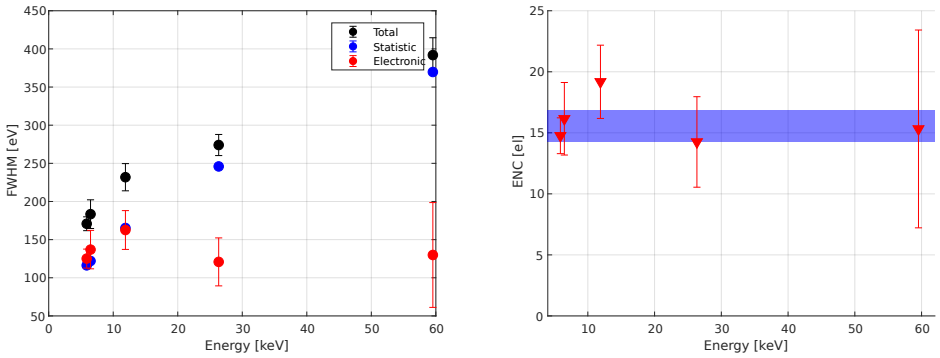

(b) (c)

Figure 5.20: ^{55}Fe and ^{241}Am measurement acquired with 3x3 cm^2 SDD operated at 150 K. In 5.20a the spectrum is reported. The good performances of the detector are evident from the well definition of the peaks. In particular, the distinction of the two ^{55}Fe lines can be used as a standard evaluation of the resolution. In 5.20b the FWHM resolution at the different peaks is reported (black dots), divided in statistic (blue dots) and electronic (red dots) components, according to section 5.1.2. The resolution at the two ^{55}Fe lines is, respectively, 170 ± 9 eV and 180 ± 19 eV. As expected, the electronic component is almost constant over the energies. In 5.20c the average ENC is calculated, obtaining the final value of 15.5 ± 1.2 RMS electrons.

To test the effects of different interaction position on the SDD surface two different calibrations have been performed: one with only the ^{55}Fe peaks and one with only the ^{241}Am peaks. In both cases the parameters of the linear calibration function $E_{\text{cal}} = mA_{\text{Fit}}$ where evaluated on the peaks and then extrapolated on the whole spectrum. The two differently calibrated spectra were analyzed, extracting the peak position and calculating the difference between these values and the actual interaction energies, called calibration residuals. Looking to the calibration residuals, reported in figure 5.21, some differences can be appreciated. Applying the ^{55}Fe calibration to ^{241}Am peaks, in fact, results in negative calibration residuals for these peaks. This means that the measured ^{241}Am signal is lower than what is expected for a linear detector. In the opposite case, the ^{241}Am calibration applied to ^{55}Fe peaks results in positive residuals for the latter peaks, meaning that the predicted position is underestimated. Such effect can be explained assuming that the ^{241}Am

induced events are happening in a region of the SDD with lower charge collection efficiency with respect to the region around the anode.

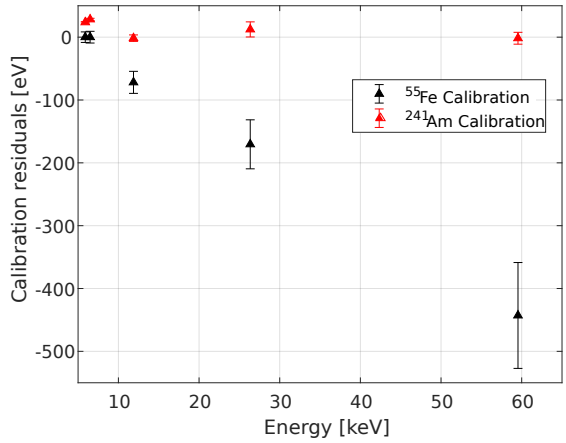

Figure 5.21: Relative calibration residual in case of ^{55}Fe (black) and ^{241}Am (red) calibrations. ^{55}Fe is placed over the anode, while ^{241}Am between anode and corner of the SDD. The ^{55}Fe calibration results in negative calibration residuals for the ^{241}Am peaks, meaning overestimation of the corresponding energies. In the opposite case, the ^{241}Am calibration applied to ^{55}Fe peaks results in positive residuals, meaning that the predicted position is underestimated. Such effect can be explained assuming that the charge collection efficiency outside the anode region decreases.

To further characterize the difference in charge collection efficiency, the measurements at different temperatures have been used. For each temperature, the distribution of σ values (see equation (5.13)) for all the collected events is extracted. With an energy selection (E>8 keV) the ^{241}Am only events could be separated by the ^{55}Fe ones, unavoidably superimposed to Compton interactions of ^{241}Am emissions. The σ distribution, divided by source, are reported in figure 5.22. At higher temperatures, the ^{241}Am (left panel) has much longer drift times with respect to ^{55}Fe events (right panel), up to 1.5μs. As the temperature lowers, the distribution narrows in both cases, because the drift time decreases (see equation (5.15)). In general, ^{241}Am events presents broader distribution with respect to ^{55}Fe ones, and this difference can be ascribed to the source positioning. ^{55}Fe, being collimated over the anode, produces events in a small active area characterized by a steady and intense drift field. As a consequence, the drift time of the produced electrons changes only with the device temperature. This results in σ values, proportional to the drift time, steady decreasing towards a minimum width distribution. In the coldest measurement a long tail can be observed in the ^{55}Fe distribution, due to the ^{241}Am induced Compton events, populating also the region with E<8 keV. On the other hand, ^{241}Am is located uncollimated on the corner of the SDD. As a consequence, its events illuminate different areas of the detector, where the drift field has different intensities. In particular, the main fraction of events produces electrons around the corner, where lower drift fields are expected. As a consequence, ^{241}Am events have different drift times also at the same temperature, resulting in a global wider spreading of the σ distribution. This spreading is still present as the temperature lowers, although it gets strongly reduced. At lower temperatures, in fact, the electron mobility increases, resulting in lower drift times even in regions with small drift fields. Thanks to this feature, the different position effect gets mitigated, although not resolved.
This results proves that the drift field varies over the SDD's area, affecting the total detector performances in terms of charge collection. The effect of this disuniformity seems to be attenuated as the temperature lowers, by looking at the σ distribution. This effect is due to the fact that σ measures the spreading of the collected electron cloud, only affected by travel time of the electrons. As the temperature lowers the electron drift gets quicker even at low fields, thanks to the increase of mobility. Consequently, at lower temperature σ becomes less sensitive to differences in the drift field, although some effect can still be identified.

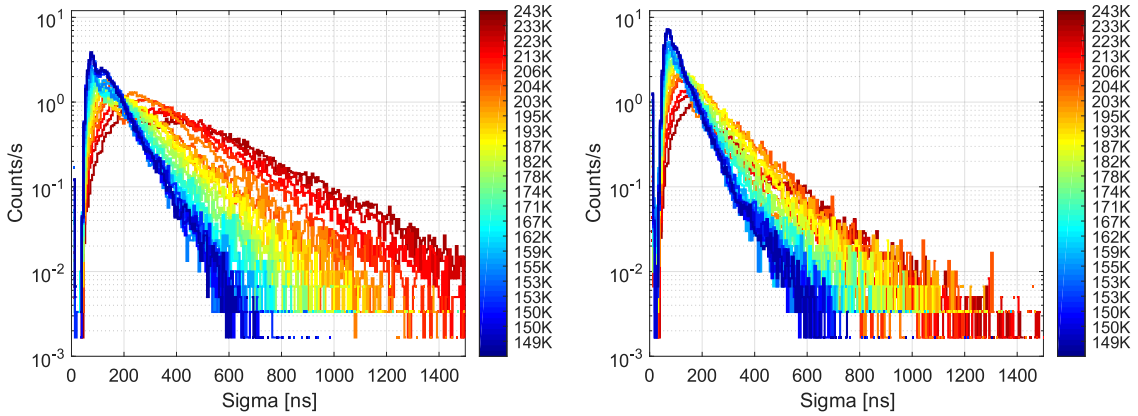

Figure 5.22: X-ray measurements at different temperatures. For each temperature, the spectrum of σ values, obtained with the pulse fit, is shown for ^{241}Am (left) and ^{55}Fe+^{241}Am pedestral (right) events. It is evident that, at higher temperatures, the ^{241}Am has much longer drift time with respect to ^{55}Fe events. At lower temperatures the difference is reduced, because the drift time decreases as temperature lowers, since electron mobility increases.

To further prove this point, two set of measurement have been performed, using only ^{55}Fe source collimated over the anode. To check the effects of the drift field, the measurements where taken with different biasing of the detector: 180 V (nominal working voltage) and 160 V. By decreasing the working tension, a low field condition is artificially created around the anode, reproducing the corner field effect. The σ spectra obtained with the two voltages are reported in figure 5.23. At 180 V the behavior is nominal: the distributions are narrow, since all the events are around the anode, and get narrower as the temperature lowers, as predicted by equation (5.15). At 160 V, instead, the distribution are wider, proving that lower fields correspond to less drift speed. As the drift fields lowers, in fact, the electron cloud can become larger due to diffusion, whose effect scales with time. Larger clouds means the electrons spread, increasing the total collection time and introducing slower components in the CUBE output. These slow components are not integrated together with the main signal, resulting in smaller charge detected in the main event. The non-integrated electrons, in fact, arrive after the main rise of the pulse, producing small increases of the baseline masked by the low frequency noise of the apparatus.

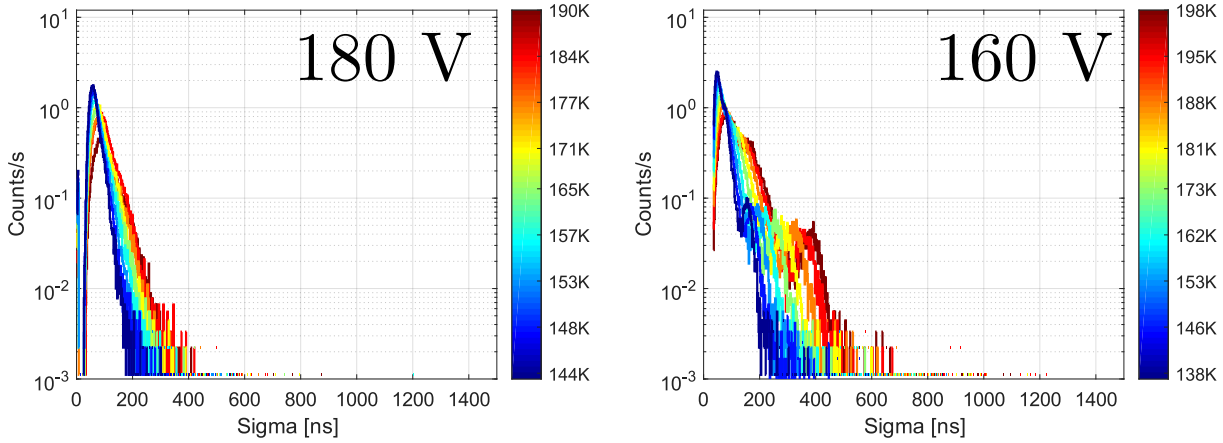

Figure 5.23: SDD drift times at different voltages and temperatures, acquired with a ^{55}Fe source collimated over the anode of the SDD. The measuement at 180 V (nominal working tension) shows the expected behaviour: the pulses are short and the maximum value decreases with temperature. Reducing the voltage to 160 V causes an abrupt change in the detected performances, with the general broadening of the measured distribution. This feature proves the effects of the non-uniform drift field on the collection of the electrons.

The non uniform drift field causes therefore large SDDs to be affected by position-dependent charge collection efficiency. This feature contributes in worsening the overall detector performances, and becomes a dominant contribution given the low level of other sources of resolution spoiling, such as the electronic noise.

5.1.5 Scintillation measurements on large area SDDs

The main goal of FLARES project is to apply large area SDDs to the readout of scintillation crystals. After the X-ray characterization, a campaign of scintillation measurements has been carried out in the same setup. The total detector is composed by coupling the 3×3 cm^2 SDD to a $CdWO_4$ scintillating crystal, by the means of BC-630 optical grease.
In the first measurement, a 3×3×3 cm^3 $CdWO_4$ crystal has been used, covering all the available active area of the SDD. The crystal, coupled to the SDD, ha been put inside the LN cryostat, and acquired in the same way as the X-ray measurement (see figure 5.18). To perform the needed studies, the crystal was irradiated with an external ^{232}Th source, in order to have events up to 2615 keV. The possibility to evaluate resolution and behavior of the device at energies close to the Q values of many $0\nu\beta\beta$ candidate is necessary, in fact, to test the FLARES approach. The measurement was carried out at 150 K, to ensure the best noise conditions and also increase the light emission of the crystal [71]. The amplitude of the pulses was calculated by fitting the acquired waveform with equation (5.14), using A_{Fit} as amplitude parameter. The result of this first measurement is shown in figure 5.24. The spectrum shows all the characteristics peaks of the used source, analyzed with a Gaussian fit subtending an exponential background to extract the relative resolution at each energy. Thanks to the previously performed X-ray measurements, the electronic noise of the system is known, as well as the conversion factor between voltage and number of collected electrons (see equations (5.7), (5.9), (5.8)). With this information, it has been possible to calculate the expected statistical and electronics component of the resolution, comparing the results with the obtained total FWHM resolution. As reported in the left panel of figure 5.24, the sum of expected electronic and statistical noise contribution is smaller than the measured resolution. In particular, at 2615 keV the total FWHM is 4.1±0.2%, while the squared sum between statistical uncertainty and electronic noise is below 2%. Such result means that other factors with respect to the known ones are responsible for the energy resolution spoiling. In particular, the known charge collection inefficiency can be addressed to as a major contributor. It is reasonable to assume that after each γ event in the crystal, the emitted scintillation photons are uniformly spread on the face of the SDD. Since the used crystal covers all the available active area of the device, at least a part of this electrons is collected in region characterized by small drift fields, causing a fraction of the measured events to be detected with a reduced charge collection efficiency. As a consequence mono-energetic events in the crystal, producing on average the same number of photons, result in measured signals with non-constant average. Such effect cause the unavoidable spreading of the scintillation peaks, showing a non optimal energy resolution. In addition, the γ energy depositions happening close to the SDD-crystal contact surface produce photons collected in a more defined area of the SDD. If this area is a border one, all these photons are collected with systematically lower charge collection efficiency, resulting in an ulterior spreading of the measured peak.
After this first test, a new set of measurements has been designed to further characterize the detector. On one hand, to test the given interpretation of the limited resolution, a smaller crystal (2.3×1.5×2.3 cm^3) has been used in order to limit the effects of different charge collection efficiency. On the other hand, a dedicated crystal removal procedure has been put to test to minimize the mechanical damage of the light entrance window. As soon as the cryostat reaches room temperature, the SDD+crystal assembly is removed and placed on a flat surface. Using the BC-630 optical grease as a lubricant, the crystal is pushed away from the SDD, exploiting the opening on the teflon frame (see figure 5.17). The key point in this maneuver is not letting the crystal resting on the SDD for a too long time. In that scenario, the weight of the crystal pushes the excess optical grease outside the contact region, making the crystal more adherent to the SDD and thus more difficult

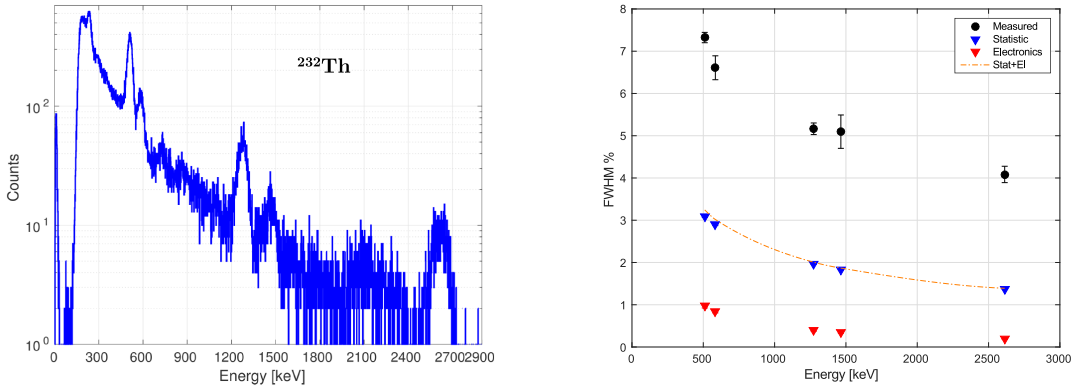

Figure 5.24: γ measurement with SDD coupled to 3×3×3 cm^3 $CdWO_4$ crystal, using a ^{232}Th source. The calibrated spectrum (left panel) shows the characteristics peak of the source. The relative FWHM (right panel) scales with the energy, as expected. At 2615 keV it reaches the value of 4.1±0.2%. This level is too high for the $0\nu\beta\beta$ requests, and appears dominated by non ideal effects, since the squared sum (orange line) between statistical uncertainty (blue triangles) and electronic noise (red triangles) is below 2%.

to remove. Thanks to the quick removal, the same SDD could be used again. The intrinsic SDD fragility is one of the key aspect to be improved, while looking at mass production of these devices. In addition, the cooling cycle was optimized, reaching a new base temperature of 125 K. To characterize this new condition, a new X-ray measurement was carried out, obtaining a new calibration factor and a new evaluation of the noise, now at the level of 16±1 RMS electrons. The value is slightly worse than what obtained at higher temperatures as a consequence of the small damage caused on the SDD by the crystal removal.
After this necessary characterization, the new crystal, wrapped in teflon tape, was coupled to the SDD. To prevent undesired movements, the crystal was placed in contact with the teflon ring surrounding the SDD (see figure 5.17). Such precaution made the whole system more stable, preventing ulterior damage of the light entrance window.
The new measurements have then been performed from 240 K to 125 K, obtaining useful information about the system behaviour. The analysis procedure has been kept identical to the previous tests, ensuring the full compatibility of the results. In figure 5.25, the amplitude spectra at different temperatures are reported. The 240 K measurement is particularly different from the others because, at that temperature, the ramp is still too long to ensure enough live time between resets, often happening in the middle of a scintillation pulse. This effect is more evident with respect to the X-ray measurements because the scintillation pulses, being ruled by the scintillation time constant of $CdWO_4$, are slower than the X-ray ones. As the temperature lowers, the mean position of the peaks increases because the phonon excitation in the crystal lattice are suppressed, favouring the radiative recombination. The total increase is ∼20%, compatible with the value reported in [71].
Considering the measurement at 125 K, each peak is characterized with a Gaussian fit subtending a linear background. Combining the obtained mean peak position and resolution with the X-ray calibration, the measured resolution is decomposed in its components and a calibration in number of detected photons can be performed. The relative FWHM resolution, reported in the left panel of figure 5.26 scales with energy, reaching the value 3.6±0.5% at 2615 keV. This value is smaller than in the case with the bigger crystal, but still fully ruled by an excess component which is the major contributor to the measured value. This effect can be linked to the side position chosen for the crystal, causing the detected photons to be measured in a low field region. Another effect of the imperfect charge collection is the asymmetry of the peaks. If different scintillation events are collected with variable efficiency, in fact, the signature corresponding to monoenergetic events in the crystal is a superimposition of peaks with different averages. Moreover, if the probabilities of detection with a certain efficiency is different for each event, the different averages have different

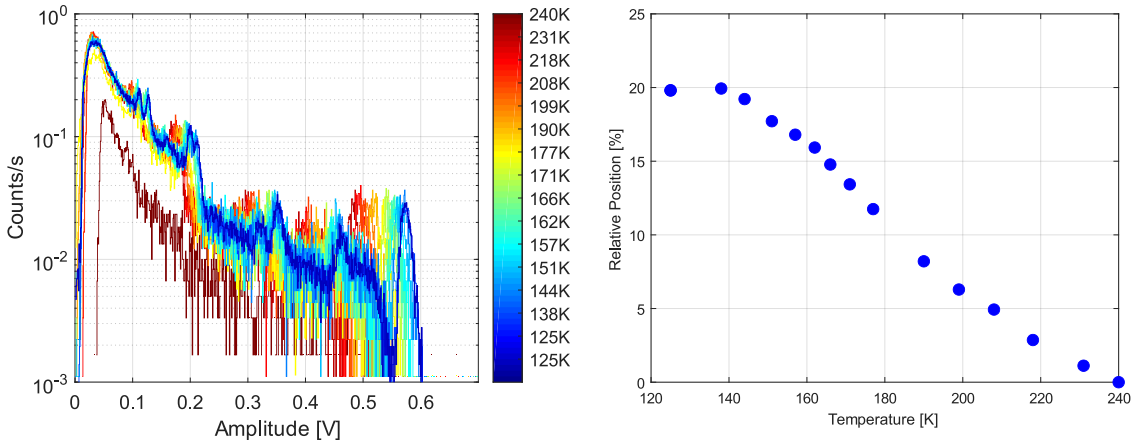

Figure 5.25: γ measurement with SDD coupled to 2.3×1.5×2.3 cm^3 $CdWO_4$ crystal at different temperatures, using a ^{232}Th source. The spectra at different temperatures (left panel) shows the characteristics peak of the source. As expected, as the temperature lowers (red to blue) the mean position of the peaks increases, since the light output of the crystal grows. On the right, the change of the 2615 keV peak position with temperature is shown, calculated as $(V(T)_{2615}/V(240\ K)_{2615}\text{-}1)\cdot 100$. The ∼20% increase is compatible with the predicted growth in literature [71].

amplitudes, resulting in an asymmetric shape of the signature. Looking at figure 5.27, the 2615 keV line presents a bump on its right-hand side, confirming this hypothesis.
In a schematic view, the signature of a monoenergetic event is a sum of single Gaussian, varying in area, average and resolution. The application of this response model to analyze the line shape of the peaks would imply the use of a fit function with a huge number of parameters. If this complete model was used, the only possible result would be a more correct evaluation of the measured resolution and not an actual improvement of the detector. In addition, the use of an overfitting model would make any evaluation fully dependent on the particular measurement setup, meaning a loss of generality in the obtained result.

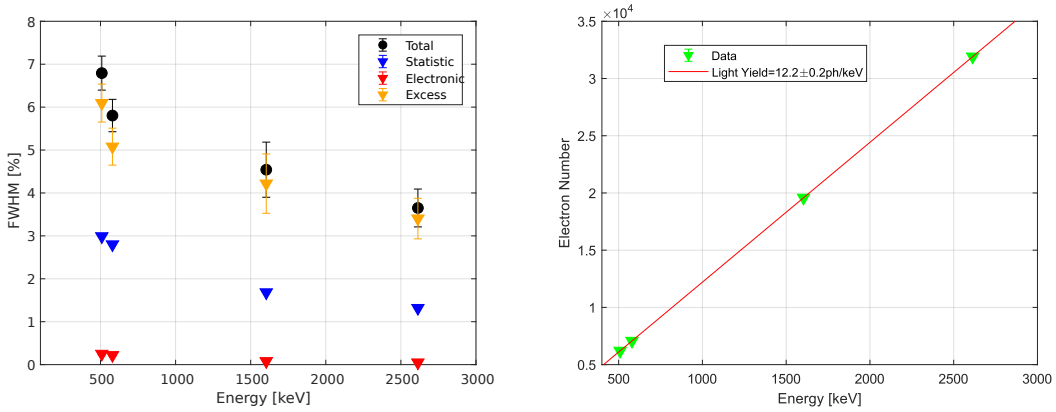

Figure 5.26: Measured resolution and light yield at 125 K with SDD coupled to 2.3×1.5×2.3 cm^3 $CdWO_4$ crystal. The relative resolution (left) scales with energy but reaches a plateau above 2 MeV, meaning that it is not ruled by statistic ($\propto 1/\sqrt{E}$, blue triangles) nor electronic components ($\propto 1/E$, red triangles). The limiting component (orange triangles) is obtained with a squared difference and is the major contributor. The errors are also wide on this parameter, meaning a non-optimal modeling of the peak shape trough a simple Gaussian. On the other hand, the measured electrons-energy calibration (right panel) shows the linearity of the detector, in the whole energy range. With a linear fit, the measured light yield is evaluated as $LY_{Measured} = 12.2 \pm 0.1$ ph/keV. Such value comprises all the detection inefficiency (photon loss, quantum efficiency, self absorption).

As a consequence, a sum of two Gaussian is used as a fit function, to take into account the

asymmetric shape in a simple way. The area ratio, as well as the mean difference, is fixed on the 2615 keV line and used to reproduce the other peaks. The resolution is taken identical on the two Gaussian in order to minimize the free parameters of the model. After the fit is performed, the resolution is evaluated as the FWHM of the total line shape. This rather simple model allows to take into account the shape of the measured peak, without adding too much complexity to the overall model. As reported in the right panel of figure 5.27, the fit gives major dominance to one of the two Gaussian, meaning that the subtending effect has not uniform probability. In particular, the structure of this sum suggest that only a small fraction of the total number of events is collected at maximum efficiency. The majority of the events, instead, suffer from the lower collection efficiency. Such result suggest that each scintillation event generates photons over inefficient areas, because both these area are large and the multiple reflections of photons inside the crystal produce uniform lightening of the crystal-SDD contact surface. The use of this fit function allows a new evaluation of the resolution, now at least partially independent by the differences in collection efficiency. As reported in the left panel of figure 5.27, in fact, the relative resolution depends on energy in the whole energy range. At 2615 keV the relative FWHM is 2.9±0.1%, significantly lower than the previous evaluated one. It although still appears to be dominated by a non statistical neither electronic component, that is although strongly reduced with this new evaluation strategy. A part of this residual excess can be attributed to the residual charge collection variation not modeled by the simple model used in the fit. The dominant Gaussian, in fact, is an approximation of the expected response function in case of continuously varying collection efficiency.
As a matter of fact, the non-uniformity in charge collection must be corrected at the SDD level, to ensure a major improvement in the attainable performances of the device. The performed analysis, alongside the X-ray measurements one, unambiguously points out that this detector feature, due to the peculiar SDD design, is a major limiting factor for the resolution of this detector.

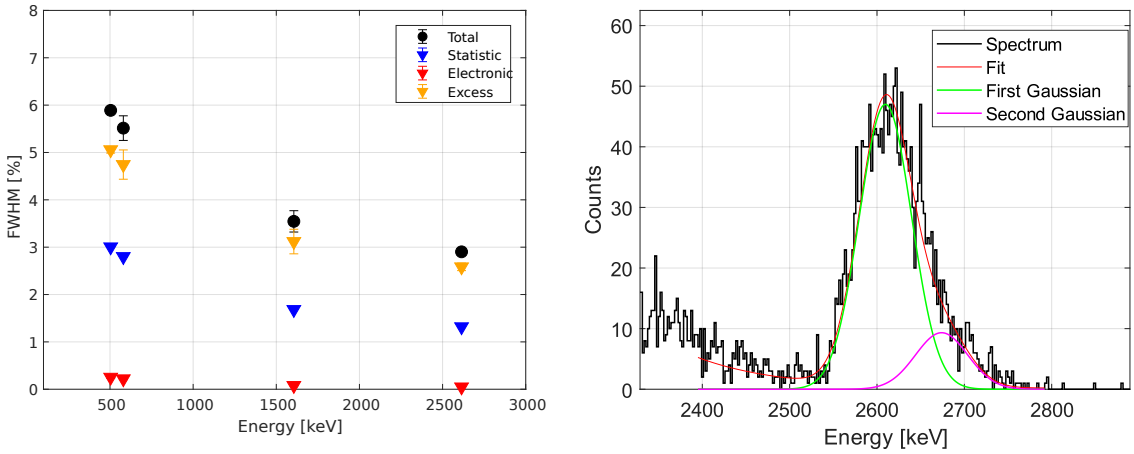

Figure 5.27: Scintillation resolution obtained with an SDD coupled to 2.3×1.5×2.3 cm^3 $CdWO_4$ crystal taking into account the asymmetric peak shape. The fit function (right panel) is the sum between two Gaussian function. The ratio between the two average values and the two areas is evaluated on the 2615 keV γ line and than used as fixed parameter when the fit is extended to the other energies. The fit gives major dominance to one of the two Gaussian, meaning that the subtending effect has not uniform probability. The obtained resolution (left panel) still presents an excess component, which still rules the attainable performances but is smaller than the one reported in figure 5.26. In particular, at 2615 keV the measured relative FWHM is 2.9±0.1%.

Alongside this evaluation, a measured electrons-energy calibration has been performed on the measured spectrum, reported in the right panel of figure 5.26. The relation between this two variables is linear on the whole energy range. This proves that the limiting factor to the resolution cannot be traced back to non-linearity effects, as validating the assumptions made on the SDD behavior. With a linear fit, the measured light yield is evaluated as $LY_{Measured} = 12.2 \pm 0.1$ ph/keV. Such value comprises all the detection inefficiency, such as surface photon losses, SDD quantum efficiency and

photon absorption in the crystal. This value is similar to the predicted value based on table 5.2, assuming a ∼50% global collection efficiency. Since the quantum efficiency of the SDD is ≤80% at the emission value of $CdWO_4$, the photon collection efficiency is ≥ 60%. This value comprehends both the surface losses and the self absorption and evaluates positively the effects of the crystal wrapping. This value implicitly takes into account also the effects of imperfect charge collection, whose absolute magnitude can only be evaluated with detailed simulation of the detector field behavior. Such simulation demand complete knowledge of the detector geometry and field structure, which is bounded by industrial secret from the SDD producer. The simulations are needed because the charge collection varies almost continuously over the surface, and is totally determined by the shape of the drift field. Without such information, only an average evaluation can be performed without an effective improvement from the obtained limits.
After the different spectral evaluations, for each temperature the characteristic rise-time of the pulses has been extracted. The parameter of interest is the τ of equation (5.14), which is proportional to the characteristic emission time of the scintillation light. Given the rise-time of X-ray measurements, the limit given by the response time of the SDD is $\sim 1\mu s$. As shown in figure 5.22, the less efficient drift fields in regions far from the anode correspond to longer pulse rise-times. This shape parameter decreases as the temperature lowers, because of electron mobility increases, reaching an almost stable condition below 150 K. The effect of low field area will be particularly evident in the scintillation measurements, because the photons irradiate uniformly the SDD-crystal contact surface. Alongisde the narrowing of charactertistic risetime, the scintillation light emission time is expected to grow as the the temperature lowers [71]. Consequently, the sensitivity of the SDD to the scintillation emission time is expected to increase as the temperature lowers.
The distribution of τ at different temperatures are shown in figure 5.28. From the highest temperature (240 K) to the middle range ones ($\mathcal{O}(190)$ K) the distribution is particularly wide and almost constant. This feature is an effect of the low drift field regions, which changes the rise-time of pulses on an event-by-event basis and reduces the sensitivity of the detector to the scintillation time. As the temperature lowers below 190 K, the increase in mobility reduces these effects that are now subdominant with respect to the scintillation time variations, that are clearly identifiable from the drift of the τ distribution. At 125 K, the average rise-time is $\overline{\tau} = 19.85 \pm 0.1\mu$s, compatible with the expected value reported in table 5.2. The meddling of SDD drift time could be included, and therefore removed, by changing the fit function used for scintillation pulses. Equation 5.14 can be modified substituting the step-function with the shape of X-ray pulses, thus trying to differentiate between these two phenomena. Unfortunately, except for the higher temperatures, the two shapes are heavily correlated, meaning that the model is over-parameterized. The use of this more complex response function would require a precise initialization of the fit parameters, based on X-ray measurement acquired in the same conditions. Since such analysis would complicate without reason the performed evaluation, the simpler function has been chosen, since it is correctly performing at the lower temperatures.
The behavior of the τ distribution at different temperatures bring a further proof that the SDD is actually sensitive to the crystal scintillation, both in amplitude and in shape. In addition, the observed features are compatible with the drift field inefficiencies, providing a further indication that such feature demands correction in order to fully unlock the performances of the device.

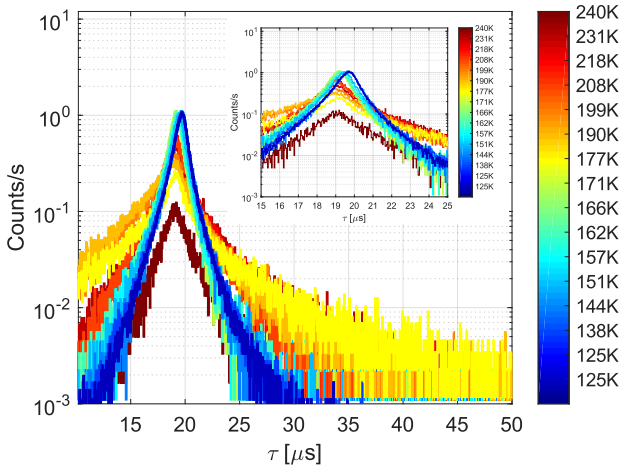

Figure 5.28: SDD+crystal rise-time distribution at different temperatures. From 240 K to 190 K (red to yellow) the distribution narrows, as an effect of the increased electron mobility. From 166 K to 125 K (green to blue), instead, the dominant mechanism becomes the scintillation time increase, causing a shift towards higher values of the distribution average. The detail shows a zoomed view of the main peak, where the drift at lower temperatures is more evident. At 125 K the average of the distribution is $\overline{\tau} = 19.85 \pm 0.1 \mu$s.

5.2 The ESQUIRE project

In developing performing scintillation detectors for the search of $0\nu\beta\beta$, a viable pathway is the study of new scintillating materials. The goal is the design of a light emitter characterized by high light output and fast emission time, to push as forward as possible the achievable performances.
A possible solution to this problem is the use of scintillating semiconductor nanocrystals [121]. These newly developed materials are characterized by $\mathcal{O}$(nm) size and have a discrete energy level structure similar to a ideal finite potential well. Given the point like structure of these materials, they are usually referred to as Quantum Dots (QD). Electrons excited to the conduction band thermalize efficiently in the lower conduction levels [122], where they can recombine with holes emitting a photon. The gap energy in these materials can be tuned by modifying the QD size, obtaining the light emission in a desired color range [123]. Such feature gives the possibility to define narrow emission spectra, characterized by high emission quantum yield and customized to meet the need of a given photodetector. The absence of non-radiative de-excitation channels makes the radiative recombination extremely quick, with scintillation emission time on the order of few ns. These outstanding performances make the scintillating QD perfect candidates for the development of innovative scintillators.
At current status, different QDs are available, in terms of different structures and constituting elements. This large choice possibility makes them versatile, since it is possible to choose the needed materials with the needed emission spectrum to fit the demands of a certain application. In particular, different QD can be built using elements with isotopes candidate to $0\nu\beta\beta$, such as Cd, Te or Se. Different studies have been performed with QDs used as doping for liquid scintillators, since these materials provide both a wavelength shifter and a source for the $0\nu\beta\beta$ [124, 125, 126]. The possibility to use these new materials to build source=detector $0\nu\beta\beta$ experiments has been investigated in the framework of the ESQUIRE (Experiment with Scintillating QUantum dots for Ionizing Radiation Events) project, which focused on testing the possibility of building scintillators fully based on this new technology [127]. ESQUIRE R&D work focused on the selection of different QDs with optical characterization, followed by a direct scintillation measurement performed with high sensitive solid state photon detectors. The baseline design is built around the use of SDDs, given their low noise performances, to guarantee the best possible energy resolution. During the R&D work, although, a SiPM detector was used for the preliminary measurements, exploiting the characteristic of these detectors to be sensitive to a small number of photons.
The final goal of ESQUIRE is to demonstrate that a nanocrystal-based scintillator can be used as absorber in a radiation measurement. To reach this goal, high concentration of QDs are needed, to guarantee enough radiation stopping power to the active part of the detector. High QD concentrations are although problematic, given the specific energy level structure of these materials. Since their band gap is responsible both for light emission and absorption, the specificity of the emission spectrum reflects in the specificity of its absorbance. As a consequence, in high density

materials, the emission of a QD is absorbed by the neighboring ones, and then reemitted with the QD quantum yield (QY). Since this value is finite, at each absorption-emission step the average number of photon is reduced, resulting in only a small light output from bulk samples. To cope with this limitation, scintillating QD are tipically used at low densities [128], or as thin films [129]. This feature poses a strong limit to the development of QD-based scintillators, since high densities of nanocrystal, generally built with high Z materials, are needed to have performing scintillation detectors. Different solutions have therefore been tried to decouple emission and absorption in these materials, introducing the so-called *Stokes-shift* between the two spectra. This effect can be achieved introducing an energy transfer mechanism from the absorber QD to a light emitting compound. In this way, the light is emitted by the latter element, while the radiation is absorbed by the former. The practical implementation of this mechanism has different possibilities, depending on the final application and from the chosen QD.
For certain QD (such as CdSe) a shell can be grown around the main crystal (CdS for CdSe), resulting in a two section core-shell quantum dot [130]. Such solution provides different advantages. By sheilding the core, the defects are reduced, leading to an increase in QY. In addition, the band-gap of the shell is designed to be smaller than the band-gap of the core, resulting in possible energy transfer between these two sections. The emission wavelength of the shell is therefore different from the core one, ensuring the Stokes-shift.
As an alternative solution, different QDs can be used to sensitize light emitting materials. In this design the nanocrystals absorb the incoming radiation energy, which is then transferred to a low-Z light emitting materials. The final result is the emission of scintillation light after a ionizing radiation event, at a wavelength avoiding its absorption by the QD. This solution is less complex than the core-shell one, since no double structure has to be grown, and can be adapted to more types of QDs. In particular, a family of nanocrystal is suitable for this application: the perovskites. The name *perovskite* was initially given to the crystal structure of calcium titanate, which was discovered in 1839 by the German mineralogist Gustav Rose and was named by the Russian mineralogist Lev Perovski. Since then, the term *perovskite* refers to all compounds with the same crystal structure. The perovskite materials have a general crystal structure described as ABX_3, where A and B are cations with varied sizes and X is an anion. A typical unit cell structure of a basic perovskite compound is shown in figure 5.29.

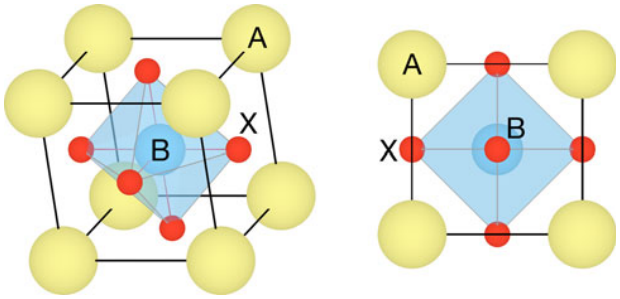

Figure 5.29: Two views of the perovskite crystal structure for ABX_3 compounds, where A and B are cations with varied sizes and X is an anion. Atoms of type A (in yellow) are positioned at the cube corners, B atoms (in blue) at the cube center, and X atoms (in red) at cube faces.

These materials show remarkable luminescent performances, and are widely investigated for application in different fields [123]. In these compounds usually the B cation is heavy, making them suitable for sensitization of light, even organic, light emitters.
Once a method is chosen for the Stoke-shift engineering, the selected luminescent compound has to be inserted in a matrix, to be used as a scintillation light emitter. The use of a specific matrix is necessary for multiple reason. Firstly, QD are produced as a powder, which is difficult to handle and to couple to a scintillation light detector. Moreover, different QDs suffer from oxidation, therefore a matrix is needed to protect them from degradation. The matrix has to be chosen to be transparent with respect to the light emission of the chosen compound, and non-interfering in the energy transfer mechanism. Both liquid or solid matrices can be used, although in the ESQUIRE R&D preference has been given to solid ones, since the coupling to photodetectors is easier in this case. In addition, the high concentration requested to build up an efficient scintillator cause the

saturation of the QD+liquid matrix solution. The consequent precipitation of the QD powder generates inhomogeneities in the sample volume, negatively affecting the energy transfer mechanism. On the other hand, using solid matrices causes the loss of the QD powder used in the construction of the sample. Such effect has a small impact if the QD can be directly produced, since their synthesis has small cost and can be performed in relatively short times. Such feature has capital importance, since makes the QD an appealing low-cost alternative to the expensive standard scintillating crystals. On the other hand, the purchase of large masses of ready-to-use quantum dots still presents consistent cost.

In between the different possible designs, the ESQUIRE R&D phase started with perovskite-sensitized light emitting compounds. The candidate design comprehends $CsPbBr_3$ perovskites coupled to an organic dye. The chosen molecule is the perylene dyad 9,9-Bis[perylene-3,4-dicarboxylic-3,4-(N-(2,5-Di-tert-butylphenyl)] (hereafter indicated as **1** or dye), characterized by a level structure matching with the perovskite one. The resulting compound has been embedded in a poly-methil-methacrylate (PMMA) matrix, to be characterized and coupled to the light detector.

Optical characterization

The first measurements have been performed at the Material Science department of the University of Milano - Bicocca. The goal of these preliminary investigation was the characterization of light emission of the synthesized QD, by the means of a photoluminescence (PL) measurement. The obtained results, reported in figure 5.30, show that the emission with and without PMMA of both the perovskites and the dye is not heavily modified. In particular, the perovskite exhibits a narrowband photoluminescence at ∼518 nm (FWHM∼25 nm) nearly resonant to the respective first absorption peak at ∼514 nm. The dye, instead has maximum emission at ∼582 nm corresponding to a ∼60 nm Stokes shift from the respective absorption edge.

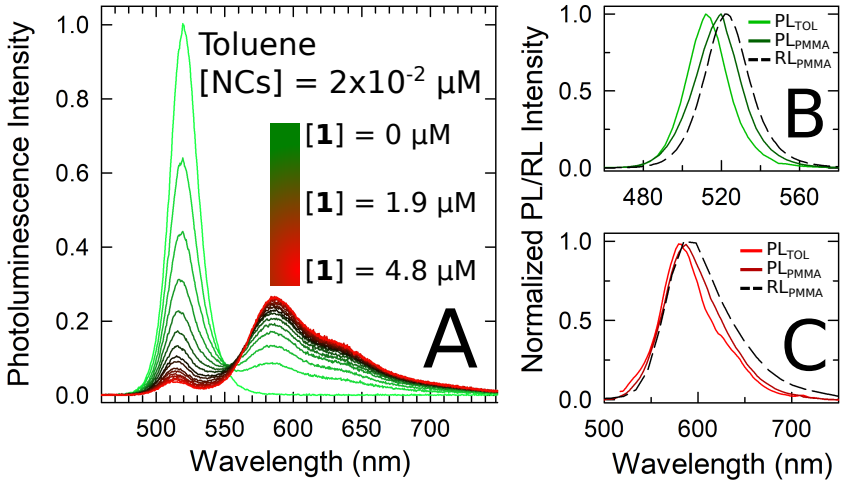

Figure 5.30: Perovskite (B) and dye (C) photoluminescence spectra. The spectra have been taken with the sample in toluene solutions (PL_{TL}), embedded in PMMA (PL_{PMMA}). The PL spectra are compared to the radioluminescence spectra (RL) with the sample embedded in PMMA (RL_{PMMA}), excited using bremsstrahlung radiation from an X-ray tube with tungsten target, operated at 30 kV. The perovskite exhibits a narrowband photoluminescence at ∼518 nm (FWHM∼25 nm). The dye, instead has maximum emission at ∼582 nm, corresponding to a ∼60 nm Stokes shift from the respective absorption edge. In A, the PL spectra of the sample varying the concentration of dye is shown. As the concentration increases (from green to red) the perovskite emission peak gets substituted by the dye one, proving the efficient energy transfer.

These characteristics answer to the design parameters needed for the prototype development. The same PL measurement have then be performed on the perovskite+dye compound, at different dye

concentrations. As the dye concentration grows with respect to the perovskite one (panel A in figure 5.30), the perovskite emission peak gets substituted by the dye one. The total integral of the emission spectrum remains constant over this change, proving that the energy transfer is efficient. After this study, the selected concentration of perovskite in the final PMMA embedded sample has been fixed to 2% of the total sample weight, and the dye concentration has been fixed to 0.115% of the total weight. After the ratio has been fixed, the timing of light emission has been characterized with time resolved photoluminescence. The PMMA-embedded mixture has been irradiated with 400 nm light for a short time to excite the perovskite, and the subsequent light emission has been measured in its time evolution. The resulting curve, reported in figure 5.31, has been fitted with a single exponential, obtaining a main relaxation time of ∼3.9 ns. This result further proves the goodness of the scintillation mechanic of the perovskite+dye mixture, characterized by quick emission times.

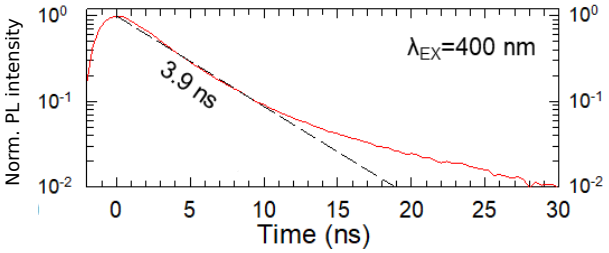

Figure 5.31: Time evolution of perovskite+dye light emission. The mixture was excited with a 400 nm light and the corresponding light output shows a main relaxation time of ∼3.9 ns.

To test more in depth the response to ionizing radiation of the chosen scintillator, a radioluminescence (RL) measurement has been performed. The emission from the dye+perovkite embedded in PMMA has been compared to both the dye-only emission and a BGO sample one. The BGO is used as a standard reference, being a crystal widely used for γ-ray spectroscopy. The results of this measurement are reported in figure 5.32. This comparison shows that the dye alone does not respond upon X-ray excitation, whilst the perovskite+dye compound presents an intense emission. Such results unambiguously proves the effectiveness of the sensitization, through which the perovskite allows the dye to respond upon ionizing radiation interaction. Moreover, the emitted light from the sensitized dye has comparable emission with respect to the BGO crystal, proving the potentiality of this combination. The narrow emission of the system can also be appreciated by comparing with the BGO one, characterized by a wider emission spectrum.

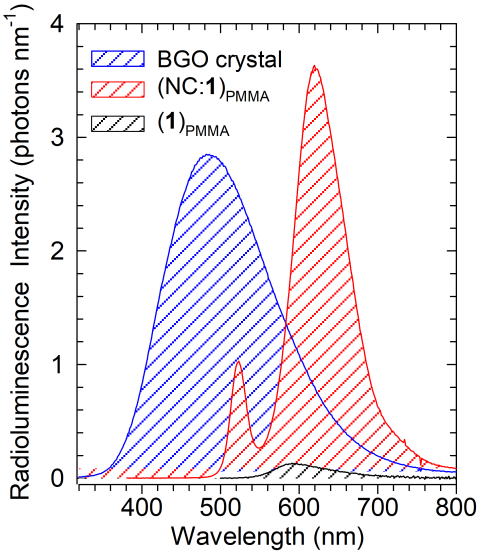

Figure 5.32: Radioluminescence measurement of the Perovskite-sensitized dye (red dashed spectrum)). The main peak is due to the sensitized dye emission, but a residual pure perovskite light is still visible around 500 nm. This sample is compared to the dye embedded in the PMMA (grey dashed spectrum) and to the BGO powder (blue dashed spectrum). The comparison shows that the dye alone does not respond to the X-ray efficiently, proving the effectiveness of the sensitization, and that the Perovskite-sensitized dye has analogous emission capability if compared to a standard scintillating crystal.

This result needs a careful interpretation although. The measurement have been performed with an high flux of soft X-ray, produced with tungsten-based tube operated at 30 kV. Since the maximum energy is 30 keV and the spectrum is continuous, the most probable energy of the flux is around 15

keV. Given the energies in play, only the most superficial section of the samples is excited, whilst the bulk of the produced specimen cannot be investigated. As a direct consequence, the measured RL spectrum does not take into account the self absorption inside the sample. Other measurements are therefore needed to quantify the actual bulk+surface properties of the produced scintillator. To characterize these features, two distinct samples have been produced with the perovskite+dye in PMMA:

1. a 2 mm thick disk of radius 1.5 cm, from now on referred to as disk, used as a scintillator prototype;

2. a thin layer (300 μm) deposited on a side of a 0.5x0.7x15 cm^3 optical grade PMMA waveguide, from now on referred to as bar, used to test the suppression of reabsorption losses after different interactions.

A PL measurement has been performed on the disk, to investigate the effect of the bulk on the scintillation light output. The absorbance spectrum has also been measured, to check if the sample is transparent to its own emitted light. The absorbance quantifies the fraction of light, at a certain wavelength, that can cross the disk thickness. It is measured by difference with respect to the transmitted intensity measured without a specimen between light source and light detector. The result of these measurements are reported in figure 5.33.

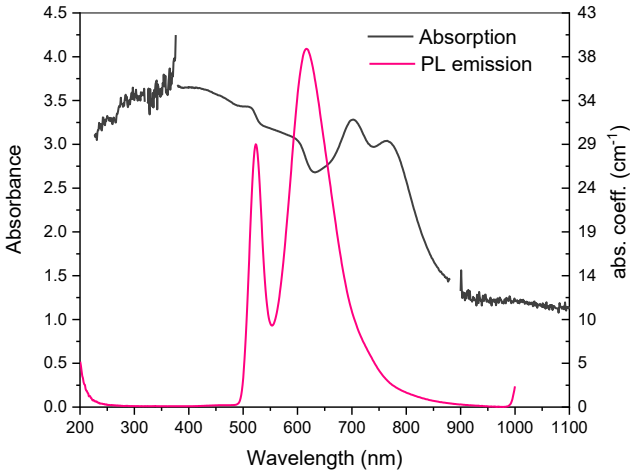

Figure 5.33: Photoluminescence (red) and absorption (black) measurement on the disk specimen with Perovskite+dye in PMMA. The PL emission is compatible with the predicted one, proving the conservation of the optical emission properties. The absorption curve, instead, is characterized by low energy (high wavelength) absorption peaks and by a general high level of absorption. Such feature suggest the creation of anomalous molecular states in the sample, spoiling the transparency of the scintillator.

The PL emission is compatible with the results in figure 5.30 A, proving that the polymerization conserved the optical emissive properties of the sample. The absorption spectrum, instead, shows different interesting fuatures. A small absorption peak is present at the perovskite emission, above 500 nm, because of the predicted perovskite absorption behaviour. The main emission peak, instead, corresponds to a relative minimum in the absorption, proving that the material is more transparent to its emitted light, as by initial design. The unexpected behaviour is the general magnitude of the absorption curve, extremely high at all the wavelengths. In particular, it is also characterized by high wavelength (low energy) absorption peaks, around 700-800 nm ($\sim$0.5 eV). This features suggest the creation of anomalous molecular states in the sample, which spoil the transparency of the scintillator. The high perovskite concentration and the temperatures needed for PMMA polymerization are the addressed motivation for such behaviour. At a visual analysis, moreover, the samples shows inhomogeneous structures, produced by the anomalous polymerization. As a consequence, the disk specimen is not expected to be transparent, and only its surfaces are

efficient light-emitters. This result shows that the polymerization has to be addressed in future developments, to ensure the realization of transparent-bulk scintillating materials based on this technology.
The bar specimen has been used alongside the disk to check the reabsorption after multiple interactions with the perovskite+dye blend. The functioning scheme of this specimen is reported in figure 5.34.

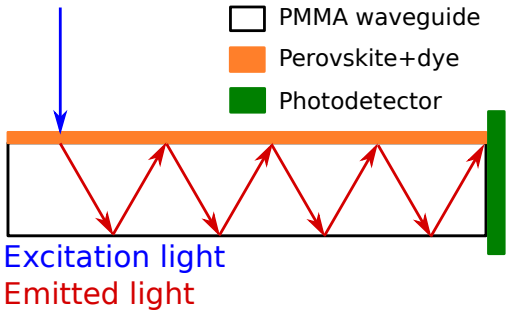

Figure 5.34: Functioning scheme of the bar specimen. After each interaction with the perovskite+dye layer, the emitted light can be reabsorbed. This will cause a difference in the measured light amplitudes depending on the excitation position.

The layer of perovskite+dye is excited at different position, while at a fixed end of the bar the photons are collected by a photodetector. The excitation causes the emission of photons by the perovskite+dye blend, trapped inside the PMMA waveguide. During the different reflections, the emitted photons interact with the perovskite+dye layer many times, reproducing the effect of multiple bulk interactions. The light detected by the photodetector, therefore, is affected by the self-absorption coefficient of the mixture. A difference in measured light intensity is therefore expected as the excitation position changes. In particular, in case of heavy self-absorption, the measured light should decrease as the excitation position gets far from the photodetector end. Alongside the optical effect, also the efficiency of photon collection decreases as the interaction position gets farther from the photodetector end. For close-up interactions, in fact, the number of photons emitted by the perovskite+dye blend and detected without reflections is higher than the case of far interactions. As a consequence, any measured decrease includes also a geometric efficiency factor reducing the amount of detected light.

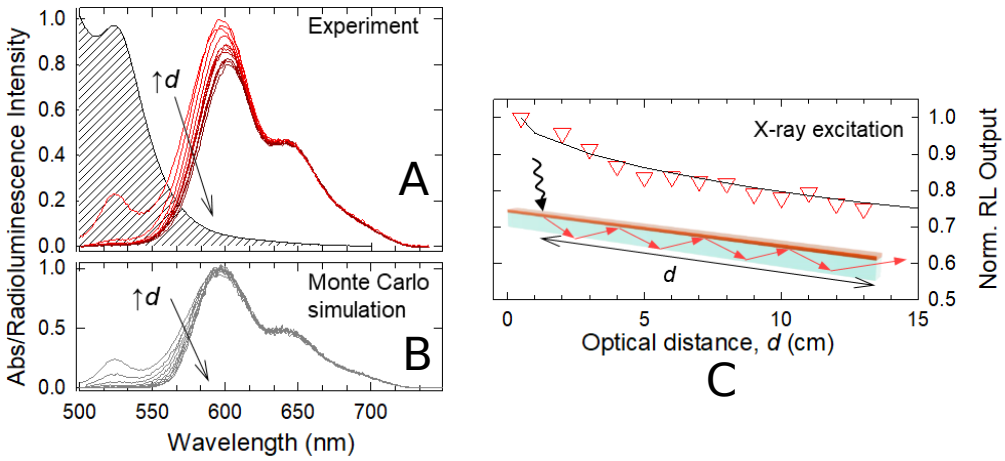

Figure 5.35: Radioluminescence spectra on the bar specimen at different distances from the photodetector. Measured data (A) are compared to Monte Carlo ray-tracing simulations (B), showing good agreement. The absorption spectra is also reported, to permit the interpretation of the measured changes. The decrease in absolute RL intensity (C) shows a ∼25% drop at ∼12 cm, both measured and predicted.

The excitation has been performed with the X-ray source used for the measurement in figure 5.32, focused at a specific distance d from the photodetector. The RL spectra is collected and difference distances, to evaluate the absorption. To ensure the understanding of the results, a ray-tracing Monte Carlo simulation has been performed and then compared to the measured data. The results

are reported in figure 5.35. The measured RL spectra show a decrease in the total integral, but this reduction is not equal at all wavelengths. The intensity of the pure perovskite peak around 500 nm decreases with distance, as predicted by the general behavior of these materials. This effect is strengthened by the aformentioned geometric efficiency, since as d grows the number of perovskite-emitted photons detected without reflection decreases. The energy-transfer dye emission, instead, decreases less, following the absorption spectra of the perovskite+dye blend. In particular, the highest portion of the emitted spectrum is almost untouched by the reabsorption, showing the effect of the used blend. The same results are shown in the Monte Carlo simulations, proving the effectiveness of the model and the given explanation to the phenomenon. The global integral reduction, reported in figure 5.35 C, shows a ∼25% drop at ∼12 cm. The slope of this reduction is small, therefore no major decreases are expected even if the number of multiple absorption-emission sequences grows. The optical measurements performed on the bar show the effect of the energy transfer-induced Stoke-shift, wich reduces the reabsorption of photons. This results proves that the designed blend effectively has the required properties. The polymerization in bulkier structures, although, induces different problems, thus limiting the blend to surface application at this stage of the R&D project.

Ionizing radiation measurements

To fully characterize the scintillation performances of the perovskyte-sensitized dye, a series of dedicated ionizing radiation measurements has been performed, coupling both the disk and the bar specimens to a SiPM photon detector. The SiPM used has a 6x6 mm^2 area, subdivided in 14400 pixels with 50 μm pitch. Each of these cell acts as an avalanche photodiode, sensitive to a single photon interaction. The total SiPM output is the sum of the voltage of the activated pixels, proportional to the number of detected photons. This proportionality is exact if each cell has detected a single photons, while multiple photons simultaneously interacting in a single cell are not detected.
The SiPM signals are acquired with a programmable oscilloscope with a sampling frequency of 2 GHz and 12-Bit resolution. The acquired waveforms are then stored and analyzed off-line with a custom MATLAB^{TM} software. The signal intensity is evaluated as the maximum voltage of the waveform. Such evaluation is correct since the examined scintillating samples are characterized by ∼3 ns scintillation time, while the SiPM integration time with the used electronic chain is $\mathcal{O}$(100 ns). As a consequence, the acquired signals integrate all the emitted photons, without the need to perform a numerical integration of the pulses.
Each activated cell corresponds to a fixed increase in voltage at the SiPM output. The determination of this value must be performed through a calibration measurement. The SiPM is switched on with a basing voltage of 55 V and it is acquired with a low trigger threshold, chosen to acquire also the single cell events. The acquired spectrum shows a series of equally spaced peaks, corresponding to the activation of different cells. Each peak is fitted with a Gaussian function to extract the central position and the resolution, building the voltage-number of active cells curve. A linear function is used to fit this curve, extracting the conversion factor from measured voltage to number of active cells. In figure 5.36 the calibrated spectrum of the low threshold measurement is reported, showing the discrete sequence of events corresponding to the activation of 1 to 4 cells used to calculate the calibration. The voltage equivalent of a single active cell is 13.4±0.5 mV. With the used electronics dynamic range, such configuration works if less than ∼300 cells are simultaneously activated. This configuration has been chosen with an high gain in order to be sensitive to the smallest possible amount of emitted light. Both the disk and the bar specimens are, in fact, expected to emit only a small amount of scintillation photons on the basis of the optical characterization previously performed.
Given the results of optical characterizations, only the surface section of the specimen provides efficient scintillation. As a consequence, α particle were used to excite the luminescence of samples. The high ionization density provided by these particles, in fact, maximizes the number of emitted

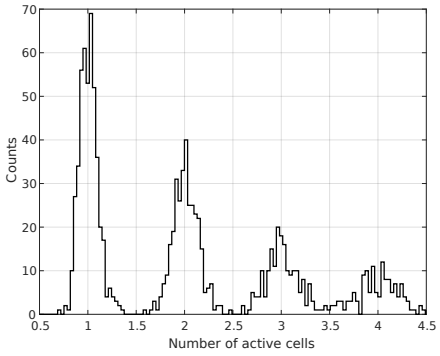

Figure 5.36: SiPM calibration spectrum, showing the peaks corresponding from 1 to 4 activated cells. The voltage equivalent of a single cell is 13.4±0.5 mV.

and extracted photons. Two radiation sources have been used in particular: a ^{241}Am superficial source and a ^{224}Ra source directly deposited on the specimen. The latter source is produced by facing a surface ^{228}Th source to the specimen under high vacuum conditions. The α decay of ^{228}Th gives a recoil energy to the ^{224}Ra daughter nucleus of $\sim$100 keV, thanks to which the nucleus exits the source and deposits on the specimen. This deposition procedure is performed over 3 days, corresponding to the half-life of ^{224}Ra, to ensure a consistent deposition of the source. Having the source directly deposited on the specimen increase the geometrical efficiency, thus making the measurement easier. The implanted source is superficial by construction, and excites the desired section of the specimen. On the other hand, the ^{241}Am source is external, therefore it has to face the desired portion of the specimen. As a consequence, in the measurements with ^{241}Am, the specimen is not directly couple to the SiPM, which reads the light coming out from the facing portion of the specimen. This configuration will be referred to as reflection, and is characterized by less light collection efficiency due to the distance between the specimen and the light detector. The avaliable excitation energies are the 5.5 MeV single α emitted by ^{241}Am or the different αs emitted by ^{224}Ra and by his daughters, ranging from 4 to 10 MeV. Basically all the emissions of the bottom section of the ^{232}Th chain are available, resulting in a non monochromatic source. This characteristics makes the acquired results more difficult to be interpreted, but it is also expected to give higher light outputs.

The disk specimen has been firstly measured with the ^{241}Am source, in the reflection configuration. In figure 5.37 the corresponding spectrum is shown, alongside the measurement performed without the specimen. This additional measurement allows to evaluate the effect of direct source-SiPM events, constituting a background for the searched light emission signal. Two different thresholds where used for the two acquisition to ensure the acquisition of enough statistics in the non-specimen case. The events at higher number of cells are, in fact, unlikely when no light-emitting specimen is used. The light output is therefore evident, proving the emission of scintillation from the surface of the disk specimen. There is no evidence of the α peak, as a consequence of the lack of homogeneity in the distribution of scintillating nanocrystals in the sample. In addition, the measurement were not performed under vacuum due to technical limitations of the used setup. The air between source and specimen caused an unavoidable degradation of α particles, further complicating the definition of a clear spectrum. The discrete structure showing the different activated cells is not present because of the limited bit-depth of the used digitizer.

The sample has then been contaminated with the ^{224}Ra source, coupled to the SiPM on the contaminated surface and measured. In this configuration, higher energies are deposited in the specimen and more photons are collected by the SiPM. As a consequence, the measured signals saturate the whole electronic chain. To increase the dynamic range of the acquisition, the biasing voltage of the SiPM has been lowered from 55 V to 53.5 V and 53 V. In these configurations, the SiPM gain reduces and the pulses stop saturating the readout chain, allowing the evaluation of the maximum emitted light. In the left panel of figure 5.38, the voltage spectra at different biases are reported. As expected, as the bias lowers, the saturated pulses reduce. At 53 V the number of saturated events is negligible. At each bias the SiPM has been calibrated, obtaining the evaluation

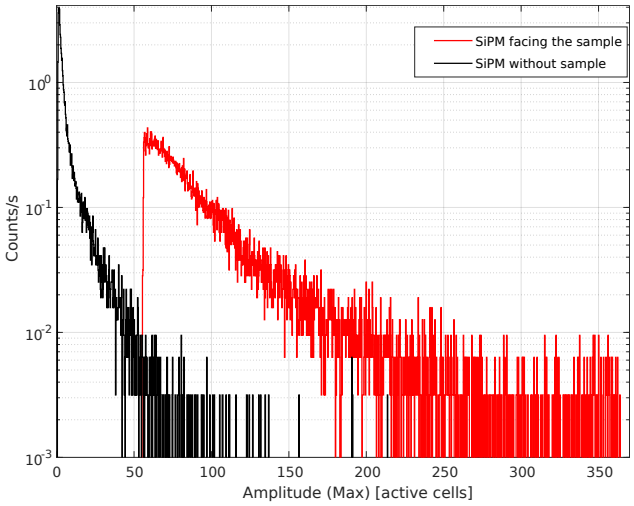

Figure 5.37: Disk specimen measured with ^{241}Am (red). The spectrum is compared with the same detector measured without the specimen but with the source (black). The threshold are different to ensure enough statistics in the non-specimen case. The effect of light output is evident proving the emission of scintillation. There is no evidence of the α peak, as a consequence of the air between source and specimen, causing an unavoidable degradation of α particles. The discrete structure showing the different activated cells is not present because of the limited bit-depth of the used digitizer.

of the detected photon number. The corresponding spectra are reported in the right panel of figure 5.38. At 53 V, the maximum number of activated cell is ∼800-900. This number of simultaneously activated channels is due to the scintillation of the perovskite specimen, proving the performances of this design.
With this deposited source different α particles are responsible for the light emission. The different energies involved in the excitation contribute in making the measured spectrum difficult to be interpreted. In addition, the density of scintillating nanocrystals in the specimen is not uniform, in the mean interaction range of α particles. Such features cause the absence of full energy peaks in the spectrum. As a consequence, the light yield cannot be determined.
To ensure such evaluations new samples are being designed, to identify the proper polymerization mechanism ensuring the conservation of the observed optical properties.

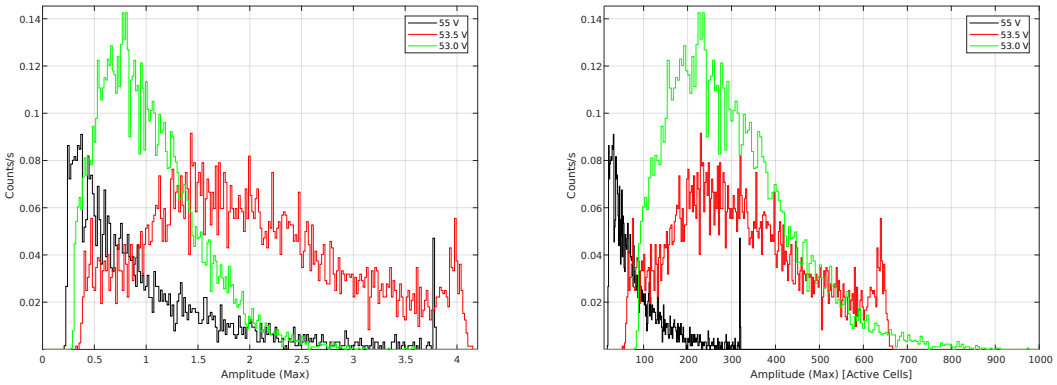

Figure 5.38: Disk specimen measured with ^{224}Ra implanted source, acquired with different biasing voltages. As the voltage lowers, the gain of each SiPM cell decreases, reducing the number of saturated events. The uncalibrated spectra (left) show the saturation peak decreasing as expected. For each voltage value the spectrum is calibrated, obtaining the active cell values corresponding to the saturated events (right). With the increased energies and the augmented light collection efficiency, up to 600 cells are simultaneously lit, proving the existence of emitted scintillation light. The absence of peaks impedes the evaluation of the light yield, but the light emission is proved.

After the disk characterization, measurement with the bar specimen have been performed. The measurement have been carried out following the scheme of figure 5.34, using ^{241}Am as exciting radiation. The ^{224}Ra cannot be used fruitfully with this specimen, since the localized implantation cannot be performed with enough precision. In addition, the decay time of the implanted source forces the measurement at different position to be performed at least 15 days away one from the other.
On the other hand, the ^{241}Am source can be moved easily over the bar, ensuring a quick screening. To further enhance the excitation position precision, a teflon wrapping has been used to mask the light emitting sample from α particles.
Three positions have been measured: 1 cm from the SiPM, 10 cm and 15 cm. The resulting spectra are reported in figure 5.39. As the distance increases, the rate decreases in the region below 75 active cell; the spectral shape, instead, remains constant. In particular, the events with highest number of active cells are almost constant in the different spectra. The independence of the spectral shape from the excitation position confirms essentially reabsorption-free waveguiding of scintillation light in the PMMA bar. This result is a confirmation of the optical characterization reported in figure 5.35. Such proof states unambiguously that the perovskite+dye blend is characterized by efficient light emission, when no PMMA polymerization is involved in the creation of a bulk structure.

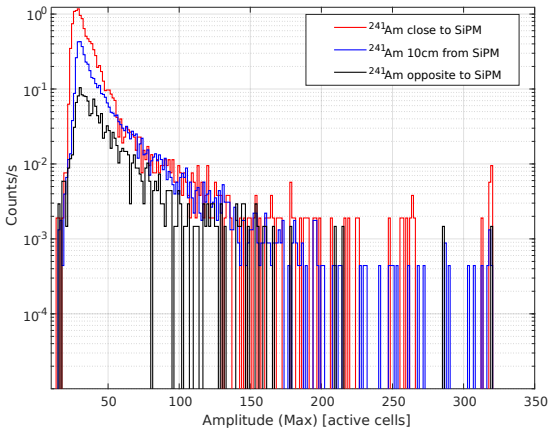

Figure 5.39: Bar speciment excited with ^{241}Am at different distances from the SiPM. As the distance increases, the overall rate decreases in the region below 75 active cell. The events with highest active cells remain although constant, proving the low reabsorption of the sample.

This evaluation adds an ulterior proof to the goodness of the chosen technique to build new generation scintillation detectors, while posing the need to define a new method to realize a bulk scintillator, through which define a new scintillator prototype.

5.3 Summary of the results

5.3.1 FLARES

The FLARES project proposes a new approach to the search of $0\nu\beta\beta$, based on the application of SDDs to detect the scintillation light of inorganic crystals containing the $0\nu\beta\beta$ candidate isotopes cooled at 120K. This proposal has the chances to meet all the desired characteristics for a $0\nu\beta\beta$ detector, because scintillators allow easy mass scalability, background reduction tools and stability over long measurement periods, while the SDDs used as photodetectors provide efficiency in light collection and low electronic noise. Moreover, the cooling at liquid nitrogen temperatures enhances both the properties of SDDs and of the scintillating crystals. The final goal of the project is the definition of a scintillator prototype with FWHM energy resolution below 2% at the Q value of the $0\nu\beta\beta$ candidate under investigation.
The FLARES R&D program has been devoted to investigate the crystal and SDD properties, to check whether if the initial assumptions of the projects were correct.
On the crystal side, the properties of $CdWO_4$ crystal have been investigated. Thanks to dedicated measurement, it has been shown that is light-energy non proportionality can be reduced by the full integration of the emitted scintillation photons. This process removes a possible resolution limit, thus increasing the detector performances. In addition, different materials have been tested to find an optimal configuration to maximize the scintillation photon collection. The best results have been obtained with a mixed rough/smooth texture on the crystal, and with the teflon tape as wrapping material.
After the crystal characterization, two SDD devices have been used to measure the final resolution performances: a pixelate SDD with 2x3 square cells each of which with 16 mm^2 area and a single-pixel SDD with 9 cm^2 area.
The pixelate SDD allowed to reach a 3.09±0.05% FWHM resolution at 2615 keV, dominated by a contribution different from the sum of electronic noise and statistical fluctuations. This excess component has been traced back to the residual uncorrected gain differences between the different cells and to the self absorption of photons in the crystal [116].
The single anode SDD is the biggest device of its kind with a single-point readout. The first tests, performed with X-ray measurement, showed good noise performances, proving the efficient design of the detector. Subsequent tests showed that the variation of the drift field across the SDD surface affects the electron propagation and the charge collection. As a consequence, this device has only a small active area where the electron drift occurs without losses. These characteristics affect also the response to scintillation events, causing the total FWHM energy resolution to be negatively affected. To partially take into account the charge collection inefficiency, a dedicated fit shape has been used to extract the FWHM resolution, obtaining a final result of 2.9±0.1% at 2615 keV. Such resolution is on the order of magnitude of the searched value, but is still dominated by an excess component localized in the charge collection inefficiency of the device.
To address the discovered limitation, a new SDD design has been developed in collaboration with FBK, Trieste University and Trieste INFN department. These new devices implement a new field geometry with increased drift field, thus obtaining a better charge collection efficiency. Moreover the optimised design produces a new patent on SDD device. The first new generation devices are in production, and will soon be available for the first measurements.

5.3.2 ESQUIRE

The ESQUIRE project is focused on the design of a quantum dot (QD) based scintillation detector for the search of $0\nu\beta\beta$. The QDs are characterized by high light emission in short times, but are limited in the application to standard scintillation detectors because their absorption and emission spectra overlap. This characteristic cause the reabsorption of the emitted light in large bulk samples, making it impossible to build large volume scintillators.

This limitation can be overcome with different solution, that have to be specifically designed and optimized for the chosen QD sample. The initial ESQUIRE R&D work focused on the $CsPbBr_3$ perovskite QD, used in combination with an organic molecule acting as a light emitting dye. The perovskite+dye blend splits the radiation absorption (both ioninzing and visible) from the light emission, using the heavy elements of the perovskite as absorbers and the dye molecule as emitter. This process is called sensitization of the dye and is based on the energy transfer phenomenon, thanks to which the energy absorbed by the perovskite levels is transferred to the dye scintillation centers. Such strategy decouples emission from absorption, resulting in a more efficient light-emitting material.
The optical tests performed on the produced samples proved the efficiency of the sensitization process, thanks to which the dye molecule is able to efficiently respond to ionizing radiation. In addition, the self absorption of the blend was proven to be effective. Unfortunately, the inclusion of the perovskite+dye in a solid PMMA matrix, to build the first bulk sample, spoiled the emission properties of the device, resulting in an almost opaque sample. A possible reason for this characteristic is the creation of inhomogeneous structures in the final specimen behaving as molecular states and thus increasing the total absorption.
Different ionizing radiation measurement with α sources have then been performed on the realized specimen, exciting the surface scintillation layers. The result proved the emission of scintillation light, although no light yield could be evaluated since both the inhomogeneity of the sample and the degradation of α particles prevented the deposition and detection of monochromatic events.
These first development steps proved the feasibility of the ESQUIRE goal and allowed to identify the steps needed to increase the detector performances. In particular, both new polymerization methods are being defined to create bulk samples of scintillating perovskites and new QD types are being investigated.

Chapter 6

Conclusion

The work of my PhD thesis has been devoted to the application and development of scintillation detectors for the study of $0\nu\beta\beta$. This class of detectors provides flexibility in application and performing features, making them ideal candidates to build high performance detectors for rare events. To accomplish this goal, a scintillation detector has to be optimized to reach performing energy resolution. Two possible strategies to solve this problem have been investigated in my work: the scintillating bolometers and the optimized scintillation detectors.
On the scintillating bolometers side, I took part in the CUPID-0 experiment from the beginning of the data acquisition. CUPID-0 is the first experiment applying the technique of scintillating bolometers on large scale using ZnSe scintillating crystals enriched in ^{82}Se, an isotope candidate to $0\nu\beta\beta$. Each of the 26 ZnSe building the CUPID-0 tower is operated as a bolometer and faces to two germanium bolometric light detectors, through which the scintillation light emitted by the crystal is detected. The combination of heat signal from the ZnSe and light signal from the light detector guarantees performing energy resolution and good background rejection capabilities, thanks to the shape analysis of the light pulses. I took part in the analysis of the collected data to extract the limit on the $0\nu\beta\beta$ of ^{82}Se, in particular defining an algorithm to decorrelate the light and heat amplitudes to improve the resolution. I also took part in the definition of the background model for the experiment, defining a method to extract a prior on the surface α contamination through the study of delayed coincidences in the detector. The successful definition of the background model then paved the way to ulterior studies on the different background components, with particular interest on the $2\nu\beta\beta$ decay of ^{82}Se.
In particular, I studied the effect of the violation of Lorentz symmetry in the $2\nu\beta\beta$ spectral shape. The violation of this symmetry is described in several Standard Model Extensions and acts on the momentum of neutrinos. This interaction modifies the $2\nu\beta\beta$ spectrum with an additional component with spectral index 4 (phase space $\sim (E - Q_{\text{value}})^4$), whose normalization depends on the coupling parameter $\mathring{a}^{(3)}_{\text{of}}$. In particular, introducing the modified $2\nu\beta\beta$ in the background model as an ulterior component, allowed the extraction of a limit on $\mathring{a}^{(3)}_{\text{of}}$. I analyzed the effect of systematic uncertainties on this limit, taking into account the nuisance parameters, the model assumption on source localization and the eventual presence of a pure beta emitter contamination. The results of these tests have been combined to obtain a posterior distribution for $\mathring{a}^{(3)}_{\text{of}}$, summarizing the different systematic uncertainties. From this distribution I extracted the final limit of $\mathring{a}^{(3)}_{\text{of}} < 4.1 \cdot 10^{-6}$ GeV. This result is competitive with the currently published ones, especially considering the low exposure of CUPID-0.
Alongside this analysis work, I performed several R&D studies on improved scintillation detectors, trying to develop a performing scintillator combining light emitting crystals with solid state light detectors.
On the light detectors side, I worked with silicon drift detectors (SDD) with large area and single

collection anode. In particular, I tested devices produced by Fondazione Bruno Kessler (FBK) in the framework of the RedSOX project, characterized by 9 cm^2 area: the biggest devices ever produced with a single readout point. To characterize these detectors, a liquid nitrogen cryostat was used, operating between 250 K and 120 K. Through different X-ray measurements the excellent noise performances of these devices have been assessed. The calibration in number of measured electrons was also evaluated, to allow a detailed study of the scintillation measurement. After the initial X-ray measurement, different test with $CdWO_4$ crystals coupled to the SDD have been performed. The $CdWO_4$ scintillating crystals has been chosen as it contains Cd, an element with an isotope candidate to $0\nu\beta\beta$: ^{116}Cd. To optimize this crystal, the best wrapping to maximize the light collection efficiency has been selected and the variation of light emission non proportionality with energy has been studied, showing that the full integration of the scintillation signal allows the reduction of this non-ideal feature. After these preliminary characterization, the attainable energy resolution of the $CdWO_4$+SDD system has been evaluated with a γ-ray measurement. The measured resolution is greater than the sum of statistical fluctuation and electronic noise, evaluated thanks to the X-ray measurements. This behavior can be addressed to the variable efficiency in charge collection over the surface of the SDD, due to the shape of the drift field. This assumption has been put to test with a dedicated X-ray measurement, performed with different sources located over different regions of the SDD. The results showed a difference in the SDD response variable with the interaction position, thus identifying an hardware limit to the attainable SDD performances. Knowing this limitation, a new set of SDDs has been produced with an improved design, in collaboration with FBK, Trieste university and Trieste INFN department. These new devices implement a new field geometry with increased drift field, increasing the charge collection efficiency. The first batch of these new detectors is under production, and will be tested in the next months.

Besides the work with standard scintillating crystals, I also studied the possibility to use nanocrystal-based compounds as scintillation emitters. These materials are subject to great interest in the current technological landscape, and provide fast and intense light emission in a narrow wavelenght region. The limit to their application in large volumes is their high absorbance, which limits the total light emitted by bulk samples. In the framework of the ESQUIRE project, a solution to this problem has been investigated testing the light emission of an organic dye sensitized with $CsPbBr_3$ perovskites. This blend is characterized by a decoupling of emission and absorption bands, increasing the total light output. The first results obtained on different samples are encouraging, since a light emission subsequent to a ionizing radiation event could be proved. To further increase the obtained results, the production of new samples featuring an improved engineering of the blend and new families of nanocrystals has begun, providing new samples for this application.

The scintillation detectors, in their different implementations, are a versatile tool to be applied in the search of $0\nu\beta\beta$. The CUPID-0 experiment, in particular, showed the potentialities of scintillating bolometers, reaching noticeable results even with a limited exposure. This remarkable demonstrator paved the way to the next generation CUPID experiment, proposing the application of this technique on the scale of CUORE detector, which demonstrated the possibility to operate 1000 crystal as bolometers in a single cryostat. On the other hand, the small R&D projects I took part in allowed to outline a possible new way of building scintillation detectors, considering both new light detectors and new scintillating compounds. Such array of possibilities highlights the potentialities related to this family of detectors, which is far away from being totally exploited and demands a continuous work to be made as performing as it actually can be.

Bibliography

[1] M. Tanabashi et al. "Review of Particle Physics". In: *Phys. Rev.* D98.3 (2018), p. 030001. DOI: 10.1103/PhysRevD.98.030001.

[2] Nicola Cabibbo. "Unitary Symmetry and Leptonic Decays". In: *Phys. Rev. Lett.* 10 (1963), pp. 531–533. DOI: 10.1103/PhysRevLett.10.531.

[3] Makoto Kobayashi and Toshihide Maskawa. "CP Violation in the Renormalizable Theory of Weak Interaction". In: *Prog. Theor. Phys.* 49 (1973), pp. 652–657. DOI: 10.1143/PTP.49.652.

[4] Y. Fukuda et al. "Evidence for oscillation of atmospheric neutrinos". In: *Phys. Rev. Lett.* 81 (1998), pp. 1562–1567. DOI: 10.1103/PhysRevLett.81.1562. arXiv: hep-ex/9807003 [hep-ex].

[5] Q. R. Ahmad et al. "Direct evidence for neutrino flavor transformation from neutral current interactions in the Sudbury Neutrino Observatory". In: *Phys. Rev. Lett.* 89 (2002), p. 011301. DOI: 10.1103/PhysRevLett.89.011301. arXiv: nucl-ex/0204008 [nucl-ex].

[6] P. Adamson et al. "Measurement of the Neutrino Mass Splitting and Flavor Mixing by MINOS". In: *Phys. Rev. Lett.* 106 (2011), p. 181801. DOI: 10.1103/PhysRevLett.106.181801. arXiv: 1103.0340 [hep-ex].

[7] K. Abe et al. "Measurement of Neutrino Oscillation Parameters from Muon Neutrino Disappearance with an Off-axis Beam". In: *Phys. Rev. Lett.* 111.21 (2013), p. 211803. DOI: 10.1103/PhysRevLett.111.211803. arXiv: 1308.0465 [hep-ex].

[8] B. Pontecorvo. "Neutrino Experiments and the Problem of Conservation of Leptonic Charge". In: *Sov. Phys. JETP* 26 (1968). [Zh. Eksp. Teor. Fiz.53,1717(1967)], pp. 984–988.

[9] Ziro Maki, Masami Nakagawa, and Shoichi Sakata. "Remarks on the unified model of elementary particles". In: *Prog. Theor. Phys.* 28 (1962), pp. 870–880. DOI: 10.1143/PTP.28.870.

[10] Alessandro Strumia and Francesco Vissani. "Neutrino masses and mixings and..." In: (2006). arXiv: hep-ph/0606054 [hep-ph].

[11] Vernon D. Barger et al. "Matter Effects on Three-Neutrino Oscillations". In: *Phys. Rev.* D22 (1980), p. 2718. DOI: 10.1103/PhysRevD.22.2718.

[12] Stefano Dell'Oro et al. "Neutrinoless double beta decay: 2015 review". In: *Adv. High Energy Phys.* 2016 (2016), p. 2162659. DOI: 10.1155/2016/2162659. arXiv: 1601.07512 [hep-ph].

[13] M. Aker et al. "An improved upper limit on the neutrino mass from a direct kinematic method by KATRIN". In: *Phys. Rev. Lett.* 123 (2019), p. 221802. DOI: 10.1103/PhysRevLett.123.221802. arXiv: 1909.06048 [hep-ex].

[14] Steven Weinberg. "Baryon and Lepton Nonconserving Processes". In: *Phys. Rev. Lett.* 43 (1979), pp. 1566–1570. DOI: 10.1103/PhysRevLett.43.1566.

[15] Tao Peng, Michael J. Ramsey-Musolf, and Peter Winslow. "TeV lepton number violation: From neutrinoless double-β decay to the LHC". In: *Phys. Rev.* D93.9 (2016), p. 093002. DOI: 10.1103/PhysRevD.93.093002. arXiv: 1508.04444 [hep-ph].

[16] Rabindra N. Mohapatra and Goran Senjanovic. "Neutrino Mass and Spontaneous Parity Nonconservation". In: *Phys. Rev. Lett.* 44 (1980), p. 912. DOI: 10.1103/PhysRevLett.44.912.

[17] Seungwon Baek, Hiroshi Okada, and Kei Yagyu. "Flavour Dependent Gauged Radiative Neutrino Mass Model". In: *JHEP* 04 (2015), p. 049. DOI: 10.1007/JHEP04(2015)049. arXiv: 1501.01530 [hep-ph].

[18] Ernest Ma. "Radiative inverse seesaw mechanism for nonzero neutrino mass". In: *Phys. Rev.* D80 (2009), p. 013013. DOI: 10.1103/PhysRevD.80.013013. arXiv: 0904.4450 [hep-ph].

[19] O. Cremonesi and M. Pavan. "Challenges in Double Beta Decay". In: *Adv. High Energy Phys.* 2014 (2014), p. 951432. DOI: 10.1155/2014/951432. arXiv: 1310.4692 [physics.ins-det].

[20] D. R. Artusa et al. "Exploring the Neutrinoless Double Beta Decay in the Inverted Neutrino Hierarchy with Bolometric Detectors". In: *Eur. Phys. J.* C74 (2014), p. 3096. DOI: 10.1140/epjc/s10052-014-3096-8. arXiv: 1404.4469 [nucl-ex].

[21] J. Schechter and J. W. F. Valle. "Neutrinoless Double beta Decay in SU(2) x U(1) Theories". In: *Phys. Rev.* D25 (1982), p. 2951. DOI: 10.1103/PhysRevD.25.2951.

[22] Jonathan Engel and Javier Menéndez. "Status and Future of Nuclear Matrix Elements for Neutrinoless Double-Beta Decay: A Review". In: *Rept. Prog. Phys.* 80.4 (2017), p. 046301. DOI: 10.1088/1361-6633/aa5bc5. arXiv: 1610.06548 [nucl-th].

[23] J. Barea, J. Kotila, and F. Iachello. "$0\nu\beta\beta$ and $2\nu\beta\beta$ nuclear matrix elements in the interacting boson model with isospin restoration". In: *Phys. Rev.* C91.3 (2015), p. 034304. DOI: 10.1103/PhysRevC.91.034304. arXiv: 1506.08530 [nucl-th].

[24] J. Barea, J. Kotila, and F. Iachello. "Nuclear matrix elements for double-β decay". In: *Phys. Rev.* C87.1 (2013), p. 014315. DOI: 10.1103/PhysRevC.87.014315. arXiv: 1301.4203 [nucl-th].

[25] P. Domin et al. "Neutrino accompanied beta+-beta+-, beta+/EC and EC/EC processes within single state dominance hypothesis". In: *Nucl. Phys.* A753 (2005), pp. 337–363. DOI: 10.1016/j.nuclphysa.2005.03.003. arXiv: nucl-th/0411002 [nucl-th].

[26] P. Bamert, C. P. Burgess, and R. N. Mohapatra. "Multi - Majoron modes for neutrinoless double beta decay". In: *Nucl. Phys.* B449 (1995), pp. 25–48. DOI: 10.1016/0550-3213(95)00273-U. arXiv: hep-ph/9412365 [hep-ph].

[27] C. S. Aulakh and Rabindra N. Mohapatra. "Neutrino as the Supersymmetric Partner of the Majoron". In: *Phys. Lett.* 119B (1982), pp. 136–140. DOI: 10.1016/0370-2693(82)90262-3.

[28] R. Arnold et al. "Detailed studies of ^{100}Mo two-neutrino double beta decay in NEMO-3". In: *Eur. Phys. J.* C79.5 (2019), p. 440. DOI: 10.1140/epjc/s10052-019-6948-4. arXiv: 1903.08084 [nucl-ex].

[29] Giovanni Amelino-Camelia. "Quantum-Spacetime Phenomenology". In: *Living Reviews in Relativity* 16.1 (2013), p. 5. ISSN: 1433-8351. DOI: 10.12942/lrr-2013-5.

[30] Jorge S. Díaz, Alan Kostelecký, and Ralf Lehnert. "Relativity violations and beta decay". In: *Phys. Rev.* D88.7 (2013), p. 071902. DOI: 10.1103/PhysRevD.88.071902. arXiv: 1305.4636 [hep-ph].

[31] Don Colladay and V. Alan Kostelecký. "CPT violation and the standard model". In: *Phys. Rev.* D55 (1997), pp. 6760–6774. DOI: 10.1103/PhysRevD.55.6760. arXiv: hep-ph/9703464 [hep-ph].

[32] Don Colladay and V. Alan Kostelecký. "Lorentz violating extension of the standard model". In: *Phys. Rev.* D58 (1998), p. 116002. DOI: 10.1103/PhysRevD.58.116002. arXiv: hep-ph/9809521 [hep-ph].

[33] V. Alan Kostelecký. "Gravity, Lorentz violation, and the standard model". In: *Phys. Rev. D* 69 (10 2004), p. 105009. DOI: 10.1103/PhysRevD.69.105009.

[34] V. Alan Kostelecký and Jay Tasson. "Prospects for Large Relativity Violations in Matter-Gravity Couplings". In: *Phys. Rev. Lett.* 102 (2009), p. 010402. DOI: 10.1103/PhysRevLett.102.010402. arXiv: 0810.1459 [gr-qc].

[35] V. Alan Kostelecký and Neil Russell. "Data Tables for Lorentz and CPT Violation". In: *Rev. Mod. Phys.* 83 (2011), pp. 11–31. DOI: 10.1103/RevModPhys.83.11. arXiv: 0801.0287 [hep-ph].

[36] Jorge S. Diaz. "Limits on Lorentz and CPT violation from double beta decay". In: *Phys. Rev.* D89 (2014), p. 036002. DOI: 10.1103/PhysRevD.89.036002. arXiv: 1311.0930 [hep-ph].

[37] J. B. Albert et al. "First Search for Lorentz and CPT Violation in Double Beta Decay with EXO-200". In: *Phys. Rev.* D93.7 (2016), p. 072001. DOI: 10.1103/PhysRevD.93.072001. arXiv: 1601.07266 [nucl-ex].

[38] W. C. Haxton and G. J. Stephenson. "Double beta Decay". In: *Prog. Part. Nucl. Phys.* 12 (1984), pp. 409–479. DOI: 10.1016/0146-6410(84)90006-1.

[39] O. Azzolini et al. "Background Model of the CUPID-0 Experiment". In: *Eur. Phys. J.* C79.7 (2019), p. 583. DOI: 10.1140/epjc/s10052-019-7078-8. arXiv: 1904.10397 [nucl-ex].

[40] K. A. Olive et al. "Review of Particle Physics". In: *Chin. Phys.* C38 (2014), p. 090001. DOI: 10.1088/1674-1137/38/9/090001.

[41] F. Bellini et al. "Monte Carlo evaluation of the external gamma, neutron and muon induced background sources in the CUORE experiment". In: *Astropart. Phys.* 33 (2010), pp. 169–174. DOI: 10.1016/j.astropartphys.2010.01.004. arXiv: 0912.0452 [physics.ins-det].

[42] R. Arnold et al. "Technical design and performance of the NEMO 3 detector". In: *Nucl. Instrum. Meth.* A536 (2005), pp. 79–122. DOI: 10.1016/j.nima.2004.07.194. arXiv: physics/0402115 [physics].

[43] R. Arnold et al. "First results of the search of neutrinoless double beta decay with the NEMO 3 detector". In: *Phys. Rev. Lett.* 95 (2005), p. 182302. DOI: 10.1103/PhysRevLett.95.182302. arXiv: hep-ex/0507083 [hep-ex].

[44] R. Arnold et al. "Detailed studies of ^{100}Mo two-neutrino double beta decay in NEMO-3". In: (2019). arXiv: 1903.08084 [nucl-ex].

[45] R. Arnold et al. "Probing New Physics Models of Neutrinoless Double Beta Decay with SuperNEMO". In: *Eur. Phys. J.* C70 (2010), pp. 927–943. DOI: 10.1140/epjc/s10052-010-1481-5. arXiv: 1005.1241 [hep-ex].

[46] M. Auger et al. "The EXO-200 detector, part I: Detector design and construction". In: *JINST* 7 (2012), P05010. DOI: 10.1088/1748-0221/7/05/P05010. arXiv: 1202.2192 [physics.ins-det].

[47] M. Auger et al. "Search for Neutrinoless Double-Beta Decay in ^{136}Xe with EXO-200". In: *Phys. Rev. Lett.* 109 (3 2012), p. 032505. DOI: 10.1103/PhysRevLett.109.032505. URL: https://link.aps.org/doi/10.1103/PhysRevLett.109.032505.

[48] J. B. Albert et al. "Sensitivity and Discovery Potential of nEXO to Neutrinoless Double Beta Decay". In: *Phys. Rev.* C97.6 (2018), p. 065503. DOI: 10.1103/PhysRevC.97.065503. arXiv: 1710.05075 [nucl-ex].

[49] E. Fiorini et al. "A search for lepton non-conservation in double beta decay with a germanium detector". In: *Physics Letters B* 25.10 (1967), pp. 602 –603. ISSN: 0370-2693. DOI: https://doi.org/10.1016/0370-2693(67)90127-X. URL: http://www.sciencedirect.com/science/article/pii/037026936790127X.

[50] C. E. Aalseth et al. "The Majorana neutrinoless double beta decay experiment". In: *Phys. Atom. Nucl.* 67 (2004). [Yad. Fiz.67,2025(2004)], pp. 2002–2010. DOI: 10.1134/1.1825519. arXiv: hep-ex/0405008 [hep-ex].

[51] K.-H. Ackermann and more. "The Gerda experiment for the search of $0\nu\beta\beta$ decay in 76Ge". In: *The European Physical Journal C* 73.3 (2013), p. 2330. ISSN: 1434-6052. DOI: 10.1140/epjc/s10052-013-2330-0. URL: https://doi.org/10.1140/epjc/s10052-013-2330-0.

[52] V. D'Andrea. "Neutrinoless Double Beta Decay Search with ^{76}Ge: Status and Prospect with LEGEND". In: *54th Rencontres de Moriond on Electroweak Interactions and Unified Theories (Moriond EW 2019) La Thuile, Italy, March 16-23, 2019*. 2019. arXiv: 1905.06572 [hep-ex].

[53] A. Gando et al. "Measurement of the double-β decay half-life of ^{136}Xe with the KamLAND-Zen experiment". In: *Phys. Rev. C* 85 (4 2012), p. 045504. DOI: 10.1103/PhysRevC.85.045504. URL: https://link.aps.org/doi/10.1103/PhysRevC.85.045504.

[54] Edward Leming. "SNO+: Current Results and Future Prospects". In: *PoS* NOW2018 (2019), p. 027. DOI: 10.22323/1.337.0027.

[55] C. Alduino et al. "First Results from CUORE: A Search for Lepton Number Violation via $0\nu\beta\beta$ Decay of ^{130}Te". In: *Phys. Rev. Lett.* 120.13 (2018), p. 132501. DOI: 10.1103/PhysRevLett.120.132501. arXiv: 1710.07988 [nucl-ex].

[56] C. Alduino et al. "The CUORE cryostat: An infrastructure for rare event searches at millikelvin temperatures". In: (2019). DOI: 10.1016/j.cryogenics.2019.06.011. arXiv: 1904.05745 [physics.ins-det].

[57] Glenn F. Knoll. *Radiation detection and measurement - IV Edition*. Ed. by Inc. John Wiley & Sons. John Wiley & Sons, Inc., 2010.

[58] Valter Bonvicini et al. "A flexible scintillation light apparatus for rare event searches". In: *Eur. Phys. J.* C74.11 (2014), p. 3151. DOI: 10.1140/epjc/s10052-014-3151-5. arXiv: 1407.4608 [physics.ins-det].

[59] L. Gonzalez-Mestres and D. Perret-Gallix. "Detection of Low-energy Solar Neutrinos and Galactic Dark Matter With Crystal Scintillators". In: *Nucl. Instrum. Meth.* A279 (1989), pp. 382–387. DOI: 10.1016/0168-9002(89)91110-8.

[60] A. Alessandrello et al. "Development of a thermal scintillating detector for double beta decay of Ca-48". In: *Nucl. Phys. Proc. Suppl.* 28A (1992), pp. 233–235. DOI: 10.1016/0920-5632(92)90178-U.

[61] C. Bobin et al. "Alpha/gamma discrimination with a CaF-2(Eu) target bolometer optically coupled to a composite infrared bolometer". In: *Nucl. Instrum. Meth.* A386 (1997), pp. 453–457. DOI: 10.1016/S0168-9002(96)01185-0.

[62] S. Pirro et al. "Scintillating double-beta-decay bolometers". In: *Physics of Atomic Nuclei* 69.12 (2006), pp. 2109–2116. ISSN: 1562-692X. DOI: 10.1134/S1063778806120155. URL: https://doi.org/10.1134/S1063778806120155.

[63] C. Arnaboldi et al. "$CdWO_4$ scintillating bolometer for Double Beta Decay: Light and Heat anticorrelation, light yield and quenching factors". In: *Astropart. Phys.* 34 (2010), pp. 143–150. DOI: 10.1016/j.astropartphys.2010.06.009. arXiv: 1005.1239 [nucl-ex].

[64] C. Arnaboldi et al. "Characterization of ZnSe scintillating bolometers for Double Beta Decay". In: *Astropart. Phys.* 34 (2011), pp. 344–353. DOI: 10.1016/j.astropartphys.2010.09.004. arXiv: 1006.2721 [nucl-ex].

[65] J.W. Beeman et al. "ZnMoO4: A promising bolometer for neutrinoless double beta decay searches". In: *Astroparticle Physics* 35.12 (2012), pp. 813 –820. ISSN: 0927-6505. DOI: https://doi.org/10.1016/j.astropartphys.2012.02.013. URL: http://www.sciencedirect.com/science/article/pii/S0927650512000539.

[66] O. Azzolini et al. "First Result on the Neutrinoless Double-β Decay of ^{82}Se with CUPID-0". In: *Phys. Rev. Lett.* 120.23 (2018), p. 232502. DOI: 10.1103/PhysRevLett.120.232502. arXiv: 1802.07791 [nucl-ex].

[67] E. Armengaud et al. "LUMINEU: a search for neutrinoless double beta decay based on $ZnMoO_4$ scintillating bolometers". In: *J. Phys. Conf. Ser.* 718.6 (2016), p. 062008. DOI: 10.1088/1742-6596/718/6/062008. arXiv: 1601.04989 [nucl-ex].

[68] G. Wang et al. "CUPID: CUORE (Cryogenic Underground Observatory for Rare Events) Upgrade with Particle IDentification". In: (2015). arXiv: 1504.03599 [physics.ins-det].

[69] G. Wang et al. "R&D towards CUPID (CUORE Upgrade with Particle IDentification)". In: (2015). arXiv: 1504.03612 [physics.ins-det].

[70] "CUPID pre-CDR". In: (2019). arXiv: 1907.09376 [physics.ins-det].

[71] V. B. Mikhailik and H. Kraus. "Performance of scintillation materials at cryogenic temperatures". In: *Phys. Status Solidi* B247 (2010), p. 1583. DOI: 10.1002/pssb.200945500. arXiv: 1001.5461 [nucl-ex].

[72] O. Azzolini et al. "CUPID-0: the first array of enriched scintillating bolometers for $0\nu\beta\beta$ decay investigations". In: *Eur. Phys. J.* C78.5 (2018), p. 428. DOI: 10.1140/epjc/s10052-018-5896-8. arXiv: 1802.06562 [physics.ins-det].

[73] E. E. Haller et al. "NTD Germanium: A Novel Material for Low Temperature Bolometers". In: *Neutron Transmutation Doping of Semiconductor Materials*. Ed. by Robert D. Larrabee. Boston, MA: Springer US, 1984, pp. 21–36. ISBN: 978-1-4613-2695-3. DOI: 10.1007/978-1-4613-2695-3_2. URL: https://doi.org/10.1007/978-1-4613-2695-3_2.

[74] J. W. Beeman et al. "Double-beta decay investigation with highly pure enriched ^{82}Se for the LUCIFER experiment". In: *Eur. Phys. J.* C75.12 (2015), p. 591. DOI: 10.1140/epjc/s10052-015-3822-x. arXiv: 1508.01709 [physics.ins-det].

[75] I. Dafinei et al. "Production of ^{82}Se enriched Zinc Selenide (ZnSe) crystals for the study of neutrinoless double beta decay". In: *J. Cryst. Growth* 475 (2017), pp. 158–170. DOI: 10.1016/j.jcrysgro.2017.06.013. arXiv: 1702.05877 [physics.ins-det].

[76] G. Zuzel et al. "The DarkSide Experiment: Present Status and Future". In: *J. Phys. Conf. Ser.* 798.1 (2017), p. 012109. DOI: 10.1088/1742-6596/798/1/012109.

[77] J. W. Beeman et al. "Characterization of bolometric Light Detectors for rare event searches". In: *JINST* 8 (2013), P07021. DOI: 10.1088/1748-0221/8/07/P07021. arXiv: 1304.6289 [physics.ins-det].

[78] E. Andreotti et al. "^{130}Te Neutrinoless Double-Beta Decay with CUORICINO". In: *Astropart. Phys.* 34 (2011), pp. 822–831. DOI: 10.1016/j.astropartphys.2011.02.002. arXiv: 1012.3266 [nucl-ex].

[79] K. Alfonso et al. "Search for Neutrinoless Double-Beta Decay of ^{130}Te with CUORE-0". In: *Phys. Rev. Lett.* 115 (10 2015), p. 102502. DOI: 10.1103/PhysRevLett.115.102502. URL: https://link.aps.org/doi/10.1103/PhysRevLett.115.102502.

[80] S. Pirro. "Further developments in mechanical decoupling of large thermal detectors". In: *Nucl. Instrum. Meth.* A559 (2006), pp. 672–674. DOI: 10.1016/j.nima.2005.12.197.

[81] A. Alessandrello et al. "Measurements of internal radioactive contamination in samples of Roman lead to be used in experiments on rare events". In: *Nucl. Instrum. Meth.* B142.1-2 (1998), pp. 163–172. DOI: 10.1016/S0168-583X(98)00279-1.

[82] C. Arnaboldi et al. "A front-end electronic system for large arrays of bolometers". In: *JINST* 13.02 (2018), P02026. DOI: 10.1088/1748-0221/13/02/P02026. arXiv: 1710.06365 [physics.ins-det].

[83] S. Di Domizio et al. "A data acquisition and control system for large mass bolometer arrays". In: *JINST* 13.12 (2018), P12003. DOI: 10.1088/1748-0221/13/12/P12003. arXiv: 1807.11446 [physics.ins-det].

[84] O. Azzolini et al. "Analysis of cryogenic calorimeters with light and heat read-out for double beta decay searches". In: *Eur. Phys. J.* C78.9 (2018), p. 734. DOI: 10.1140/epjc/s10052-018-6202-5. arXiv: 1806.02826 [physics.ins-det].

[85] E. Gatti and P. F. Manfredi. "Processing the Signals From Solid State Detectors in Elementary Particle Physics". In: *Riv. Nuovo Cim.* 9N1 (1986), pp. 1–146. DOI: 10.1007/BF02822156.

[86] V. Radeka and N. Karlovac. "Least-square-error amplitude measurement of pulse signals in presence of noise". In: *Nuclear Instruments and Methods* 52.1 (1967), pp. 86 –92. ISSN: 0029-554X. DOI: https://doi.org/10.1016/0029-554X(67)90561-7. URL: http://www.sciencedirect.com/science/article/pii/0029554X67905617.

[87] David L. Lincoln et al. "First direct double-β decay Q-Value measurement of ^{82}Se in support of understanding the nature of the Neutrino". In: *Phys. Rev. Lett.* 110.1 (2013), p. 012501. DOI: 10.1103/PhysRevLett.110.012501. arXiv: 1211.5659 [nucl-ex].

[88] C. Alduino et al. "Analysis techniques for the evaluation of the neutrinoless double-β decay lifetime in ^{130}Te with the CUORE-0 detector". In: *Phys. Rev.* C93.4 (2016), p. 045503. DOI: 10.1103/PhysRevC.93.045503. arXiv: 1601.01334 [nucl-ex].

[89] C. Arnaboldi et al. "$CdWO_4$ scintillating bolometer for Double Beta Decay:Light and Heat anticorrelation, light yield and quenching factors". In: *Astropart. Phys.* 34 (2010), pp. 143–150. DOI: 10.1016/j.astropartphys.2010.06.009. arXiv: 1005.1239 [nucl-ex].

[90] Louis Lyons, Duncan Gibaut, and Peter Clifford. "How to Combine Correlated Estimates of a Single Physical Quantity". In: *Nucl. Instrum. Meth.* A270 (1988), p. 110. DOI: 10.1016/0168-9002(88)90018-6.

[91] J. W. Beeman et al. "Performances of a large mass ZnSe bolometer to search for rare events". In: *JINST* 8 (2013), P05021. DOI: 10.1088/1748-0221/8/05/P05021. arXiv: 1303.4080 [physics.ins-det].

[92] William H. Press et al. *Numerical Recipes in C, the art of scientific computing*. Ed. by CAMBRIDGE UNIVERSITY PRESS. Press Syndicate of the University of Cambridge, 2002.

[93] O. Azzolini et al. "Final result of CUPID-0 phase-I in the search for the ^{82}Se Neutrinoless Double Beta Decay". In: *Phys. Rev. Lett.* 123.3 (2019), p. 032501. DOI: 10.1103/PhysRevLett.123.032501. arXiv: 1906.05001 [nucl-ex].

[94] C. Alduino et al. "Measurement of the two-neutrino double-beta decay half-life of ^{130} Te with the CUORE-0 experiment". In: *Eur. Phys. J.* C77.1 (2017), p. 13. DOI: 10.1140/epjc/s10052-016-4498-6. arXiv: 1609.01666 [nucl-ex].

[95] S. Agostinelli et al. "GEANT4: A Simulation toolkit". In: *Nucl. Instrum. Meth.* A506 (2003), pp. 250–303. DOI: 10.1016/S0168-9002(03)01368-8.

[96] N. Yoshida and F. Iachello. "Two-neutrino double- decay in the interacting boson-fermion model". In: *Progress of Theoretical and Experimental Physics* 2013.4 (Apr. 2013). ISSN: 2050-3911. DOI: 10.1093/ptep/ptt007. eprint: http://oup.prod.sis.lan/ptep/article-pdf/2013/4/043D01/9719443/ptt007.pdf. URL: https://doi.org/10.1093/ptep/ptt007.

[97] *JAGS Version 4.3.0*.

[98] Irene Nutini. "The CUORE experiment: detector optimization and modelling and CPT conservation limit". PhD thesis. Gran Sasso Science Institute, 2018.

[99] O. Azzolini et al. "First search for Lorentz violation in double beta decay with scintillating calorimeters". In: *Phys. Rev.* D100.9 (2019), p. 092002. DOI: 10.1103/PhysRevD.100.092002. arXiv: 1911.02446 [nucl-ex].

[100] C. Fiorini et al. "Silicon Drift Detectors for Readout of Scintillators in Gamma-Ray Spectroscopy". In: *IEEE Transactions on Nuclear Science* 60.4 (2013), pp. 2923–2933. ISSN: 0018-9499. DOI: 10.1109/TNS.2013.2273418.

[101] Emilio Gatti and Pavel Rehak. "SEMICONDUCTOR DRIFT CHAMBER - AN APPLICATION OF A NOVEL CHARGE TRANSPORT SCHEME". In: *Nucl. Instrum. Meth.* A225 (1984), pp. 608–614. DOI: 10.1016/0167-5087(84)90113-3.

[102] C. Fiorini et al. "Gamma ray spectroscopy with CsI(Tl) scintillator coupled to silicon drift chamber". In: *IEEE Trans. Nucl. Sci* 44.6 (1997), pp. 2553–2560. DOI: 10.1109/23.650862.

[103] C. Fiorini, A. Gola, M. Zanchi, A. Longoni, P. Lechner, and H. Soltau *et al.* "Gamma-ray spectroscopy with $LaBr_3$:Ce scintillator readout by a silicon drift detector". In: *IEEE Nucl. Sci. Symp. Med. Imag. Conf. Rec.* 2005, pp. 230–234. DOI: 10.1109/NSSMIC.2005.1596243.

[104] A. D. Butt, R. Quaglia, C. Fiorini, P. Busca, M. Occhipinti, and G. Giacomini *et al.* "Development of a Detector for Gamma-Ray Spectroscopy Based on Silicon Drift Detector Arrays and 2" Lanthanum Bromide Scintillator". In: *IEEE Trans. Nucl. Sci* 62.5 (2015), pp. 2334–2342. DOI: 10.1109/TNS.2015.2464676.

[105] M. Moszynski, M. Balcerzyk, M. Kapusta, A. Syntfeld, D. Wolski, and G. Pausch *et al.* "$CdWO_4$ crystal in gamma-ray spectrometry". In: *IEEE Trans. Nucl. Sci* 52.6 (2005), pp. 3124–3128. DOI: 10.1109/TNS.2005.855704.

[106] M. Moszyski et al. "Energy resolution of scintillation detectors". In: *Nuclear Instruments and Methods in Physics Research Section A* (2016). ISSN: 0168-9002. DOI: 10.1016/j.nima.2015.07.059.

[107] J. D. Valentine, B. D. Rooney, and J. Li. "The light yield nonproportionality component of scintillator energy resolution". In: *IEEE Transactions on Nuclear Science* 45.3 (1998), pp. 512–517. ISSN: 0018-9499. DOI: 10.1109/23.682438.

[108] P. Dorenbos, J. T. M. de Haas, and C. W. E. van Eijk. "Non-proportionality in the scintillation response and the energy resolution obtainable with scintillation crystals". In: *IEEE Transactions on Nuclear Science* 42.6 (1995), pp. 2190–2202. ISSN: 0018-9499. DOI: 10.1109/23.489415.

[109] John D. Valentine and Brian D. Rooney. "Design of a Compton spectrometer experiment for studying scintillator non-linearity and intrinsic energy resolution". In: *Nuclear Instruments and Methods in Physics Research Section A: Accelerators, Spectrometers, Detectors and Associated Equipment* 353.1 (1994), pp. 37 –40. ISSN: 0168-9002. DOI: https://doi.org/10.1016/0168-9002(94)91597-0. URL: http://www.sciencedirect.com/science/article/pii/0168900294915970.

[110] John D. Valentine and Brian D. Rooney. "Benchmarking the Compton coincidence technique for measuring electron response non-proportionality in inorganic scintillators". In: 1 (1995), 404–408 vol.1. DOI: 10.1109/NSSMIC.1995.504254.

[111] Z. Guzik and T. Krakowski. "Algorithms for digital -ray spectroscopy". In: *Nukleonika* Vol. 58, No. 2 (2013), pp. 333–338. URL: http://yadda.icm.edu.pl/baztech/element/bwmeta1.element.baztech-03f42dd8-2384-402a-a62a-67538c01f48d.

[112] M. Beretta et al. "Non proportionality dependence on shaping time". In: *JINST* 12.04 (2017), P04007. DOI: 10.1088/1748-0221/12/04/P04007. arXiv: 1702.07614 [physics.ins-det].

[113] C. Fiorini, A. Longoni, and P. Lechner. "Single-side biasing of silicon drift detectors with homogeneous light-entrance window". In: *IEEE Transactions on Nuclear Science* 47.4 (2000), pp. 1691–1695. ISSN: 0018-9499. DOI: 10.1109/23.870862.

[114] R.T. Goldberg. *Low Temperature Electronics and HighTemperature Superconductivity*. Ed. by C.L. Claeys et al. The Electrochemical Society, Inc., 1995.

[115] L. Bombelli et al. "CUBE A low-noise CMOS preamplifier as alternative to JFET front-end for high-count rate spectroscopy". In: *Nuclear Science Symposium and Medical Imaging Conference (NSS/MIC), 2011 IEEE*. 2011, pp. 1972–1975. DOI: 10.1109/NSSMIC.2011.6154396.

[116] A. D. Butt et al. "Application of Silicon Drift Detectors for the Readout of a $CdWO_4$ Scintillating Crystal". In: *IEEE Trans. Nucl. Sci.* 65.4 (2018), pp. 1040–1046. DOI: 10.1109/TNS.2018.2810703.

[117] R. Quaglia, A. Abba, L. Bombelli, P. Busca, F. Caponio, and A. Cusimano *et al.* "Readout electronics and DAQ system for silicon drift detector arrays in gamma ray spectroscopy applications". In: *IEEE Nucl. Sci. Symp. Med. Imag. Conf. Rec.* 2012, pp. 922–926. DOI: 10.1109/NSSMIC.2012.6551241.

[118] L. Bardelli, M. Bini, P.G. Bizzeti, L. Carraresi, F.A. Danevich, and T.F. Fazzini *et al.* "Further study of $CdWO_4$ crystal scintillators as detectors for high sensitivity 2β experiments: Scintillation properties and pulse-shape discrimination". In: *Nuclear Instruments and Methods in Physics Research Section A: Accelerators, Spectrometers, Detectors and Associated Equipment* 569 (Dec. 2006), pp. 743–753. DOI: 10.1016/j.nima.2006.09.094.

[119] M. Sisti et al. "FLARES: A flexible scintillation light apparatus for rare event searches". In: *Nucl. Instrum. Meth.* A824 (2016), pp. 661–664. DOI: 10.1016/j.nima.2015.09.028.

[120] Arslan Dawood Butt. "Silicon drift detectors for X- and Gamma-ray detection applications". PhD thesis. Milan, Italy: Politecnico di Milano, 2016.

[121] A. G. J. MacFarlane, Jonathan P. Dowling, and Gerard J. Milburn. "Quantum technology: the second quantum revolution". In: *Philosophical Transactions of the Royal Society of London. Series A: Mathematical, Physical and Engineering Sciences* 361.1809 (2003), pp. 1655–1674. DOI: 10.1098/rsta.2003.1227. eprint: https://royalsocietypublishing.org/doi/pdf/10.1098/rsta.2003.1227. URL: https://royalsocietypublishing.org/doi/abs/10.1098/rsta.2003.1227.

[122] Marco Califano, Alex Zunger, and Alberto Franceschetti. "Direct carrier multiplication due to inverse Auger scattering in CdSe quantum dots". In: *Applied Physics Letters* 84.13 (2004), pp. 2409–2411. DOI: 10.1063/1.1690104. eprint: https://doi.org/10.1063/1.1690104. URL: https://doi.org/10.1063/1.1690104.

[123] Nam Joong et al. Jeon. "Compositional engineering of perovskite materials for high-performance solar cells". In: *Nature* 517 (2015), p. 486. DOI: 10.1038/nature14133. URL: https://doi.org/10.1038/nature14133.

[124] Eleanor Graham et al. "Light Yield of Perovskite Nanocrystal-Doped Liquid Scintillator". In: (2019). arXiv: 1908.03564 [physics.ins-det].

[125] L. Winslow and R. Simpson. "Characterizing Quantum-Dot-Doped Liquid Scintillator for Applications to Neutrino Detectors". In: *JINST* 7 (2012), P07010. DOI: 10.1088/1748-0221/7/07/P07010. arXiv: 1202.4733 [physics.ins-det].

[126] C. Aberle et al. "Optical Properties of Quantum-Dot-Doped Liquid Scintillators". In: *JINST* 8 (2013), P10015. DOI: 10.1088/1748-0221/8/10/P10015. arXiv: 1307.4742 [physics.ins-det].

[127] M. Beretta and others. "The ESQUIRE project: Quantum Dots as scintillation detectors". In: *IL NUOVO CIMENTO* 42 C (2019). DOI: 10.1393/ncc/i2019-19188-4.

[128] Meinardi et al. "Large-area luminescent solar concentrators based on 'Stokes-shift-engineered' nanocrystals in a mass-polymerized PMMA matrix". In: *Nature Photonics* 8 (2014), pp. 392399. DOI: 10.1038/nphoton.2014.54. URL: https://doi.org/10.1038/nphoton.2014.54.

[129] Yong Churl et al. Kim. "Printable organometallic perovskite enables large-area, low-dose X-ray imaging". In: *Nature* 550 (2017), p. 87. DOI: 10.1038/nature24032. URL: https://doi.org/10.1038/nature24032.

[130] *Low Temperature Electronics and HighTemperature Superconductivity*. Taylor& Francis Publisher, CRC Press, 2010.

List of Figures

2.1 Graphic view of the possible mass hierarchies of neutrinos . . . 9
2.2 Mass Diagram for double beta decays . . . 12
2.3 Double beta Decay Diagram . . . 13
2.4 Double Beta Decay spectra . . . 14
2.5 Effective Majorana Mass as a function of the lighest neutrino mass . . . 15
2.6 Matrix element for different Neutrinoless Double Beta Decay candidates . . . 16
2.7 Lorentz violating interaction effect on $2\nu\beta\beta$ spectrum of ^{82}Se . . . 19

3.1 ^{232}Th decay chain . . . 24
3.2 ^{238}U decay chain . . . 25
3.3 Bi-Tl and Bi-Po sequences in ^{238}U and ^{232}Th chains . . . 26
3.4 Ratio between 0ν signal and 2ν background for ^{82}Se and ^{130}Te . . . 27
3.5 Candidate $\beta\beta$ event in NEMO-3 Detector . . . 29

4.1 Picure and rendering of CUPID-0 detector . . . 37
4.2 Schematical representation of CUPID-0 cryostat . . . 38
4.3 Example of ZnSe and LD pulses from CUPID-0 . . . 39
4.4 ZnSe templates . . . 41
4.5 LD templates . . . 41
4.6 α/β selection in CUPID-0 . . . 42
4.7 ^{232}Th spectrum and response function of CUPID-0 . . . 43
4.8 ^{56}Co calibration and FWHM energy resolution evaluation . . . 43
4.9 Light/Heat scatter plot . . . 44
4.10 Unbinned maximum likelihood fit of the 2615 keV line . . . 45
4.11 Results for one-dimensional light/heat decorrelation . . . 46
4.12 $\overline{\mathrm{RG}}$ evaluation for Bottom (up) and Top (low) decorrelations on ^{56}Co calibration . . . 46
4.13 Minima region in Bottom/Top light plane . . . 47
4.14 $\overline{\mathrm{RG}}$ evaluation with two subsequent rotations, the first in the Bottom light/heat plane and the second in the Top light/Bottom corrected heat plane . . . 48
4.15 Result of light/heat decorrelation . . . 49
4.16 Renormalization of shape parameters . . . 50
4.17 Efficiency evaluation on ^{65}Zn peak . . . 50
4.18 Efficiency and Signal/Background ratio for Decay time cuts . . . 51
4.19 CUPID-0 background spectrum with selection cuts . . . 52
4.20 $\Gamma^{0\nu}$ posterior distribution . . . 53
4.21 CUPID-0 multiplicity one spectra . . . 55
4.22 CUPID-0 multiplicity two spectra . . . 56
4.23 Effect of surface and bulk *alpha* contamination . . . 57
4.24 Result of *alpha-alpha* delayed coincidences . . . 58

4.25 Spectrum of single pulses α-α delayed coincidences . . . 59
4.26 Pull distribution of the background model fit . . . 61
4.27 $\mathcal{M}_{1\beta/\gamma}$ and $\mathcal{M}_{1\alpha}$ reconstruction . . . 62
4.28 $\mathcal{M}_2$ and Σ_2 reconstruction . . . 63
4.29 Background components in $\mathcal{M}_{1\beta/\gamma}$ . . . 64
4.30 Simulation of standard and Lorentz-Violating $2\nu\beta\beta$ spectra for ^{82}Se . . . 67
4.31 Marginal posteriors for standard and Lorentz-Violating $2\nu\beta\beta$ normalization . . . 68
4.32 Total posterior distribution for $\mathring{a}^{(3)}_{\rm of}$ and corresponding $\mathcal{M}_{1\beta/\gamma}$reconstruction . . . 71
4.33 Posterior distribution for each systematic test family . . . 72
4.34 Posterior distribution for Bin, Threshold and Calibration systematics . . . 73
4.35 Posterior distribution for ^{40}K, ^{60}Co, ^{232}Th,^{238}U, ^{90}Sr systematics . . . 73

5.1 Effect on different wrapping and surface texture on scintillator resolution . . . 78
5.2 CCT diagram . . . 78
5.3 Measured non-proportionality behaviour for a $CdWO_4$ crystal . . . 80
5.4 SDD scheme . . . 81
5.5 Scheme of the Punch-trough polarization mechanism . . . 81
5.6 Simplified schematic of CUBE preamplifier . . . 83
5.7 Pixelate SDD detector picture . . . 85
5.8 Block diagram of the acquisition system . . . 86
5.9 Output of CUBE preamplifiers on the pixelate matrix . . . 87
5.10 Sum Pulse fit . . . 88
5.11 X-ray intercalibration of the cells . . . 89
5.12 Fit of calibration spectra . . . 89
5.13 Iterative gain correction . . . 90
5.14 Calibrated ^{228}Th spectrum . . . 90
5.15 Photoelectron Calibration . . . 91
5.16 Resolutions Calibrated . . . 91
5.17 Picture of large area SDD mounted on the holder . . . 92
5.18 Schematic view of the large area SDD acquisition system . . . 93
5.19 CUBE pulses for X-ray and γ-ray measurements . . . 94
5.20 ^{55}Fe and ^{241}Am measurement acquired with 3x3 cm^2 SDD operated at 150 K . . . 96
5.21 Relative calibration residual for ^{55}Fe and ^{241}Am peaks . . . 97
5.22 SDD drift times at different temperatures . . . 98
5.23 SDD drift times at different voltages and temperatures . . . 98
5.24 γ measurement with SDD coupled to 3×3×3 cm^3 $CdWO_4$ crystal . . . 100
5.25 γ measurement with SDD coupled to 2.3×1.5×2.3 cm^3 $CdWO_4$ crystal . . . 101
5.26 Resolution and light yield at 125 K with SDD coupled to 2.3×1.5×2.3 cm^3 $CdWO_4$ crystal . . . 101
5.27 Scintillation resolution obtained taking into account the asymmetric peak shape . . . 102
5.28 SDD+crystal rise-time distribution at different temperatures . . . 104
5.29 Perovskite crystal structure . . . 105
5.30 Perovskite and dye photoluminescence spectra . . . 106
5.31 Time evolution of perovskite+dye light emission . . . 107
5.32 Radioluminescence measurement of the Perovskite-sensitized dye . . . 107
5.33 Photoluminescence and absorption measurement on the disk specimen with Perovskite 108
5.34 Functioning scheme of the bar specimen . . . 109
5.35 Radioluminescence measurment on the bar specimen . . . 109
5.36 SiPM calibration spectrum . . . 111
5.37 Disk specimen measured with ^{241}Am . . . 112
5.38 Disk specimen measured with ^{224}Ra implanted source . . . 112
5.39 Bar speciment excited with ^{241}Am at different distances from the SiPM . . . 113

List of Tables

2.1 Actual limits on flavoured neutrino masses 10
2.2 Properties of most commonly investigated $0\nu\beta\beta$ candidates 12

4.1 Effect of different selection cuts 52
4.2 Results of CUPID-0 backgorund model 60
4.3 Background contributors in ROI 61
4.4 Results of the systematic test in the search for LV $2\nu\beta\beta$ 70

5.1 Properties of $0\nu\beta\beta$ candidates contained in available scintillation crystals 75
5.2 Properties of $CaMoO_4$ and $CdWO_4$ scintillation crystals 76
5.4 Major emission from ^{55}Fe and ^{241}Am 95